

Shining Light on the Dark Milky Way: Probing our Galaxy's Hidden Gas

Hiep Nguyen

Supervisors:

Dr. Joanne Dawson

Dr. Marc-Antoine Miville-Deschênes



MACQUARIE
University
SYDNEY · AUSTRALIA

A thesis submitted to Macquarie University in accordance with
the requirements of the degree of Doctor of Philosophy

Department of Physics and Astronomy

July 2019

Examiner's Copy

This thesis is submitted in fulfillment of the requirements of the degree of Doctor of Philosophy at Macquarie University, New South Wales. This thesis has not been submitted in whole or part for a higher degree to any other university or institution, either in Australia or overseas. This research has been accomplished with formal supervisions from Dr. Joanne Dawson (Department of Physics and Astronomy, Macquarie University, Australia) and Dr. Marc-Antoine Miville-Deschênes (AIM Laboratory, CEA-Saclay, France).

I certify that to the best of my knowledge and belief, all sources used and assistance received in the preparation of this thesis have been duly acknowledged. Some of the text found within has previously been published peer-reviewed scientific journals (The Astrophysical Journal and The Astrophysical Journal Supplement Series), on which I have been the first author or co-author.

Any views expressed in this dissertation are those of the author and do not represent those of Macquarie University.

Hiep Nguyen

Statement of Originality

The material presented in this thesis is original (except where cited) and has not been submitted to any university.

Each of Chapters 2 and 3 is a journal article, one published and one reviewed. My co-authors in these projects contributed general discussions for the work, but the data analysis, interpretation of results, and writing was led by me. Chapter 4 is a published journal article, to which I contributed to as a co-author. Specifically, I performed the data analysis and provided the text for Sections 2.1, 3 and 4.1.

Chapter 2 has been accepted for publication in *The Astrophysical Journal* (ApJ) on 16th June 2019 under the title “*Exploring the properties of warm and cold atomic hydrogen in the Taurus and Gemini regions*”.

Chapter 3 has been published in ApJ, Volume 862, Issue 1, under the title “*Dust-Gas Scaling Relations and OH Abundance in the Galactic ISM*” (Nguyen et al., 2018).

Chapter 4 has been published in *The Astrophysical Journal Supplement Series*, Volume 235, Issue 1, under the title “*Where is OH and Does it trace the Dark Molecular Gas (DMG)?*” (Li et al., 2018).

Hiep Nguyen

July 02, 2019

Acknowledgements

The three years of working for this thesis has been a life-changing experience for me, it would never possible without the support and encouragement from many people to whom I wish to thank today.

First and foremost, I would like to express my sincere gratitude to my supervisor, Joanne Dawson, for her continuous guidance throughout my PhD study, for her patience, motivation and stimulating conversations. Without her, this thesis would never have seen the light of day.

I am also grateful to my co-supervisor, Marc-Antoine Miville-Deschênes, for his encouragement and mentoring during my time in Paris and Stockholm. Thanks for patiently explaining the evolution of dust in space, the modified black-body fit and the dust radiance, and especially for listening to my unrealistic ideas of radio observations.

A special thanks goes to Min-Young Lee, Claire Murray, Snežana Stanimirović and Carl Heiles who shared their data, taught me Arecibo data reduction, followed my work closely and gave me much advice.

To my friends at Macquarie University, thank you for distracting me from stressful work and pulling me away from my desk for a cup of coffee or for some soccer game. Big thanks to Anita, Danica and Chika for helping me to improve my English. I am indebted to all my friends in Sydney and in Vietnam who were always so helpful in numerous ways. Special thanks to Florian and Thiên who have been always willing to go bush-walking with me almost every Sunday to explore the beautiful nature of Australia.

I would like to say a heartfelt thank you to my Mum, Dad, Kim Zung and Hữu Hùng for always believing in me and encouraging me to pursue my dreams, and also my young sister Thi Hòa for inspiring me during this challenging period.

And finally to my fiancé Thanh Hoài, who has been by my side throughout this PhD. Without her love and support, I do not know to where I would float in this world. Thank you.

Abstract

The evolution of galaxies is driven by the gas-to-stars cycle of matter in the interstellar medium (ISM). Throughout this process, the transition of hydrogen gas from its atomic (HI) to molecular (H_2) form is at the heart of the story. This transition is strongly coupled with the evolution of interstellar dust, as dust grains play a key role in the formation of molecules. However, despite decades of effort, there still remains much uncertainty on the constraints for the physical properties of both the gas and dust in the ISM, due to the limits of our observational capabilities. Presented here in this thesis are attempts to address some of these outstanding issues via observations of atomic and molecular media and detailed data analyses of thermal dust emission and reddening.

To begin with, I present a large-scale survey of HI emission and absorption using the Arecibo radio telescope, which explores the physical properties of the cold and warm atomic gas in the vicinity of five giant molecular clouds (GMCs): Taurus, California, Rosette, Mon OB1, NGC 2264. Strong HI absorption was detected towards all 79 background continuum sources in the 60×20 square degree area of the sky. Both Gaussian and pseudo-Voigt spectral decompositions were performed to derive the temperatures, optical depths and column densities of the cold and warm atomic gas. The properties of the cold gas in these regions of interest appear to be universal with an excitation (or spin) temperature of ~ 50 K, consistent with existing estimates. The fraction of warm gas is about 60%, and nearly 40% of this warm gas resides in thermally unstable regime 500–5000 K. There is more cold gas around GMCs than in diffuse regions. The optically thin assumption, on average, underestimates HI column density by $\sim 24\%$. Comparing the total HI column densities with those derived under the optically thin assumption also allowed me to assess the impact of opacity effects, and determine the most suitable method for opacity correction – that is to apply region-dependent uniform spin temperatures for available HI emission data.

Next, I dived into several data sets including opacity-corrected HI column densities from the Arecibo Millennium Survey and 21-SPONGE, together with thermal dust emission data from the

Planck satellite, new dust reddening maps from Pan-STARRS 1 and 2MASS, newly published Millennium Survey OH data, and follow-up CO emission observations. In combining all of these datasets, I confirmed linear correlations between dust optical depth τ_{353} , dust reddening $E(B-V)$ and total gas column density N_{H} in the range $(1-30) \times 10^{20} \text{ cm}^{-2}$, along atomic sightlines with no molecular gas detections. I found a 60% higher $N_{\text{H}}/E(B-V)$ ratio than the current “standard” value, and was able to disentangle the effects of dust grain evolution and so-called “dark gas” (the gas component not detected by HI and CO) on the variation of dust opacity $\sigma_{353} = \tau_{353}/N_{\text{H}}$. I also derived an OH/H₂ abundance ratio of $X_{\text{OH}} \sim 1 \times 10^{-7}$, finding no evidence for systematic trends in X_{OH} with molecular column density N_{H_2} in the range $N_{\text{H}_2} \sim (1-100) \times 10^{20} \text{ cm}^{-2}$. These results suggest that the OH molecule may be used as a reliable tracer for the molecular ISM this range, which includes sightlines with both CO-dark and CO-bright gas.

Finally, I was involved as co-author in a third project on OH emission-absorption measurements and dark molecular gas. We used OH absorption measurements from the Arecibo Millennium Survey and our own follow-up CO survey. The derived excitation temperatures of the two OH main lines at 1665 and 1667 MHz peak at $\sim 3.5 \text{ K}$, close to the background continuum temperature (CMB + synchrotron), providing an explanation for why OH is often difficult to detect in emission. The OH main lines are optically thin with optical depths always below 0.25; and in general these lines are not in local thermodynamic equilibrium, with a difference in excitation temperatures of $|T_{\text{ex}}(1667) - T_{\text{ex}}(1665)| < 2 \text{ K}$. About half of all detected OH absorption components do not have corresponding CO emission detections. This implies that the OH ground-state main lines trace more effectively molecular gas than traditional CO emission. In this work, I performed all the OH analysis, which is the main part of this study. However, I did not contribute to the discussions on CO analysis and the dark molecular gas.

Contents

Statement of Originality	v
Acknowledgements	vii
Abstract	ix
Contents	xi
List of Figures	xiii
List of Tables	xvii
1 Introduction	1
1.1 The Interstellar Medium: A multiphase structure	3
1.2 Thermal states of atomic hydrogen: Theory to observations	5
1.2.1 Theoretical models of H I	5
1.2.2 Observations of neutral atomic ISM	9
1.3 Evolution from CNM to molecular clouds	14
1.3.1 CNM to molecular clouds	14
1.3.2 Formation of H ₂ and CO	16
1.4 Interstellar dust	19
1.4.1 Interstellar dust extinction	19
1.4.2 Dust emission	21
1.4.3 Evolution of interstellar dust	22
1.4.4 Correlation between gas and dust	25
1.5 Dark gas in the ISM	28

1.5.1	What is dark gas?	28
1.5.2	Contribution and distribution of dark gas	30
1.5.3	OH as a tracer of diffuse molecular clouds	31
1.5.4	Dust as a tracer of dark gas	34
1.6	Observational techniques used in the thesis	34
1.6.1	Radiative transfer	34
1.6.2	Absorption and emission technique for HI	39
1.6.3	OH column density	41
1.7	Thesis outline	44
2	Properties of warm and cold atomic hydrogen in the Taurus and Gemini regions	45
3	Dust – gas relations and OH abundance	77
4	OH as a reliable tracer of “CO-dark” gas	97
5	Conclusions and future work	115
5.1	Conclusions	115
5.2	Future work	121
	Bibliography	125

List of Figures

1.1	The gas cycle in the interstellar medium. Credits: R. Gendler, the FORS Team, D. Malin, SAO/Chandra, D.Thilker.	5
1.2	Pressure-density diagram of atomic gas. Left panel: Thermal equilibrium curve for the atomic ISM (thick line), taken from Jenkins & Tripp (2011). Portions of this that have positive slopes are thermally stable and form the distinct phases: warm neutral medium (WNM) and cold neutral medium (CNM), as indicated. The portion of the curve where the slope is negative corresponds to thermally unstable gas (UNM) (see Figure 1 in Jenkins & Tripp 2011 for more details). Right panel: Gas mass fraction from high resolution 3-dimensional hydrodynamical simulations of converging atomic hydrogen flows by Audit & Hennebelle 2010. The solid black line shows the thermal equilibrium curve. The isothermal curves are shown as dashed-dotted lines ($T = 5000$ K left, 200 K right). The dashed curve illustrates the Hugoniot curve of shocked gas. The region between the dotted curves is the region where the gas is thermally unstable.	7
1.3	Hydrogen 21 cm line from the spin-flip transition. Credits: Pearson Education, Inc., publishing as Pearson Addison-Wesley (2008).	9
1.4	Different gas phases in a photodissociation region model, taken from Snow & McCall (2006). The model shows the abundances of species relative to H along the depth into the gas cloud. The external UV radiation enters from the left. . . .	15

- 1.5 Left panel: Extinction curves for different values of R_V (adopted from Draine, 2003). The inset shows a zoomed-in view of the curve at infrared wavelengths. Right panel: diffuse ISM extinction curve (taken from Compiègne et al., 2008). The dotted line plots the contribution polycyclic aromatic hydrocarbons (PAHs), the dashed line from Very Small Grains (VSGs) and the dashed-dotted line from Big Grains (BGs). The solid line shows the model of Compiègne et al. (2008). Diamonds represent the mean observational extinction curve from Savage & Mathis (1979). 20
- 1.6 Emission spectrum for the diffuse ISM, taken from (Compiègne et al., 2008). The thick solid line is a dust model for $N_H = 10^{20} \text{ cm}^{-2}$, with three dust components: big grains (dotted-dashed line), very small grains (dashed line) and PAHs (dotted line). Observational data are the $3.3 \mu\text{m}$ emission from cirrus associated with the molecular ring (triangle, Giard et al., 1994); the ISOCAM-CVF spectrum between $5 \mu\text{m}$ and $16 \mu\text{m}$ of the diffuse Galactic emission (light solid black line, Flagey et al., 2006); DIRBE measurements (squares, Arendt et al., 1998) and the FIRAS sub-millimeter spectrum (light solid black line, Boulanger et al., 1996). 22
- 1.7 Left panel: This figure is adopted from Figure 4 of Grenier et al. (2005). Map of the column densities of dark gas found in the dust halos, as measured from their γ -ray intensity with the reddening map. The map is in Galactic coordinates centered on $l = 70^\circ$. Right panel: Map of the excess column density derived from 857 GHz data (adopted from Planck Collaboration et al. 2011a). The map is shown in Galactic coordinates with the Galactic centre at the centre of the image. The grey mask shows the regions where no IRAS or CO data are available, regions with intense CO emission ($W_{\text{CO}} > 1 \text{ K km s}^{-1}$) and the Galactic plane ($|b_{\text{II}}| < 5^\circ$). The insets represent dark gas column density maps for the Chamaeleon, Aquila-Ophiuchus flare, Polaris flare and Taurus regions, as indicated. 31
- 1.8 Illustration of intensity passing through an isothermal medium. The change in intensity over an interval $d\tau$ is described by the radiative transfer equation (Equation 1.14) in terms of the absorption and emission coefficients (κ_ν and ϵ_ν respectively) of the medium. 35
- 1.9 Hyperfine splitting of the 1s ground state of atomic hydrogen (taken from Figure 8.1 of Draine (2011). 38

1.10	Energy level diagram for the $^2\Pi_{3/2}$ ground state of OH.	42
5.1	Locations of 194 radio continuum sources used in the GNOME survey for emission and absorption measurements of HI and OH, overlaid on the <i>Planck</i> map of dust optical depth, τ_{353} (Planck Collaboration et al., 2014a). The Galactic coordinates at center of the figure are ($l = 180^\circ$, $b = 0^\circ$).	122

List of Tables

1.1	Characteristics of the phases of the ISM (adapted from Tielens, 2005)	3
1.2	Rest frequencies and Einstein A coefficients of the four OH lines	43

1

Introduction

The flow of matter from the gas of the interstellar medium (ISM) to stars is at the heart of how galaxies in the Universe evolve. Stars form out of clouds of molecular gas and dust in the densest and coldest regions of the ISM; however the reservoirs of raw fuel initially exist in the form of warm, diffuse atomic or hot ionised hydrogen. This means that a conversion of hot gas into cold molecular structures must take place throughout cosmic time. This process involves cooling and accumulating atomic gas up to the point where both density and the column-density of shielding material become high enough for molecules to form and survive. As a molecular cloud is formed, some regions within it will become denser than others, and will further condense until localised gravitational collapse begins, with the help of dust grains in removing the excess energy, and stars are formed. A comprehensive understanding of these gas transitions is crucial to the evolution of baryonic matter in galaxies – and our ability to observationally track material through all stages is key.

During their lifetime, stars enrich the ISM with heavy elements produced by nuclear fusion in their interior via stellar winds or supernova explosions. Part of this ejected matter is interstellar

dust, which is deeply entwined with the physics of the ISM, from thermodynamics and chemistry, through to star formation. Dust grains can act as a heating agent via the photoelectric effect, can be a catalytic chemical agent for the formation of molecular hydrogen, and can also provide the shielding necessary to protect molecules from dissociating radiation. The evolution of dust grains themselves is tied to gas phases and chemistry. Dust is in general well mixed with gas in the ISM, meaning that infrared (IR) emission and optical extinction (A_V) can be used as a proxy to trace gas column densities – a topic explored in this work.

Despite the impact of gas phase transitions and cosmic dust in building the star-formation factories of galaxies, observational constraints on the relationship between gas and dust, and between the gas phases themselves in different interstellar environments, are still far from complete. This thesis makes a contribution to this field; it is an observational study exploring the atomic and diffuse molecular media in our Milky Way Galaxy, focusing mainly on the parameter space between warm atomic gas and cold highly-molecular clouds. Here, I investigate the physical properties of the warm and cold neutral medium in the Galactic ISM, via HI absorption and emission measurements. I carry out spectral decompositions in order to tease apart the contributions and properties of the warm and cold HI gas along my lines of sight, using the derived parameters to drive a comparison of different opacity correction techniques to recover full total atomic column densities. The origins of this work came from a desire to understand better the so-called “dark” ISM – usually understood to be a combination of cold, opaque atomic gas not well seen in HI emission spectra, and diffuse molecular gas not well traced by CO. One part of this thesis will explore alternative techniques to observationally recover this dark gas, including molecular spectral line tracers such as OH, and the broadband emission and absorption from dust. An important aspect of these latter techniques is the conversion between dust observables and gas column. Accordingly, another part of this work attempts to calibrate these crucial gas-dust scaling factors over parts of parameter space, making use of the accurate HI measurements described above.

In this introductory section, I outline the key physics that supports the research carried out in this PhD thesis. Firstly, I give a brief overview of the multiphase Galactic ISM (§1.1), then discuss the theory and observations of the thermal states of hydrogen gas (§1.2), and briefly describe the process by which cool atomic gas transforms into molecular clouds (§1.3). Next, I will consider interstellar dust and gas-dust relations (§1.4), and review the properties of dark gas in the ISM, as well as the tools for tracing this often-undetected gas component (§1.5). Finally, I outline the key observational techniques used in this work (§1.6).

1.1 The Interstellar Medium: A multiphase structure

The interstellar medium is the matter and radiation that permeate the space between the stars in the Galaxy. The ISM matter is a mixture of gas, dust grains and cosmic rays, pervaded by magnetic fields. The electromagnetic radiation produced by stars and interstellar matter is called the interstellar radiation field (ISRF).

The ISM consists mainly of gas (71% hydrogen, 28% helium) and dust (1%); in the Milky Way, it accounts for approximately 10–15% of the baryonic matter. The Galactic ISM is extremely dilute, but highly inhomogeneous and multiphase with wide ranges of temperature and density, due to local differences in the dominant heating/cooling mechanisms, and the influence of dynamical processes. However, observations have shown that the ISM can be grouped into five phases according to its chemical and physical properties. From the coldest/densest to hottest/most diffuse, those phases are: molecular gas, atomic cold neutral medium (CNM), atomic warm neutral medium (WNM), warm ionized medium (WIM), hot (ionized) intercloud medium (HIM). Table 1.1 lists the basic physical conditions for each phase, the given values are just approximate.

Table 1.1: Characteristics of the phases of the ISM (adapted from Tielens, 2005)

Phases	T [K] ^a	n_{H} [cm ⁻³] ^b	ϕ_{v} [%] ^c	H [pc] ^d	State of hydrogen
Molecular	10	> 200	0.05%	75	molecular
CNM	80	50	1%	94	neutral atomic
WNM	8000	0.5	30%	220	neutral atomic
WIM	8000	0.1	25%	900	ionized
HIM	10 ⁶	0.003	50%	3000	ionized

^aTypical gas temperature.

^bTypical gas density.

^cVolume filling factor (very uncertain).

^dGaussian scale height.

In this study I am interested in the WNM, CNM and molecular clouds. The WNM contains at maximum about 75–90% of the Galactic HI mass and occupies ~30% of the ISM volume. It has a typical kinetic temperature of ~8000 K and density of ~0.5 cm⁻³. However, in actual fact a significant amount (~20–50%) of the WNM lies in the thermally unstable regime (the unstable neutral medium, UNM) with $T \sim 500\text{--}5000$ K (e.g. Heiles & Troland, 2003b, Roy et al., 2013b,

Murray et al., 2015). The CNM occupies only $\sim 1\text{--}4\%$ of the ISM volume, but accounts for $\sim 10\text{--}25\%$ of the total atomic mass within the Galaxy (e.g. Dickey et al., 2009). This cold gas is present almost everywhere in the Galactic ISM in the form of sheets or filaments (e.g. Gibson, 2002, Heiles & Troland, 2003b), however, it has been conventionally described as ‘clouds’ which may on occasion be misleading. The kinetic temperature and density of the CNM is typically ~ 80 K and $\sim 50\text{ cm}^{-3}$ (Wolfire et al., 2003). The Gaussian scale heights of the WNM and CNM in the Galactic disk are ~ 220 pc and ~ 94 pc, respectively (Tielens, 2005).

Molecular clouds are the coldest and densest component of the ISM, where the hydrogen primarily exists in the form of molecules (H_2) at a temperature of $10\text{--}20$ K and a density of $10^2\text{--}10^6\text{ cm}^{-3}$. Although molecular clouds occupy only $\sim 1\%$ of the total Galactic volume, they contain $\sim 40\%$ of the total mass of the ISM (e.g. Biswas, 2013). A best estimate of the Galactic H_2 mass to-date from combining multiple CO surveys (Heyer & Dame, 2015) is $(1.0 \pm 0.3) \times 10^9 M_\odot$; the molecular layer scale height (defined as the full width at half maximum of the layer thickness) rises from ~ 90 pc at a Galactocentric radius of $R = 2$ kpc to ~ 120 pc at $R = 8$ kpc, and to $\sim 300\text{--}500$ pc at much larger radii ($R = 10\text{--}18$ kpc). The (equal-sized bin) mass and size distributions of molecular clouds can be described by power-law functions, $dN/dX \sim X^{-\alpha_X}$ with N as the number of clouds and X representing either mass (M) or size (L). The largest molecular gas structures are giant molecular clouds (GMCs), typically $\sim 10\text{--}100$ pc in size, with masses of $10^4\text{--}10^6 M_\odot$. Observations show that they are located primarily within or close to the Galactic disk of our spiral galaxy (see e.g. Lada, 1976, Blitz & Thaddeus, 1980, Dame et al., 2001). In the denser regions of molecular clouds, dust and gas concentrate into filaments and clumps. These clumps are the sites of star formation, since they often contain substructures that are locally gravitationally unstable.

The ISM plays a vital role in the Galactic ecosystem as it is the medium through which matter and energy flow between gas and stars. Specifically, the ISM provides the fuel for star formation, and during their lifetime, stars fuse hydrogen into heavier elements and emit radiation into interstellar space, which both shapes and heats the ISM. After running out of nuclear fuel, stars die and eject part of their material (and energy) back into the ISM via supernovae explosions or stellar winds. This material can then form new molecular clouds and trigger a new cycle over again. The interstellar matter in the Galaxy thus undergoes a cycle as illustrated in Figure 1.1. After each generation of stars, the ISM is progressively enriched with more heavy elements, so that new stars will have a higher metallicity than older stars.

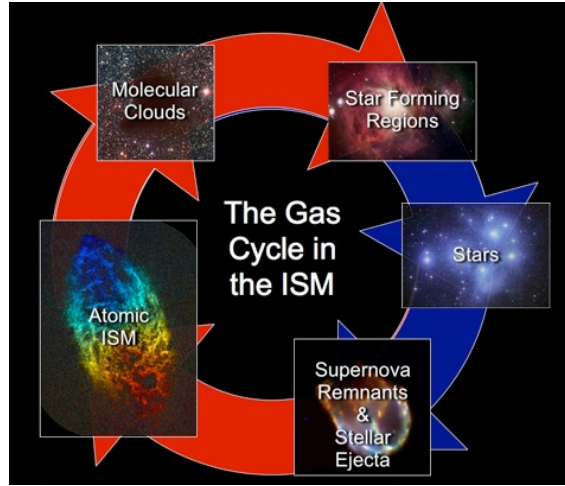


Figure 1.1: The gas cycle in the interstellar medium. Credits: R. Gendler, the FORS Team, D. Malin, SAO/Chandra, D.Thilker.

1.2 Thermal states of atomic hydrogen: Theory to observations

1.2.1 Theoretical models of H I

The thermodynamic properties of the atomic ISM are determined by the local balance between heating and cooling from various radiative and dynamical processes. The heating rate per unit volume (cm^3) is $n\Gamma$ ($\text{erg cm}^{-3} \text{ s}^{-1}$), where n is the number density of the gas, and Γ is the heating function, which does not depend on gas parameters (to a first approximation) such as temperature or number density. In contrast, the energy radiated away in cooling processes is basically produced by the collision of two particles; thus, cooling rates are proportional to the square of particle density and equal to $n^2\Lambda(T)$ ($\text{erg cm}^{-3} \text{ s}^{-1}$), where $\Lambda(T)$ is the cooling function, which strongly depends on the temperature of the gas. As a consequence, the thermal equilibrium of the interstellar gas is determined by the shape of the cooling curve $\Lambda(T)$.

There exist several heating mechanisms in the interstellar medium. However, depending on the local conditions, different ISM phases will be dominated by different heating sources. In the WNM, the photoelectric effect from small dust grains and large molecules (like polycyclic aromatic hydrocarbons, PAHs) is the primary heating source at densities $n > 0.1 \text{ cm}^{-3}$, but at lower densities cosmic rays and X-rays become the dominant heating agents. In the CNM, photoelectric heating dominates over its entire density range (Field et al., 1969, Wolfire et al., 1995, 2003). So, in general, the photoelectric effect plays a key role in heating for both neutral atomic phases, and the responsible radiation is FUV photons with energies $< 13.6 \text{ eV}$ – below the ionization threshold

of hydrogen. Photons with energies higher than the material's photoelectric work function will kick one or more electrons out of the surfaces of grains, then the ejected electrons will share the excess kinetic energy with other electrons or neutral atoms via elastic collisions.

In contrast, cooling relates to the process of converting the kinetic energy of the gas into radiation, which escapes and removes energy from the system. For neutral gas, cooling is mainly due to spectral line emission from collisionally excited transitions. The cooling of atomic gas is dominated by fine structure transitions emitted in the far-infrared: the dominant coolant for the CNM at $T \sim 100$ K is the C II fine structure line at $158 \mu\text{m}$ (at higher densities, spectral lines of C I at $370 \mu\text{m}$ and $609 \mu\text{m}$ become important); for the WNM at $T \lesssim 8000$ K the C II and O I fine structure lines are the dominant cooling mechanisms, but for $T \gtrsim 10,000$ K the gas mainly cools through the emission of H I Ly- α lines (tiny excitation but the abundance is high) (Wolfire et al., 1995). Since collisions initiate all cooling processes, their cooling rates are proportional to the square of gas density (n^2).

The two traditional phases of atomic gas exist because the pressure of the ISM falls in a range where the heating and cooling processes allow two thermally stable states: cool, dense gas in equilibrium with a surrounding warmer and more diffuse medium. Here the key physical parameter is the pressure, which is mostly set by the hydrostatic pressure of the disk (Ostriker et al., 2010). A number of theoretical studies have addressed the multiphase nature of the ISM. Field et al. (1969) published the first two-phase model of the atomic ISM, where heating by low-energy cosmic rays is balanced by radiative cooling from the excitation of H, He and C II. In this model, thermal instability under isobaric perturbation results in a thermally bistable neutral medium, in which gas with different temperatures and densities can coexist in thermal pressure equilibrium. The cold phase ($T \sim 100$ K) is in the form of dense clumps surrounded by a diffuse, warm intercloud medium ($T \sim 10^4$ K). Subsequently, various studies were carried out to refine the Field et al. (1969) model by considering other heating mechanisms such as photo-ionization by soft X-rays (Silk & Werner, 1969), the dissipation of hydro-magnetic waves (Silk, 1975), photoelectric emission from dust grains (Draine 1978) or large molecules (i.e. PAHs, Lepp & Dalgarno 1988), even from the mechanical work done by supernova blast waves (Cox 1979). However, the temperatures of both the cold and warm phases still remained at their characteristic ranges. McKee & Ostriker (1977) took into account the effect of supernovae on heating and ionization of the interstellar gas and updated to a three-phase model of the ISM, in which most of the space is filled with hot ionized medium (HIM). This third phase is shock-heated by supernova explosions to very high temperature ($T =$

4.5×10^5 K) with low density (typically $n \sim 3.5 \times 10^{-3} \text{ cm}^{-3}$). The HIM surrounds a warm photo-ionized corona ($T \sim 8000$ K, $n \sim 0.3 \text{ cm}^{-3}$, filling factor $\sim 20\%$), composed of a warm ionized medium (WIM) and warm neutral medium (WNM); the cold neutral, dense clouds are embedded deeply in the center with $T \sim 80$ K, $n \sim 40 \text{ cm}^{-3}$ and a filling factor of $\sim 2\text{--}4\%$. All phases in this model are found in comparable pressure equilibrium. This onion-shell model had a huge impact on our understanding of the multiphase nature of the ISM, however it is not really compatible with the observations. Indeed, most of the HI is not found as the skin of molecular clouds, and the ISM is highly dynamical and more complex than this rather static description.

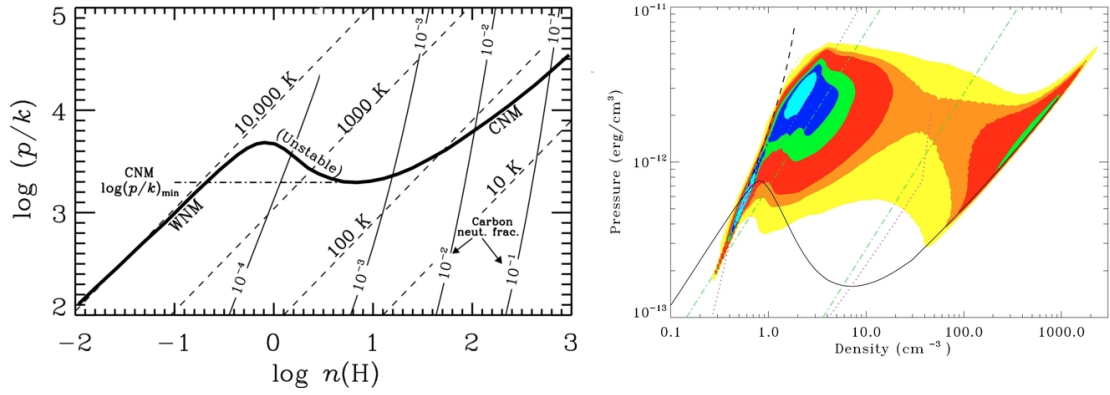


Figure 1.2: Pressure-density diagram of atomic gas. Left panel: Thermal equilibrium curve for the atomic ISM (thick line), taken from Jenkins & Tripp (2011). Portions of this that have positive slopes are thermally stable and form the distinct phases: warm neutral medium (WNM) and cold neutral medium (CNM), as indicated. The portion of the curve where the slope is negative corresponds to thermally unstable gas (UNM) (see Figure 1 in Jenkins & Tripp 2011 for more details). Right panel: Gas mass fraction from high resolution 3-dimensional hydrodynamical simulations of converging atomic hydrogen flows by Audit & Hennebelle 2010. The solid black line shows the thermal equilibrium curve. The isothermal curves are shown as dashed-dotted lines ($T = 5000$ K left, 200 K right). The dashed curve illustrates the Hugoniot curve of shocked gas. The region between the dotted curves is the region where the gas is thermally unstable.

Figure 1.2 illustrates a pressure-density (P - n) phase diagram for the atomic gas (adopted from Jenkins & Tripp, 2011). At thermal equilibrium the relation between pressure and volume density is non-monotonic. For certain pressures, the positive-gradient sections ($dP/dn > 0$) of this curve correspond directly to two stable phases at the same pressure but different temperatures and densities, e.g. $n, T_k = 5\text{--}120 \text{ cm}^{-3}, 30\text{--}400$ K for CNM, and $n, T_k = 0.03\text{--}1.3 \text{ cm}^{-3}, 5000\text{--}9000$

K for WNM (Wolfire et al., 2003). It is worth noting that this bistability of HI exists only for a narrow range of thermal pressures, with the maximum P_{\max} determined by the warm branch and the minimum P_{\min} by the cold branch, where $P_{\max} \leq 3P_{\min}$ (Field et al., 1969). If $P > P_{\max}$ all gas is CNM; and if $P < P_{\min}$ all gas lies in the warm phase. The negative-gradient section ($dP/dn < 0$) of the curve within between the CNM and WNM branches corresponds to gas that is in thermally unstable pressure equilibrium (UNM with $T_k = 500\text{--}5000$ K). If the pressure lies within this unstable range, any perturbation would cause the gas to naturally move quickly toward one of the two stable branches. Therefore, non-thermal processes (such as shocks driven by supernova, turbulence, time-dependent heating sources) are required to keep the gas in the thermally unstable regime.

Numerical simulations suggest the importance of dynamical processes in creating the phase structure of the ISM. From a two-dimensional model of turbulent interstellar gas including magnetic fields, self-gravity, the Coriolis force, stellar energy injection, and a realistic cooling function, Gazol et al. (2001) found that turbulent forcing could maintain a significant portion ($\sim 50\%$) of the gas in the thermally unstable regime. Three-dimensional hydrodynamical simulations of 2-phase, isothermal and polytropic compressible flows from Audit & Hennebelle (2010) found a UNM fraction of 30–50% depending on the strength of turbulence (as illustrated in the right panel of Figure 1.2). Mac Low et al. (2005) showed that a substantial fraction of the turbulent, magnetized gas driven by supernovae remains entirely out of the stable zone, and the amount of thermally unstable gas depends strongly on the supernova rate. In models including the magnetic field, and the circulation of matter between the disk and halo, the ISM gas driven by supernovae resides in a multiphase structure where up to 49% of the mass is concentrated in the thermally unstable regime (de Avillez & Breitschwerdt, 2005). In simulations of the collision between two superbubbles blown by time-dependent winds and supernovae, Ntormousi et al. (2011) found that most of the gas is organized in the form of dense, cold clumps and filaments, about 8–10% by mass in the thermally unstable range. More recently, simulations with detailed prescriptions of heating and cooling processes (including additional feedback from young stars and heating by FUV radiation field (e.g. Kim et al., 2013, Hill et al., 2018) find a thermally unstable fraction of no more than 20%. In general, the results from these numerical studies show that the fraction of UNM depends on the level of kinetic energy that the dynamical processes inject into the medium. If the dynamical timescale is shorter than the typical cooling timescale, more gas stays in the UNM.

In summary, the complex interaction between heating and cooling processes produces multiple

atomic ISM phases in stable pressure equilibrium. The mass fraction of each phase found in numerical studies depends strongly on the details of prescriptions for cooling and heating, turbulence and supernova rate. Connecting these models to reality requires detailed observational constraints on the physical properties of HI gas.

1.2.2 Observations of neutral atomic ISM

The HI 21 cm line

The atomic gas in the ISM has traditionally been traced by the 21 cm hyperfine structure line of neutral hydrogen (with a rest frequency of 1420.40575 MHz). The line arises from the transition between the two hyperfine levels of the HI ground state, which are slightly split by the interaction between the spins of the electron and proton. The state with parallel spins has higher energy. The 21 cm line of atomic hydrogen was detected for the first time in emission by Ewen & Purcell (1951) and Muller & Oort (1951). The observation of this hyperfine transition can be marked as the dawn of spectral-line radio astronomy.

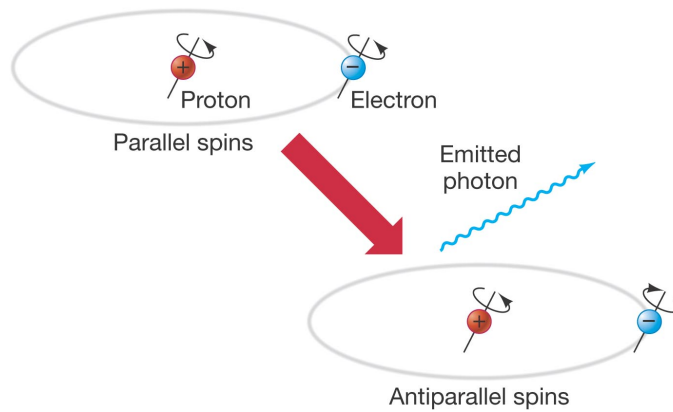


Figure 1.3: Hydrogen 21 cm line from the spin-flip transition. Credits: Pearson Education, Inc., publishing as Pearson Addison-Wesley (2008).

The transition is highly forbidden with an extremely small probability $A_{21\text{cm}} = 2.87 \times 10^{-15} \text{ s}^{-1}$, resulting in a radiative lifetime for the upper level of $1/A_{21\text{cm}} \sim 1.1 \times 10^7$ years. However, the 21 cm transition is readily detectable by radio telescopes because of the enormously high abundance of atomic hydrogen in the ISM. Moreover, in many environments in the atomic ISM, the time between collisions is much shorter than the radiative lifetime, and collisional de-excitation occurs before most atoms can decay spontaneously. This is followed later by other collisions, and therefore collisional excitation, meaning that a proportion of the hydrogen atoms will be in the

excited state at any time. The population balance between the two hyperfine levels is therefore determined entirely by collisions, so that Boltzmann equilibrium applies, with the excitation temperature referred to as the spin temperature, T_s . In such cases where the excitation of HI atoms is dominated by collisions, the spin temperature can be taken as the kinetic temperature.

Located in the radio range of the electromagnetic spectrum, the 21 cm emission from hydrogen penetrates through dust clouds and gives us a relatively complete map of the atomic hydrogen in the ISM. Observationally, the HI line is detected primarily in emission, but can also be observed in absorption against a sufficiently bright radio continuum sources (e.g. H II regions, radio galaxies, quasars or active galactic nuclei), or in self-absorption when the arrangement of gas along the line of sight permits it. Thus, while 21 cm emission is ubiquitous along any direction in the sky, 21 cm absorption is not.

Current observational understanding of neutral HI phases

HI was first detected in absorption by Hagen et al. (1955), and in general, the velocity structure of HI absorption is significantly different from its emission. The 21 cm emission lines always contain broader features than the absorption lines, some emission features do not have corresponding absorption, and the width of emission features are typically about three times broader than the width of absorption lines (Clark, 1965, Dickey et al., 1978, Dickey & Lockman, 1990). It was suggested that the differences between absorption and emission profiles either indicated a cloud-intercloud structure (Hagen et al., 1955) or arose from the inconsistency between the solid angles covered by the background source for absorption and the beam of the telescope that measures the emission (Greisen, 1973). Observations at high resolution with smaller beam sizes for both absorption and emission showed that the variation of HI spin temperature along the line of sight was the main culprit (Clark, 1965, Dickey & Lockman, 1990). These observations indeed indicate an inhomogeneous medium along the sightline with different temperatures, where the absorption features are associated with regions of cold gas. Along a line of sight, the cold gas clouds are quite discrete; for this reason, and due to their intrinsically smaller thermal line widths, they produce narrower lines than the widespread warm gas that contributes more strongly to the emission. These emission/absorption measurements are evidence for a multiphase atomic ISM, as predicted by the theoretical models (as discussed above in Section 1.2).

The combination of 21 cm emission and absorption along a line of sight provides the most direct method of estimating the physical properties of the atomic ISM. Such observational pairs

allow us to infer optical depths, temperatures (either spin temperatures or upper limits to kinetic temperature) and column densities – the important parameters for observationally distinguishing the different phases of HI gas including CNM, UNM and WNM, as well as constraining their fractions (see Section 1.6.2 for more details).

The cold gas is easy to detect in HI absorption, even with low sensitivity observations, due to its high optical depth (Dickey et al., 1977, 1983, Payne et al., 1978, Braun & Walterbos, 1992, Heiles & Troland, 2003a, Kanekar et al., 2003, Begum et al., 2010, Roy et al., 2013b, Stanimirović et al., 2014, Murray et al., 2015). During the last few decades, observational studies have shown that CNM temperatures range from ~ 10 – 300 K (e.g. Dickey et al. 1978, Heiles & Troland 2003b, Murray et al. 2018b), consistent with the predictions of theoretical models. The CNM can be found throughout the Galaxy, with its mean spin temperature staying at nearly constant with Galactic radius up to 25 kpc (~ 50 K, e.g. Dickey et al. 2003, Strasser et al. 2007, Dickey et al. 2009). The high volume density of the CNM implies that the 21 cm transition should be thermalized by collisions (with electrons, protons and other H atoms), with the spin temperature approximately equal to the kinetic temperature (e.g. Kulkarni & Heiles 1988). The fraction of cold gas varies widely across the ISM (typically about 10–50%) and is poorly constrained (i.e. so are the other phases). However, it seems that more CNM resides in/around GMCs than in average fields of the ISM (Stanimirović et al., 2014). This likely supports a scenario of staged build-up for molecular clouds, in which a high CNM fraction is required for molecule formation. The observed CNM fraction is somewhat lower than the 40–70% range suggested from some simulations (e.g. Kim et al., 2014), but they do reproduce its large variation. More interestingly, the properties of individual CNM clouds (such as kinetic temperature, column density, Mach number) along random Galactic sightlines agree well with those in/around molecular clouds (Stanimirović et al., 2014). This may suggest a universality of cold HI properties. The results of the current work also point to a similar conclusion, however more measurements are needed to confirm this (if true).

Unlike the CNM, the WNM can be easily observed in 21 cm emission along any direction on the sky; but due to its low optical depth it requires extremely high sensitivity to detect WNM in absorption. The spin temperature of the WNM is expected to be lower than the kinetic temperature (e.g. Liszt 2001) because at low densities, collisions are insufficient to thermalize the 21 cm transition (e.g. Deguchi & Watson, 1985, Liszt, 2001) (but a strong Ly- α radiation field that permeates the WNM can couple the HI spin temperature to the motion of the ambient gas). Most recent observational studies have used indirect methods to infer the spin temperature and fraction of warm gas

along sightlines: (1) the Doppler temperature (upper limits to kinetic temperature) estimated from the line-widths of Gaussian components (Mebold et al. 1982; Heiles & Troland 2003b; Roy et al. 2013b; Murray et al. 2015) or (2) a single harmonic-mean spin temperature along full sightline (Kanekar et al. 2011; Roy et al. 2013a). These observations have found that a significant fraction of the neutral ISM lies in the thermally unstable temperature range of 500–5000 K (e.g. Dickey et al. 1977; Mebold et al. 1982; Kanekar et al. 2003; Heiles & Troland 2003b; Murray et al. 2015, 2018b). Namely, about 30% of the total gas column density in the Arecibo Millennium survey is thermally unstable (Heiles & Troland 2003b), and Roy et al. (2013b) claimed that at least 28% of the observed towards 33 compact extragalactic radio sources lies in the thermally unstable range. Murray et al. (2015) found a thermally unstable fraction of at most $\sim 20\%$ in the high sensitivity 21-SPONGE survey. Recently, Kalberla & Haud (2018) decomposed HI emission spectra from all-sky HI4PI survey (HI4PI Collaboration et al. 2016) and stated that $\sim 40\%$ of the local Galactic gas is thermally unstable. These UNM fractions are all basically compatible, particularly given that the statistics of absorption-emission studies are still relatively small.

A few efforts to directly measure the spin temperature of WNM from absorption have been carried out. Carilli et al. (1998) and Dwarakanath et al. (2002) measured WNM T_s values of 3600 K, 4800 K and 6000 K, somewhat higher than the T_s range of 1000–4000 K predicted from theoretical analysis (Liszt 2001; Wolfire et al. 2003). However, their small samples of a few sightlines do not allow them to state a solid conclusion, nor deduce the fractions of each gas phase. With a sample of 57 lines of sight from the high sensitivity 21-SPONGE survey using the VLA for absorption and the Arecibo single-dish for emission, Murray et al. (2018b) found the total mass fractions for the CNM, UNM, and WNM are 28%, 20%, and 52%, respectively. Nevertheless, they detected very little WNM from absorption with $1000 < T_s < 4000$ K, which indicates that the spin temperature of warm gas may be higher than analytical predictions.

In a general sense, the properties of the atomic ISM phases – especially the mass fraction and temperature of the WNM – are poorly constrained, both because of limits on our observational capabilities, and because of inherent uncertainties in the data analysis. This implies that detailed observations on large scales and in different regions are required to narrow down the parameter space of HI properties, and refine our understanding of its thermodynamic state. Furthermore, new approaches are also needed to reduce or eliminate the biases in the HI spectral line analysis.

Optical depth effects and opacity correction

Combined emission and absorption measurements provide a direct way to estimate the optical depth and spin temperature, the two crucial parameters for determining the column density of HI gas. The column density under the optically-thin assumption (N_{HI}^*) is proportional to the brightness temperature, hence, can be readily obtained from emission profiles. However, this assumption may miss a significant amount of gas mass because the emission includes not only contributions from warm, optically-thin gas, but also from cold, optically-thick gas.

Recent studies using absorption-emission measurements toward strong continuum background sources showed that the true (opacity-corrected) N_{HI} is approximately equal to N_{HI}^* only in low column density regimes with $N_{\text{HI}} < 5 \times 10^{20} \text{ cm}^{-2}$. For higher column densities, the optically thin assumption, on average, underestimates the true column density by $\sim 10\%$, but these underestimations also exhibit large variations, with values of up to 70% measured along high column density sightlines (Dickey et al. 2003, Heiles & Troland 2003b, Liszt 2014a, Lee et al. 2015, Murray et al. 2018a). The column density obtained from the optically thin approximation is hence a lower limit to the total HI column density.

The main difficulties in observing emission and absorption simultaneously are the requirement of a good signal-to-noise for absorption, and the limited number of strong radio continuum background sources. Therefore, it is almost impossible to build high resolution, large-area maps of the true HI column density outside of low column density regions where the optically thin assumption holds. In the case when emission/absorption pairs are not available, we alternatively have to apply some kind of opacity correction to the available emission data. A few methods have been used in recent studies; for example, Dickey et al. (2000), Lee et al. (2015) obtain a general linear correlation between $f = N_{\text{HI}}/N_{\text{HI}}^*$ and $\log_{10}(N_{\text{HI}}^*)$ from a known sample of emission-absorption pairs and apply this trend for specific regions; Liszt (2014b) and Remy et al. (2017) employed an isothermal correction assuming the uniform single spin temperature along all lines of sight; and Fukui et al. (2015) attempted to use dust optical depth to indirectly infer spin temperatures and optical depths.

Two of the papers (one published and one reviewed) presented in this thesis (Chapters 2 and 3) assess the importance of HI opacity effects. In particular, Nguyen et al. (2019, Chapter 2) carries out detailed comparisons of two methods of obtaining opacity-corrected HI column densities, finding that the correction for optical depth is region-dependent, and becomes more important in/around dense clouds.

1.3 Evolution from CNM to molecular clouds

1.3.1 CNM to molecular clouds

Molecular clouds (MCs) are the sites of star formation and play an important role in galaxy evolution. However, there remain open questions on how MCs themselves form and evolve. A standard picture is that MCs are formed in-situ from cold atomic gas (e.g. Woodward, 1976, Blitz & Thaddeus, 1980, Engargiola et al., 2003). Alternatively, they may form from the coagulation of molecular gas that pre-exists in the ISM (e.g. Scoville & Hersch, 1979, Kwan, 1979, Hausman, 1981, 1982, Elmegreen & Elmegreen, 1983, Kwan & Valdes, 1983, Tomisaka, 1984, Efremov, 1995, Pringle et al., 2001, Dobbs et al., 2008, Blitz & Rosolowsky, 2004, Dobbs et al., 2011, Hopkins et al., 2011). In principle, both scenarios may take place, for example, in galaxies/regions where atomic gas is predominant, the MCs may tend to form via the former scenario; but in galaxies/regions that contain more molecular gas, the formation of MCs may follow the latter.

Another related question is what are astrophysical mechanisms responsible for cloud formation. A number of mechanisms have theoretically been proposed: e.g. thermal instabilities (Field, 1965); gravitational instabilities (Goldreich & Lynden-Bell, 1965, Kim & Ostriker, 2001, 2007, Li et al., 2005, Wada et al., 2011); colliding flows from turbulence or stellar feedback (McCray & Kafatos, 1987, Gazol-Patiño & Passot, 1999, de Avillez, 2000, de Avillez & Mac Low, 2001, de Avillez & Breitschwerdt, 2005, Kim et al., 2011, Ntormousi et al., 2011); and Parker magnetic instabilities (or magnetic buoyancy instability) in which horizontal magnetic field lines rise or sink due to the buoyancy in the gravitational field, accumulating dense gas at the midplane (Parker, 1966, Mouschovias, 1974, Kim et al., 2002, Kim & Ostriker, 2006, Machida et al., 2009, Mouschovias et al., 2009). Yet, there is little consensus on which processes dominate. Each of these mechanisms could be at work over different sizes and timescales, thus different mechanisms may govern different environments in the ISM, potentially resulting in different cloud properties.

However, at any rate, all of these processes require the transition of atomic gas into molecular form. This transition involves accumulating significant column densities of H I, thus reducing or blocking external destructive UV radiation, protecting molecular species from photo-destruction and hence permitting the evolution from atomic to molecular gas. In addition, the rates for producing molecules need to be high enough, such that the atomic-to-molecular transformation can proceed on an appropriate astronomical timescales (at most a few 10^7 years). In general, the rate depends on the volume density of the gas, so the molecules form faster in denser regions. For

instance, since the time scale for H_2 formation is inversely proportional to the number density of the gas (n) by the order of $10^9/n$ Myr (Hollenbach & McKee, 1979), once the gas density exceeds 100 cm^{-3} , a large fraction of the hydrogen can convert into molecular form within the order of a few Myr. Recent surveys of atomic hydrogen have found that the fraction of CNM in or around molecular clouds is higher than in diffuse regions (Stanimirović et al. 2014), and that a significant amount of cold atomic hydrogen is present in the cores of molecular clouds and is mixed with molecular gas (Li & Goldsmith 2003, Krčo & Goldsmith 2010, Gibson 2010, Zuo et al. 2018). Both of these results underscore the importance of CNM in the formation and evolution of molecular clouds.

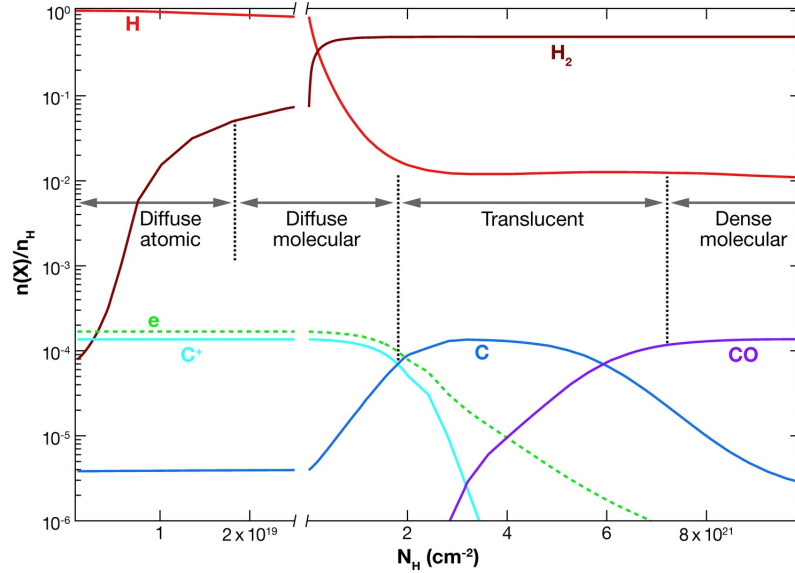


Figure 1.4: Different gas phases in a photodissociation region model, taken from Snow & McCall (2006). The model shows the abundances of species relative to H along the depth into the gas cloud. The external UV radiation enters from the left.

The intermediate layer between atomic and molecular media is (theoretically) called the photodissociation region (PDR), where the physical and chemical properties are controlled by the flux of penetrating FUV (6–13.6 eV) radiation from OB stars. These photons can ionize and heat the gas (through the photoelectric effect on dust grains) and dissociate molecules. Therefore, shielding is required for the molecular species to form and survive. Generally, dust grains can provide a shielding effect by absorbing and attenuating the incident UV field; self-shielding is very effective for H_2 even at relatively low column densities in the outer layers of a cloud; furthermore, molecules can be mutually shielded by other molecular species. The model PDR illustrated in

Figure 1.4 shows the variation in abundances of different species relative to H with depth into the cloud. H_2 dominates the molecular layers; CO cannot self-shield significantly and is photo-dissociated more easily in outer layers, thus CO forms in inner layers and its abundance relative to H_2 increases gradually to a maximum of $\sim 10^{-4}$ deep inside the cloud. As a result, the CO/H_2 abundance ratio is different at different depths inside the cloud, permitting a significant portion of molecular hydrogen gas that is not traced by CO emission lines (see Section 1.5 for detailed discussion).

Observations have shown a dramatic increase in molecular hydrogen column density from $N_{\text{H}_2} \sim 10^{15} \text{ cm}^{-2}$ to $\sim 10^{19} \text{ cm}^{-2}$, at a reddening of $E(B-V) \sim 0.08 \text{ mag}$, corresponding to a total gas column density of $N_{\text{H}} \sim 5 \times 10^{20} \text{ cm}^{-2}$ (Spitzer & Jenkins, 1975, Savage et al., 1977, Gillmon et al., 2006). This remarkable rise in H_2 fraction confirms the effect of molecular self-shielding (Field et al. 1966; Stecher & Williams 1967).

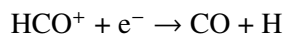
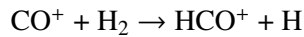
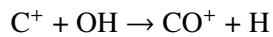
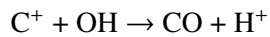
1.3.2 Formation of H_2 and CO

In the cool regions of the ISM, molecular hydrogen forms from the recombination of hydrogen atoms. The simplest process would be an encounter of two H atoms, followed by the emission of a binding photon ($\text{H} + \text{H} \rightarrow \text{H}_2 + h\nu$). However, the formation of H_2 in this gas phase reaction is very slow because the radiative association of two hydrogen atoms via a ro-vibrational quadrupole interaction is extremely weak (the transition of two ground-state hydrogen atoms is forbidden under the electric dipole approximation) and the collisional cross-section is too small to be effective in HI regions (Herzberg, 1955, Gould & Salpeter, 1963). Other possible formation pathways for H_2 in the gas phase via intermediate ions (like H^- or H_2^+) are also suppressed by the incident ISRF (Glover, 2003). It is generally accepted that H_2 is formed on dust grains, with the grain surface acting as a catalyst and enhancing the reaction rate by orders of magnitude (McCrea & McNally 1960, Gould & Salpeter 1963, Hollenbach & Salpeter 1971). Incident H atoms can be adsorbed onto the grain surface in different (weakly bound or strongly bound) sites, and can then move across the surface through thermal diffusion and quantum tunneling until encountering other bound atoms to form H_2 molecules, which leave the surface. Each of these processes depends on the temperatures of the gas and dust and the characteristics of the surface (Barlow & Silk 1976; Leitch-Devlin & Williams 1984). The molecular hydrogen formation efficiency is almost unity for grains with irregular surfaces (Hollenbach & Salpeter, 1971), or for dusty regions at low temperatures ($T < 20 \text{ K}$), then drops to ~ 0.3 at higher temperature ($100 < T < 500 \text{ K}$),

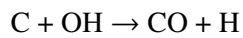
Cazaux & Tielens 2004). In this way, the volume formation rate of H_2 is governed by the densities as well as temperatures of gas and dust, and the ability of H atoms to stick onto the grain surfaces (described as a “sticking factor”). The characteristic timescale for H_2 formation in the CNM is $\sim 3 \times 10^7$ years, but can be sped up greatly by turbulence, which mixes gas in and out of transient dense regions (e.g. Glover & Mac Low, 2007, Mac Low & Glover, 2012) and also by local compression (Ballesteros-Paredes et al., 1999, Koyama & Inutsuka, 2000, Hartmann et al., 2001, Vázquez-Semadeni et al., 2006, Hennebelle et al., 2008, Heitsch & Hartmann, 2008, Inoue & Inutsuka, 2009). In warm regions ($T > 300$ K), H_2 can be formed from the radiative association of H ions (both positive and negative) and electrons (if necessary). In very dense regions (e.g. cool stellar atmospheres, young stellar object disks and jets), the hydrogen molecules can form via the three-body reactions.

While molecular hydrogen is by far the dominant species in molecular clouds, it unfortunately cannot be directly detected. The reason is that it is perfectly symmetric with no permanent dipole moment; thus the transitions of its low-energy excited levels have extremely small probabilities, meaning that its spectral lines are particularly weak. In addition, it also requires a significant amount of energy (approximately equivalent to 510 K) to excite its lowest rotational transition, whereas the temperature inside the molecular clouds where it is formed is about 10 K – just above absolute zero. Hence, most hydrogen molecules will enjoy relaxing in their ground state.

In practice, most of what we know about molecular clouds comes from the observations of other molecular species known as “tracers”. Chief among these is carbon monoxide (CO), the second most abundant molecule in the ISM. Unlike molecular hydrogen, CO can form efficiently by a chain of gas phase reactions. In general, CO formation requires the presence of H_2 and a crucial intermediate OH molecule. In typical conditions in the CNM, CO is rapidly formed from OH by fast ion-molecule reactions (Watson, 1974, van Dishoeck & Black, 1988):



In regions where neutral C is more abundant than the ion C^+ , neutral reactions can take place:



The ionisation in cool regions for all of these reactions is presumed to come from cosmic rays.

Numerical simulations of the formation of dense molecular clouds in slow (6.8 km s^{-1}) and

fast (13.6 km s^{-1}) colliding flows by Clark et al. (2012) show that there exists a rapid rise in the amount of H_2 from essentially zero to around one per cent (with respect to the available hydrogen) early in the evolution of the flows – within a short period of around 6.5 Myr in the slow flow, and 1.5 Myr in the fast flow. In contrast, the appearance of CO is significantly delayed with respect to the appearance of H_2 . In both flows, the authors found that significant amounts of CO do not form until around 2 Myr before the onset of star formation (which occurs at around 16 Myr for the slow flow and 4.4 Myr for the fast flow in their calculations). Furthermore, it is also found that the clouds produce very little emission from CO, thus they would probably not be identified as molecular clouds in observations. Another relevant aspect of H_2 and CO formation is that H_2 can be formed rapidly in relatively dense clumps, then quickly spread into low-density interclump gas, resulting in a significant fraction of warm H_2 gas existing within diffuse clouds (e.g. Valdivia et al., 2016).

The most commonly observed emission from CO is its $J=1 \rightarrow 0$ rotational transition at 2.6 mm – the microwave part of the spectrum. With an energy of only $\Delta E/k \sim 5 \text{ K}$, this electric dipole transition is easily excited in molecular gas with $T \sim 10 \text{ K}$. A huge number of observations using the ^{12}CO ($J=1-0$) line have been carried out to study the distribution and physical properties of the molecular ISM (e.g. Scoville & Solomon, 1975, Larson, 1981, Dame et al., 1987, 2001, Goldsmith et al., 2008, Heyer & Dame, 2015).

Despite the fact that CO may not be abundant in the most diffuse molecular regions, and that the ^{12}CO ($J=1-0$) emission line is often extremely optically thick (implying that it is impossible to directly convert brightness temperature to column density), a good correlation between CO velocity integrated intensity (W_{CO} [K km s^{-1}]) and H_2 column density has been measured – albeit for large ensembles of molecular clouds and with a large scatter (e.g. Sanders et al. 1984, Dame & Thaddeus 1985). The mass of molecular hydrogen can hence be estimated from the integrated intensity W_{CO} using a conversion factor – the so-called X -factor – defined as $X_{\text{CO}} \equiv N(\text{H}_2)/W_{\text{CO}}$. The average value of X_{CO} in the Milky Way is $\sim 2.0 \times 10^{20} \text{ cm}^{-2} (\text{K km s}^{-1})^{-1}$ (Bolatto et al. 2013), but this conversion factor depends on the temperature, density and metallicity. Other transitions from less common isotopologues such as ^{13}CO , C^{17}O and C^{18}O can also be used as alternatives, since these lines are often optically thin even at higher column densities, so a direct estimate of molecular column density under the LTE assumption can be obtained. However, ^{12}CO is still the most commonly-used tracer for the properties and distribution of the molecular ISM thanks to its strong intensity (high signal-to-noise).

1.4 Interstellar dust

Dust grains are macroscopic solid particles composed of mainly carbon, silicates, oxygen and iron. Interstellar dust is believed to be well mixed with the gas in the ISM, and contributes about 1% of the ISM mass. Dust absorbs and scatters short wavelength light (optical and ultra-violet) and re-emits it at longer wavelengths (infrared to millimeter). The interstellar extinction – the sum of absorption and scattering – and emission in the diffuse ISM (defined here and throughout this chapter as regions where extinction is low ($A_V < 1$) so that the ISM is illuminated uniformly by the ISRF) may be modelled as arising from three dust components: (1) big grains (BGs, ~ 10 – 500 nm) composed of silicate and a refractory mantle; (2) very small grains (VSGs, 1 – 10 nm) made of carbonaceous grains and (3) macro-molecules of Polycyclic Aromatic Hydrocarbons (PAHs) (Desert et al., 1990).

1.4.1 Interstellar dust extinction

Dust extinction is most reliably measured via the pair method, which compares two stars of the same spectral class, one with negligible foreground dust and the other affected by dust extinction. For a grain of typical size a , the cross-section for extinction, $\sigma_{\text{ext}}(\lambda)$, at wavelength λ is:

$$\sigma_{\text{ext}}(\lambda) = \pi a^2 Q_{\text{ext}}(\lambda). \quad (1.1)$$

Here Q_{ext} is the total extinction coefficient, $Q_{\text{ext}} = Q_{\text{abs}} + Q_{\text{sca}}$, with absorption and scattering coefficients Q_{abs} and Q_{sca} , respectively. In general, the extinction cross-section depends on the composition, size and shape of the grains.

With the assumption of a uniform distribution of dust along the line of sight, the optical depth $\tau_{\text{ext}}(\lambda)$ at wavelength λ along a sightline of volumetric dust density $n_{\text{dust}}(s)$ can be expressed as:

$$\tau_{\text{ext}}(\lambda) = \sigma_{\text{ext}}(\lambda) \int n_{\text{dust}}(s) ds = \sigma_{\text{ext}}(\lambda) N_{\text{dust}}, \quad (1.2)$$

where N_{dust} is the dust column density. The observed intensity, $I(\lambda)$, reduced from the incident intensity, $I_0(\lambda)$, by the presence of dust grains is:

$$I(\lambda) = I_0(\lambda) e^{-\tau_{\text{ext}}(\lambda)} \quad (1.3)$$

Hence, we define the extinction in magnitude A_λ at wavelength λ :

$$\begin{aligned} A_\lambda &= -2.5 \log_{10} \frac{I(\lambda)}{I_0(\lambda)} = 2.5 \log_{10}(e^{\tau_{\text{ext}}(\lambda)}) \\ &= 1.086 \tau_{\text{ext}}(\lambda) = 1.086 \sigma(\lambda) N_{\text{dust}} \end{aligned} \quad (1.4)$$

This expression shows that the extinction magnitude is proportional to the dust column density. The difference in extinction at two different wavelengths is known as the “color excess” (or reddening):

$$E(B - V) \equiv A_B - A_V = (B - V) - (B - V)_0 \quad (1.5)$$

where the quantities are in units of magnitudes, B is blue band centered at 440 nm and V is the visible band centered at 547 nm, $(B - V)$ is the observed difference and $(B - V)_0$ is the intrinsic difference of the star. Dust extinction depends on the wavelength of light, and this relation is described by an extinction curve (Figure 1.5). The pair method has been used to determine the extinction curves along many sightlines throughout the Milky Way, across a wide range of wavelengths from near-IR to ultraviolet. Observed dust extinction curves vary in shape from region to region in the Galaxy depending on grain sizes and/or compositions.

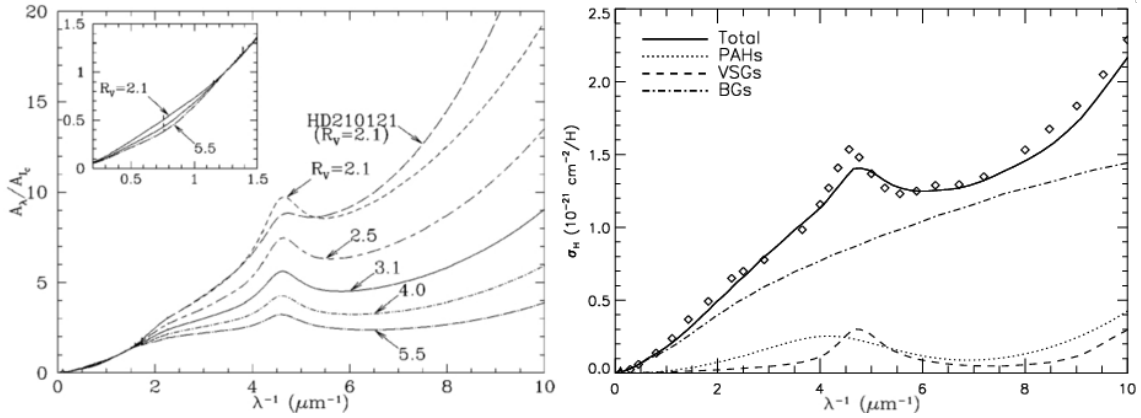


Figure 1.5: Left panel: Extinction curves for different values of R_V (adopted from Draine, 2003). The inset shows a zoomed-in view of the curve at infrared wavelengths. Right panel: diffuse ISM extinction curve (taken from Compiègne et al., 2008). The dotted line plots the contribution polycyclic aromatic hydrocarbons (PAHs), the dashed line from Very Small Grains (VSGs) and the dashed-dotted line from Big Grains (BGs). The solid line shows the model of Compiègne et al. (2008). Diamonds represent the mean observational extinction curve from Savage & Mathis (1979).

The “ratio of total to selective extinction”, defined as:

$$R_V \equiv \frac{A_V}{A_B - A_V} = \frac{A_V}{E(B - V)}, \quad (1.6)$$

is commonly characterised as the slope of the extinction curve in the optical band, with higher R_V corresponding to a flatter extinction curve. The Rayleigh scattering from small grains can result

in steep extinction with $R_V \sim 1.2$; whereas for large grains, $R_V \rightarrow \infty$ and the curve in this limit is flat, meaning that dust grains absorb all wavelengths equally, or are ideal “gray” absorbers. The observed R_V is an effective value and contains information on the size distribution of grains along the line of sight. Throughout the Milky Way, R_V varies from one sightline to another. Sightlines through diffuse ISM have an average slope of $R_V = 3.1$ (Savage & Mathis, 1979, Cardelli et al., 1989, Wegner, 1993, Schlegel et al., 2003), but those toward dense regions (where gas is primarily in molecular form) tend to have higher R_V (Foster et al., 2013, Schlafly et al., 2016), e.g. in the direction of HD 36982 $R_V \approx 5.7$ (Cardelli et al., 1989, Fitzpatrick, 1999). The smallest observed R_V is 2.1 in the direction of HD 210121 (Welty & Fowler, 1992).

1.4.2 Dust emission

Dust grains absorb optical/UV photons from starlight then re-radiate at infrared-millimeter wavelengths. The emission spectra of grains give information on their size distribution. Figure 1.6 illustrates the continuum radiation from $3 \mu\text{m}$ to $\sim 1 \text{ mm}$ of dust grains in the diffuse ISM; the wide wavelength range of dust emission reflects the fact that dust particles also emit over a large range of temperatures (Desert et al., 1988, Dwek et al., 1997). The far-infrared ($\lambda > 60 \mu\text{m}$) continuum arises predominantly from large grains in thermal equilibrium with the ambient radiation field at temperatures of $\sim 20\text{--}40 \text{ K}$ (Draine, 2003, Draine & Li, 2007). The emission from PAH molecules and VSGs dominates in the near- and mid-infrared regimes ($3 \sim 70 \mu\text{m}$) and consists of a continuum plus characteristic spiky emission features – the latter arising from PAHs experiencing stochastic heating.

In this study I make use of the FIR and submillimeter emission arising primarily from big grains. In general, big dust grains do not emit as blackbodies ($B_\lambda(T)$); they are imperfect radiators at long wavelengths, with a wavelength-dependent emission efficiency factor ($Q_{\text{em}} \propto \lambda^{-\beta}$ with $\beta = 1\text{--}2$). Instead, grains radiate as modified blackbodies (MBB), $I_\lambda \propto \lambda^{-\beta} B_\lambda(T)$. This means that the temperature of dust grains will be higher than that of a blackbody in thermal equilibrium with the same radiation field. As an illustrative example, consider a dust grain with radius a located at distance d away from a star of a luminosity L_ν . The temperature of the grain (T_d) can be estimated from the balance between absorption and emission:

$$\pi a^2 \int_0^\infty \frac{L_\nu}{4\pi d^2} Q_{\text{abs}}(\nu) d\nu = 4\pi a^2 \int_0^\infty Q_{\text{em}}(\nu) \pi B_\lambda(T_d) d\nu. \quad (1.7)$$

The left-hand side is the total energy absorbed by the grain, and the right-hand side is the total thermal energy emitted by the grain. In the diffuse ISM, BGs are in thermal equilibrium with

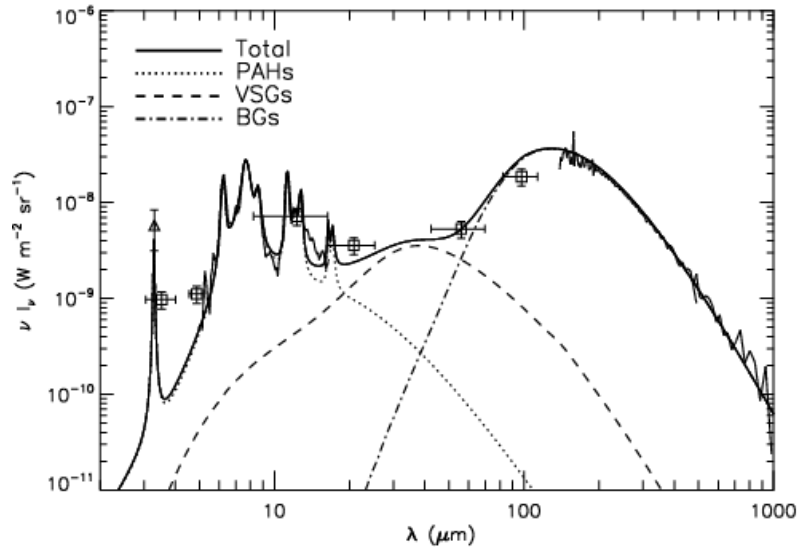


Figure 1.6: Emission spectrum for the diffuse ISM, taken from (Compiègne et al., 2008). The thick solid line is a dust model for $N_H = 10^{20} \text{ cm}^{-2}$, with three dust components: big grains (dotted-dashed line), very small grains (dashed line) and PAHs (dotted line). Observational data are the $3.3 \mu\text{m}$ emission from cirrus associated with the molecular ring (triangle, Giard et al., 1994); the ISOCAM-CVF spectrum between $5 \mu\text{m}$ and $16 \mu\text{m}$ of the diffuse Galactic emission (light solid black line, Flagey et al., 2006); DIRBE measurements (squares, Arendt et al., 1998) and the FIRAS sub-millimeter spectrum (light solid black line, Boulanger et al., 1996).

the local ISRF because their sizes are big enough to absorb photons on a shorter timescale than their cooling time (e.g. Draine, 2003, Draine & Li, 2007, Compiègne et al., 2011). These grains also have a distribution of sizes, so they must have a distribution of temperatures (Mathis et al., 1977, Boulanger, 1999); however this distribution of T_d must be very small (as seen in Draine & Lee, 1984). Thus using a single temperature for any given sightline has been shown to be a good description of the infrared-submillimeter emission spectrum (Planck Collaboration et al., 2014a). In practice, the thermal dust emission detected at FIR-submillimeter wavelengths by Planck, IRAS, COBE and DIRBE satellites showed the temperature of grains in the range of $T_d \sim 15\text{--}27 \text{ K}$ (e.g. Galametz et al., 2012, Planck Collaboration et al., 2014a).

1.4.3 Evolution of interstellar dust

Dust grains form generally in regions of high density, such as in the material ejected from stars (e.g. slow and dense stellar winds), proto-planetary nebulae, within the envelopes of red giants,

asymptotic giant branch (AGB) stars, planetary nebulae, novae and supernovae (e.g. Cernuschi & Codina, 1967, Field, 1974, Dwek & Scalo, 1980, Draine, 1990, McCray, 1993, Kozasa et al., 2009, Valiante et al., 2009). In this circumstance, the composition of the dust grains depends on the chemical abundances inside the stellar outflows. If the source stars are oxygen-rich ($O/C > 1$, e.g. M-type stars), nearly all C is bound in the form of CO, therefore the most abundant dust particles are oxygen-rich grains, e.g. silicates. Observations show that there exist strong $10\mu\text{m}$ silicate features in the spectra of outflows from oxygen-rich stars (Van Cleve et al., 1994, Speck et al., 2000, Bowey & Adamson, 2001, Bowey et al., 2003). Conversely, if the source stars are carbon-rich ($C/O > 1$, e.g. C-stars), then most of the O is bound in the form of CO, hence the carbonaceous solid particles like graphite, amorphous carbon, PAHs, SiC, etc. will be formed. Weak $11.3\mu\text{m}$ SiC emission features have been observed in the mid-IR spectra of C-stars, whereas the $10\mu\text{m}$ silicate feature is absent. If $C/O \approx 1$ (e.g. S-stars), both C and O are locked up in CO, and only small amount of dust may be formed; however dynamic processes are expected to enhance dust formation since they play an important role in circumstellar shells and the ejecta/outflows.

The timescale for dust grain supply from stellar sources (e.g. stellar winds and supernovae) is about $\sim 3 \times 10^9$ years (McKee, 1989, Jenkins, 1989, Tielens et al., 1994). However the lifetime of dust is $(\sim 2.2\text{--}4) \times 10^8$ years (Jones et al., 1994, 1996, Jones & Nuth, 2011) – about an order of magnitude shorter than the dust replenishment timescale. This suggests that there must exist an efficient mechanism of accretion in the ISM that permits dust grains to reform from the gaseous phase and that is not associated with the injection of grains (from stellar sources) into the ISM (Dwek & Scalo, 1980, Draine, 1990). A few potential processes have been proposed such as the accretion of metals onto small grains (Weingartner & Draine, 1999, Inoue, 2003, Draine, 2009), or the accretion of a mantle of high-sticking-coefficient volatile material onto non-volatile dust grains (Jones et al., 1994). However, these suggested mechanisms are not yet fully understood and are still under debate.

Observational and theoretical studies have shown that dust grains can also form and evolve within molecular clouds when the typical number density of hydrogen molecules is high enough ($\sim 10^3 \text{ cm}^{-3}$) (Draine, 1990, Ossenkopf & Henning, 1994, Hirashita, 2000, 2012, Stepnik et al., 2003, Ormel et al., 2011). According to recent theoretical models (e.g. Köhler et al., 2015, Jones et al., 2017), small dust grains can grow in these regions via a few steps: firstly, a core with an aromatic-rich mantle in environments well exposed to UV radiation will acquire an additional aliphatic-rich carbon mantle when moving into UV-shielded regions, then grain-grain collisions

will result in coagulation and the formation of larger grains from smaller ones and/or nanoparticles (e.g. Stepanik et al., 2003, Hirashita, 2012). Finally, when the temperature is low enough, a mantle of ices of CO_2 , H_2O , CH_4 , NH_3 (about $0.5\mu\text{m}$ across) can condense onto the surfaces of dust grains, leading to changes in both composition and structure. Numerical analysis (Chokshi et al., 1993, Ossenkopf, 1993) showed that the coagulation is efficient for collisions with small relative velocities ($\sim 1\text{--}10\text{ m s}^{-1}$). Recently, Planck Collaboration et al. (2014a, 2015), Remy et al. (2017), Okamoto et al. (2017) have presented evidence for the evolution of dust grains in the ISM from significant variations of dust opacity at 353 GHz (dust optical depth per H) as a function of total gas column density, particularly from diffuse atomic to high-density molecular regions. In the range of gas column densities characteristic of such regions, recent models have suggested that dust evolution should be primarily determined by the accretion of ice mantles on the surfaces of dust grains (e.g. Ysard et al., 2015, Jones, 2016).

By contrast, grains are destroyed by supernova shocks, or by interactions with other bodies such as gas, photons, cosmic rays and other grains. Gas-grain interactions are the primary mechanism for dust destruction. In this processes, dust is destroyed via collisions with high-velocity ions ($\gtrsim 50\text{ km s}^{-1}$) in high temperature, high density environments, releasing material back into the gas phase. These conditions are typically found in shock waves in the hot interstellar medium, produced by supernova explosions. In addition, collisions with cosmic rays can also disintegrate grains completely. Here, cosmic rays with lower kinetic energies (with velocity v_{CR}) have a stronger effect on dust particles (e.g. Byleveld et al., 1993, Draine & Salpeter, 1979, Jones, 2004) since the Rutherford scattering cross section for the interactions between cosmic rays and dust grains is proportional to v_{CR}^{-3} .

By absorbing photons, dust grains can erode via the evaporation of atoms/molecules from their surfaces (Tielens et al., 1994, Jones et al., 1996). Indeed, these photon-grain interactions can result in several possibilities. If the energy of the photon is smaller than the photoelectric work of the material, it will simply add to the thermal energy of the grain, then the grain will re-emit this amount of energy as a modified black-body at a temperature T . Conversely, if the photon has an energy higher than the material's photoelectric work, it can kick an electron, excite an atom/molecule, and eject the component off the grain. Generally, photons with energies higher than 5 eV can effectively strip atoms/molecules from the surfaces of dust particles. The evaporation thus is enhanced if the dust particles are in a strong visible/UV radiation field.

Dust grains can also be vaporised or melted via collisions with other grains at high relative

velocities ($\gtrsim 1 \text{ km s}^{-1}$) (Tielens et al., 1994, Jones et al., 1996). This process is important in high density clouds.

1.4.4 Correlation between gas and dust

Dust is in general well mixed with the gas in the interstellar medium, and it has long been recognized that observations of dust can be used as an effective tracer of total gas column density (N_{H}) (e.g. Jenkins & Savage, 1974, Bohlin et al., 1978, Hildebrand, 1983, Lada et al., 1994, Diplaz & Savage, 1994, Rachford et al., 2009, Planck Collaboration et al., 2014a). While dust-gas scaling factors that relate gas column density to measurables such as dust emissivity (FIR intensity per nucleon – I_{ν}/N_{H}), dust opacity (optical depth per nucleon – τ_{ν}/N_{H}) and specific reddening (reddening per nucleon – $E(B-V)/N_{\text{H}}$), are often assumed to be constant (Bohlin et al., 1978, Draine & Fraise, 2009, Jones et al., 2013, Liszt, 2014a, Lenz et al., 2017, Fukui et al., 2015), there are many reasons to expect these factors to change with environment. For example, variation of grain properties with ISM phase, or differences of conditions and physical properties in different regions (e.g. ISRF, metallicity, dust-to-gas mass ratio). This indicates that a more nuanced approach is required to well constrain the correlations between gas and dust.

To-date, relationships between dust observables and total gas column density have been calibrated empirically such that dust can be used to estimate N_{H} . As discussed above, two important observables of dust grains are extinction (including both the absorption and scattering of incident light from stars) and emission. The most well-known method to determine the dust-gas relation is to use H_2 UV absorption to measure N_{H_2} , use $\text{Ly}\alpha$ absorption to obtain the HI column density in front of UV-emitting OB stars, and then to use stellar spectra and color excess $E(B-V)$ to measure the dust extinction A_{V} . Such observations have established a strong correlation between visual extinction and the total hydrogen column density along typical sightlines through the Galactic ISM (Savage & Jenkins, 1972, Bohlin et al., 1978). In particular, Bohlin et al. (1978) derived a “standard” conversion between extinction and hydrogen column density in the diffuse ISM:

$$\frac{N_{\text{H}}}{E(B-V)} = 5.8 \times 10^{21} \text{ cm}^{-2} \text{ mag}^{-1}. \quad (1.8)$$

For $R_{\text{V}} = 3.1$, we can therefore write the ratio between total visual extinction, A_{V} , and total hydrogen column density as:

$$\frac{N_{\text{H}}}{A_{\text{V}}} \approx 1.87 \times 10^{21} \text{ cm}^{-2} \text{ mag}^{-1}. \quad (1.9)$$

The reddening fit from Fitzpatrick (1999) shows that $A_{I_C}/A_V = 0.554$ for Cousins I_C band with $\lambda = 0.802 \mu\text{m}$, this means that:

$$\frac{A_{I_C}}{N_H} \approx 2.96 \times 10^{-22} \text{ cm}^2 \text{ mag} \quad (1.10)$$

These ratios have been widely used as the current standard conversion between reddening (or extinction) and N_H . However, as Rachford et al. (2002) have pointed out, A_{I_C}/A_V is not universal for dust in the local ISM; it instead varies as R_V deviates from 3.1. More generally, the extinction per unit total gas column density increases with higher values of R_V :

$$\frac{A_{I_C}}{N_H} = [2.96 - 3.55 \left(\frac{3.1}{R_V} - 1 \right)] \times 10^{-22} \text{ cm}^2 \text{ mag} \quad (1.11)$$

Furthermore, recent studies using available HI 21 cm data and improved reddening maps have found significantly higher values of N_H/A_V (as high as $\sim 3 \times 10^{21} \text{ cm}^{-2} \text{ mag}^{-1}$; Planck Collaboration et al., 2014a, Liszt, 2014a, Lenz et al., 2017), using $R_V = 3.1$. Meanwhile, observations using X-ray absorption have found N_H/A_V ratios for the diffuse ISM typically ranging from $(1.8\text{--}2.2) \times 10^{21} \text{ cm}^{-2} \text{ mag}^{-1}$ (Gorenstein, 1975, Vuong et al., 2003, Güver & Özel, 2009, Pillitteri et al., 2013). These differences may come from several possible sources: the evolution of dust grains that leads to changes in grain properties in cold, dense regions (e.g. Goldsmith et al., 1997, Roman-Duval et al., 2014, Planck Collaboration et al., 2014a), changes in gas-to-dust mass ratio (e.g. Vuong et al., 2003), or different metal abundances in different regions (e.g. Vuong et al., 2003, Watson et al., 2011, Hasenberger et al., 2016).

The emission from dust grains can also be used as a proxy for the total hydrogen column density. This emission is in the FIR-to-millimetre range, and predominantly arises from the largest grains in thermal equilibrium with the local ISRF (Draine, 2003, Draine & Li, 2007). As mentioned above, FIR dust emission is believed to trace N_H better than the combination of HI and CO (deVries et al., 1987, Heiles et al., 1988, Blitz et al., 1990, Reach et al., 1994). However, the correlation between dust emission and total N_H is not observationally well constrained either.

Boulanger & Perault (1988) showed that the IR intensities from IRAS at $60\mu\text{m}$ and $100\mu\text{m}$ are correlated with N_{HI} , but that the IR emission to HI column density ratios vary significantly in different regions: $I_\nu(60\mu\text{m})/N_{\text{HI}} = (0.11\text{--}0.55) \text{ M Jy sr}^{-1} \text{ cm}^2$, and $I_\nu(100\mu\text{m})/N_{\text{HI}} = (0.51\text{--}2.4) \text{ M Jy sr}^{-1} \text{ cm}^2$. Planck Collaboration et al. (2014a) used *Planck* and IRAS data observed at 3000, 875, 545 and 353 GHz to model the spectral energy distributions of thermal dust emission and estimate the dust optical depth at 353 GHz (τ_{353}). Then, combining with total gas column densities measured from LAB survey HI (Kalberla et al., 2005), and CO from Dame et al. (2001),

these authors found a linear relationship between τ_{353} and N_{H} in low N_{HI} regimes (where there exists very little H_2): $\tau_{353} = \sigma_{353} N_{\text{H}}$ with the dust opacity $\sigma_{353} = (6.6 \pm 1.7) \times 10^{-27} \text{ cm}^2 \text{ H}^{-1}$ – consistent with the mean value measured by Planck Collaboration et al. (2014b) ($\sigma_{353} = (7.1 \pm 0.6) \times 10^{-27} \text{ cm}^2 \text{ H}^{-1}$). Nevertheless, their all-sky map of dust opacity shows clear variations in σ_{353} , ranging from $\sim (2\text{--}18) \times 10^{-27} \text{ cm}^2 \text{ H}^{-1}$, even in the diffuse atomic ISM at high latitudes where N_{H} is well constrained. Based on the same *Planck* maps, Fukui et al. (2015) derived a smaller σ_{353} of $\sim 4.8 \times 10^{-27} \text{ cm}^2 \text{ H}^{-1}$ by limiting their analysis to the hottest range of dust temperatures, under the assumption that the HI gas in such sightlines is truly optically thin. These σ_{353} values seem applicable only for low column densities in the diffuse ISM where dust properties are assumed to be uniform ($N_{\text{H}} < 5 \times 10^{20} \text{ cm}^2$, e.g. found by Boulanger et al. 1996). However, recent observational and theoretical studies have shown that the properties of dust grains may vary even within such diffuse gas, urging further caution in the usage and interpretation of these relationships.

As already mentioned above, grains are also known to evolve from the diffuse ISM to denser regimes (Köhler et al., 2012, 2015, Ysard et al., 2013, Planck Collaboration et al., 2011a, 2014c,a). Indeed, significant increases up to a factor of 2.5 in the dust opacity σ_{353} have been observed when moving from diffuse to the high-density, molecular regime (e.g., Planck Collaboration et al. 2014a, 2015, Remy et al. 2017, Okamoto et al. 2017). These variations may reflect changes in dust properties, and/or variation in the dust-to-gas ratio, but may also arise from the presence of an additional gas component that is untraced by HI and CO – the so-called “dark gas” (see Section 1.5). This ambiguity that arises from dust-only analyses cannot differentiate between a dust excess due to additional gas or to intrinsic variations in dust grain properties, in particular for the early suggestions of the existence for dark gas. The non-linearity of the relations between dust quantities (optical depths or reddening) and total gas column densities (Planck Collaboration et al., 2015, Remy et al., 2017), and their variations from region to region, have not yet diffused far in the community.

In this thesis work, with improved constraints on the total column densities along a sample of sightlines, I examine the correlations between total N_{H} dust reddening $E(B-V)$ and dust optical depth τ_{353} . Here I was able to separate the contributions of dark gas and the evolution of interstellar dust to the increase of opacity σ_{353} observed from diffuse to higher column densities. In addition, I found that $E(B-V)$ may be a more reliable proxy for total N_{H} than dust optical depth τ_{353} since the specific reddening $\sigma_V = E(B-V)/N_{\text{H}}$ is more stable than the dust opacity σ_{353} in the range of

$N_{\text{H}} = (1\text{--}30) \times 10^{20} \text{ cm}^{-2}$ (see Chapter 3 for more details).

1.5 Dark gas in the ISM

1.5.1 What is dark gas?

Traditionally, the quantity and distribution of the atomic ISM has been measured via the 21 cm HI emission line, and that of the molecular medium has most commonly been measured via CO emission. There is however a growing body of strong evidence for extra neutral gas undetected by either HI or CO. For instance, observations of interstellar dust show excess in both extinction and infrared emission with respect to what is inferred from HI and CO (Blitz et al. 1990, Reach et al. 1994, Meyerdierks & Heithausen 1996, Douglas & Taylor 2007, Roman-Duval et al. 2010, Planck Collaboration et al. 2011a, 2014c, Paradis et al. 2012). Significant diffuse γ -ray emission unaccounted for by 21 cm or 2.6 mm lines is found in the local ISM (Grenier et al. 2005, Abdo et al. 2010, Ackermann et al. 2011, 2012). Strong emission/absorption from interstellar molecules (e.g. OH, CH) have been detected toward lines of sight without corresponding CO emission (Wannier et al., 1993, Magnani & Onello, 1995, Liszt & Lucas, 1996, Barriault et al., 2010, Allen et al., 2012, 2015, Engelke & Allen, 2018). And the distribution of C^+ emission in the Galaxy has also revealed a large amount of an extra gas mass undetected by standard gas tracers (Pineda et al. 2013, Langer et al. 2010, 2014, Tang et al. 2016). This missing gas component is commonly referred to as “dark gas”, a term first coined by Grenier et al. (2005). It is worth noting that the early findings of the amount of dark gas from interstellar dust measurements were highly uncertain due to the assumption that the ISM dust linearly traces total gas column density.

The dark gas may lie in the molecular phase, the atomic form, or both; which one dominates is currently a topic of debate. Some authors have argued that optically thick cold HI dominates the dark gas, due to the opacity effect in HI measurements. Fukui et al. (2014, 2015) indirectly inferred the HI optical depth and spin temperature using *Planck* and *IRAS* dust emission data on large-scales at high Galactic latitudes ($|b| > 15^\circ$, excluding CO-bright areas). They estimated 2–2.5 times higher HI column densities than obtained under the optically thin approximation, then concluded that the optically thick HI with $\tau_{\text{HI}} \gtrsim 1$ dominates the local dark ISM. However, Fukui et al. (2014, 2015)’s measurements do not agree with any recent observations using direct measurements of HI spin temperature and optical depth (Dickey et al. 2000, 2003, Heiles & Troland 2003b, Liszt 2014a, Lee et al. 2015): such studies find that the opacity correction is generally only

about 10%. In particular, Murray et al. (2018a) combined *Planck* dust emission data and a large-area 21 cm GALFA-HI (Peek et al., 2011, 2018) emission map to reproduce the Fukui et al. (2015) model of HI properties (spin temperature and optical depth). They then compared the opacity corrections inferred from the Fukui et al. method with direct measurements, and concluded that the two are inconsistent, and that optically thick HI does not dominate the dark gas of the local ISM. Recently, the latest paper in the Fukui et al. series claims that the discrepancy can be resolved (in favour of a dark ISM dominated by atomic gas) if the CNM is highly clumped such that much of the mass is missed by HI absorption measurements (Tachihara et al., 2018), however this explanation is at the present time not widely accepted. Indeed, Murray et al. (2018a) recently ruled out the hypothesis that sight lines with pencil-beam HI absorption measurements miss high optical-depth CNM “blobs” with small covering fraction, as such atomic HI structures would require densities and pressures which are incompatible with typical conditions in the Galactic ISM.

Instead, the dark ISM is expected to predominantly consist of both opaque atomic gas and molecular hydrogen. Chemical and photodissociation region models (e.g., van Dishoeck & Black 1988, Tielens 2005, Wolfire et al. 2010, Smith et al. 2014) have long predicted the existence of dark molecular gas (CO-dark H_2). In this picture, H_2 can survive in the diffuse and translucent molecular regions thanks to its effective self-shielding, but CO has a greater self-shielding threshold (for example, in the local ISM, the extinction threshold for H_2 to form is $A_V \geq 0.14$, but CO requires $A_V \geq 0.8$; Wolfire et al. 2010) and thus is typically photodissociated by external UV radiation (Tielens & Hollenbach 1985a,b, van Dishoeck & Black 1988, Wolfire et al. 2010, Glover & Mac Low 2011, Glover & Smith 2016). Consequently, CO can well trace H_2 only in the inner part of molecular clouds, and overall it is not a perfect tracer for molecular hydrogen. Thus observations of CO emission alone may miss a significant fraction of the molecular gas, especially in diffuse molecular clouds where the UV shielding is poor (Reach et al., 1994, Meyerdierks & Heithausen, 1996). Early comparisons of thermal dust emission from IRAS at 100 μm with HI and CO emission surveys showed evidence of H_2 without CO detection (deVries et al., 1987, Heiles et al., 1988, Desert et al., 1988, Blitz et al., 1990). The analysis of C^+ surveys at 158 μm also claim that the missing gas contains a CO-dark H_2 component (Pineda et al., 2013, Langer et al., 2010). Lee et al. (2012) also found a significant portion of H_2 gas present in the envelope of the Perseus molecular cloud where CO is not detectable. These results in general agree well with the predictions of theoretical PDR models.

1.5.2 Contribution and distribution of dark gas

The fraction of dark gas measured by different studies indicates its significant contribution to the mass of the ISM. γ -ray observations suggest that the mass of CO-dark gas in the local Galactic ISM is comparable to that of the gas traced by both HI and CO [$N_{\text{HI}}^* + 2X_{\text{CO}}^*W_{\text{CO}}$] (e.g. Grenier et al., 2005). The dark gas masses in the Cepheus, Cassiopeia, and Polaris Flare clouds range from 40–60% of the molecular gas mass traced by CO (Abdo et al. 2010). Planck Collaboration et al. (2011a) estimated that the mass of the local dark ISM is about 28% of the HI gas and 118% of the gas traced by CO – about three times higher than predicted by Wolfire et al. (2010)’s PDR models. The fraction of CO-dark gas in the Perseus molecular cloud is $\sim 30\%$ of the total H_2 gas (Lee et al., 2012). Similarly, Pineda et al. (2013) also found that, on average, dark molecular gas accounts for $\sim 30\%$ of the molecular mass in the Galactic ISM (equivalent to $\sim 12\%$ of the total hydrogen gas mass), and that the fraction of CO-dark molecular gas (with respect to total H_2) increases with Galactocentric radius, from $\sim 20\%$ at 4 kpc to $\sim 80\%$ at 10 kpc. The fraction of dark gas with respect to total hydrogen column density derived from Planck Collaboration et al. (2011b) ranges from $\sim 10\%$ in the anti-centre direction up to $\sim 60\%$ towards the Galactic centre; while in the molecular ring (Galactic latitudes, $-40^\circ \leq l \leq 40^\circ$) and toward the anti-centre direction, the CO-dark and CO-bright gas are roughly comparable, and outside of the molecular ring the fraction of CO-dark gas is higher than the CO-bright gas. Here, the results from Pineda et al. (2013) and Planck Collaboration et al. (2011b) are both rather uncertain and show very different mass fractions and radial distributions of the Galactic dark ISM.

The column density distribution of dark gas in the local Galactic ISM, from Grenier et al. (2005) and Planck Collaboration et al. (2011a), is shown in Figure 1.7. In general, the dark gas is concentrated around well-known GMCs such as Taurus, Chamaeleon and Orion, or the Cepheus and Polaris flares (Planck Collaboration et al. 2011a) This is consistent with the conclusion from Lee et al. (2015) that most of CO-dark H_2 in the Perseus region appears in the envelope of the cloud, which is also supported by theoretical models (Wolfire et al., 2010). In addition, some fraction of dark gas is also present at high latitudes in both maps derived from γ -ray (Grenier et al. 2005) and dust emission (Planck Collaboration et al. 2011a), but this may partially originate from the unaccounted-for protons in the WIM instead (i.e. the presence of dust in the WIM).

Neutral hydrogen gas in both the atomic and molecular phases dominates the mass of the Galactic ISM. Therefore, an accurate measure of its mass is key to understanding ISM phase transitions, star formation and galaxy evolution. Accurate densities of each gas phase are crucial

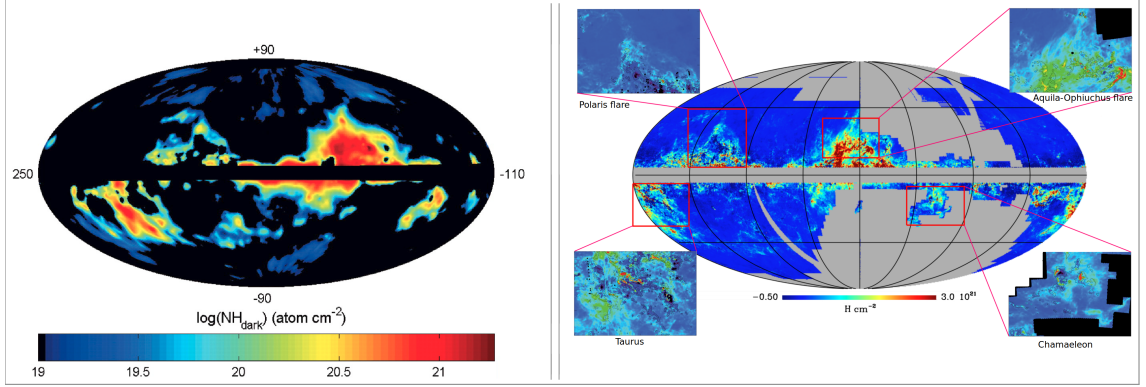


Figure 1.7: Left panel: This figure is adopted from Figure 4 of Grenier et al. (2005). Map of the column densities of dark gas found in the dust halos, as measured from their γ -ray intensity with the reddening map. The map is in Galactic coordinates centered on $l = 70^\circ$. Right panel: Map of the excess column density derived from 857 GHz data (adopted from Planck Collaboration et al. 2011a). The map is shown in Galactic coordinates with the Galactic centre at the centre of the image. The grey mask shows the regions where no IRAS or CO data are available, regions with intense CO emission ($W_{\text{CO}} > 1 \text{ K km s}^{-1}$) and the Galactic plane ($|b_{\text{II}}| < 5^\circ$). The insets represent dark gas column density maps for the Chamaeleon, Aquila-Ophiuchus flare, Polaris flare and Taurus regions, as indicated.

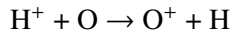
to examine models of H_2 formation. The prediction is that in typical Milky Way conditions where dust and H_2 self-shielding contribute approximately equally, there exists a minimum threshold of HI column density for hydrogen molecules to form. In this case, Krumholz et al. (2008, 2009) predicted that the distribution of HI surface density as a function of total gas surface density is uniform. Lee et al. (2012) have observed such a uniform distribution in the Perseus GMC.

1.5.3 OH as a tracer of diffuse molecular clouds

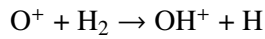
The CO rotational lines have been used to trace molecular clouds, but they are not detectable in some diffuse/translucent regimes where the balance between H_2 self-shielding and photodissociation allows significant amounts of molecular hydrogen to form, but only minimal amounts of CO. Other candidates are required as tracers of this diffuse H_2 . Among these, the 18 cm lines of Hydroxyl (OH) are a promising tracer for the diffuse molecular ISM. Indeed, they are readily detectable both in absorption and emission in lines of sight toward molecular clouds, including both CO-bright and CO-dark gas (e.g. Dickey et al., 1981, Magnani & Siskind, 1990, Li et al., 2015,

Barriault et al., 2010). Additionally, OH is a crucial intermediary molecule for CO formation (Black & Dalgarno, 1977, Barriault et al., 2010), and is believed to be abundant in diffuse molecular gas where CO is dissociated. In practice, numerous recent observations have suggested OH as an effective tracer of the molecular ISM (Cotten et al. 2012, Li et al. 2015, Allen et al. 2015, Rugel et al. 2018, Engelke & Allen 2018), particularly for low-density molecular gas. The ability of OH to effectively trace molecular hydrogen was pointed out decades ago by Wouterloot (1981), Maggani et al. (1988). Then, Andersson & Wannier (1993) and Wannier et al. (1993) also claimed that OH may trace molecular gas that is invisible in CO(1-0) line observations. Recently, Allen et al. (2015) detected more bright OH features without corresponding ^{12}CO ($J=1-0$) emission (at 2σ level of the CO CfA survey), but no CO components without corresponding OH emission, leading to a conclusion that OH main lines provide promising means to probe the CO-dark molecular gas.

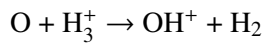
With the presence of H_2 , OH can form quickly via ion-molecular reactions with the ionization provided by cosmic-rays (de Jong, 1972, van Dishoeck & Black, 1986). At low temperatures (30–100 K) in diffuse molecular clouds, the charge-transfer reaction of H^+ and O enriches the oxygen ions (Huntress, 1977):



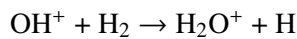
The oxygen ions then react rapidly with molecular hydrogen to produce OH^+ (Herbst & Klemperer, 1973, Dalgarno et al., 1973, Watson, 1974):



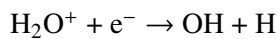
The OH^+ ions can also be produced through the fast exothermic proton-transfer reaction:



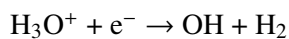
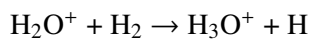
This reaction depends on the abundance of H_3^+ , which should be high in diffuse/translucent clouds because electrons do not combine/neutralize H_3^+ at the temperatures of these clouds (Watson, 1973, Oppenheimer & Dalgarno, 1974, Herbst & Klemperer, 1973, van Dishoeck, 1990). Once both OH^+ and H_2 are available, they react to form H_2O^+ and H:



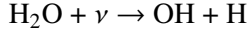
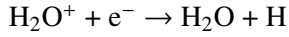
Then the water ion can combine with a free electron to produce OH and a hydrogen atom:



This is the main path to form OH in diffuse/translucent clouds, but other paths for OH formation can also occur with a few more steps (Singh & de Almeida, 1980):



Or through a path of forming and photodissociating water molecule:



The series of all these reactions depends on the local conditions such as the radiation field, cosmic ray ionization rate, shielding content, initial abundances of the reactants, and heating sources.

The formation of OH molecules is the base for CO formation (as discussed in Section 1.3.2). The four ground-state OH transitions (see Section 1.5.3) also have some observational advantages compared to CO emission lines. As discussed above for the case of HI, spectral line absorption measurements can directly provide the opacity along the line of sight – an important parameter for radiative transfer of the molecular region. Detecting CO in absorption is mostly impossible because the CO rotational transitions have wavelengths in the mm or sub-mm regimes, where few strong continuum background sources are available. But the OH hyperfine spectral lines lie in the radio regime with wavelengths of ~ 18 cm, where there exist many strong radio continuum sources. Therefore it is convenient to measure OH in absorption, and also in emission with high sensitivity observations (e.g. using the Arecibo telescope, since compared to CO, observations of OH require more integration time to achieve comparable sensitivities; e.g. Allen et al. 2015). Another benefit of OH observations is that the OH spectral lines are generally optically thin, so column densities can be calculated directly from optical depth, brightness temperature, and excitation temperatures, whereas the $^{12}\text{CO}(J=1-0)$ transition is usually optically thick. Moreover, the critical density of the OH lines is low ($\sim 10 \text{ cm}^{-3}$), whereas the critical density of CO is about $(10^3 \text{ cm}^{-3})/\tau$, so OH should be a effective tracer for probing molecular gas in low density regions.

OH can be used as a tracer of dark molecular ISM if the OH/H₂ abundance ratio ($X_{\text{OH}} \equiv N_{\text{OH}}/N_{\text{H}_2}$) is constrained. While estimates of OH column density are feasible, the column density of H₂ cannot often be measured directly. Many theoretical and observational studies have been performed to constrain the OH abundance ratio in different Galactic environments. Model calculations show some variation of X_{OH} within a wide range, $8 \times 10^{-9} - 4 \times 10^{-6}$ (Black & Dalgarno, 1977, van Dishoeck & Black, 1986, Viala, 1986, Nercessian et al., 1988, Andersson & Wannier, 1993), meanwhile the X_{OH} measured from observations is scattered as much as an order of magnitude around 1×10^{-7} , and may decrease with increasing H₂ column densities (Magnani et al., 1988, Liszt & Lucas, 2002, Weselak et al., 2010, Xu et al., 2016, Rugel et al., 2018). In Chapter 3, I present new measurements of the OH abundance along diffuse sightlines. I use absorption and emission measurements from the Arecibo Millennium survey to directly derive N_{HI} and N_{OH} , then

indirectly estimate the H_2 column density using dust optical depth and dust reddening as proxies for the total gas column density. I find mean values of $X_{\text{OH}} \sim 1 \times 10^{-7}$ from dust reddening and $X_{\text{OH}} \sim 0.5 \times 10^{-7}$ from dust optical depth; but no evidence for a systematic decreasing trend of X_{OH} as a function of H_2 column density.

1.5.4 Dust as a tracer of dark gas

Dust observations have been used to trace the dark ISM, thanks to their ability to probe the total gas column density regardless of whether hydrogen is atomic or molecular. Measurements of total gas column density from dust extinction or dust emission with the techniques discussed in Section 1.4.4 allow a comparison with N_{H} derived from HI and CO observations. The differences may then be used to infer how much neutral gas is missed by these two spectral line tracers. Most of the dark gas studies mentioned earlier in Section 1.5.1 did indeed make use of this method to find evidence for dark gas, and to determine its fraction.

However, the task of accurately estimating the dark gas fraction may be far from complete, because of the difficulties in constraining the correlations between dust and the different gas phases via the scaling factors for dust emissivity, dust opacity and specific reddening. As seen in Section 1.4.4, the uncertainty space for these conversion factors are relatively large, including the existence of additional gas, changes in the properties of the dust grains themselves and variations in the properties of their ambient environments (Planck Collaboration et al., 2011a, 2014d). A coupling of gamma-ray and dust analyses may be the only present means to narrow down this uncertainty space since a strong spatial correlation between the dust and gamma-ray maps can only arise from gas mass. While a linear approximation with constant scaling factors is fair for individual sky regions (e.g. Miville-Deschênes et al., 2005, Saul et al., 2014, Lenz et al., 2015), advanced methods with more sophisticated models are required obtain detailed pictures of dust-gas relations on large scales.

1.6 Observational techniques used in the thesis

1.6.1 Radiative transfer

Observations of the Galactic ISM are primarily carried out by studying electromagnetic radiation received by telescopes. The specific (or monochromatic) intensity at frequency ν , I_ν , is the electromagnetic power per unit area, per frequency interval $d\nu$, per steradian. The units of I_ν is

$Jm^{-2}s^{-1}Hz^{-1}sr^{-1}$ (where sr = steradians, the unit of solid angle, $d\Omega$).

Radiative transfer is a useful mathematical tool for describing how an electromagnetic wave propagates and interacts through media. At radio wavelengths, it is adequate to ignore the existence of scattering, therefore, the change in the intensity of radiation dI_ν along an infinitesimal path ds as it passes through a medium is given by:

$$dI_\nu = \epsilon_\nu ds - \kappa_\nu I_\nu ds \quad (1.12)$$

where ϵ_ν is the emission coefficient ($J\text{ cm}^{-3}\text{s}^{-1}\text{Hz}^{-1}\text{sr}^{-1}$), and κ_ν is the absorption coefficient (cm^{-1}). Since $\kappa_\nu = \sigma \cdot n$, the absorption coefficient contains both the cross section per particle σ (cm^2) and the particle density n (cm^{-3}). Rearranging Equation 1.12 we can write the radiative transfer equation as a first order differential equation:

$$\frac{dI_\nu}{ds} = \epsilon_\nu - \kappa_\nu I_\nu \quad (1.13)$$

It is useful to define the optical depth as $d\tau_\nu = -\kappa_\nu ds$ and the source function as $S_\nu = \epsilon_\nu / \kappa_\nu$, then Equation 1.13 can be expressed as:

$$\frac{dI_\nu}{d\tau_\nu} = I_\nu - \frac{\epsilon_\nu}{\kappa_\nu} = I_\nu - S_\nu \quad (1.14)$$

The source function S_ν is the ratio of emission and absorption coefficients of the medium, so it describes the intrinsic properties of the medium.

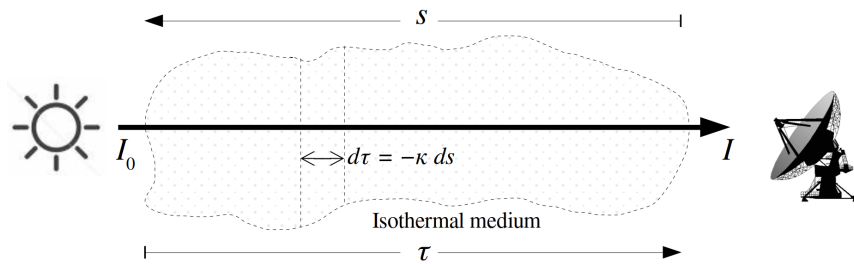


Figure 1.8: Illustration of intensity passing through an isothermal medium. The change in intensity over an interval $d\tau$ is described by the radiative transfer equation (Equation 1.14) in terms of the absorption and emission coefficients (κ_ν and ϵ_ν respectively) of the medium.

The formal solution for Equation 1.14 is:

$$I_\nu(\tau_\nu) = I_\nu(0)e^{-\tau_\nu} + \int_0^{\tau_\nu} S_\nu(\tau'_\nu)e^{-(\tau_\nu-\tau'_\nu)} d\tau'_\nu \quad (1.15)$$

where $I_\nu(0)$ is the incident intensity of the background source before entering the medium, and τ' is an intermediate optical depth. Simple solutions for Equation 1.15 are found only under the approximation of an isothermal, homogeneous medium as illustrated in Figure 1.8:

$$I_\nu(\tau_\nu) = I_\nu(0)e^{-\tau_\nu} + S_\nu(1 - e^{-\tau_\nu}) \quad (1.16)$$

The intensity of the radiation detected by telescope is thus the sum of two terms: (1) the attenuated radiation from the background source $I_\nu(0)e^{-\tau_\nu}$, and (2) the self-attenuated radiation emitted by the medium $S_\nu(1 - e^{-\tau_\nu})$.

- If the medium is **optically thick**: $\tau_\nu \gg 1$ and $e^{-\tau_\nu} \approx 0$, then the result is:

$$I_\nu(\tau_\nu) \approx S_\nu. \quad (1.17)$$

The incident radiation from the background source $I_\nu(0)$ is totally absorbed by the medium and can not penetrate to the other side; the intensity received by the telescope is equal to source function of the medium.

- If the medium is **optically thin**: $\tau_\nu \ll 1$ and $e^{-\tau_\nu} \approx 1 - \tau_\nu$:

$$I_\nu(\tau_\nu) \approx I_\nu(0) + [S_\nu - I_\nu(0)] \tau_\nu. \quad (1.18)$$

The received intensity $I_\nu(\tau_\nu)$ equals $I_\nu(0)$ when $\tau_\nu = 0$. So, if $S_\nu < I_\nu(0)$ then $I_\nu(\tau_\nu) \leq I_\nu(0)$, inversely if $S_\nu > I_\nu(0)$ then $I_\nu(\tau_\nu) \geq I_\nu(0)$.

The source function, S_ν

Now, one has to find the form of the source function S_ν . Suppose that an atom has two energy levels with an energy difference of $\Delta E = h\nu_{ul}$ (h is the Planck constant). The excitation temperature (T_{ex}) is then defined as:

$$\frac{n_u}{n_l} = \frac{g_u}{g_l} e^{-\Delta E/kT_{\text{ex}}} \quad (1.19)$$

where k is the Boltzmann constant, n and g are the population and degeneracy of the upper and lower levels. There are three Einstein coefficients that describe the transition rates caused by the interaction of radiation with these discrete energy levels: A_{ul} for the spontaneous photon emission rate, B_{lu} for the spontaneous photon absorption rate and B_{ul} for the stimulated photon emission rate. The Einstein A and B coefficients are related through:

$$g_u B_{ul} = g_l B_{lu} \quad \text{and} \quad B_{ul} = \frac{c^2}{2h\nu^3} A_{ul} \quad (1.20)$$

where c is the speed of the light in vacuum. The absorption and emission coefficients relate to the Einstein coefficients via:

$$\kappa_\nu = \frac{h\nu_{ul}}{4\pi}(n_l B_{lu} - n_u B_{ul})\phi(\nu) \quad (1.21)$$

$$\epsilon_\nu = \frac{h\nu_{ul}}{4\pi}n_u A_{ul}\phi(\nu) \quad (1.22)$$

where $\phi(\nu)$ is the line profile function, which satisfies the normalization condition ($\int_0^\infty \phi(\nu)d\nu = 1$). Now, we can re-write the source function in terms of the Einstein coefficients as:

$$S_\nu \equiv \frac{\epsilon_\nu}{\kappa_\nu} = \frac{n_u A_{ul}}{n_l B_{lu} - n_u B_{ul}} \quad (1.23)$$

Dividing by B_{ul} and using the relations between the coefficients we get:

$$S_\nu = \frac{2h\nu^3}{c^2} \frac{1}{\frac{n_l g_u}{g_l n_u} - 1} \quad (1.24)$$

Now using the definition of excitation temperature and the Boltzmann equation for level populations, we have:

$$S_\nu = \frac{2h\nu^3}{c^2} \frac{1}{e^{\frac{h\nu}{kT_{\text{ex}}}} - 1} \quad (1.25)$$

Thus, the source function is always the Planck function with $T = T_{\text{ex}}$, even when the radiation field is not a black body.

Brightness temperature

In the Rayleigh-Jeans limit attained in the radio regime ($h\nu \ll kT$), the Planck function $B_\nu(T_{\text{ex}})$ is linearly related to temperature, so that:

$$S_\nu = B_\nu(T_{\text{ex}}) \approx \frac{2k\nu^2}{c^2} T_{\text{ex}}, \quad (1.26)$$

and we may also define a “brightness temperature” $T_B(\nu)$ that allows us to relate I_ν to a temperature in the same way:

$$I_\nu = \frac{2k\nu^2}{c^2} T_B(\nu). \quad (1.27)$$

The solutions of Equation 1.16 then can be written as:

$$T_B(\tau_\nu) = T_B(0)e^{-\tau_\nu} + T_{\text{ex}}(1 - e^{-\tau_\nu}) \quad (1.28)$$

In practice, (beam-averaged) brightness temperature is a direct measurable in radio astronomy, and we usually determine:

$$\Delta T_B(\tau_\nu) = T_B(\tau_\nu) - T_c = (T_{\text{ex}} - T_c)(1 - e^{-\tau_\nu}) \quad (1.29)$$

with the continuum background temperature $T_c = T_B(0)$. In the infinitely high optical depth limit ($e^{-\tau_\nu} \approx 0$), $\Delta T_B = (T_{\text{ex}} - T_c)$; and in the small optical depth limit ($1 - e^{-\tau_\nu} \approx \tau_\nu$). We can thus observe an absorption line in the case of strong background source ($T_c > T_{\text{ex}}$) or an emission line for a weak background source ($T_c < T_{\text{ex}}$).

Column density of HI (N_{HI})

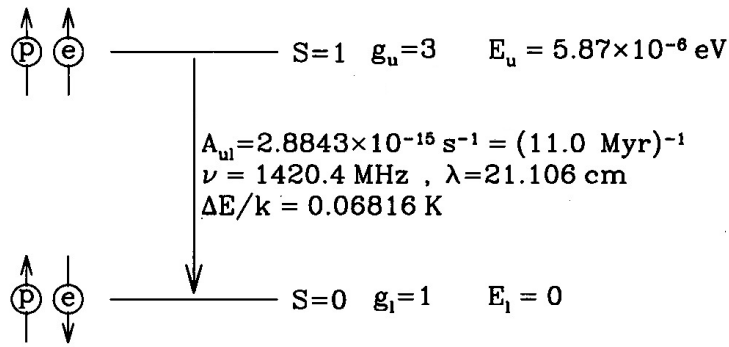


Figure 1.9: Hyperfine splitting of the 1s ground state of atomic hydrogen (taken from Figure 8.1 of Draine (2011)).

Recall that $d\tau_\nu = -\kappa_\nu ds$, where the absorption coefficient κ_ν is defined in Equation 1.21, thus we can integrate along distance to convert κ_ν to τ_ν , with the assumption of an isothermal medium (excitation temperature is independent of the path length):

$$\tau_\nu = \int \kappa_\nu ds = \frac{c^2}{8\pi\nu^2} \frac{g_u}{g_l} A_{ul} (1 - e^{-\frac{h\nu}{kT_{\text{ex}}}}) \phi(\nu) \int n_l ds \quad (1.30)$$

Integrating the number density n_l along the path length gives the column density $N_l = \int n_l ds$ (in cm^{-2}). therefore, we obtain a relation between optical depth and the column density in the lower level:

$$\tau_\nu = \frac{c^2}{8\pi\nu^2} \frac{g_u}{g_l} N_l A_{ul} (1 - e^{-\frac{h\nu}{kT_{\text{ex}}}}) \phi(\nu) \quad (1.31)$$

For the case of the 21 cm line of atomic hydrogen, we have $h\nu_{ul} \ll kT_s$ (where T_s is the excitation temperature of HI, the “spin” temperature); the energy difference between the upper and lower levels is $\Delta E = 5.87 \times 10^{-6}$ eV with $A_{ul} = 2.8843 \times 10^{-15} \text{ s}^{-1}$, corresponding to a small temperature of $h\nu_{ul}/k = 0.06816$ K, so that in the Boltzmann equation the ratio $n_u/n_l \approx g_u/g_l$.

Additionally, the degeneracy $g_u = 3$ and $g_l = 1$, so $N_u = 3N_l$ and $N_{\text{total}} = 4N_l$. Hence:

$$\begin{aligned}\tau_\nu &= \frac{c^2}{8\pi\nu^2} \frac{g_u}{g_l} N_l A_{ul} (1 - e^{-\frac{h\nu}{kT_s}}) \phi(\nu) \\ &= \frac{3c^2}{8\pi\nu} N_l A_{ul} \frac{h}{kT_s} \phi(\nu) \\ &= \frac{3c^2}{32\pi\nu} N_{\text{HI}} A_{ul} \frac{h}{kT_s} \phi(\nu)\end{aligned}\tag{1.32}$$

We can convert the line profile from frequency space to velocity space via $\phi_\nu(\nu) = \phi_v(v)c/\nu_0$, then integrate both sides over the whole line profile and note that $\int \phi_\nu(\nu)d\nu = \int \phi_v(v)dv = 1$. This will give us the expression for total HI column density along the line-of-sight:

$$N_{\text{HI}} = \frac{32\pi k\nu^2}{3A_{ul}hc^3} T_s \int \tau_\nu dv\tag{1.33}$$

Substituting the values of the constants, we obtain the general expression for HI column density:

$$\frac{N_{\text{HI}}}{[\text{cm}^{-2}]} = 1.8224 \times 10^{18} \frac{T_s}{[\text{K}]} \int \tau_\nu \frac{dv}{[\text{km s}^{-1}]}\tag{1.34}$$

For an optically thin HI gas cloud ($\tau_\nu \ll 1$) without a background continuum source ($T_c = 0$), $T_B = T_s \tau_\nu$ and the optically thin HI column density can be obtained by integrating the observed emission profile over the velocity range of the line:

$$\frac{N_{\text{HI}}}{[\text{cm}^{-2}]} = 1.8224 \times 10^{18} \int \frac{T_B}{[\text{K}]} \frac{dv}{[\text{km s}^{-1}]}\tag{1.35}$$

1.6.2 Absorption and emission technique for HI

To directly derive the properties of neutral atomic ISM (optical depth, spin temperature, column density), simultaneous absorption and emission observations of the 21 cm line are needed. The HI absorption measurement requires a strong background continuum source behind the clouds (so that $T_c > T_s$); however we cannot measure the pure emission spectrum of the gas along the same direction because of contamination from the background source. We must therefore observe the emission T_B in the (very close) vicinity of the radio continuum source and assume that the emission and absorption sample the same gas population. This observational technique is referred to as taking “on-source” and “off-source” measurements in which the absorption and emission brightness temperatures are respectively given by:

$$T_{\text{B,on}}(v) = (T_{\text{bg}} + T_c)e^{-\tau_\nu} + T_s (1 - e^{-\tau_\nu})\tag{1.36}$$

$$T_{\text{B,off}}(v) = T_{\text{bg}}e^{-\tau_\nu} + T_s (1 - e^{-\tau_\nu})\tag{1.37}$$

Hence:

$$e^{-\tau_v} = \frac{T_{B,on}(v) - T_{B,off}(v)}{T_c} \quad (1.38)$$

where T_{bg} is the temperature of blank sky (the sum of isotropic radiation from the CMB at 2.725 K and Galactic diffuse synchrotron background at the source direction) and T_c is the brightness temperature of the radio continuum source. The two equations (Equation 1.36 and 1.37) with two unknown variables (τ_v and T_s) allow us to directly estimate the HI optical depth and spin temperature – two crucial parameters for constraining the physical state of atomic ISM, and therefore, observationally distinguishing the HI gas phases.

In practice, the emission spectrum may vary significantly at different positions around the source and may also be contaminated by the absorption if the background source falls into the main beam (HPBW) or high order sidelobes. So, several off-source measurements are required for an accurate emission spectrum. For example, several studies with the Arecibo telescope (with an angular resolution of $3'.5$) have used a so-called Z16 pattern to make a 17 data point observation: one on-source absorption measurement at the position of the background source (with $\sim 50\%$ of the total integration time) and 16 off-source emission measurements within radii of 1.0 HPBW and $\sqrt{2}$ HPBW around the central source (Heiles & Troland, 2003a, Stanimirović et al., 2014, Lee et al., 2015, Murray et al., 2015). The spatial fluctuations in 21 cm intensity as seen from these spectra may then be taken into account to derive an accurate off-source “expected” emission spectrum (T_{exp}) – the emission profile we would observe if the background source were turned off. In the works cited above (and in the work presented in this thesis), the 16 off-source spectra are expressed as Taylor series expansions of T_{exp} , plus a contribution from the source intensity attenuated by optical depth of the medium; then the on-source and off-source T_{exp} profiles together with their spatial derivatives are obtained from a least-squares fit for the 17 data point measurements.

Given pairs of absorption/emission spectra, there are several independent methods to estimate the spin temperature and column density. These include assuming that each velocity channel contains gas at a unique T_s (e.g. Roy et al., 2013a, Lee et al., 2015), assuming a single harmonic-mean T_s along a full sightline (e.g. Kanekar et al., 2011), the “slope method” (e.g. Mebold et al., 1997, Dickey et al., 2000), and spectral decomposition (e.g. Heiles & Troland, 2003a, Stanimirović et al., 2014, Lee et al., 2015, Murray et al., 2015). In this thesis, I have adopted the spectral decomposition method (Heiles & Troland, 2003a) where the T_{exp} emission profile is assumed to arise from the contributions of both CNM and WNM, and the absorption spectrum arises from the CNM only. Spectral decomposition can separate the temperatures and column densities of WNM

and CNM components along a line of sight, whereas these properties obtained from the other methods are the combination of both CNM and WNM along the sightline, or within a velocity channel. This implies that the spectral decomposition method may give the more meaningful results (see Chapter 1 for detailed comparisons, also in Dickey et al. 2003, Murray et al. 2015), provided that the decomposition itself can be carried out reliably.

In general, 21 cm emission-absorption measurements from a single-dish can give the spin temperature of the CNM and upper limits to the kinetic temperatures of both the CNM and WNM (e.g. Heiles & Troland 2003a, Stanimirović et al. 2014, Lee et al. 2015). But to derive the WNM spin temperature, observations at extremely high optical-depth sensitivity are required as the optical depth of the WNM is very low ($< 10^{-3}$). In this case, a long baseline interferometer would be ideal, as it can achieve higher resolution than any single-dish, and hence push up the effective brightness temperature of a compact continuum background source. However, observing HI emission spectra with an array is not economical because it requires an enormously long integration time to achieve the same noise level as absorption (with the same observing configuration), and probably also resolves out the extended emission component. The best option is to use an interferometer for absorption, and combine with emission spectra measured from a single-dish telescope (as in the 21-SPONGE survey by Murray et al. 2015, 2018b).

1.6.3 OH column density

OH is a diatomic molecule with seven electrons, of which one is unpaired. Its ground state has a non-zero electronic orbital angular momentum along the molecular axis ($L = 1$) and a non-zero electronic spin angular momentum $S = 1/2$. The non-zero spin and orbital angular momenta can couple – the spin angular momentum can be parallel or anti-parallel to the orbital angular momentum, resulting in a splitting into two rotational energy states: $\Pi_{1/2}$ and $\Pi_{3/2}$. Then the $^2\Pi_{3/2}$ ground state is split by Λ -doubling (the interaction between the nuclei rotation and the unpaired electron motion around its orbit) into $+$ and $-$ states. Then each of these $+$ and $-$ parity states is split again, due to the hyperfine interaction of the proton with the unpaired electron spin, into $F = 1$ and $F = 2$ states (Figure 1.10). Here \mathbf{F} is the total angular momentum:

$$\mathbf{F} = \mathbf{K} + \mathbf{L} + \mathbf{S} + \mathbf{I}, \quad (1.39)$$

where \mathbf{K} is the molecular rotational angular momentum, \mathbf{L} is the electronic angular momentum, \mathbf{S} is the electronic spin and \mathbf{I} is the nuclear spin. The allowed transitions must satisfy $\Delta F = 0, \pm 1$;

if F is unchanged the transitions are the main lines, otherwise the transitions are the satellites. With two values of F ($F = 1$ and $F = 2$), there are four allowed transitions 1612, 1665, 1667 and 1720.530 MHz, all at around 18 cm in wavelength; the main lines are the 1665 and 1667 MHz transitions, the 1612 and 1720 MHz transitions are the satellites (their rest frequencies and Einstein A coefficients are listed in Table 1.2). All four hyperfine transitions are readily detected from the ground.

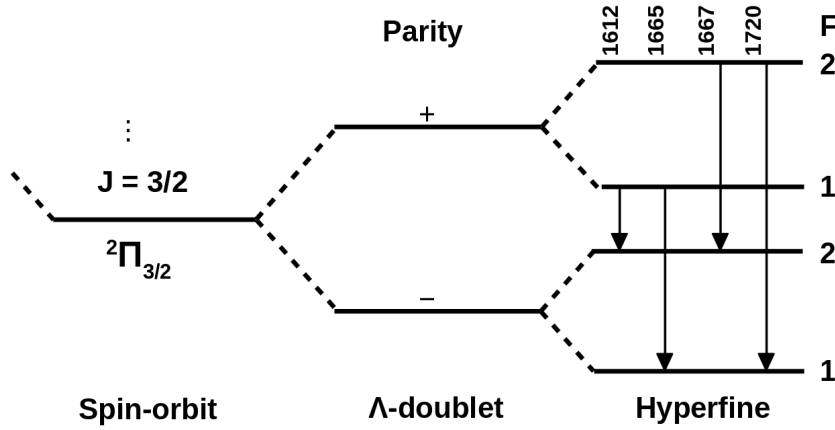


Figure 1.10: Energy level diagram for the $^2\Pi_{3/2}$ ground state of OH.

These transitions obey a universal sum rule in their excitation temperatures (Rogers & Barrett, 1967):

$$\frac{\nu_{1612}}{T_{\text{ex}}(1612)} + \frac{\nu_{1720}}{T_{\text{ex}}(1720)} = \frac{\nu_{1665}}{T_{\text{ex}}(1665)} + \frac{\nu_{1667}}{T_{\text{ex}}(1667)} \quad (1.40)$$

Additionally, we may generally assume that $h\nu \ll |kT_{\text{ex}}|$, which leads to the following optical depth relation for the four OH transitions:

$$\tau_{1612} + \tau_{1720} = \frac{\tau_{1665}}{5} + \frac{\tau_{1667}}{9}. \quad (1.41)$$

The only requirement for Equation 1.41 is $h\nu \ll |kT_{\text{ex}}|$, thus, this relation of optical depths of four OH lines is valid even for non-LTE conditions. While this rule can basically be regarded as universal, care must be taken since OH can have quite anomalous excitation, and in theory some rare configurations where the condition is not well fulfilled can occur.

Finally, if the four OH lines are optically thin ($\tau \ll 1$), and the brightness temperature of the radio continuum background does not vary significantly in the frequency range of the four lines, we have the sum rule for brightness temperatures of observed absorption profiles (Rogers & Barrett, 1967, Robinson & McGee, 1967):

$$T_{\text{B}}(1612) + T_{\text{B}}(1720) = \frac{T_{\text{B}}(1665)}{5} + \frac{T_{\text{B}}(1667)}{9} \quad (1.42)$$

Table 1.2: Rest frequencies and Einstein A coefficients of the four OH lines

Line	Rest frequency [MHz]	Einstein A coefficient [s^{-1}] ^a
1612	1612.2307	1.302×10^{-11}
1665	1665.4017	7.177×10^{-11}
1667	1667.3587	7.778×10^{-11}
1720	1720.5297	9.496×10^{-12}

^aTaken from Destombes et al. (1977)

These rules can provide useful constraints that aid in interpreting observations, particularly in cases where all four OH lines can be observed simultaneously.

The column densities for the two OH main lines at 1665 and 1667 MHz are given by:

$$N(\text{OH})_{1665} = \frac{8\pi k T_{\text{ex},1665} \nu_{1665}^2}{A_{1665} c^3 h} \frac{16}{3} \int \tau_{1665} dv \quad (1.43)$$

$$N(\text{OH})_{1667} = \frac{8\pi k T_{\text{ex},1667} \nu_{1667}^2}{A_{1667} c^3 h} \frac{16}{5} \int \tau_{1667} dv \quad (1.44)$$

where $A_{1665} = 7.177 \times 10^{-11} s^{-1}$ and $A_{1667} = 7.778 \times 10^{-11} s^{-1}$ are the Einstein A coefficients of the OH main lines (Destombes et al., 1977). These expressions are derived in an analogous fashion to Equation 1.33 above, assuming that the ratios of the level populations are given by the statistical weights. Substituting the constants, Equations 1.43 and 1.44 can be written as:

$$\frac{N(\text{OH})_{1665}}{[10^{14} \text{ cm}^{-2}]} = 4.30 \cdot \tau_{1665} \cdot \frac{T_{\text{ex},1665}}{[\text{K}]} \cdot \frac{\Delta v_{1665}}{[\text{km s}^{-1}]} \quad (1.45)$$

$$\frac{N(\text{OH})_{1667}}{[10^{14} \text{ cm}^{-2}]} = 2.39 \cdot \tau_{1667} \cdot \frac{T_{\text{ex},1667}}{[\text{K}]} \cdot \frac{\Delta v_{1667}}{[\text{km s}^{-1}]} \quad (1.46)$$

As in the case of HI, the optical depths, excitation temperatures and column densities of OH can be estimated from emission and absorption of the ground-state transitions (mostly by the two main lines, which are usually brighter) via on- and off-source measurements. Since the HI and OH lines have similar wavelengths, they may be measured simultaneously by the Arecibo telescope with the same observing strategy. The OH/H₂ abundance ratio and anomalies in main line excitation temperatures motivate our work in Chapter 2 and 3. Briefly, by analyzing OH data observed with Arecibo, we found that the two OH main lines are always optically thin (with $\tau < 0.25$), but they are not generally in LTE. These results are consistent with the conclusions of Dawson et al. (2014).

1.7 Thesis outline

In this thesis, with the use of various data sets for atomic gas, molecular gas and dust, I address several open questions: How best to correct for HI opacity effects? Which radio lines may best trace the total mass and extent of the molecular ISM? What is the best tracer for total gas column density? And how to shine light on the “dark” Milky Way?

In Chapter 2, I present an observational survey investigating the properties of warm and cold atomic gas in the vicinity of the Taurus and Gemini regions via emission and absorption measurements conducted with the Arecibo telescope. Based on the derived results, I examine two methods for HI opacity correction.

Chapter 3 describes a study of the dust-gas relationship, which finds evidence for the evolution of dust grains in interstellar space. Another part of this chapter focuses on the relative abundance of OH and H₂ molecules.

Chapter 4 provides the details of OH and CO observations in which we confirm that the OH ground-state main lines trace molecular hydrogen gas more significantly than CO emission. I contributed to this work as a co-author by performing a deep analysis of the OH data.

Chapter 5 summarizes my results, and sketches out the future directions of this work.

2

Properties of warm and cold atomic hydrogen in the Taurus and Gemini regions

At the heart of our desire to understand how galaxies convert their raw fuel of atomic gas to stars is to track the flow of material at every stage via high-sensitivity observations. During the last decades, many observational surveys have been carried out to study the physical properties of interstellar gas, yet our understanding of the transition between various gas phases of the ISM remains very limited. On the journey to becoming star-forming molecular gas, atomic hydrogen at 5000–8000 K must cool down and settle itself into a cold dense phase at 40–200 K. This transition in the atomic phase is strongly affected by the given conditions of different regions in the Galaxy, implying that observations at large scale and in various Galactic environments are essential.

This Chapter presents a large-scale 21 cm survey using the Arecibo telescope to probe the atomic gas in the vicinity of giant molecular clouds in the Taurus and Gemini regions. 21 cm absorption and emission measurements toward 79 strong radio continuum sources have been conducted, and the spectral decomposition method (Heiles & Troland, 2003a) was used to derive

temperatures, optical depths and column densities for both the warm and cold gas components. This study not only provides additional detailed observations of atomic hydrogen in a large sky region, but primarily addresses important questions on the fractions of each atomic gas phase, the variation of cold gas content around molecular clouds, as well as in different ISM regions, and the impact of H I opacity effects as a component of dark gas.

This survey was originally conducted as Arecibo project A2769, with Stanimirović as the Principal investigator. It is also a part of the GNOMES collaboration (the Galactic Neutral Opacity and Molecular Excitation Survey), which aims to explore the atomic and molecular hydrogen gas in and around molecular clouds. The study presented in this Chapter has been accepted for publication in the *Astrophysical Journal*. I was the first author in this work: I carried out all data reduction and analysis, largely determined the scientific directions of the paper, led the discussion, and carried out the writing. The co-authors provided comments, assessments on the quality of the analysis, and polished the English.

EXPLORING THE PROPERTIES OF WARM AND COLD ATOMIC HYDROGEN IN THE TAURUS AND GEMINI REGIONS

HIEP NGUYEN^{1,2}, J. R. DAWSON¹, MIN-YOUNG LEE^{3,4}, CLAIRE E. MURRAY^{5,6}, SNEŽANA STANIMIROVIĆ⁷, CARL HEILES⁸,
 M.-A. MIVILLE-DESCHÊNES⁹, ANITA PETZLER¹

Draft version July 2, 2019

ABSTRACT

We report Arecibo 21 cm absorption-emission observations to characterise the physical properties of neutral hydrogen (H I) in the proximity of five giant molecular clouds (GMCs): Taurus, California, Rosette, Mon OB1, NGC 2264. Strong H I absorption was detected toward all 79 background continuum sources in the $\sim 60 \times 20$ square degree region. Gaussian decompositions were performed to estimate temperatures, optical depths and column densities of the cold and warm neutral medium (CNM and WNM). The properties of individual CNM components are similar to those previously observed along random Galactic sightlines and in the vicinity of molecular clouds, suggesting a universality of cold H I properties. The CNM spin temperature (T_s) histogram peaks at ~ 50 K. The turbulent Mach numbers of CNM components vary widely, with a typical value of ~ 4 , indicating that their motions are supersonic. About 60% of the total H I gas is WNM, and nearly 40% of the WNM lies in thermally unstable regime 500–5000 K. The observed CNM fraction is higher around GMCs than in diffuse regions, and increases with increasing column density (N_{HI}) to a maximum of $\sim 75\%$. On average, the optically thin approximation (N_{HI}^*) underestimates the total column density by $\sim 21\%$, but we find large regional differences in the relationship between N_{HI} and the required correction factor, $f = N_{\text{HI}}/N_{\text{HI}}^*$. We examine two different methods (linear fit of f vs $\log_{10}(N_{\text{HI}}^*)$ and uniform T_s) to correct for opacity effects using emission data from the GALFA-H I survey. We prefer the uniform T_s method, since the linear relationship does not produce convincing fits for all subregions.

Subject headings: ISM: clouds — ISM: structure — radio lines.

1. INTRODUCTION

Neutral atomic hydrogen (H I), the most abundant gas in the interstellar medium (ISM), exists in multiple phases basically distinguished by temperature. Theoretical studies (Field et al. 1969; Silk & Werner 1969; Watson 1972; Silk 1975; McKee & Ostriker 1977; Wolfire et al. 1995, 2010) and practical observations (Radhakrishnan et al. 1972; Davies & Cummings 1975; Garwood & Dickey 1989; Liszt et al. 1993; Heiles & Troland 2003a,b) have well established a two phase model for interstellar H I gas, in which the phases (characterized by temperature and density) exist because the pressure of the ISM falls in a range where heating and cooling mechanisms permit two thermally stable states to co-exist. This model consists of cold, dense neutral medium (CNM) with kinetic temperatures $T_k \sim 30$ –200 K and volume densities of $n \sim 5$ –120

cm^{-3} , and warm, diffuse neutral medium (WNM) typically at $T_k \sim 4100$ –8800 K, $n \sim 0.03$ –1.3 cm^{-3} (McKee & Ostriker 1977; Liszt 2001; Wolfire et al. 2003). The cold gas is readily detected in H I 21 cm absorption and contributes typically 10–50% to the total H I mass (Heiles & Troland 2003a,b; Dickey et al. 2009; Stanimirović et al. 2014; Lee et al. 2015; Murray et al. 2015). The variation of the CNM fraction across interstellar environments is poorly constrained; however, it is likely higher in and around molecular clouds (Stanimirović et al. 2014, hereafter S14). The WNM can be easily detected in any direction on the sky via 21 cm emission, and plays an important role in the formation of cold gas, as well as constraining models of the interstellar medium.

The fraction of the neutral ISM that lies in the thermally unstable regime with intermediate kinetic temperatures of 500–5000 K (e.g. Dickey et al. 1977; Mebold et al. 1982; Kanekar et al. 2003; Heiles & Troland 2003a,b, hereby HT03) has been a topic of intense debate. For instance, HT03 observationally found that 48% of the total H I column density (or 30% of total out-of-plane gas) in the Arecibo Millennium survey was thermally unstable; Roy et al. (2013) estimated that at least $\sim 28\%$ of H I gas toward a sample of 33 compact extragalactic radio sources is in the unstable temperature range. From the highly sensitive 21-SPONGE survey, Murray et al. (2015) and Murray et al. (2018b) (hereafter M15 and M18, respectively) find a thermally unstable fraction of $\sim 20\%$. While these measurements (all from observations of emission/absorption pairs) are broadly consistent with a recent study by Kalberla & Haud (2018), which decomposed all-sky H I emission spectra

¹ Department of Physics and Astronomy and MQ Research Centre in Astronomy, Astrophysics and Astrophotonics, Macquarie University, NSW 2109, Australia. Email: vanhiep.nguyen@hdr.mq.edu.au, nguyenvanhiepiop@gmail.com

² Australia Telescope National Facility, CSIRO Astronomy and Space Science, PO Box 76, Epping, NSW 1710, Australia

³ Max-Planck-Institut für Radioastronomie, Auf dem Hugel 69, D-53121 Bonn, Germany

⁴ Korea Astronomy and Space Science Institute, Daedeokdae-ro 776, 34055 Daejeon, Republic of Korea

⁵ Department of Physics and Astronomy, Johns Hopkins University, Baltimore, MD 21218, USA

⁶ NSF Astronomy and Astrophysics Postdoctoral Fellow

⁷ Department of Astronomy, University of Wisconsin-Madison, 475 North Charter Street, Madison, WI 53706, USA

⁸ Department of Astronomy, University of California, Berkeley, 601 Campbell Hall 3411, Berkeley, CA 94720-3411

⁹ Laboratoire AIM, Paris-Saclay, CEA/IRFU/DAP - CNRS - Université Paris Diderot, 91191, Gif-sur-Yvette Cedex, France

from the HI4PI survey (HI4PI Collaboration et al. 2016), their estimated $\sim 41\%$ of thermally unstable HI is on the higher side relative to most recent observational studies. To keep the gas in a thermally unstable state, non-thermal processes are required, since otherwise such gas is expected to settle quickly into one of the two stable phases. Numerical ISM models suggest that dynamical processes (e.g. turbulence, shocks driven by supernova, time-dependent heating processes) may push the gas from stable phases to the thermally unstable phase (e.g. Gazol et al. 2001; Audit & Hennebelle 2005; Kim et al. 2013; Saury et al. 2014), resulting in significant amounts of unstable neutral gas. However, most recent numerical studies with detailed heating and cooling prescriptions, e.g. Kim et al. (2013); Hill et al. (2018), find a thermally unstable fraction of $< 20\%$ which is in agreement with most recent observational studies.

The measurement of HI physical properties is most commonly based on observations of the 21 cm line in emission and/or absorption. For warm HI gas at low optical depth, the column density (N_{HI}) is proportional to the brightness temperature (T_{B}) and can be directly estimated from the emission profile under the optically thin assumption, N_{HI}^* . Yet, the relation between N_{HI} and T_{B} is not as simple for cold gas, as opacity effects become significant. In that case, one needs to know both the optical depth and spin temperature to determine the true gas column density. Fortunately these can be estimated by combining the absorption and emission spectra from on-/off-source observations toward strong continuum background sources. Such studies find that in the low column density regime below $\sim 5 \times 10^{20} \text{ cm}^{-2}$, the total N_{HI} is comparable to N_{HI}^* ; but in denser regions optically thin approximation underestimates the total HI column density by at least (typically) $\sim 10\%$ (Dickey et al. 2003; HT03; Liszt 2014a; Lee et al. 2015; Nguyen et al. 2018; Murray et al. 2018a). Thus N_{HI}^* is in general a lower limit to the true N_{HI} .

On-/off-source measurements require good signal-to-noise absorption spectra, and are limited by the population of bright, compact radio continuum background sources, which precludes the creation of high-resolution, large-area Galactic maps of the true HI column density (at least in regions where the optically thin approximation is invalid). Furthermore, the derivation of true N_{HI} from these measurements can remain ambiguous due to the fact that each velocity channel contains a mixture of gas at different temperatures, and it is also possible that pencil-beam absorption measurements may under-sample the true sky distribution of dense, compact CNM structures (e.g. Fukui et al. 2018). An alternative is to use the available emission data and correct for the effects of opacity (e.g. by assuming a uniform T_{s} ; Liszt 2014b; Remy et al. 2017) or attempt to infer spin temperatures and optical depths indirectly (e.g. from dust optical depth; Fukui et al. 2015).

As a follow-up to the HI study of the Perseus molecular cloud (Stanimirović et al. 2014; Lee et al. 2015), the main goals of the present study are to (1) explore the properties of the cold and warm atomic HI gas in the proximity of five giant molecular clouds (Taurus, California, Rosette, Mon OB1, NGC 2264) as well as neighbouring diffuse and dense sightlines in and above the Galactic Plane; and (2) to build opacity-corrected HI maps by

applying optical depth corrections to emission data from the GALFA-HI survey (Stanimirović et al. 2006; Peek et al. 2011, 2018). This paper is a part of the GNOMES collaboration (the Galactic Neutral Opacity and Molecular Excitation Survey), which aims to understand the properties of neutral and molecular gas in and around molecular clouds.

There are many reasons why it is crucial to properly take into account HI opacity effects. Estimating the exact amount of each ISM phase is critical to understand the WNM-to-CNM phase transition, and to estimate the contribution made by cold optically thick HI to the so-called “dark” ISM (e.g. Grenier et al. 2005). Accurate HI column densities are also essential to test models of H_2 formation, which predict that there exists a minimum N_{HI} for H_2 formation in environments where dust shielding is dominant (compared to H_2 self-shielding); in this case, the distribution of HI column density is expected to be uniform (Krumholz et al. 2009). Interestingly, such a uniform distribution has been observed in Perseus molecular cloud by Lee et al. (2012).

Our regions of interest cover a wide range of environments, including the Galactic Plane, diffuse off-Plane sightlines and molecule-rich regions. In this work, we first employ the most direct way to estimate the optical depth, spin temperature and HI column density, by using absorption/emission spectra observed with the Arecibo radio telescope toward 79 radio continuum sources. We then derive the ratio of the “true” HI column density to the optically thin HI column density, and use this to evaluate two different methods for opacity correction.

Note that in this paper, we will define “WNM” as components detected only in emission, and “CNM” as components detected in absorption.

We organize this article as follows. In Section 2, we briefly summarize the observations and data processing techniques. In Section 3, we describe the Gaussian/pseudo-Voigt decomposition methods for absorption and emission spectral line data. In Section 4, we calculate spin temperatures, optical depths and column densities for all CNM and WNM components, and compare our results with previous observational surveys. In Section 5, we examine two methods for opacity correction and produce opacity-corrected HI maps. Finally, we summarize the results and discuss our future work.

2. OBSERVATIONS

We have conducted HI and OH absorption/emission measurements toward 79 extragalactic radio continuum sources in the vicinity of five giant molecular clouds (Taurus, California, Rosette, Mon OB1 and NGC 2264) using the Arecibo 305-m radio telescope (project a2769, PI Stanimirović). The continuum sources used in this work were selected from the NVSS catalogue (Condon et al. 1998) and have typical flux densities of $S \gtrsim 0.6 \text{ Jy}$ at 1.4 GHz. The source positions in equatorial coordinates (J2000) are presented in Figure 1. In Table 1, we list the basic information of these sources: right ascension (R.A.), declination (DEC), Galactic longitude/latitude, flux density at 1.4 GHz, and the diffuse background radio continuum emission.

The observations were conducted with Arecibo using the L-wide receiver, which permits simultaneous recording of HI (centered at 1420.406 MHz), and the two OH

TABLE 1
79 SIGHTLINES

Sources (NVSS name)	R.A (J2000) (hh:mm:ss)	DEC (J2000) (dd:mm:ss)	l ($^{\circ}$)	b ($^{\circ}$)	$S_{1.4 \text{ GHz}}$ (Jy)*	T_{sky} (K)
J034053+073525 (4C+07.13)	03:40:53.73	07:35:25.40	178.87	-36.27	1.01	4.07
J032153+122114 (PKS0319+12)	03:21:53.11	12:21:14.00	170.59	-36.24	1.91	4.51
J032723+120835 (4C+11.15)	03:27:23.11	12:08:35.80	171.98	-35.48	1.21	4.17
J031857+162833 (4C+16.09)	03:18:57.77	16:28:33.10	166.64	-33.6	8.03	6.93
J033626+130233 (3C090)	03:36:26.56	13:02:33.20	173.15	-33.29	1.99	4.67
J035613+130535	03:56:13.81	13:05:35.80	177.02	-29.78	0.89	4.14
J035900+143622 (3C096)	03:59:00.91	14:36:22.50	176.27	-28.26	1.2	4.37
J042725+085330 (4C+08.15)	04:27:25.05	08:53:30.30	186.21	-26.51	0.94	4.08
J032504+244445 (4C+24.06)	03:25:04.35	24:44:45.60	161.92	-26.26	0.81	4.13
J035633+190034 (4C+18.11)	03:56:33.46	19:00:34.60	172.23	-25.66	1.05	4.15
J041140+171405 (4C+17.23)	04:11:40.77	17:14:05.10	176.36	-24.24	1.03	4.26
J042022+175355 (3C114)	04:20:22.17	17:53:55.20	177.3	-22.24	1.11	4.23
J042524+175525 (4C+17.25)	04:25:24.43	17:55:25.30	178.11	-21.31	0.88	4.16
J042756+175242 (4C+17.26)	04:27:56.98	17:52:42.80	178.56	-20.88	1.01	4.22
J044907+112128 (PKS0446+11)	04:49:07.65	11:21:28.20	187.43	-20.74	0.85	4.16
J034008+320901 (3C092)	03:40:08.54	32:09:01.30	159.74	-18.41	1.61	3.95
J042846+213331 (4C+21.17)	04:28:46.64	21:33:31.40	175.7	-18.36	1.34	4.35
J040442+290215 (4C+28.11)	04:04:42.82	29:02:15.90	166.06	-17.22	0.95	3.69
J052424+074957 (4C+07.16)	05:24:24.04	07:49:57.10	195.51	-15.35	0.82	4.25
J051240+151723 (PKS0509+152)	05:12:40.99	15:17:23.80	187.41	-13.79	0.97	4.11
J053239+073243	05:32:39.01	07:32:43.50	196.84	-13.74	2.73	4.96
J051930+142829 (4C+14.14)	05:19:30.95	14:28:29.00	189.04	-12.85	0.86	4.15
J053450+100430 (4C+09.21)	05:34:50.82	10:04:30.30	194.89	-11.98	1.06	4.62
J041236+353543 (4C+35.07)	04:12:36.28	35:35:43.20	162.58	-11.36	0.86	3.93
J052109+163822 (3C138)	05:21:09.93	16:38:22.20	187.41	-11.34	8.6	7.59
J053056+133155 (PKS0528+134)	05:30:56.44	13:31:55.30	191.37	-11.01	1.56	4.64
J042353+345144 (3C115)	04:23:53.25	34:51:44.80	164.76	-10.24	1.3	3.88
J060536+014512 (4C+01.17)	06:05:36.56	01:45:12.70	206.08	-9.37	0.61	4.07
J045956+270602 (4C+27.14)	04:59:56.09	27:06:02.90	175.83	-9.36	0.93	3.9
J051740+235110 (4C+23.14)	05:17:40.81	23:51:10.20	180.86	-8.01	0.97	4.32
J045323+312924 (3C131)	04:53:23.34	31:29:24.20	171.44	-7.8	2.87	4.04
J053557+175600 (4C+17.33)	05:35:57.42	17:56:00.70	188.22	-7.67	0.83	4.23
J053444+192721 (PKS0531+19)	05:34:44.51	19:27:21.70	186.76	-7.11	7.02	6.48
J054046+172839 (4C+17.34)	05:40:46.05	17:28:39.20	189.21	-6.93	1.47	4.5
J050929+295755 (4C+29.16)	05:09:29.51	29:57:55.80	174.77	-5.97	1.06	4.03
J061900+050630	06:19:00.21	05:06:30.80	204.66	-4.84	0.69	4.19
J062812+010926 (4C+01.19)	06:28:12.55	01:09:26.00	209.24	-4.64	0.94	4.27
J062152+043834 (4C+04.22)	06:21:52.90	04:38:34.50	205.41	-4.43	1.06	4.35
J062551+043540 (4C+04.24)	06:25:51.89	04:35:40.20	205.92	-3.57	0.81	4.28
J053425+273223 (B0531+2730)	05:34:25.73	27:32:23.90	179.87	-2.83	1.04	4.25
J061622+115553	06:16:22.32	11:55:53.90	198.33	-2.2	0.83	4.41
J055955+190852 (4C+19.18)	05:59:55.70	19:08:52.50	190.09	-2.17	1.03	4.45
J060157+192216 (4C+19.19)	06:01:57.97	19:22:16.30	190.13	-1.64	0.8	4.43
J060933+162207 (4C+16.15)**	06:09:33.51	16:22:07.00	193.64	-1.53	0.73	4.58
J061857+133631 (4C+13.32)	06:18:57.50	13:36:31.50	197.15	-0.85	1.96	4.86
J054844+263600 (4C+26.18)**	05:48:44.28	26:36:00.30	182.36	-0.62	1.16	3.98
J054211+290147 (4C+29.19)	05:42:11.81	29:01:47.80	179.53	-0.59	0.98	4.13
J063313+081318 (4C+08.21)	06:33:13.01	08:13:18.90	203.54	-0.27	1.1	4.46
J060351+215937 (4C+22.12)	06:03:51.56	21:59:37.50	188.07	0.04	2.77	5.15
J062141+143211 (3C158)	06:21:41.09	14:32:11.90	196.64	0.17	2.24	4.86
J063215+102201 (4C+10.20)	06:32:15.34	10:22:01.10	201.53	0.51	2.38	5.0
J062545+144019 (4C+14.18)	06:25:45.97	14:40:19.70	196.98	1.1	2.44	5.01
J064516+053132 (3C167)	06:45:16.84	05:31:32.00	207.31	1.15	1.33	4.76
J053752+361112 (4C+36.10)	05:37:52.39	36:11:12.90	172.98	2.44	1.04	4.34
J062019+210229	06:20:19.54	21:02:29.70	190.74	2.94	0.9	4.33
J062250+220025 (4C+22.16)	06:22:50.64	22:00:25.60	190.16	3.91	1.06	4.34
J065601+083407 (4C+08.23)	06:56:01.03	08:34:07.10	205.81	4.91	0.68	4.12
J063451+190940	06:34:51.38	19:09:40.90	193.99	5.1	0.84	4.31
J065917+081331	06:59:17.97	08:13:31.80	206.48	5.48	0.91	4.12
J065548+104258 (4C+10.21)	06:55:48.36	10:42:58.80	203.85	5.82	0.91	4.15
J064841+144020 (4C+14.20)	06:48:41.15	14:40:20.60	199.52	6.04	1.03	4.17
J071523+031105 (4C+03.12)	07:15:23.75	03:11:05.00	212.82	6.78	0.67	3.97
J071004+061705 (4C+06.28)	07:10:04.83	06:17:05.40	209.43	7.0	0.58	4.05
J071924+021035	07:19:24.88	02:10:35.80	214.18	7.22	0.66	3.87
J064524+212145 (3C166)	06:45:24.08	21:21:45.70	193.12	8.3	2.59	4.8
J071028+091954 (4C+09.27)	07:10:28.52	09:19:54.30	206.72	8.44	1.02	4.09
J072140+053050 (PKS0719+056)	07:21:40.87	05:30:50.90	211.43	9.23	0.83	4.01
J070001+170922	07:00:01.52	17:09:22.30	198.47	9.58	0.65	4.09
J065937+211742 (4C+21.22)	06:59:37.81	21:17:42.20	194.63	11.26	0.57	3.98
J071404+143620 (3C175.1)	07:14:04.70	14:36:20.90	202.29	11.53	1.93	4.38
J072551+103202 (4C+10.22)	07:25:51.27	10:32:02.30	207.31	12.37	1.23	4.09
J070937+195443 (4C+19.26)	07:09:37.27	19:54:43.00	196.91	12.8	0.69	4.03
J072525+123624 (PKS0722+12)	07:25:25.60	12:36:24.60	205.35	13.17	0.61	3.77
J072832+121010 (4C+12.30)	07:28:32.88	12:10:10.50	206.09	13.67	1.07	3.92
J072516+142513 (4C+14.23)	07:25:16.80	14:25:13.50	203.64	13.91	1.07	3.87
J072810+143736 (3C181)	07:28:10.26	14:37:36.00	203.75	14.63	2.3	4.53
J071810+201002 (PKS0715+20)	07:18:10.64	20:10:02.70	197.52	14.74	0.73	3.98
J073035+151512 (4C+15.20)	07:30:35.41	15:15:12.60	203.42	15.42	1.54	4.23
J073037+173951 (4C+17.41)	07:30:37.09	17:39:51.50	201.13	16.42	0.69	3.94

*Condon et al. (1998)

**Excluded from the analysis

ground-state main lines at 1665.402 and 1667.359 MHz, with a velocity resolution of 0.16 km s^{-1} and an angular resolution of $3'.5$ at these frequencies.

We use the same observing procedure described in detail by Heiles & Troland (2003a). Briefly, we make a 17 data point observation (so-called Z16), consisting of one on-source absorption spectrum at the position of the background radio source, and 16 off-source emission spectra with innermost positions located at 1.0 HPBW and the outermost positions at $\sqrt{2} \text{ HPBW}$ from the central source. This particular observation pattern was designed to measure the fluctuations of 21 cm intensity within an area with an angular diameter of $\sim 13'.5$ around the source, and take these spatial variations into account to derive an accurate off-source “expected” emission spectrum (T_{exp} , the emission profile we would observe in the absence of the radio source; see Section 3 for details of the T_{exp} derivation). Our integration time, on average, is ~ 1 hour per source (including all on- and off-source integrations); leading to a characteristic noise level in optical depth of $\sim 5 \times 10^{-3}$ per 1 km s^{-1} velocity channel.

In the 21-SPONGE survey, M15 apply a main beam efficiency of 0.94 to Arecibo emission spectra taken with the L-wide receiver. To verify that this factor is also appropriate for our dataset, we compare our T_{exp} profiles with emission data from the Arecibo GALFA-HI survey (Data Release 2, DR2; Peek et al. 2018). We extract the GALFA-HI emission spectra around the location of each source within the outermost angular radius of the Z16 observation pattern, excluding the central pixels inside the Arecibo main beam (since these may be affected by absorption), and average the remaining pixels. We then compare the resultant spectra with our T_{exp} profiles on a channel-by-channel basis, for all channels above our 5σ noise level, and find that the T_{exp} values from the present work are systematically lower by a factor of ~ 1.06 (standard deviation of 0.08). Similarly, our T_{exp} integrated intensities are found to be systematically lower than GALFA-HI by the same factor of ~ 1.06 (standard deviation of 0.04). We also make the same comparison using the Leiden-Argentine-Bonn (LAB, Hartmann & Burton 1997; Kalberla et al. 2005) and HI4PI (HI4PI Collaboration et al. 2016) surveys. While these have lower resolutions than Arecibo ($36'$ and $16'$ respectively), they are both stray-radiation-corrected and have excellent absolute calibration. We find a consistent factor of ~ 1.07 (standard deviation of 0.07). We therefore apply a beam efficiency factor of $\eta_b = 1/1.07 = 0.93$ to our data.

Note that while we do not attempt to correct for the effects of stray radiation in our data, visual inspection of our spectra reveal no strong signs of the broad, wide wings that typically characterise such contamination. Peek et al. (2011) note that contamination from stray radiation in GALFA-HI is small – typically within their 1σ uncertainties. Once the main beam efficiency has been applied, the absolute differences between our spectra and those of GALFA-HI are also small; specifically, on a velocity channel basis, the difference spectra have broad features, but these mostly fall within the 2σ uncertainty profiles of our $T_{\text{exp}}(v)$. This results in a relative difference of at most 12% between the optically thin column densities of the two surveys along our 79 sightlines, with a median difference of $(2.0 \pm 1.1)\%$ (the uncertainty of the

median is estimated by bootstrap re-sampling). Thus, our visual inspection suggests that while stray radiation is likely present at a low level, its contribution to our profiles is not significant enough to affect our scientific conclusions.

3. DATA ANALYSIS: HI ABSORPTION & EMISSION FITTING

The root of the analysis is to solve the two equations of radiative transfer for on-/off-source measurements, under the assumption that the on and off positions sample the same gas:

$$T_{\text{B}}^{\text{ON}}(v) = (T_{\text{bg}} + T_{\text{c}})e^{-\tau_v} + T_{\text{s}}(1 - e^{-\tau_v}), \quad (1)$$

$$T_{\text{B}}^{\text{OFF}}(v) = T_{\text{bg}}e^{-\tau_v} + T_{\text{s}}(1 - e^{-\tau_v}), \quad (2)$$

$$T_{\text{exp}}(v) = T_{\text{B}}^{\text{OFF}}(v) - T_{\text{bg}}. \quad (3)$$

Hence:

$$e^{-\tau_v} = \frac{T_{\text{B}}^{\text{ON}}(v) - T_{\text{B}}^{\text{OFF}}(v)}{T_{\text{c}}}. \quad (4)$$

In the above, $T_{\text{B}}^{\text{ON}}(v)$ and $T_{\text{B}}^{\text{OFF}}(v)$ are the brightness temperatures of the on-source and off-source profiles respectively, T_{s} is the spin temperature, τ_v is the optical depth, T_{c} is the brightness temperature of the continuum source, and T_{bg} is the background brightness temperature including the 2.725 K isotropic radiation from the CMB and the Galactic synchrotron background at the source position. We obtain T_{bg} from the 1.4 GHz radio continuum maps of CHIPASS (in the Southern sky Calabretta et al. 2014) and from the Stockert and Villa-Elisa telescopes (for the Northern sky Reich et al. 2001), with typical values of around 4.4 K.

Following HT03, we derive T_{exp} , the “expected” emission profile at the location of the background source. We express the 16 off-source spectra as both first and second order Taylor series expansions of T_{exp} , plus a small contribution from the source intensity attenuated by optical depth, and perform a least-squares fit for the 17-point measurements to derive simultaneously: (1) the on-source optical depth profile ($e^{-\tau_v}$), (2) the off-source expected emission spectrum as well as its spatial derivatives, (3) their uncertainty profiles: σ_{τ} (also $\sigma_{e^{-\tau}}$) and $\sigma_{T_{\text{exp}}}$. Here, we use a slightly simpler approach than HT03, by not including their fine-tuning for gain variation, under the assumption that an accurate knowledge of the spatially-varying telescope gain and beam-shape properties is required to properly account for the off-source gain. As pointed out by Stanimirović et al. (2014), we also find that the second-order Taylor expansion is noisier (because the higher order variation in HI emission requires more fitting parameters) but likely better models the actual complex variations in HI emission and thus is the more accurate approach. We therefore use the $T_{\text{exp}}(v)$ and $\tau(v)$ profiles from the second-order expansion for all sources.

In this paper, to estimate the physical properties of individual HI clouds along a sightline, we follow the methodology applied by Heiles & Troland (2003a) to the Millennium Survey HI profiles. Essentially we assume

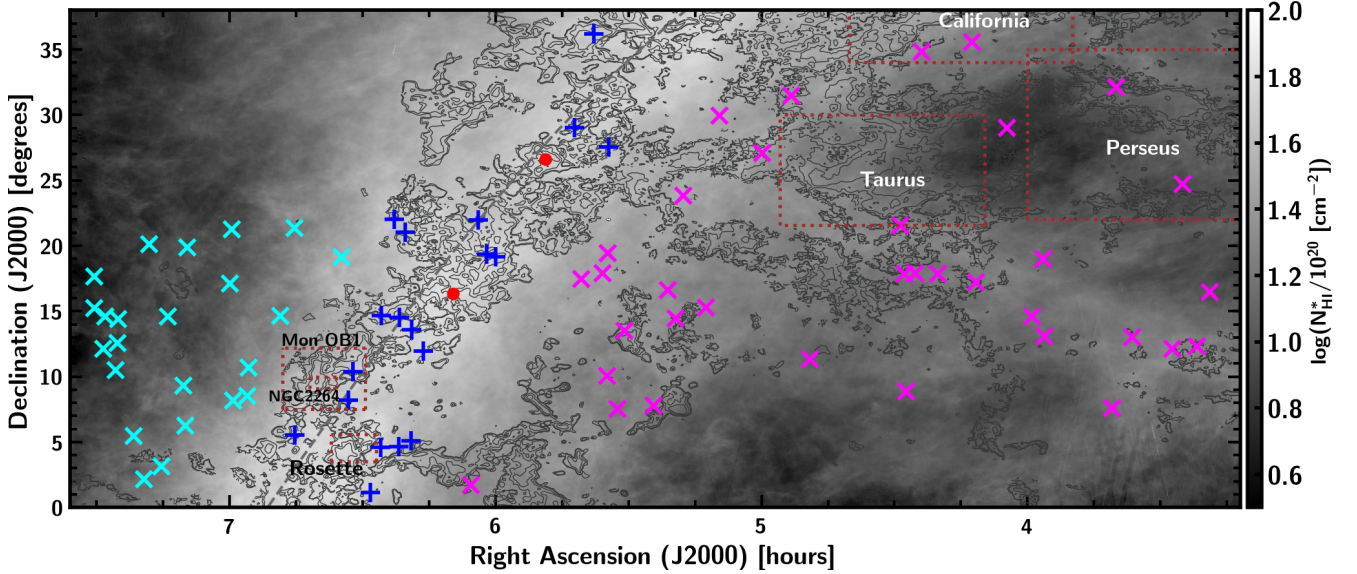


FIG. 1.— Locations of all 79 background radio continuum sources considered in this study, overlaid on the map of H I column density N_{HI}^* from the Arecibo GALFA-H I survey (DR2; Peek et al. 2018). The N_{HI}^* range is $(1-80) \times 10^{20} \text{ cm}^{-2}$. The blue plus markers show the sightlines toward 19 radio sources near the Galactic plane ($|b| < 5^\circ$), cyan crosses show the 23 sightlines above the Galactic plane, magenta crosses show the 35 sightlines below the Galactic plane, and the red dots show the two saturated sightlines excluded from the analysis (4C+16.15 and 4C+26.18). The dashed line shows the Galactic plane (Galactic latitude $b = 0^\circ$). Dotted boxes show roughly the locations of five molecular clouds. The contours represent the logarithm of integrated intensity $W_{\text{CO}(1-0)}$ from the all-sky extension to the maps of Dame et al. (2001) (T. Dame, private communication). The levels are $[0.01, 0.25, 0.75, 1.0, 1.75]$ in units of $\log_{10}(\text{K km s}^{-1})$.

cold gas (‘CNM’) components are seen in both absorption and emission (i.e. in both opacity and brightness temperature profiles), and warm gas (‘WNM’) is seen only in emission, giving only a brightness temperature (see Heiles & Troland 2003a for further detail). A key difference in the present work, however, is that besides Gaussian profile fitting, we also carry out pseudo-Voigt fitting, to examine whether the derived properties are affected by the choice of profile shape. Each Gaussian has three free parameters, and each pseudo-Voigt has four (see Section 3.3 for details).

3.1. Initial Component Generation

The opacity and expected emission profiles consist of multiple components at different velocities. A crucial question is how many components should be added to fit each spectrum. The noise level of the spectrum and residuals of the fit can be used as a measure of the goodness of the fit. However, while adding more components will naturally reduce the residuals, it may result in overfitting, and may not necessarily reflect physical reality. To minimise subjective judgment as much as possible, we generate a common set of initial guesses for both Gaussian and pseudo-Voigt fittings using a Savitzky-Golay filter for peak/trough detections. Note that the numbers of CNM and WNM components from these common initial guesses are not optimized for both types of fittings. We then employ the Bayesian Information Criterion (BIC) to automatically obtain the number of fit components, N_C , for the absorption ($e^{-\tau(v)}$) and emission spectra ($T_{\text{exp}}(v)$):

$$BIC = \chi^2 + d \ln(N) \quad (5)$$

where χ^2 is the chi-squared from the fit, d is the

number of free parameters (which is proportional to N_C , e.g. $d = 3N_C$ for Gaussians, and $d = 4N_C$ for pseudo-Voigts) and N is the sample size. Clearly, the BIC adds a new term to χ^2 to penalize the number of parameters in the model. For two given models, the model with the lower value of BIC is preferred. We calculate the BIC value for each value of d , and adopt the number of components from the most preferred d (see also Allison et al. 2012; Gordon et al. 2017). After this step, we have two sets of initial guesses for the Gaussian and pseudo-Voigt fittings, each with typically a different number of components. In the few cases where the spectra are either noisy or marginally saturated, we slightly adjust the initial guesses (central velocities and number of components) to allow the fits to converge.

3.2. Gaussian spectral decomposition

In this section, we decompose both the absorption and emission spectra into sets of Gaussian components. The expected emission profile $T_{\text{exp}}(v)$ consists of both warm and cold components:

$$T_{\text{exp}}(v) = T_{\text{B,CNM}}(v) + T_{\text{B,WNM}}(v) \quad (6)$$

where $T_{\text{B,CNM}}(v)$ is the brightness temperature of the cold gas and $T_{\text{B,WNM}}(v)$ is the brightness temperature of the warm gas. The on-source spectrum (Equation 4) contains only cold gas seen in absorption.

First, we fit the opacity spectrum $\tau(v)$ with a set of N Gaussian components using a least-squares method with the assumption that each component is independent and isothermal with a spin temperature $T_{\text{s,n}}$:

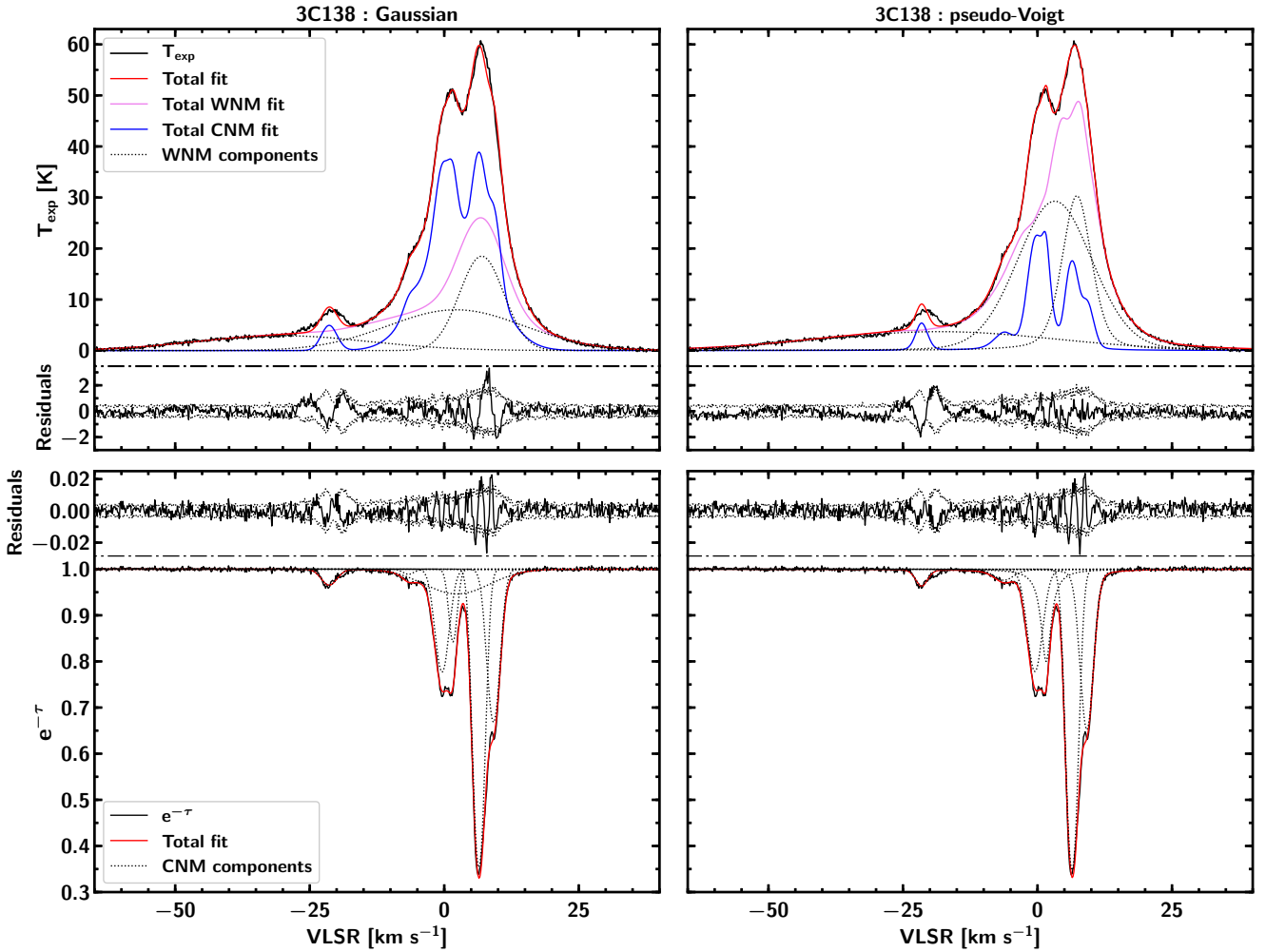


FIG. 2.— Example of Gaussian (left) and pseudo-Voigt (right) fits to a pair of emission and absorption spectra^a. In the upper panels, the black solid line is the expected emission profile T_{exp} ; the black dotted lines are the WNM Gaussian/pseudo-Voigt components; the pink line shows the contribution of the WNM components to the T_{exp} profile; the blue line displays the contribution to the T_{exp} profile by the CNM components from the absorption profile; the red solid line is the total WNM and CNM fit. The residuals from the fit are plotted below zero, with $\pm\sigma_{T_{\text{exp}}}$ superimposed. In the lower panels, the black line shows the optical depth profile ($e^{-\tau}$); the dotted lines are the CNM Gaussian/pseudo-Voigt components, the red line represents the fit to the optical depth profile. The residuals from the absorption fit are plotted above one, with $\pm\sigma_{e^{-\tau}}$ superimposed. The derivation of uncertainty profiles ($\sigma_{T_{\text{exp}}}$ and $\sigma_{e^{-\tau}}$) is described in Section 3.

^aA .tar.gz package containing 77 FITS tables of the Arecibo observational data and Gaussian/pseudo-Voigt fits is also available.

tribution of the cold components is given by

$$\tau(v) = \sum_{n=0}^{N-1} \tau_{0,n} e^{-4 \ln 2 [(v-v_{0,n})/\delta v_n]^2}. \quad (7)$$

Here the parameters used to fit the absorption spectrum, $\tau_{0,n}$, $v_{0,n}$, δv_n are respectively the peak optical depth, central velocity and FWHM of n^{th} component. These parameters are assumed to be independent, and the number of components and the initial guesses for the fit parameters are generated as described in Section 3.1. This least-squares fit gives all the values of $\tau_{0,n}$, $v_{0,n}$ and δv_n .

We now fix all the parameters derived for these CNM components (namely $\tau_{0,n}$, $v_{0,n}$ and δv_n). Next, we also use the least squares technique to fit the expected emission profile, $T_{\text{exp}}(v)$, which is assumed to consist of the N cold components seen in the absorption spectrum, plus any warm components seen only in emission. The con-

$$T_{\text{B,CNM}}(v) = \sum_{n=0}^{N-1} T_{s,n} (1 - e^{-\tau_n(v)}) e^{-\sum_{m=0}^{M-1} \tau_m(v)} \quad (8)$$

in which the subscript m describes M absorption clouds lying in front of the n^{th} cloud. For WNM, we use a set of K Gaussian functions to represent the contribution to the expected profile $T_{\text{exp}}(v)$, (where the number of components and their initial guesses are also generated as described in Section 3.1). For each k^{th} component, we assume that a fraction F_k of WNM lies in front of all CNM components, so the remaining $(1 - F_k)$ lies behind and is absorbed by CNM components. Therefore, the brightness temperature from these K WNM components

is:

$$T_{\text{B,WNM}}(v) = \sum_{k=0}^{K-1} [F_k + (1 - F_k)e^{-\tau_v}] \times T_{0,k} e^{-4 \ln 2 [(v-v_{0,k})/\delta v_k]^2} \quad (9)$$

Here the independent fit parameters $T_{0,k}$, $v_{0,k}$, δv_k are respectively the peak brightness temperature, central velocity and FWHM of the k^{th} emission component. This least-squares fit to the emission spectrum gives $T_{0,k}$, $v_{0,k}$, δv_k , F_k for warm components and $T_{s,n}$ for cold components. For each sightline, we perform the $T_{\text{exp}}(v)$ fit with all possible orderings of the N absorption components ($N!$), and choose the one that gives the smallest residuals. As seen in Equation 9, the fraction F_k determines the contribution of $T_{\text{B,WNM}}$ to T_{exp} and so it has an important effect on the derived CNM spin temperatures ($T_{s,n}$). However, the results of the F_k fractions from different CNM ordering fits are difficult to distinguish statistically by the difference in the fit residuals. Hence, following the suggestion in HT03, after including K WNM emission-only components, we calculate the spin temperature of CNM by assigning three values (0, 0.5, 1) to each F_k . We then experiment with all possible combinations of K WNM components (3^K) along the line of sight. We obtain the final spin temperatures $T_{s,n}$ for CNM components as a weighted average over all trials, and the weight of each trial is the inverse of the variance estimated from the residuals the $T_{\text{exp}}(v)$ fit. The uncertainty of the final spin temperature for each CNM component is estimated from the variations in T_s with F_k in all trials (as described in Section 3.5 of Heiles & Troland 2003a). Apart from the dependence of CNM T_s on the ordering of the N CNM components and the fraction F_k , we do not observe strong correlations between other independent CNM and WNM Gaussian parameters. Example spectra and fits are shown in Figures 2 and 3.

3.3. Pseudo-Voigt spectral decomposition

Gaussian fitting has been widely used in ISM radio astronomy because the velocity profiles are assumed to be truly Gaussian. This assumption holds when internal motions are characterized by thermal processes or small-scale turbulence, and the damping wings in the spectra are insignificant. However, some authors have chosen to fit pseudo-Voigt profiles instead (Planck Collaboration et al. 2015; Remy et al. 2017), with the reasoning that pseudo-Voigt function fits broad pedestals better. Therefore, we have tested both options in this work and assess the impact (if any) on the astrophysical conclusions (see Appendix A for more details).

We repeat the above fitting procedures using pseudo-Voigt functions instead of pure Gaussians. A pseudo-Voigt profile, a simple approximation for the Voigt function (Wertheim et al. 1974), is a linear combination of a Gaussian curve $G(x)$ and a Lorentzian curve $L(x)$ sharing the same full width at half-maximum values. The normalized pseudo-Voigt profile by definition is given by:

$$V(x) = \eta L(x) + (1 - \eta)G(x) \quad (10)$$

where $L(x)$ and $G(x)$ are the normalized Gaussian and Lorentzian functions, with FWHM $\delta_V = \sqrt{2(\ln 2)}\delta_G =$

$2\delta_L$:

$$G(x) = \frac{1}{\sqrt{\pi}\delta_G} e^{-x^2/\delta_G^2} \quad (11)$$

$$L(x) = \frac{1}{\pi\delta_L} \left(\frac{1}{1 + x^2/\delta_L^2} \right) \quad (12)$$

and η is a parameter which mixes the two functions. The results for the pseudo-Voigt fits are shown in Table 3; example spectra and fits are shown in Figures 2 and 3.

4. RESULTS

In Table 3 we list the parameters obtained from both the pseudo-Voigt and Gaussian fits for all CNM and WNM components along each sightline¹⁰. Column 1 shows the Galactic longitude and latitude for each sightline; Columns 2 and 10 list the peak brightness temperature for each component. For the WNM components, this is the unabsorbed height T_B , quoted with its error from the fits. For the CNM components, this is the spin temperature obtained from the fits multiplied by $(1 - e^{-\tau})$ (see Equation 8), and is quoted without uncertainty. In Columns 3 and 11, we list the optical depth of each component: for CNM components this is the peak optical depth and its associated uncertainty, for WNM components it is the upper limit to peak opacity (set to be equal to the 1σ noise level in absorption at the central velocity of the emission component) and its error is not quoted. Columns 4 and 12 show the central velocities for each CNM and WNM component; Columns 5 and 13 are the linewidth (FWHM) in VLSR of each CNM and WNM component; Columns 7 and 14 list the spin temperatures: for CNM components the spin temperature is derived from the fit to the T_{exp} profile and is quoted with its error, for WNM components T_s is a lower limit calculated by the upper limit on optical depth in Columns (3, 11) $T_{s,k} = T_{0,k}/\tau_{0,k}$ and has a very large error. In Columns 8 and 15, we quote the HI column densities and their errors for each CNM and WNM component; Columns 9 and 16 are the fraction (F) of each WNM component lying in front of all CNM components or the order (O) of each CNM component along the sightline (integer numbers). The η values in Column 6 are the fractions of the Lorentzian function in the pseudo-Voigt profile. Note that while we detect HI absorption along all 79 sightlines, we exclude two sightlines (4C+16.15 and 4C+26.18) from further analysis because their opacity spectra ($e^{-\tau}$) are saturated and result in huge optical depths with enormous uncertainties.

Along the remaining 77 sightlines, the total numbers of CNM components from the Gaussian and pseudo-Voigt fits are (349, 323), with column densities of $(956.1, 1013.8) \times 10^{20} \text{ cm}^{-2}$. The numbers of WNM components are (327, 284), with column densities of $(1609.7, 1712.5) \times 10^{20} \text{ cm}^{-2}$. Thus the total (WNM+CNM) column densities derived from Gaussian and pseudo-Voigt fits in this study are $(2565.8, 2726.3) \times 10^{20} \text{ cm}^{-2}$, which equates to cold and warm gas fractions of 40% and 60%.

The distributions of properties derived from Gaussian and pseudo-Voigt fits are almost indistinguishable. For

¹⁰ A .tar.gz package containing four FITS tables of the fitted parameters obtained from Gaussian and pseudo-Voigt fittings for WNM and CNM components as listed in Table 3 is also available.

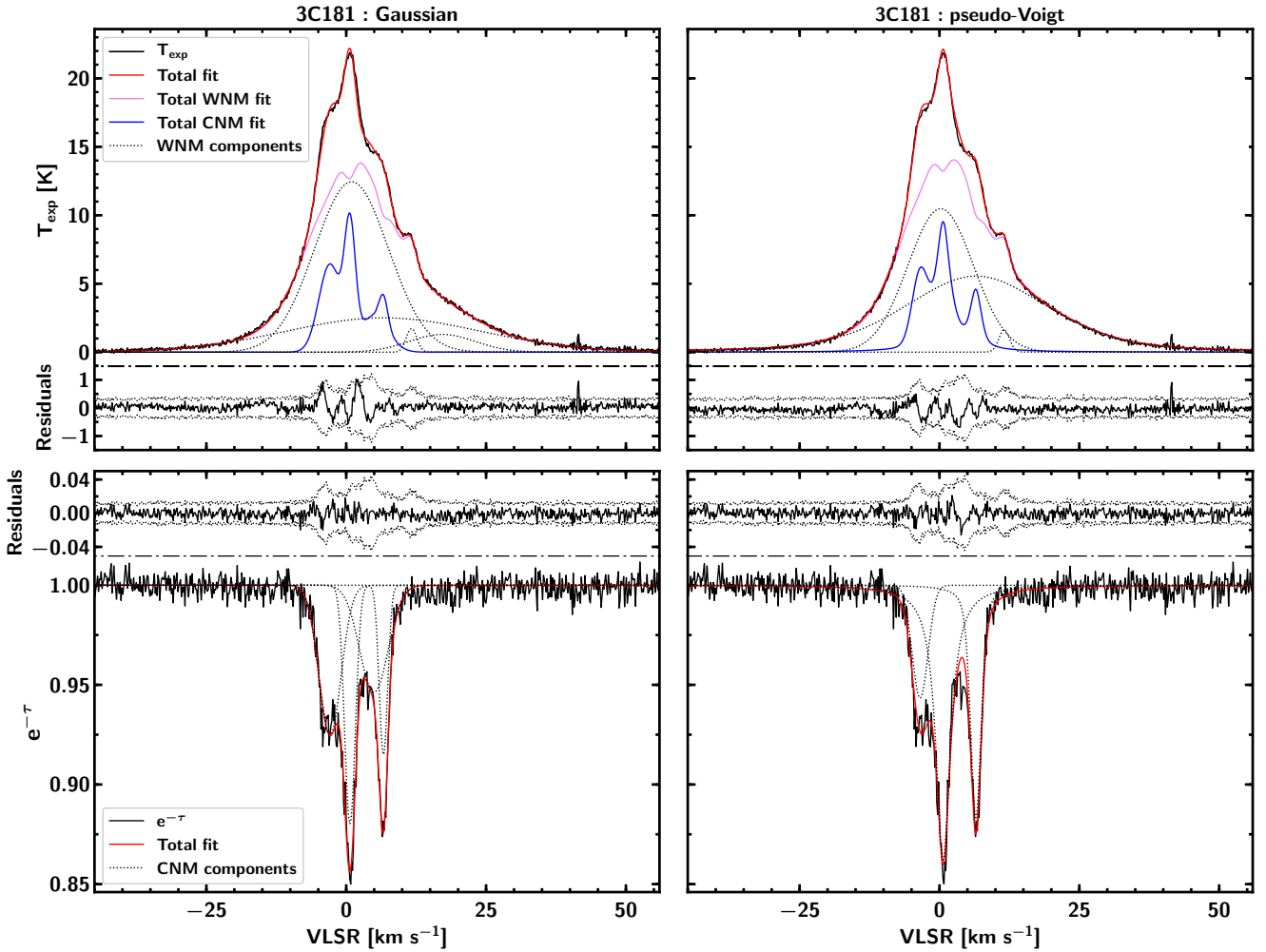


FIG. 3.— See Figure 2 for details.

consistency with past studies, we will present the results of the Gaussian fits for the rest of this paper, however, we present a detailed comparison between the Gaussian and pseudo-Voigt fits in the Appendix A.

Figures 4, 5 and 6 show the absorption and emission spectra for all sightlines, in the Galactic Plane, Gemini and Taurus regions respectively. In a few cases, we see the presence of “emission” features in absorption spectra ($e^{-\tau} > 1$) toward the weakest background sources. These sources are probably quite faint to measure the HI absorption with Arecibo telescope, thus their derived absorption spectra are essentially noisier. During the spectral decompositions, we do not take these “emission” features into the fit.

Here (and from hereon) we define the ‘Galactic Plane’ as $|b| < 5^\circ$ (19 sightlines), including Rosette, Mon OB1 and NGC 2264; the ‘Gemini region’ as $b > 5^\circ$ (23 sightlines), including minimal molecular gas; and the ‘Taurus region’, including both Taurus and California, as $b < -5^\circ$ (35 sightlines) (as illustrated in Figure 1). These latitude divisions (basically based on the distribution of $W_{\text{CO}(1-0)}$ from Dame et al. 2001) roughly divide our sample into three characteristic physical regimes – in-Plane, out-of-Plane with mostly diffuse sightlines (Gemini) and out-of-Plane with many dense/molecular sightlines (Taurus).

The colors in the absorption spectra in the plots indicate the HI spin temperature of each CNM component. In general, we detect strong absorption and emission in a wide range of VLSR from -10 to 50 km s^{-1} for sightlines in Gemini, from -20 to 20 km s^{-1} for those in Taurus and -50 to 50 km s^{-1} near the Galactic plane. The strongest absorption/emission is located at $\sim 0 \text{ km s}^{-1}$, and the closer to the Galactic plane, the more complex the profile shapes.

Besides the spectral decompositions, we also applied two alternative methods (one T_s per velocity channel and single harmonic-mean T_s along full sightline) to estimate the HI spin temperature and column density from the absorption/emission pairs. We compare the results obtained from these different approaches in Appendix B.

4.1. Optical depth

The peak optical depths, τ_{peak} , derived from Gaussian fitting range from ~ 0.01 to 16.2 . The values are summarized in histograms in Figure 7 (top panel), where we show the τ_{peak} distribution for all CNM components, as well as for each individual region. As expected, the optical depths in the Galactic plane sample are the highest, with a mean and median of $(1.0, 0.63)$, and also relatively high toward Taurus, with mean and median

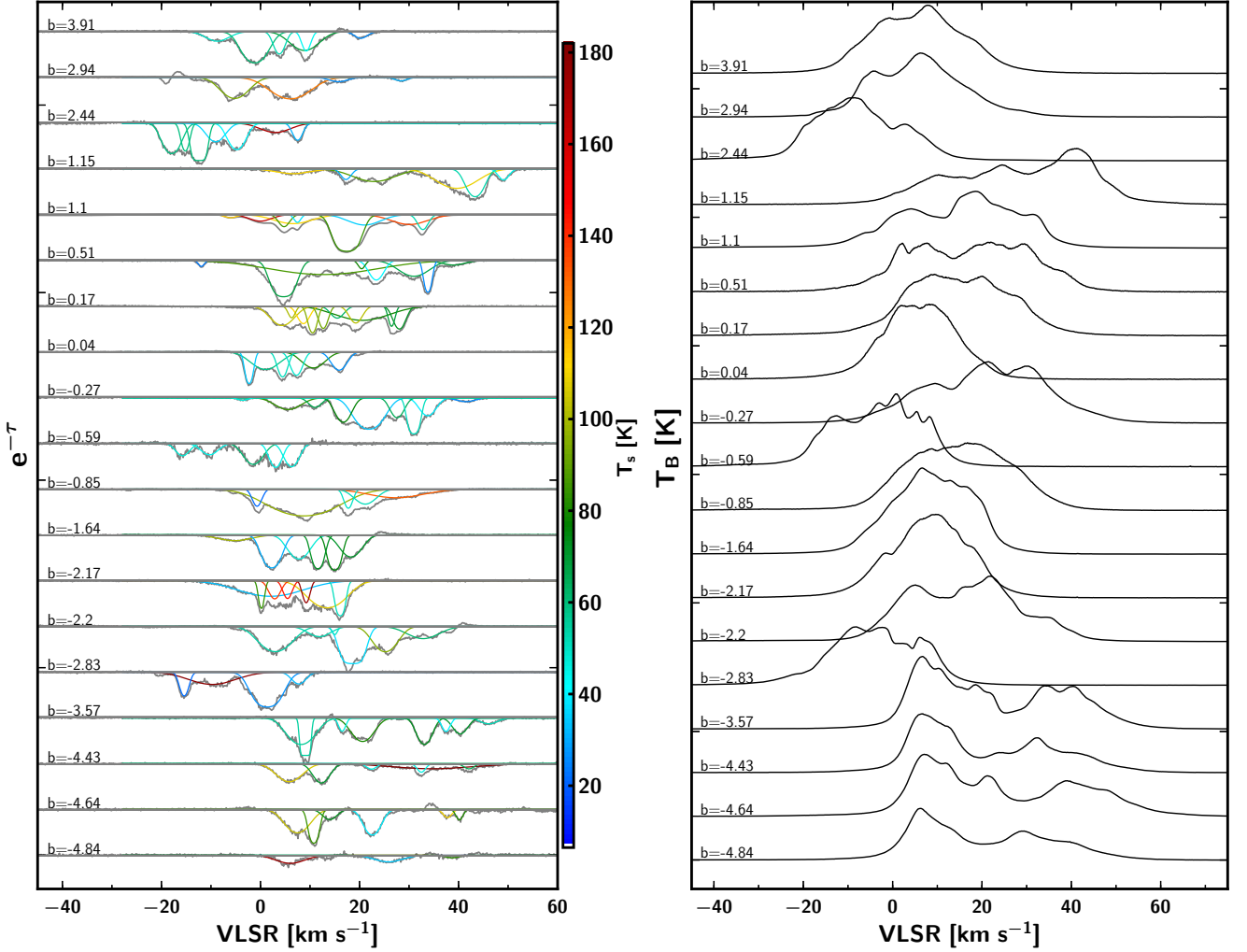


FIG. 4.— Comparisons of absorption profiles (left) and emission expected profiles (right) for 19 sightlines in near Galactic plane. The colorbar on the left panel shows the HI spin temperatures of CNM components. The sightlines are sorted in order of decreasing Galactic latitude b and are offset along the y-axis for comparison.

values (0.54, 0.37) – triple those toward the Gemini region (0.18, 0.13). The mean and median values for the total sample are ~ 0.64 and ~ 0.35 . About 17% of the CNM components have $\tau_{\text{peak}} > 1$, namely 60/349 Gaussian components; corresponding to dense gas regions. As shown in bottom panel of Figure 7, the locations of these high optical depths are all either coincident with or close to sightlines with CO detections.

4.2. Temperatures of cold and warm gas

The cold gas is characterized by spin temperature T_s , defined from the populations of the upper and lower hyperfine levels. The spin temperature is influenced by many factors from the surrounding environment: the ambient radiation field, scattering by Lyman- α radiation, or collisions of HI atoms with electrons, protons and other H atoms. In high density CNM regions ($n \gtrsim 100 \text{ cm}^{-3}$, e.g. Shaw et al. 2017), collisions dominate the excitation of HI atoms, so that T_s is approximately equal to the kinetic temperature, T_k (e.g. Kulkarni & Heiles 1988). In contrast, in more diffuse WNM gas, collisions are insufficient to thermalise the 21 cm transition, hence T_s is generally expected to be lower than T_k (e.g. Field

1958; Deguchi & Watson 1985; Liszt 2001). However, the Lyman- α radiation field from Galactic and extragalactic sources can couple the HI spin temperature in the WNM with local gas motions. This mechanism, known as the Wouthuysen-Field effect (Wouthuysen 1952; Field 1958, 1959), requires a large number of resonance scatterings of Lyman- α photons (i.e. large optical depth) and a recoil effect of the scattering atom (i.e. momentum transfer between HI atom and Lyman- α photon). The Wouthuysen-Field effect is likely responsible for the high WNM spin temperatures inferred from sensitive absorption studies ($\sim 10^4 \text{ K}$; Murray et al. 2014, 2017, 2018b), which cannot be explained by steady-state collisional excitation.

As expected, our Gaussian fitting shows that the FWHM of WNM components is obviously broader than that of CNM components, with a mean value of 16 km s^{-1} vs 4 km s^{-1} respectively. For the warm gas, we calculate Doppler temperature (Payne et al. 1982) from the line-width ($\Delta V = \text{FWHM}$) of each WNM component:

$$T_D = 21.86 \times \Delta V^2 \quad (13)$$

T_D is an upper limit on the kinetic temperature because

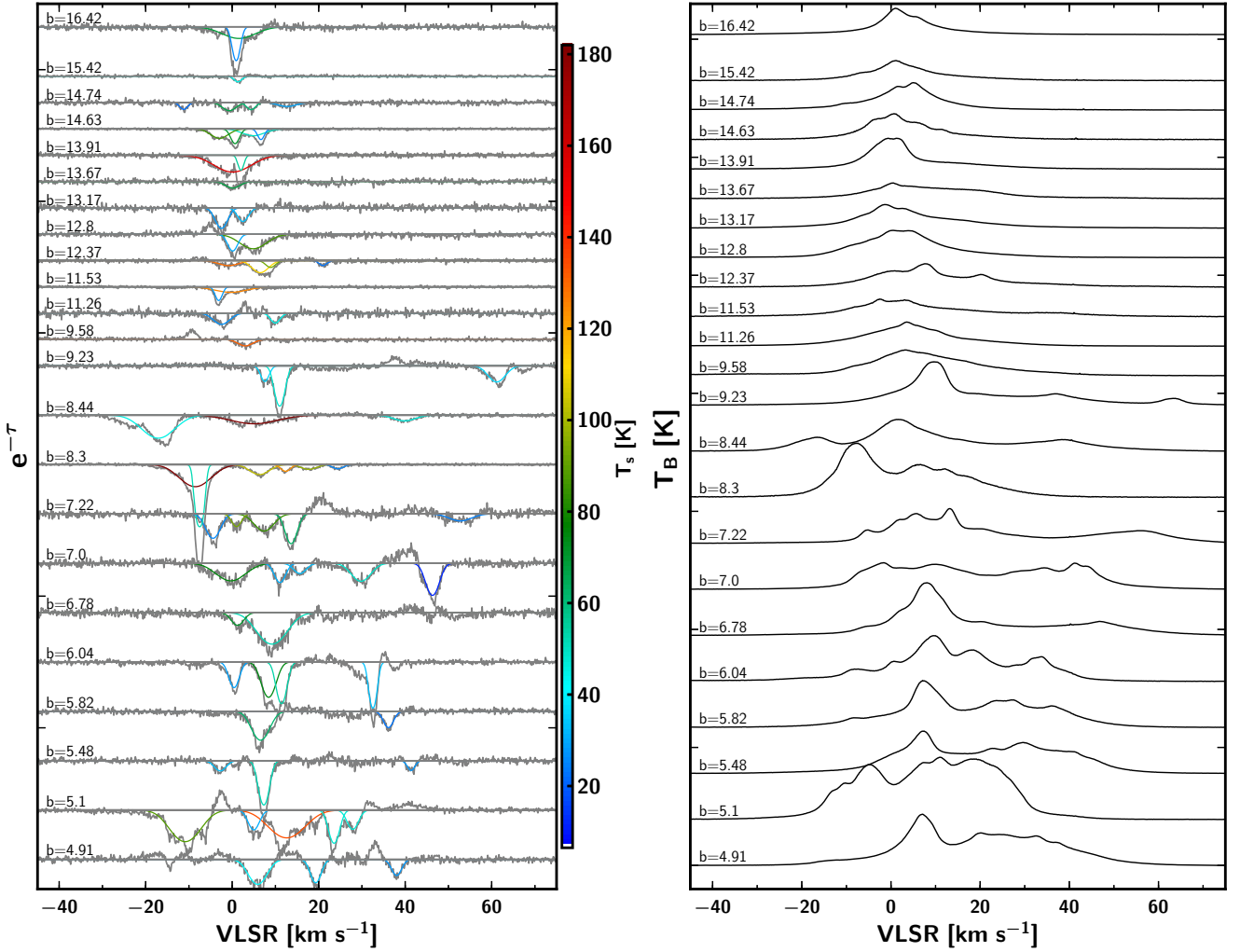


FIG. 5.— The same as Figure 4 but for 23 sightlines toward Gemini region.

the observed FWHM results from the combination of thermal and turbulent broadening. We also estimate *lower* limits on T_s for our WNM component, imposed by the upper limits on optical depth (see Table 3).

In Figure 8, we show the distributions of temperatures derived from the Gaussian fits to all 77 sightlines, with the top and middle panels showing CNM T_s ; and the bottom panel WNM T_D . In the top panel, we also show the T_s distributions of our three different regions; in the others, we plot the temperature histograms obtained from other studies (HT03, S14, M15) for comparison. Here is important to note that our optical depth sensitivity ($\sim 5 \times 10^{-3}$ per 1 km s^{-1} , obtained from the median of the 1σ noise level in optical depth spectra) is lower than that of previous studies: $\sim 2 \times 10^{-3}$ per 1 km s^{-1} for both HT03 and S14, and $\sim 9 \times 10^{-4}$ per 0.42 km s^{-1} for M15.

4.2.1. Temperatures of cold gas

For the CNM components, the spin temperatures fall in the range ~ 10 – 480 K , with our T_s distribution spreading mostly from 25 – 150 K with a peak at $\sim 50 \text{ K}$ and a median at $54.6 \pm 4.6 \text{ K}$, as well as a column-density-weighted median of $74.8 \pm 9.6 \text{ K}$ (the uncertainties of the medians are obtained from bootstrap re-sampling). Indeed, we

see no obvious tail at $T_s > 200 \text{ K}$. In order to examine how T_s medians vary with the sensitivity in optical depth, we group the T_s of CNM components into four different ranges of optical depth sensitivity with similar sample sizes. From high to low sensitivities, the spin temperature medians are $61.7 \pm 16.5 \text{ K}$, $61.2 \pm 10.4 \text{ K}$, $54.3 \pm 6.6 \text{ K}$ and $48.3 \pm 8.3 \text{ K}$ respectively; and the highest T_s values belong to the highest sensitivity range. Hence, while the uncertainty is large, this (unsurprisingly) suggests a dependence of the median measured T_s on the opacity sensitivity. This is also consistent with the fact that the highest-sensitivity survey plotted in Figure 8 (21-SPONGE; M15) measured a median T_s 25 K higher than the three others. This simply indicates that observations with improved sensitivity in H I absorption are able to directly measure the T_s of warmer H I gas (in the temperature range of UNM or WNM), resulting in a higher T_s median.

From our results, $\sim 98\%$ of CNM components (equivalent to 97% by column density of the cold gas) lie below 200 K . In fact, most of the CNM gas (80% by number of components and 74% by column density) has $T_s = 25$ – 100 K . About 14% of the gas has $100 < T_s < 200 \text{ K}$, and it contributes $\sim 22\%$ to CNM column density. The

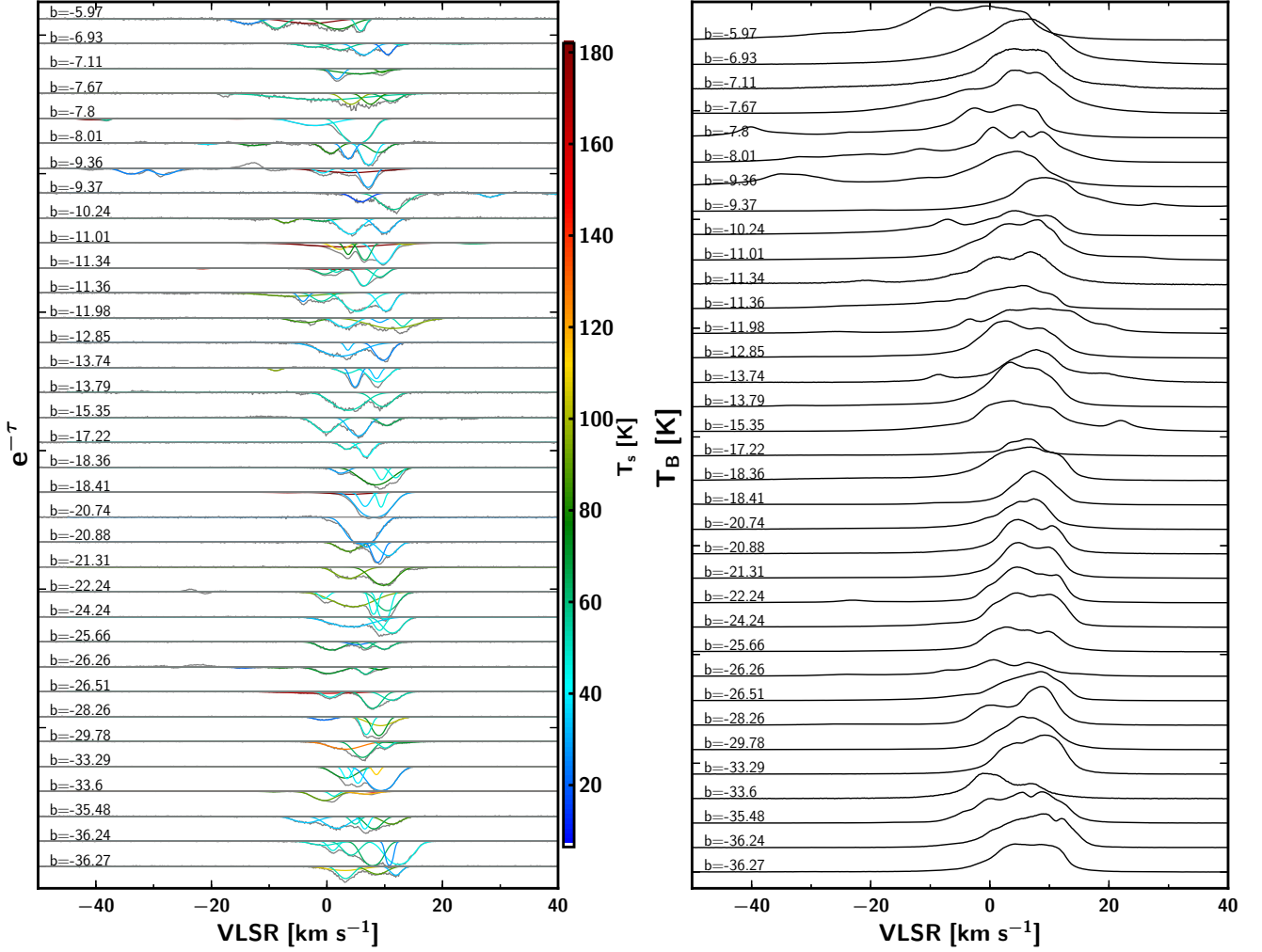


FIG. 6.— The same as Figure 4 but for 35 sightlines toward Taurus region.

remaining of 4% of the gas is very cold with $T_s < 25$ K but contributes only $< 1\%$ in CNM column density. Such extremely cold gas has been observed by several studies: HT03, S14, M15, Meyer et al. (2006, 2012). In particular, Knapp & Verschuur (1972) claimed to have observed a cold HI cloud with spin temperature of 7–20 K; and Wannier et al. (1999) also measured a T_s of 20–60 K in the Perseus B5 molecular cloud. While some fraction of very low T_s components may be spurious fits, the minimum CNM T_s from analytical models is ~ 20 K (Wolfire et al. 2003), and such low temperatures might also occur in regions where photoelectric heating by dust grains is reduced (e.g. Wolfire et al. 1995; Heiles & Troland 2003b).

We find no evidence for differences in the distribution of CNM spin temperatures in our three regions, despite their different characteristic environments (as shown in top panel of Figure 8). The CNM T_s distributions for the Gemini, Galactic plane and Taurus regions, have relatively close medians of 48.1 ± 8.8 K, 61.6 ± 8.7 K, 53.5 ± 4.9 K respectively, and the differences are broadly consistent with the background continuum source flux density distributions – Gemini has the highest proportion of weak sources; the Galactic plane has the lowest (as listed in Table 1). Conversely, if there were significant differences

in the underlying CNM T_s distribution, then we might have observed different medians that do not scale with the background source intensity.

These T_s medians are also in good general agreement with the results from HT03 (48.8 K, along random sightlines in the Arecibo sky), S14 (49.0 K, around the Perseus molecular cloud), and Dénes et al. (2018) (48.0 K, in the Riegel-Crutcher cloud). Our values are lower than those of the 21-SPONGE survey (M15, M18 at 77.6 K, 73.6 K respectively), reflecting its higher optical depth sensitivity. More importantly, the general shape of the spin temperature histograms of the various surveys are similar, with the exception of the obvious higher- T_s tail in 21-SPONGE (see the middle panel of Figure 8). Together, this is consistent with a picture in which the spin temperature distribution of the CNM remains relatively consistent throughout the Galactic ISM; in particular, measurements along random Galactic sightlines agree well with those in fields focused around molecular clouds. Any measured differences are largely a result of higher-sensitivity observations recovering larger portions of the higher- T_s tail. This may suggest a universality of cold HI properties, which will be explored more in the following sections. The same conclusion was drawn by

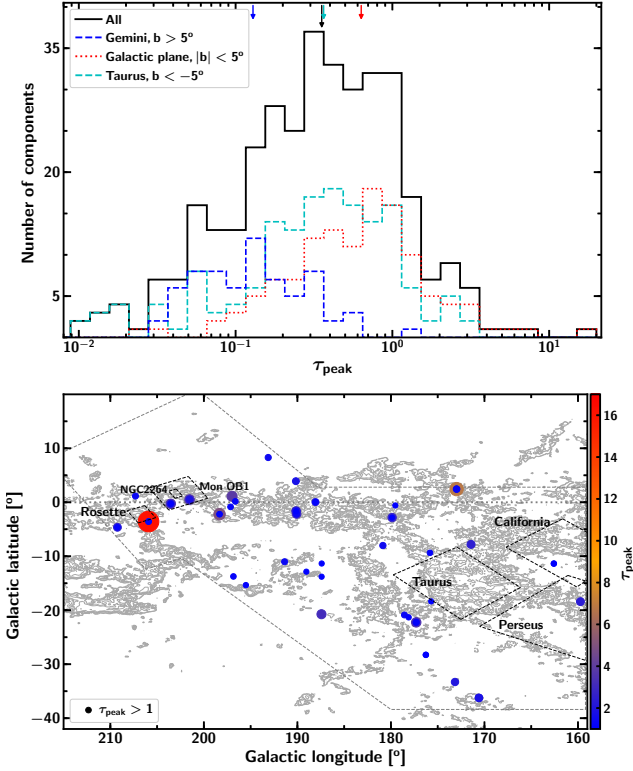


FIG. 7.— Top panel: Histograms of τ_{peak} for CNM components along 77 sightlines: black for all CNM components, blue, red and cyan for the subsamples in Gemini, Galactic plane and Taurus respectively. The arrows show the medians. Bottom panel: The locations of components having $\tau_{\text{peak}} > 1$; both the colors and sizes of the circles represent the magnitudes of τ_{peak} ; the horizontal dotted line marks the Galactic plane; the dashed rectangles roughly show the areas of molecular clouds; and the gray dashed lines roughly show the boundaries of the regions of interest. S14.

4.2.2. Temperatures of warm gas

For the WNM components on the bottom panel of Figure 8, we show the histogram of T_D . Most of the WNM lies below 5000 K, but the T_D distribution exhibits a long tail well beyond 20,000 K. About 45% of the WNM components (equivalent to 40% by column density) is in the thermally unstable regime with $T_D = 500$ –5000 K (see e.g. HT03, Roy et al. 2013, M15, M18), implying that $\sim 24\%$ of all of the atomic gas does not lie in thermal equilibrium. This fraction is consistent with previous studies: HT03 found that at least 48% of the WNM (equivalent to 30% of the total gas) is thermally unstable, and Roy et al. (2013) also found at least $\sim 28\%$ of the gas in the unstable range. The fractions in M15 and M18 are slightly lower, at $\sim 20\%$, but agree well with our finding within their uncertainties of $\gtrsim 10\%$. Nearly 14% of our WNM components have $T_D < 500$ K, corresponding to 4% in WNM column density, with the lowest limit at ~ 108 K (only two out of 349 WNM components have $T_D < 200$ K, one of which is shown in the upper panels of Figure 3). In this temperature range the WNM gas is too cold to classify as thermally unstable. From examination of the spectra, we believe these components are real, and not artifacts of poor fitting. They are not seen in absorption likely because they are thin, cold HI clouds in the diffuse medium with very low column density (as reported

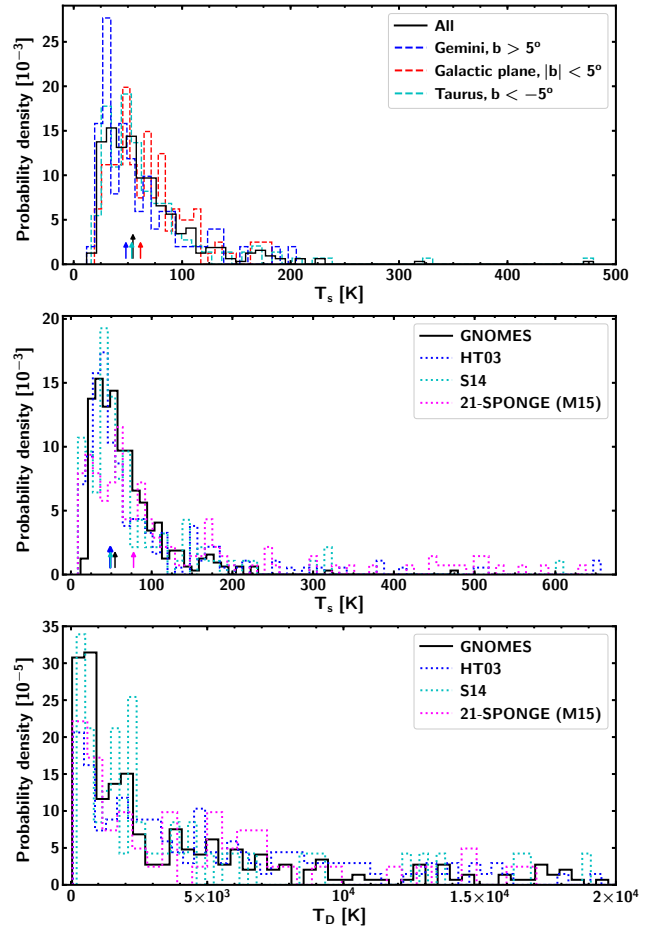


FIG. 8.— Normalized histograms of T_s for CNM components (top and middle), T_D for WNM components (bottom). In the top panel, the solid black line shows all CNM components; blue, red and cyan dashed lines show the subsamples in Gemini, the Galactic plane and Taurus respectively. In the middle and bottom panels, GNOMES is shown in solid black, HT03 in dotted blue, S14 in dotted cyan, and 21-SPONGE (M15) in dotted pink. The arrows show the medians.

by Stanimirović & Heiles 2005 and Stanimirović et al. 2007). Typical 1σ upper limits on τ for these “cold” WNM components ($T_D < 500$ K) are at a median of ~ 0.07 , and thus their lower limits on T_s are at a median of 148 K. Most of the rest of the WNM (25% in component number, 37% in column density) lies between 5000 K and 20,000 K. The fraction of the gas with $T_D > 20,000$ K (not shown in the histogram) is 16% in components and 19% in column density. In reality, the gas would be ionized at temperatures above $\sim 10,000$ K, so WNM components with $T_D > 10,000$ K either must include multiple narrower components or have highly supersonic motions (e.g. HT03).

4.3. Turbulent Mach Number Distribution

From HI observations, it is almost impossible to constrain the sonic Mach number for the WNM. However, the Mach number of non-thermal CNM motions can be estimated from the line-width ($\Delta V = \text{FWHM}$) and spin temperature. Assuming that the FWHM of each CNM component results from both thermal broadening and turbulent motions (Leung & Liszt 1976; Liszt 2001), ΔV

can be expressed as:

$$\frac{(\Delta V)^2}{8 \ln 2} = \frac{k_B T_k}{m_H} + V_{\text{turb},1D}^2 \quad (14)$$

where k_B is Boltzmann's constant, T_k is the kinetic temperature, m_H is the mass of a hydrogen atom and $V_{\text{turb},1D}^2$ is the one-dimensional mean square turbulent velocity which relates to the mean square three-dimensional turbulence velocity of the CNM as $V_{\text{turb},3D}^2 = 3V_{\text{turb},1D}^2$. For the CNM, since thermal equilibrium is established quickly, we may assume $T_k = T_s$, then the isothermal sound speed can be computed as $C_s = \sqrt{kT_s/\mu m_H}$. Dividing ΔV and $V_{\text{turb},3D}$ by the sound speed C_s will respectively give the sonic Mach number (M_s) and the turbulent Mach number (M_t) of the CNM. Adopting a mean atomic weight of $\mu = 1.4$ for the Galactic ISM, we may write:

$$M_t = \frac{V_{\text{turb},3D}}{C_s} = \sqrt{3 \left(\frac{M_s^2}{8 \ln 2} - \mu \right)}. \quad (15)$$

We show a histogram of derived M_t values in Figure 9. The median sonic Mach number for the whole sample of 77 sources is $M_t = 4.1 \pm 0.3$, and the histogram peaks around $M_t = 3.5$ – 4.0 . This result is slightly higher than found by HT03, M15 and M18 (at $M_t = 3.4$, 2.9 and 3.1 respectively) and agrees best with S14 in the Perseus molecular cloud region ($M_t = 4.0$). We also note that Burkhart et al. (2010) find $M_t \sim 4.0$, for CNM around the SMC bar even though the gas properties in the SMC are very different from those in the Milky Way. All of these results support a picture in which internal macroscopic motions in the CNM are highly supersonic. One possible explanation for this dynamical property of the CNM is that the cold HI gas along the line of sight consists of a few individual long living CNM structures (clumps); while the individual clumps are subsonic, their relative velocities are supersonic with respect to the CNM sound speed as they were inherited from the velocity dispersion of the WNM (from which CNM was formed). This would imply that the observed Mach number along Galactic sightlines is due to the velocity dispersion from the relative motions of clumps rather than the internal velocity dispersion of the cold HI medium (e.g. Koyama & Inutsuka 2002; Heitsch et al. 2005; Hennebelle & Audit 2007; Hennebelle et al. 2007; Saury et al. 2014). Alternatively, it has been suggested that the supersonic motions of the cold HI along the edges of the SMC bar may be related to the shearing/turbulent flows and/or shocks between the bar and the surrounding gas (Burkhart et al. 2010); it is possible that similar processes may also be implicated in some Milky Way gas.

4.4. HI column density distributions

The HI column density of the cold absorbing HI along each sightline is calculated by:

$$N_{\text{HI,CNM}} = C_0 \int T_s \tau_v dv \quad (16)$$

where $C_0 = 1.823 \times 10^{18} \text{ cm}^{-2} \text{ K}^{-1} (\text{km s}^{-1})^{-1}$, and for the non-absorbing emission components, we estimate the column density as

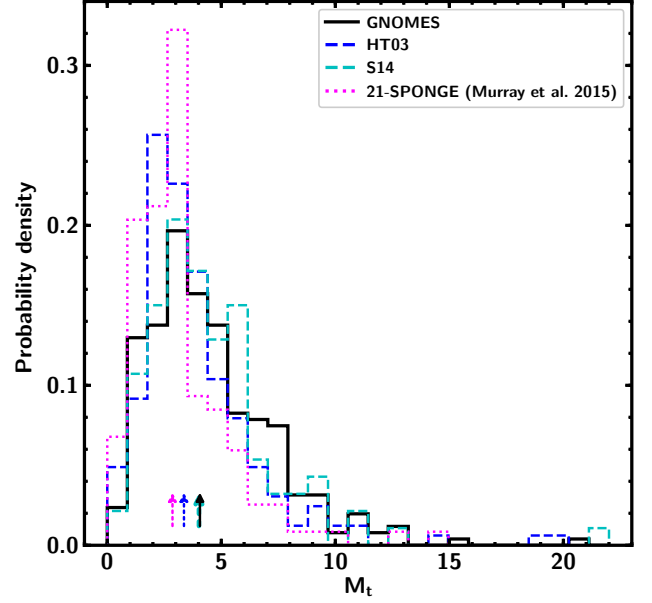


FIG. 9.— Normalized histograms of turbulent Mach numbers for all CNM Gaussian components: GNOMES in black, HT03 in blue, S14 in green and M15 in pink.

$$N_{\text{HI,WNM}} = C_0 \int T_B dv \quad (17)$$

where T_B is the brightness temperature.

We summarize the column densities from the Gaussian fits in Figure 10. In the top panel we plot histograms of N_{HI} for all CNM and WNM Gaussian components. The two phases have similar column density distributions regardless of Galactic latitudes. They have relatively close medians ($1.4 \times 10^{20} \text{ cm}^{-2}$ for CNM and $2.3 \times 10^{20} \text{ cm}^{-2}$ for WNM) even though the column density ranges are enormous ($(0.04\text{--}32.0) \times 10^{20} \text{ cm}^{-2}$ for CNM and $(0.06\text{--}48.6) \times 10^{20} \text{ cm}^{-2}$ for WNM). In the three remaining panels of Figure 10, we show histograms of $\sum N_{\text{HI,CNM}}$, $\sum N_{\text{HI,WNM}}$ and total N_{HI} along sightlines (color-coded by region). Table 2 lists the means and medians of the distributions (also indicated by arrows in the histograms). Now, when summing column densities of all CNM and WNM components along each line of sight, it is obvious that the column densities distributions in the three regions are well separated, except for the case of $\sum N_{\text{HI,WNM}}$ in Gemini and Taurus. Gemini occupies the low N_{HI} regimes, the Galactic plane samples the highest N_{HI} with the sightlines toward the Perseus and Outer arms, and so Taurus is in the intermediate range. Our total CNM column density is about two thirds of the total WNM column density ($956.1 \times 10^{20} \text{ cm}^{-2}$ versus $1609.7 \times 10^{20} \text{ cm}^{-2}$). The median of total N_{HI} in Taurus is nearly double that of Gemini ($23.8 \times 10^{20} \text{ cm}^{-2}$ against $11.5 \times 10^{20} \text{ cm}^{-2}$), but only about one third of the N_{HI} median in Galactic plane ($79.0 \times 10^{20} \text{ cm}^{-2}$). While the N_{HI} distribution in Galactic plane is widely spread, the histograms of other regions are concentrated in well-defined ranges. Most Galactic plane sightlines ($|b| < 5^\circ$) with high column densities ($N_{\text{HI}} > 50 \times 10^{20} \text{ cm}^{-2}$) are close to NGC 2264 and Rosette molecular clouds where

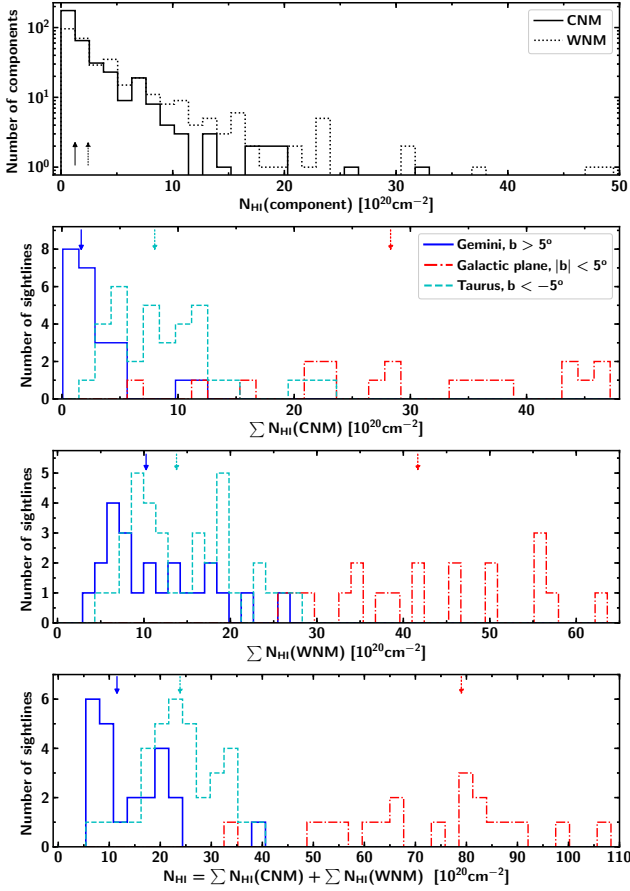


FIG. 10.— Histograms of N_{HI} for all CNM (solid) and WNM (dotted) Gaussian components (top), $\sum N_{\text{HI,CNM}}$ (second panel), $\sum N_{\text{HI,WNM}}$ (third panel), and total $N_{\text{HI}} = \sum N_{\text{HI,CNM}} + \sum N_{\text{HI,WNM}}$ (bottom) for all sightlines in different regions: blue for Gemini, red for Galactic plane, cyan for Taurus. The arrows show the medians.

TABLE 2
MEANS AND MEDIANS OF HISTOGRAMS IN FIGURE 10

Region	Mean N_{HI} [10^{20} cm^{-2}]	Median N_{HI} [10^{20} cm^{-2}]
CNM, Gemini ($b > 5^\circ$)	2.7	1.7
CNM, Galactic plane ($ b < 5^\circ$)	30.3	28.3
CNM, Taurus ($b < -5^\circ$)	9.1	8.0
WNM, Gemini	11.6	10.3
WNM, Galactic plane	43.4	41.7
WNM, Taurus	14.8	13.8
CNM+WNM, Gemini	14.3	11.5
CNM+WNM, Galactic plane	73.7	79.0
CNM+WNM, Taurus	23.9	23.8

the CO contours peak; on the contrary, all other diffuse sightlines above the plane are found further away from the two molecular clouds ($b > 5^\circ$), and apparently do not have significant CO detections. In most cases, the CNM contributes significantly to the total HI column density.

In Figure 11, we compare our results with the findings of previous surveys (here HT03, S14 and M15) that applied the same basic methodology in observation and

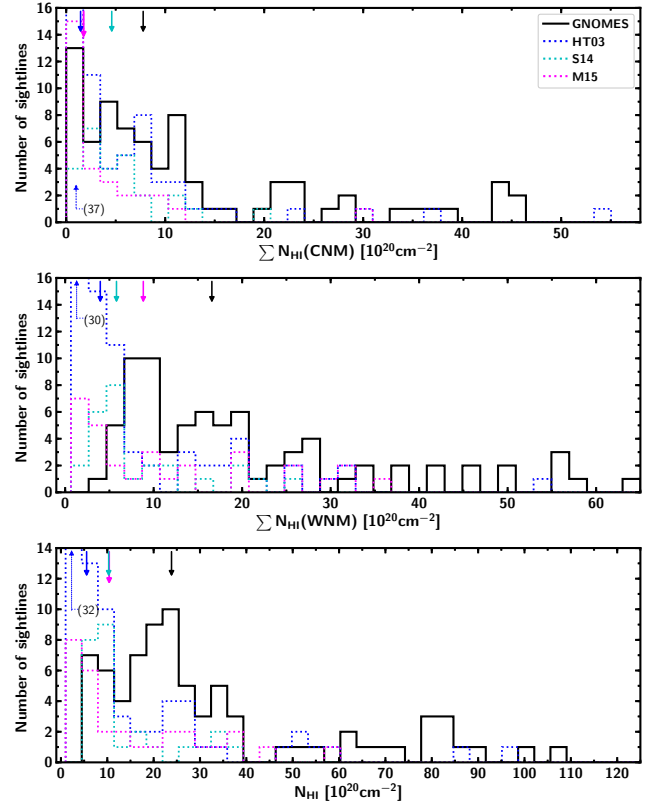


FIG. 11.— Histograms of $\sum N_{\text{HI,CNM}}$ (top), $\sum N_{\text{HI,WNM}}$ (middle) and total $N_{\text{HI}} = \sum N_{\text{HI,CNM}} + \sum N_{\text{HI,WNM}}$ (bottom) for each sightline estimated from Gaussian decomposition fit: black for GNOMES, blue for HT03, cyan for S14 and pink for M15. The solid downward arrows show the medians. The upward arrows indicate the maximum values beyond the tops of the figure (HT03 only).

data analysis, but for different regions of the sky. In all cases, our N_{HI} distributions are slightly shifted toward higher column densities. Our lowest N_{HI} median is found in the Gemini region, which is comparable with the median from S14 for Perseus molecular cloud ($10.3 \times 10^{20} \text{ cm}^{-2}$) and M15 ($10.4 \times 10^{20} \text{ cm}^{-2}$), but still higher than that obtained by HT03 ($5.5 \times 10^{20} \text{ cm}^{-2}$). These differences likely reflect genuine differences in the sightlines probed by the different studies. The present work contains a high proportion of positions either in the Galactic Plane or close to molecular regions; meanwhile, HT03 and M15 mostly observed random sightlines in the neighborhood of the Solar system, and the S14 sightlines around Perseus mostly sampled material away from the main body of the molecular cloud.

4.5. N_{HI}^* vs N_{HI}

The optically thin HI column density, N_{HI}^* , is directly estimated from the expected emission profile, so is proportional to the profile area. On the contrary, to calculate the opacity-corrected N_{HI} one needs both spin temperature and optical depth, which can be derived from the combination of on-/off-source spectra. Based on our results, we can compare the two estimates. The ratio $f = N_{\text{HI}}/N_{\text{HI}}^*$ for all 77 sightlines is plotted as a function of total N_{HI} in Figure 12. For the full sample, f has a mean and median of 1.28 and 1.21 respectively. At low column

densities below $\sim 1 \times 10^{21} \text{ cm}^{-2}$, N_{HI}^* is comparable to the corrected N_{HI} ($f \sim 1.0$); the ratio then rises as column density increases, reaching $f \sim 1.8$ by the time N_{HI} has increased by an order of magnitude ($1 \times 10^{22} \text{ cm}^{-2}$). Interestingly, the ratio $N_{\text{HI}}/N_{\text{HI}}^*$ for the Gemini region is almost flat and consistent with unity over the whole of its N_{HI} range $(5\text{--}40) \times 10^{20} \text{ cm}^{-2}$, and as seen in the lower panel, no sightlines in this region fall within CO contours. Meanwhile, the ratio f around Taurus stays mostly around the mean value of 1.3, whereas within the Galactic plane it exhibits a rising trend with N_{HI} . This indicates that significant corrections are needed to account for opacity effects, especially in denser gas regimes or at low latitudes (see also Dickey et al. 2003; Bihr et al. 2015).

Nevertheless, the question of how best to correct for HI opacity effects when emission/absorption pairs are not available is still open (see the discussion in Section 5). A few methods have been proposed: e.g. a linear correlation between f and $\log_{10}(N_{\text{HI}})$ (Dickey et al. 2000; Lee et al. 2015) or a simple isothermal correction assuming the same T_s along the lines-of-sight (as employed by Liszt 2014b; Remy et al. 2017). The general increase of the correction factor f as a function of N_{HI} is obvious, but the relationship between the two appears to be environmentally dependent, as just discussed above for our regions. Literature values of f include ~ 1.1 in the range $N_{\text{HI}} = (3.9\text{--}13.0) \times 10^{20} \text{ cm}^{-2}$ for 26 sightlines within and around the Perseus molecular cloud (Lee et al. 2015); $f \sim (1.1\text{--}1.3)$ for 79 random sightlines in Millennium survey (HT03); and $f < 1.2$ for reddening of $E(B - V) \lesssim 0.5$ mag, for sightlines at high Galactic latitudes (Liszt 2014a).

4.6. The CNM fraction, F_{CNM}

In the first panel of Figure 13, we present the variation of the CNM fraction ($F_{\text{CNM}} = N_{\text{CNM}}/N_{\text{HI}}$) as a function of N_{HI} . While the F_{CNM} does increase with N_{HI} , there is clearly a very large scatter. We measure median values of $F_{\text{CNM}} = 0.43$ and 0.37 respectively for the Galactic plane and Taurus regions – more than double the value of 0.16 for Gemini. We find 9/77 sightlines with $F_{\text{CNM}} < 0.1$, all of them in Gemini, above the Galactic Plane. The highest F_{CNM} values are found in the proximity of the giant molecular clouds (Rosette, NGC 2264 and in the south of Taurus and California) as shown in the map in the lower panel of the Figure. The Taurus F_{CNM} median is comparable to the value of 0.35 found in Perseus (S14) – a similar region in and around a molecular cloud. Similarly, the median for the Gemini region is consistent with the value of 0.20 found by M15 and 0.23 by HT03, both of which sampled largely diffuse sightlines. Thus, the CNM fraction around molecular clouds seems to be higher than in diffuse regions. This agrees well with a scenario in which a high CNM fraction is required for molecule formation, and GMCs are built-up stage by stage – from WNM-rich gas to CNM-rich gas to molecular clouds.

Overall the F_{CNM} from all GNOMES sightlines does not exceed 75% – a result that agrees with the F_{CNM} range observed in different regions of the Galaxy by HT03 and S14, also using the Arecibo telescope, and M15 and M18, using the VLA for absorption. Our CNM fraction is also close to the range of $F_{\text{CNM}} \sim 40\text{--}70\%$

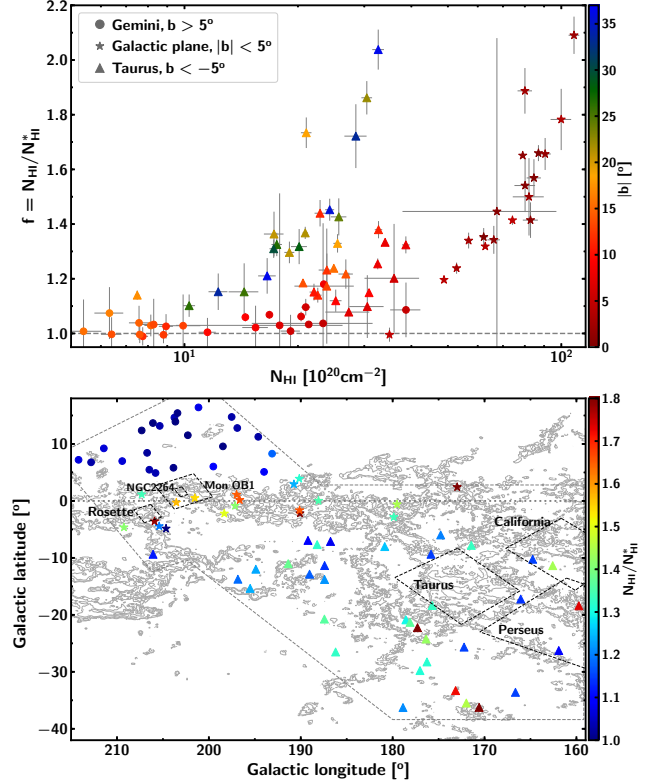


FIG. 12.— Top panel: $f = N_{\text{HI}}/N_{\text{HI}}^*$ as a function of N_{HI} in Gemini (dots), Galactic plane (stars) and Taurus (triangles) regions. The colors represent the absolute values of Galactic latitude $|b|$; the dashed line marks where $N_{\text{HI}} = N_{\text{HI}}^*$. Bottom panel: The map of $f = N_{\text{HI}}/N_{\text{HI}}^*$ for our 77 sightlines toward the three regions; the horizontal dotted line shows the Galactic plane; the dashed rectangles roughly show the areas of molecular clouds; and the gray dashed lines roughly show the boundaries of the regions of interest. The colors represent the values of the ratio f .

found in the numerical simulations of Kim et al. (2014).

In Figure 14, we plot F_{CNM} against the $N_{\text{HI}}/N_{\text{HI}}^*$ ratio. Obviously, $N_{\text{HI}}/N_{\text{HI}}^*$ increases with the increase of F_{CNM} as expected. This simply demonstrates that the higher the CNM fraction is along the line-of-sight, the more important the opacity correction is. Nevertheless, we note that with the CNM fraction below 20%, N_{HI}^* is consistent with N_{HI} , to within the errors. After this point, the $N_{\text{HI}}/N_{\text{HI}}^*$ ratio rises up to a value of ~ 2 as F_{CNM} increases from 20% to 75%.

5. HI OPACITY CORRECTIONS

Pursuing the ultimate goal of deriving “true” N_{HI} maps toward our three regions around Taurus and Gemini, we will test two methods of opacity correction using HI emission data from the GALFA-HI survey. This is an important preparatory step for future work aiming to derive dark gas maps in these two regions using dust and γ -ray data as tracers of total proton column density.

5.1. From the best fit of $f = N_{\text{HI}}/N_{\text{HI}}^*$ vs $\log_{10}(N_{\text{HI}})$

The first method estimates an appropriate correction factor for each sightline from the best fit of $f = N_{\text{HI}}/N_{\text{HI}}^*$ vs $\log_{10}(N_{\text{HI}}/10^{20})$, using the data from all 77 sightlines (e.g. Lee et al. 2015). From our data, the ratio

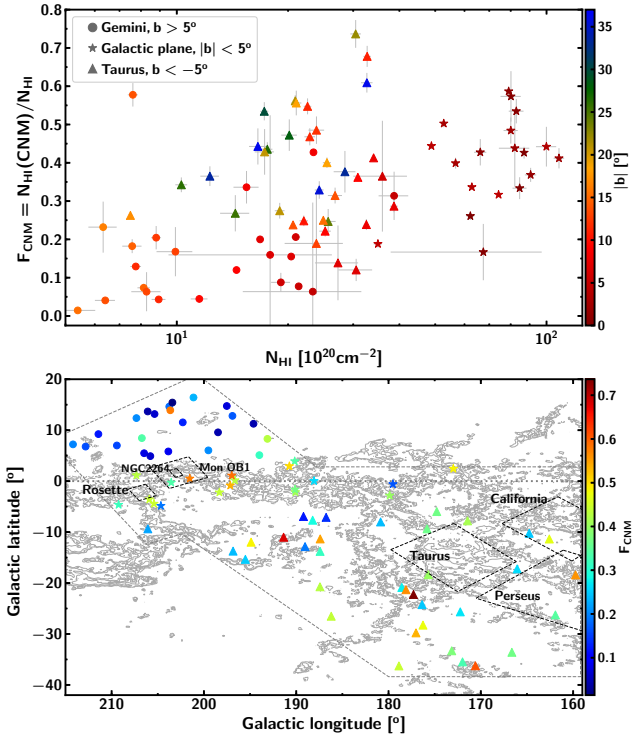


FIG. 13.— Top panel: $F_{\text{CNM}} = N_{\text{CNM}}/N_{\text{HI}}$ as a function of total N_{HI} toward Gemini (dots), Galactic plane (stars) and Taurus (triangles) regions. The colors represent the absolute values of Galactic latitude $|b|$. Bottom panel: The map of F_{CNM} for all 77 sightlines toward the three regions; the horizontal dotted line shows the Galactic plane; the dashed rectangles roughly show the areas of molecular clouds; and the gray dashed lines roughly show the boundaries of the regions of interest. The colors represent the values of F_{CNM} .

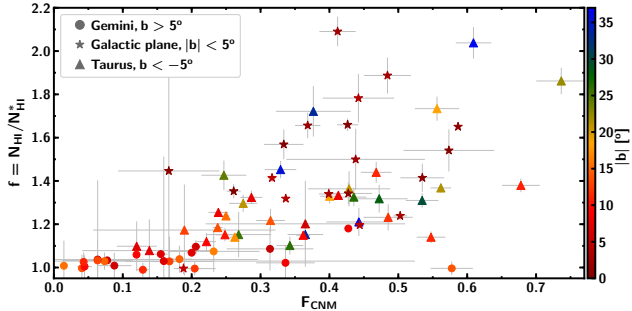


FIG. 14.— $f = N_{\text{HI}}/N_{\text{HI}}^*$ versus F_{CNM} along 77 sightlines. The colors represent the absolute values of Galactic latitude $|b|$.

f increases with increasing N_{HI}^* , with a Pearson linear coefficient of 0.5. To find an appropriate correlation, we fit the datapoints using four models: linear, quadratic, first-order exponential (in the form of $e^{ax} + b$) and second-order exponential ($e^{ax^2} + b$). We then compute the “Bayesian factors” (R) and “Bayesian p -values” (p) from the Bayesian model selection for each pair of models, finding $R(\text{linear/quadratic}) = 72.08$, $p(\text{linear}) = 98.6\%$; $R(\text{linear/first-order exponential}) = 1.22$, $p(\text{linear}) = 54.9\%$; $R(\text{linear/second-order exponential}) = 1.02$, $p(\text{linear}) = 50.5\%$. Thus the Bayesian factors favor the linear model (since their R values are greater than 1 and their p -values are greater than 50%). It is worth noting

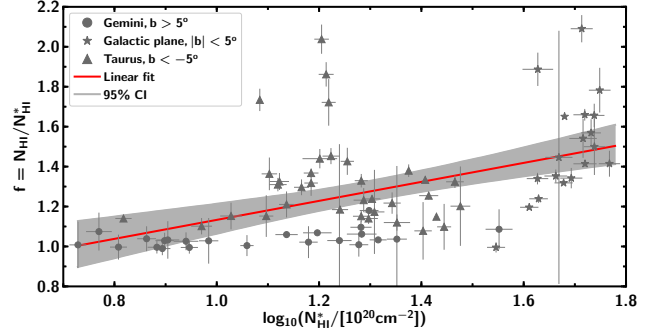


FIG. 15.— Ratio $f = N_{\text{HI}}/N_{\text{HI}}^*$ versus $\log_{10}(N_{\text{HI}}^*/10^{20})$. The red line represents the best linear fit: $f = (0.47 \pm 0.09)\log_{10}(N_{\text{HI}}^*/10^{20}) + (0.66 \pm 0.12)$. The shaded region shows the 95% confidence interval (CI) obtained from bootstrap re-sampling.

that the linear model is definitely much more preferred than the quadratic, but the posterior probability in favor of the first-order exponential model is 46% (compared to the linear model), which is too large to support rejecting the exponential model; meanwhile the posterior probabilities in favor of the second-order exponential and linear models are almost the same. Figure 15 shows the *general* linear fit of $f = N_{\text{HI}}/N_{\text{HI}}^*$ vs $\log_{10}(N_{\text{HI}}^*/10^{20})$ with 95% confidence intervals obtained from bootstrap re-sampling. The correction factor from the best fit is: $f = (0.47 \pm 0.09)\log_{10}(N_{\text{HI}}^*/10^{20}) + (0.66 \pm 0.12)$ (see also Lee et al. 2015, for the gas around Perseus molecular cloud). The HI column density obtained from this method is denoted as $N_{\text{HI}}^{\text{fit}}$. We note that our slope is quite different from Lee et al. (2015)’s. However, as mentioned before, it is clear that the correction factor and its variation with N_{HI} for each region are quite distinct, hence applying a single linear relationship for all regions may not be reliable. In fact, when fitting on a region-by-region basis we find that the best fit for the Gemini region is nearly flat with $f = (0.09 \pm 0.04)\log_{10}(N_{\text{HI}}^*/10^{20}) + (0.94 \pm 0.04)$; for sightlines through the Galactic plane area the correction factor increases rapidly as N_{HI}^* increases: $f = (2.41 \pm 0.93)\log_{10}(N_{\text{HI}}^*/10^{20}) - (2.57 \pm 1.57)$; but the best fit f for Taurus region *decreases* with increasing N_{HI}^* : $f = (-0.18 \pm 0.26)\log_{10}(N_{\text{HI}}^*/10^{20}) + (1.54 \pm 0.32)$. A linear correlation between f and $\log_{10}(N_{\text{HI}}^*)$ is therefore not convincing for every region.

5.2. Using region-dependent uniform T_s

The second approach is to apply a simple isothermal correction to GALFA- HI using a single value of spin temperature for each sub-region. Here, an opacity-corrected HI column density is obtained by integrating the following function of brightness temperature (T_B), and spin temperature T_s (e.g. Lockman & Savage 1995; Wakker et al. 2011):

$$N_{\text{HI}}^{\text{ISO}} = 1.823 \times 10^{18} \int T_s \ln \left[\frac{T_s}{T_s - T_{\text{exp}}} \right] dv. \quad (18)$$

This approximation has the advantage that with an appropriate value of T_s , it only requires HI emission spectra to estimate N_{HI} , but it is not applicable at high optical depths where $T_s \approx T_B$ because the denominator in Equation 18 approaches zero. By conducting a least square

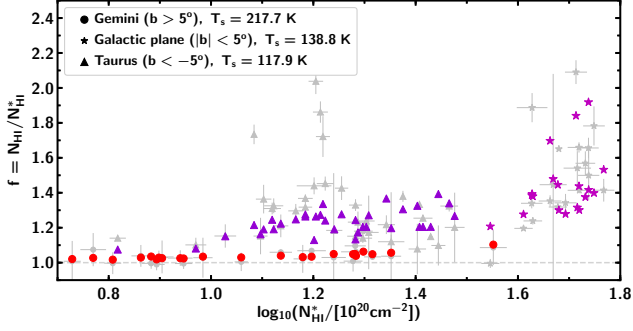


FIG. 16.— Ratio $f = N_{\text{HI}}/N_{\text{HI}}^*$ versus $\log_{10}(N_{\text{HI}}^*/10^{20})$. The gray data points are results from Gaussian fit (same as for Figures 12 and 15). The color markers show the ratios estimated from corrected N_{HI} using single values of T_s for different regions: stars for Galactic plane $|b| < 5^\circ$, triangles for Taurus region $b < -5^\circ$, and dots for Gemini area $b > 5^\circ$.

fit of the HI column densities obtained from this isothermal assumption and those from the Gaussian decomposition method (Section 4.4) using T_s as a parameter, we find best fit spin temperatures of $T_s = 217.7$ K for the Gemini region ($b > 5^\circ$), $T_s = 138.8$ K for the Galactic Plane ($|b| < 5^\circ$), and $T_s = 117.9$ K for the Taurus region ($b < -5^\circ$). The HI column density corrected by this method is denoted as $N(\text{HI})_{\text{uniform}}$, and its corresponding f ratios are shown in Figure 16. It can be seen that the isothermal approximation with uniform spin temperatures generally reproduces quite well the correction factors derived from the original Gaussian decomposition.

5.3. Comparing corrected N_{HI} maps

We apply the two methods described above to correct for opacity effects pixel-by-pixel in the GALFA-HI maps of the Gemini, Galactic plane and Taurus regions. In upper panel of Figure 17 we compare the corrected N_{HI} results from the *general* linear fit and uniform T_s maps by plotting the histograms of their relative differences in different regions, and Figure 18 projects these relative differences onto the corresponding maps. Although we see individual pixel-by-pixel differences of up to $\sim 25\%$, the N_{HI} corrected from the two methods are in general comparable with a median difference of 0.6%, a mean of 0.1%, and standard deviation of 7.9%. The difference between the two corrected column densities is largest in the Gemini region ($b > 5^\circ$) with (median, mean, standard deviation) of (6.1%, 6.5%, 10.0%). In the Taurus region, the two correction methods agree well, with (median, mean, standard deviation) of (1.4%, 1.1%, 5.0%). Within the Galactic plane, N_{HI} corrected with uniform T_s is slightly lower than from the linear fit, the values of (median, mean, standard deviation) are (0.2%, 1.2%, 11.5%). Generally, the largest differences (more than 10%) are found in regions assumed to have higher CNM fractions: near the Galactic plane and in close vicinity to GMCs (see Figure 13 and 18).

These differences may arise in part from the fact that the *general* linear fit is made to the whole map for all three areas, whereas the different uniform spin temperatures were applied to each region. It appears that the two types of opacity correction are not consistent in Gemini and Galactic plane, but agree much better for the Taurus region, probably because our *general* linear fit seems to reproduce well the correction factors for the Taurus area

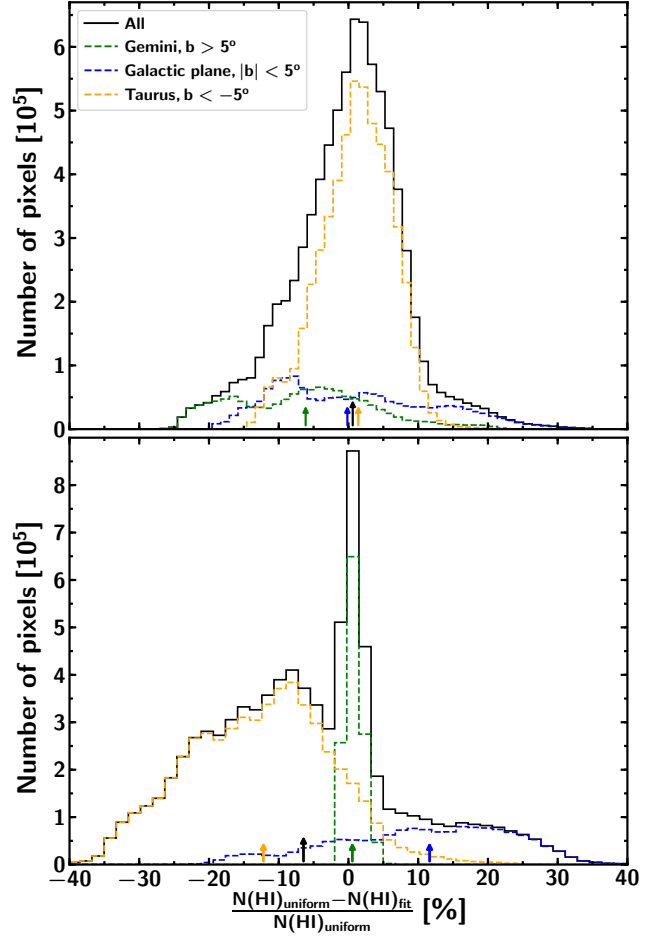


FIG. 17.— Comparisons of HI column densities obtained from two methods of opacity correction for GALFA-HI data toward the regions around Taurus and Gemini: (1) from the best fit of $f = N_{\text{HI}}/N_{\text{HI}}^*$ vs $\log_{10}(N_{\text{HI}}^*)$ (subscript “fit”) and (2) from uniform spin temperature maps (subscript “uniform”). Upper panel for the *general* best linear fit, lower panel for three region-dependent linear fits. The blue histogram shows the N_{HI} relative difference for Galactic plane area ($|b| < 5^\circ$), the green histogram for Gemini ($b > 5^\circ$), the yellow one for Taurus region ($b < -5^\circ$) and black line for all three areas. The arrows show the medians.

only (as seen in Figure 15). By contrast, when region-by-region linear fitting is applied, the two opacity correction methods agree very well for the Gemini region only, and depart further in the others, as seen in the lower panel of Figure 17. This means that a regional linear correlation could be a good choice for Gemini, but is not suitable for our sightline samples toward the Galactic plane and Taurus regions. In addition, our region of interest spreads over a large sky area of different conditions, therefore, we prefer a region-based uniform spin temperature correction for HI opacity throughout the Galactic ISM.

6. SUMMARY AND FUTURE WORK

As a follow-up of the HI study in the Perseus molecular cloud (Stanimirović et al. 2014; Lee et al. 2015), we have presented a large-scale Arecibo survey of HI emission/absorption observations to investigate the physical properties of cold and warm gas in the vicinity of five GMCs (Taurus, California, Rosette, Mon OB1, NGC 2264). This study is also a part of the GNOMES (Galac-

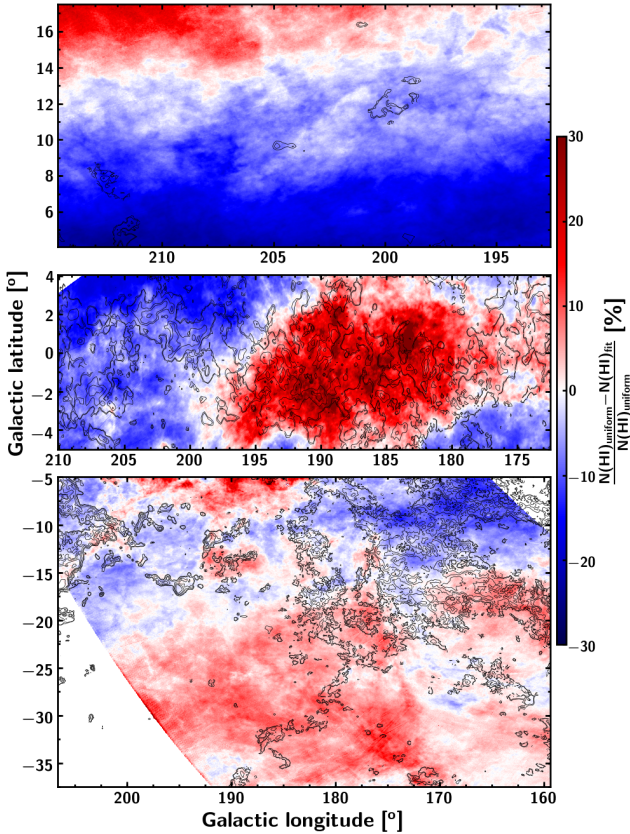


FIG. 18.— Relative difference of opacity-corrected GALFA-HI column densities obtained from the two methods discussed in the text (linear fit and region-dependent uniform spin temperature). The top panel shows the Gemini region ($b > 5^\circ$), the middle panel for the Galactic plane region ($|b| < 5^\circ$), and the bottom panel shows the Taurus region ($b < -5^\circ$). The colors indicate the relative difference $[N(\text{HI})_{\text{uniform}} - N(\text{HI})_{\text{fit}}]/N(\text{HI})_{\text{uniform}}$ (%). The contours are from $W_{\text{CO}(1-0)}$ map as described in Figure 1.

tic Neutral Opacity and Molecular Excitation Survey) collaboration, which aims to explore the properties of neutral and molecular gas in/around molecular clouds. We detected strong HI absorption in all directions toward 79 background radio continuum sources. By performing Gaussian decompositions (following the method of Heiles & Troland 2003a) for all pairs of absorption/emission spectra, we directly determined HI optical depths, temperatures and column densities for 349 CNM and 327 WNM Gaussian components. We used the distribution of CO integrated intensity $W_{\text{CO}(1-0)}$ (Dame et al. 2001) to separate our sample into three different interstellar environments – diffuse ($b > 5^\circ$), in-Plane ($|b| < 5^\circ$), and around giant molecular clouds ($b < -5^\circ$). Comparing the HI column density N_{HI} with that derived under the optically-thin assumption (N_{HI}^*) allows us to test two different methods for opacity-correction, which we apply to the GALFA-HI data. Our key conclusions are as follows:

1. The peak optical depth of individual Gaussian components ranges from ~ 0.01 – 16.2 , with a median value of 0.35 . We measure CNM spin temperatures between ~ 10 – 480 K, finding that the distribution peaks at ~ 50 K. The typical sonic Mach number for CNM is ~ 4 , which is consistent with previous studies and suggests that the turbulent motion of cold gas in the ISM is strongly supersonic. The median values of column densities for indi-

vidual CNM and WNM components are $1.4 \times 10^{20} \text{ cm}^{-2}$ and $2.3 \times 10^{20} \text{ cm}^{-2}$, respectively.

2. The properties of individual CNM components in our survey toward the three characteristic physical regions are consistent. More interestingly, they also agree well with those of previous observations along all-sky sightlines (HT03, M15, M18) and in/around the intermediate-mass Perseus molecular cloud (S14). This suggests that the properties of cold HI gas in the Galactic ISM are fairly universal. The same conclusion was pointed out by S14.

3. The WNM constitutes $\sim 60\%$ of the total HI gas, about 40% of which is in thermally unstable regime with an upper limit on kinetic temperature of 500 – 5000 K. The implied fractions of cold, unstable and warm medium (by mass) are therefore 40% , 24% and 36% , respectively.

4. The fraction of cold gas along each sightline, F_{CNM} , increases with increasing N_{HI} to a maximum of 75% . This is consistent with previous observations (HT03, M15, M18, S14) and also close to the 40 – 70% F_{CNM} range found in the numerical simulations of Kim et al. (2014). The F_{CNM} around molecular clouds is higher than in diffuse regions. This may support a staged build-up scenario for GMCs: from WNM-rich gas to CNM-rich gas to molecular clouds, with a high fraction of cold gas required for molecules to form.

5. The HI opacity correction factor $f = N_{\text{HI}}/N_{\text{HI}}^*$ increases as total N_{HI} increases, with a median value of 1.21 for the full sample of 77 sightlines. However, the variation behaves differently in each individual region: while the ratio f for Gemini is almost flat, it scatters around a mean value of 1.3 in Taurus and rises very steeply within the Galactic plane. Therefore, a linear relationship between the correction factor f and $\log_{10}(N_{\text{HI}}^*)$ is not convincing for every region.

6. We tested two methods of opacity correction: A linear fit of $f = N_{\text{HI}}/N_{\text{HI}}^*$ vs $\log_{10}(N_{\text{HI}}^*)$ made to the full sample, and the use of region-dependent uniform spin temperatures. We applied both methods to GALFA-HI emission cubes, finding that the relative difference on a pixel-by-pixel basis is up to $\sim 25\%$, however the mean offset between the derived N_{HI} distributions is small ($\sim 1\%$). Because separate linear fits do not well describe the relation between f and N_{HI}^* for each region, we prefer the uniform T_s method.

Future work will analyse OH observations toward the same continuum source sample (A. Petzler in prep.), then combine these with CO data, and broad-band tracers of molecular hydrogen and total proton column density to begin constructing dark gas maps of the Taurus and Gemini regions.

ACKNOWLEDGMENTS

JRD is the recipient of an Australian Research Council (ARC) DECRA Fellowship (project number DE170101086). MYL was partially funded through the sub-project A6 of the Collaborative Research Council 956, funded by the Deutsche Forschungsgemeinschaft (DFG). CEM is supported by a National Science Foundation Astronomy and Astrophysics Postdoctoral Fellowship under award AST-1801471.

We are very grateful to Professor Isabelle Grenier and Professor Mark Wardle for a number of useful discuss-

sions. We are indebted to T. Dame for generously providing the CO survey data. We thank the anonymous referee for constructive comments and criticisms which allowed us to improve this work. This publication utilizes data from Galactic ALFA HI (GALFA HI) survey data set obtained with the Arecibo L-band Feed Array (ALFA) on the Arecibo 305m telescope. The Arecibo Observatory is operated by SRI International under a cooperative agreement with the National Science Foundation (AST-1100968), and in alliance with Ana G. Méndez – Universidad Metropolitana, and the Universities Space Research Association. The GALFA HI surveys have been funded by the NSF through grants to Columbia University, the University of Wisconsin, and the University of California.

APPENDIX A: COMPARISON OF GAUSSIAN AND PSEUDO-VOIGT FITTINGS

In this section, we will carry out a detailed comparison of the parameters obtained from Gaussian and pseudo-Voigt decomposition fittings. The left panel of Figure 19 shows a histogram of η_{Lorentz} , the fraction of the Lorentzian function in the pseudo-Voigt profile, for all CNM and WNM components obtained from pseudo-Voigt absorption and emission fits. For 327 CNM components, 67% (217 out of 327) are pure Gaussian ($\eta_{\text{Lorentz}} = 0$), 25% (81/327) are a mixture of Gaussian and Lorentzian functions ($0 < \eta_{\text{Lorentz}} < 1$) (and basically in the mixture the components are more Gaussian than Lorentzian), and only 8% (26/303) are pure Lorentzian ($\eta_{\text{Lorentz}} = 1$). Of the 284 WNM components, 42% (119/284) are pure Gaussian, 40% (114/284) are mixed, and they in general distribute evenly in the range $0 < \eta_{\text{Lorentz}} < 1$, and 18% (51/284) are pure Lorentzian. Our results show that, compared to WNM, the CNM in general appears to have a smaller portion of Lorentzian components.

In the upper right panel of Figure 19 we compare the numbers of WNM and CNM components from Gaussian and pseudo-Voigt fits. In general, Gaussian fits require more components than pseudo-Voigt. For absorption, 44 out of 77 sightlines (57%) require the same numbers of Gaussian and pseudo-Voigt CNM components, 28 sightlines (36%) need more Gaussians (up to 3 components), 5 sightlines (7%) take more pseudo-Voigt components. In the case of emission, most of the sightlines (28/77, or 36%) demand one extra Gaussian component compared to pseudo-Voigt; the number of sightlines having the same number of Gaussian and pseudo-Voigt components is 31 (corresponding to 40%); 10 sightlines (13%) need more Gaussian than pseudo-Voigt from two to three extra components; 11% of the remaining 8 sightlines take at maximum two more pseudo-Voigt components than Gaussian ones. However, when the numbers of free parameters for the two line-shape functions are taken into consideration, pseudo-Voigt fits turn out to require more components than Gaussian in a major part of sightlines, namely 65% for emission and 86% for absorption (as shown in the lower right panel).

The first column of Figure 20 shows violin plots of the widths for both WNM and CNM components derived from Gaussian and pseudo-Voigt fits; the middle column displays violin plots of the FWHM/height ratios

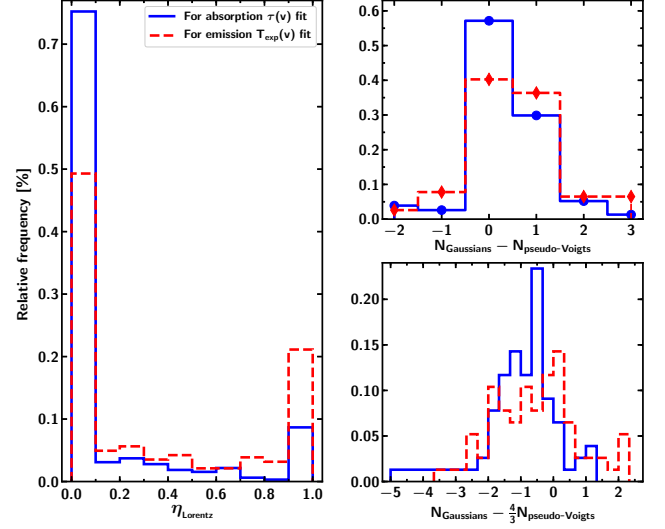


FIG. 19.— Left: Histograms of η_{Lorentz} , the fraction of Lorentzian in pseudo-Voigt function, for CNM and WNM components from absorption (blue) and emission (red) fits. Right: Comparison of the number of WNM/CNM components from Gaussian and pseudo-Voigt fittings without (top) and with (bottom) consideration of free parameter number for each mathematical function (3 for Gaussian and 4 for pseudo-Voigt).

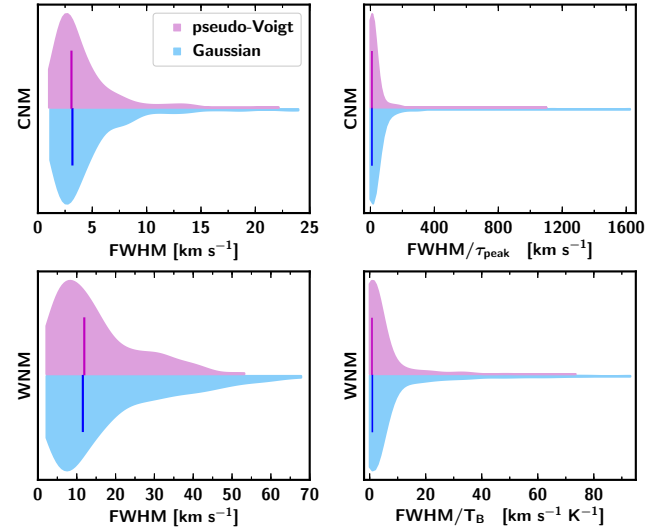


FIG. 20.— Left column: Violin plots for comparing the widths (FWHM) of Gaussian (pink) and pseudo-Voigt (blue) components for CNM (top) and WNM (bottom). Right column: Violin plots of FWHM/τ_{peak} ratio for CNM and FWHM/T_B for WNM. The vertical lines show the medians.

for each component. The medians of the widths and the FWHM/height ratios are almost identical, but compared to pseudo-Voigt, the Gaussian fitting needs slightly more wider WNM and CNM components; it also has more broad-but-weak components.

We plot the histograms of τ_{peak} , T_s , T_D and total N_{HI} derived from pseudo-Voigt and Gaussian decompositions in Figure 21. The fittings with the two different line-shapes appear to be consistent, since the distributions of their properties are almost equivalent. The mean and median values from each pair are close; namely the medians of the Gaussian and pseudo-Voigt fits are (0.35, 0.39) respectively for τ_{peak} , (54.6 K, 55.8 K) for T_s , (2926 K,

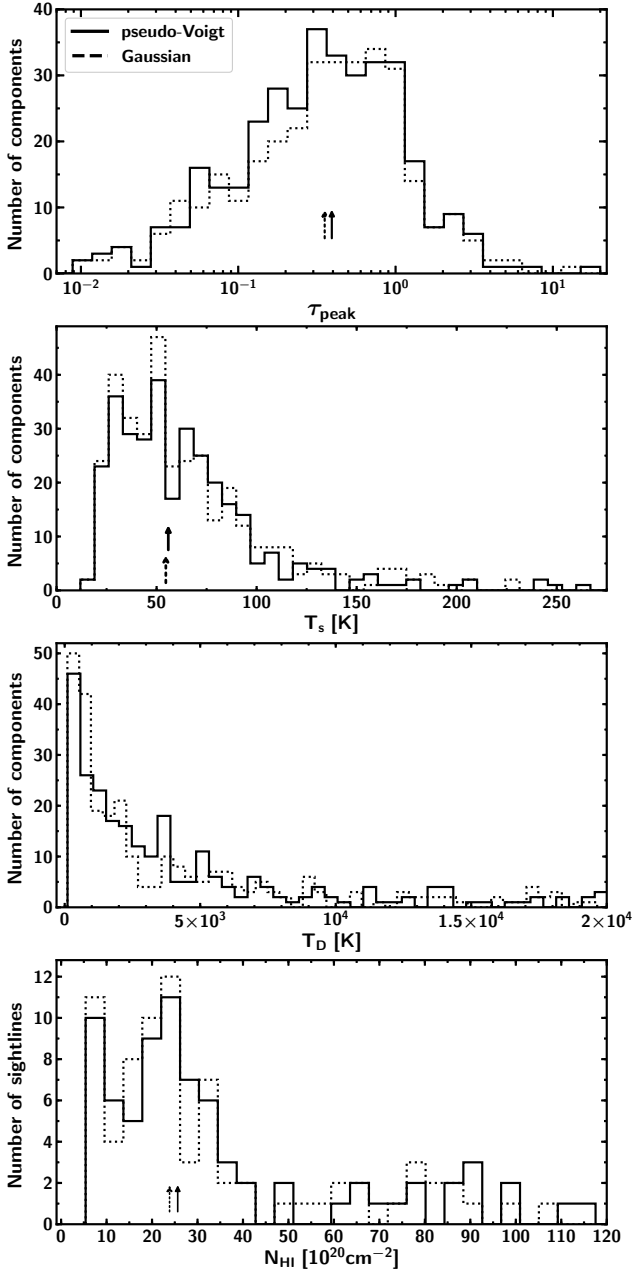


FIG. 21.— Histograms of peak optical depth τ_{peak} , spin temperature T_s , Doppler temperature T_D , and total column density N_{HI} derived from Gaussian (dotted) and pseudo-Voigt (solid) fits.

3116 K) for T_D and $(23.9, 25.6) \times 10^{20} \text{ cm}^{-2}$ for total N_{HI} . Figure 22 shows the relative difference between N_{HI} as derived from Gaussian and pseudo-Voigt fittings. The distribution is well fit by a Gaussian with a peak at -5.2% and a width of 6.1% . This means the N_{HI} from Gaussian fitting is $\sim 5\%$ slightly lower than that obtained from the pseudo-Voigt fits. This leads us to a conclusion that the derived properties of Gaussian and pseudo-Voigt fits are compatible.

APPENDIX B: COMPARISON OF T_s AND N_{HI} ESTIMATED FROM OTHER METHODS

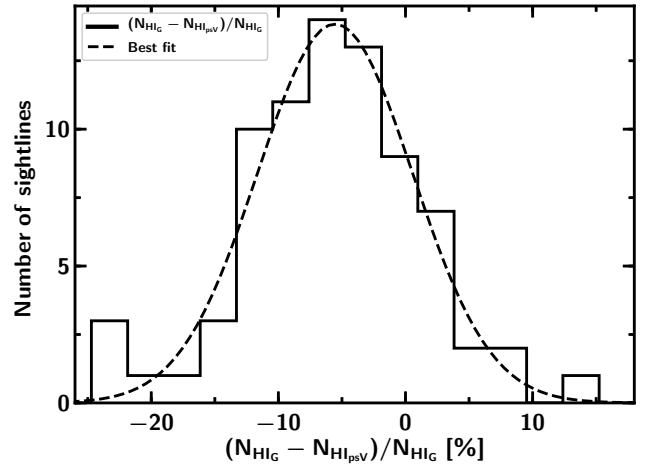


FIG. 22.— Comparison of N_{HI} derived from Gaussian (subscript G) and pseudo-Voigt (subscript psV) fits.

Given pairs of emission (off-source) and absorption (on-source) observations, our goal is to combine them to find the spin temperature and column density of interstellar HI. This is challenging because gas at different temperatures can be projected onto the same velocity channel along a line of sight. In a general sense, every sightline will contain a mixture of cold and warm gas: cold gas can be seen in the opacity spectrum; whereas warm gas is almost invisible in the opacity spectrum but is easily detected from the off-source (emission) measurements. Then the question is how best to use on-source and off-source spectra to distinguish these two phases. Beside the multi-component decomposition used in this work, there exist several independent methods to estimate HI spin temperature and column density. In this Section, we will apply two alternative methods (one T_s per velocity channel and single harmonic-mean T_s along full sightline) to derive the spin temperature and column density, and compare their results with those from our spectral decompositions. Similar analyses have been performed by M15, they found that these alternative methods overestimate the spin temperature; and that the Gaussian fit method is the most successful in reproducing the T_s range predicted by theoretical models. We repeat the analyses here for our three regions for completeness.

B1: Isothermal assumption: One T_s per velocity channel

This method is established from the assumption that the gas in each velocity channel is isothermal with a single corresponding spin temperature (e.g. Dickey & Benson 1982; Chengalur et al. 2013; M18). In this case the spin temperature spectrum, $T_{s,\text{chan}}(v)$, can be computed as:

$$T_{s,\text{chan}}(v) = \frac{T_{\text{exp}}(v)}{1 - e^{-\tau(v)}} \quad (19)$$

where $T_{\text{exp}}(v)$ is expected emission profile, $\tau(v)$ is opacity profile, and the effect of the T_{bg} term (see Equation 2) is assumed to be negligible. Here we use this method to calculate spin temperature for each velocity channel above our 5σ detection limit in absorption, with a velocity resolution of 0.16 km s^{-1} . The total column density

along the sightline is thus given by:

$$N_{\text{HI}} = C_0 \int \frac{\tau(v) T_{\text{exp}}(v)}{1 - e^{-\tau(v)}} dv \quad (20)$$

B2: Single harmonic-mean T_s along full sightline

This method assumes that there exists a uniform T_s along the full sightline, also known as harmonic-mean spin temperature, $T_{s,\text{mean}}$, which is computed from the emission and absorption profiles as:

$$T_{s,\text{mean}} = \frac{\int T_{\text{exp}}(v) dv}{\int (1 - e^{-\tau(v)}) dv} \quad (21)$$

where the quantities are the same as in Equation 19. Then we calculate N_{HI} as:

$$\begin{aligned} N_{\text{HI}} &= C_0 T_{s,\text{mean}} \int \tau(v) dv \\ &= -C_0 T_{s,\text{mean}} \int \ln \left[1 - \frac{T_{\text{exp}}(v)}{T_{s,\text{mean}}} \right] dv \end{aligned} \quad (22)$$

B3: Comparing T_s and N_{HI} from these methods

We apply both the isothermal channel approximation and the harmonic-mean method to our GNOMES HI data. We then compare the derived T_s and N_{HI} with those from our Gaussian decompositions. The upper panel of Figure 23 shows histograms of the spin temperatures. The $T_{s,\text{chan}}$ from the isothermal channel method spans a large range from 2 K to 4500 K with mean and median of (236 K, 186 K). Meanwhile, the harmonic-mean spin temperatures lie in a much narrower range, from 75 K to 467 K, with a mean and median of (173 K, 157 K). This is not surprising because these two methods both include warm and cold gas in their spin temperature estimates, thus their median temperatures are comparable. For the isothermal channel method, $T_{s,\text{chan}}(v)$ is the mean temperature of the various clouds that contribute to each velocity channel. For the harmonic-mean assumption, $T_{s,\text{mean}}$ is the column density weighted mean spin temperature of all warm and cold clouds along the line of sight. Thus, compared to spin temperatures from Gaussian decomposition fit, both $T_{s,\text{mean}}$ and $T_{s,\text{chan}}$ tend to be higher because the WNM accounts for a significant fraction of the emission along the sightline.

Compared to these methods, the advantage of the spectral decomposition approach is that it separates the two thermal phases within channels, and along the line of sight. As mentioned earlier, our CNM spin temperatures from Gaussian fitting range from 10 K to 465 K, peak at ~ 50 K and have a median of 54.6 K, which is much lower than the estimates from the two single-phase approximations (which include both CNM and WNM). Theoretical models of a thermally bistable ISM (Field et al. 1969; McKee & Ostriker 1977; Wolfire et al. 2003) predict that the neutral CNM has typical temperatures of $30 \lesssim T \lesssim 200$ K. So it is obvious that the spectral decomposition method in the current study successfully reproduces this T_s range. The isothermal channel method gives a large fraction of thermally unstable gas with $500 < T < 5000$ K; by contrast, the T_s distribution from the harmonic-mean method overlaps with the CNM spin

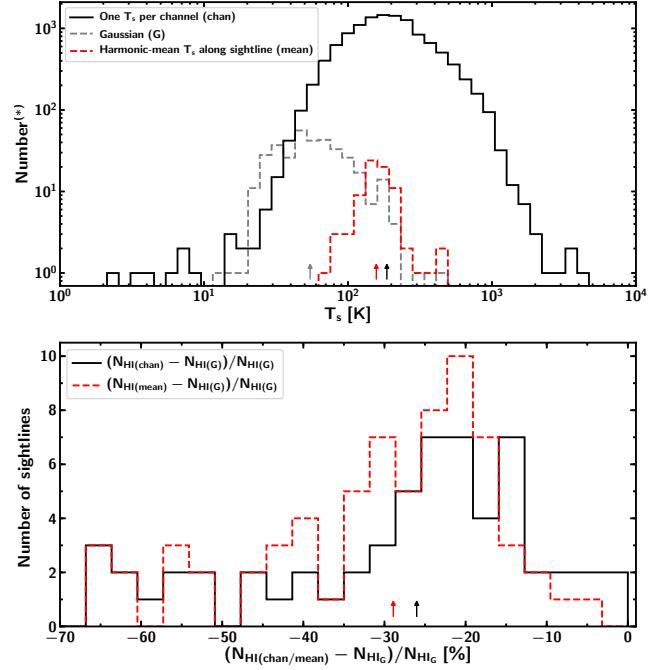


FIG. 23.— Comparison of T_s and N_{HI} derived from different methods: one-phase-per-channel (subscript “(chan)”) and single harmonic mean T_s along full sightline “(mean)”. Top panel: Histograms of spin temperatures; black solid line for (chan) and red dashed line for (mean). Spin temperature from HI Gaussian decomposition fit “(G)” is shown in gray for reference. Bottom panel: Relative difference of N_{HI} from isothermal channel (black) method and harmonic-mean assumption (red) compared with decomposition fit. The arrows show the medians.

(*)Note: For (chan): y-axis is the number of velocity channels; for (G): number of components; and for (mean): the number of sightlines.

temperatures from our Gaussian fits at the high T_s end, but cannot return colder temperatures (since the WNM always makes some contribution along a sightline).

In the bottom panel, we compare N_{HI} derived from the three methods. The column densities from the isothermal channel and harmonic-mean methods are relatively consistent, with differences mostly smaller than 8%. However both underestimate the total N_{HI} by between ~ 10 –70% (median $\sim 27\%$) when compared to the Gaussian fits. These differences arise from the fact that the HI gas in the ISM is a complex structure of multiple phases at different temperatures, where cold components contribute significantly to the total gas column density, but that both of the single-phase methods can only return a mean T_s from the mixture of CNM and WNM within a sightline or channel. Based on a Monte Carlo simulation of multi-phase gas, Chengalur et al. (2013) examined how well the per-channel method is able to recover the true column density for gas with a complex spatial and temperature distribution along the sightline. They find that for $N_{\text{HI}} > 10^{21} \text{ cm}^{-2}$, the ratio $[N_{\text{HI}}/N_{\text{HI,chan}}] = -112.88 + 10.144 \times \log_{10} N_{\text{HI}} - 0.2248 \times [\log_{10} N_{\text{HI}}]^2$. In our column density range $(5\text{--}120) \times 10^{20} \text{ cm}^{-2}$, this translates to a true N_{HI} that is 20–50% higher than $N_{\text{HI,chan}}$. Our findings are thus in excellent agreement with their predictions.

REFERENCES

- Allison, J. R., Sadler, E. M., & Whiting, M. T. 2012, *PASA*, 29, 221
- Audit, E., & Hennebelle, P. 2005, *A&A*, 433, 1
- Bihl, S., Beuther, H., Ott, J., et al. 2015, *A&A*, 580, A112
- Burkhart, B., Stanimirović, S., Lazarian, A., & Kowal, G. 2010, *ApJ*, 708, 1204
- Calabretta, M. R., Staveley-Smith, L., & Barnes, D. G. 2014, *PASA*, 31, e007
- Chengalur, J. N., Kanekar, N., & Roy, N. 2013, *MNRAS*, 432, 3074
- Condon, J. J., Cotton, W. D., Greisen, E. W., et al. 1998, *AJ*, 115, 1693
- Dame, T. M., Hartmann, D., & Thaddeus, P. 2001, *ApJ*, 547, 792
- Davies, R. D., & Cummings, E. R. 1975, *MNRAS*, 170, 95
- Deguchi, S., & Watson, W. D. 1985, *ApJ*, 290, 578
- Dénes, H., McClure-Griiffiths, N. M., Dickey, J. M., Dawson, J. R., & Murray, C. E. 2018, *MNRAS*, 479, 1465
- Dickey, J. M., & Benson, J. M. 1982, *AJ*, 87, 278
- Dickey, J. M., McClure-Griiffiths, N. M., Gaensler, B. M., & Green, A. J. 2003, *ApJ*, 585, 801
- Dickey, J. M., Mebold, U., Stanimirovic, S., & Staveley-Smith, L. 2000, *ApJ*, 536, 756
- Dickey, J. M., Salpeter, E. E., & Terzian, Y. 1977, *ApJ*, 211, L77
- Dickey, J. M., Strasser, S., Gaensler, B. M., et al. 2009, *ApJ*, 693, 1250
- Field, G. B. 1958, *Proceedings of the IRE*, 46, 240
- . 1959, *ApJ*, 129, 536
- Field, G. B., Goldsmith, D. W., & Habing, H. J. 1969, *ApJ*, 155, L149
- Fukui, Y., Hayakawa, T., Inoue, T., et al. 2018, *ApJ*, 860, 33
- Fukui, Y., Torii, K., Onishi, T., et al. 2015, *ApJ*, 798, 6
- Garwood, R. W., & Dickey, J. M. 1989, *ApJ*, 338, 841
- Gazol, A., Vázquez-Semadeni, E., Sánchez-Salcedo, F. J., & Scalo, J. 2001, *ApJ*, 557, L121
- Gordon, Y. A., Owers, M. S., Pimbblet, K. A., et al. 2017, *MNRAS*, 465, 2671
- Grenier, I. A., Casandjian, J.-M., & Terrier, R. 2005, *Science*, 307, 1292
- Hartmann, D., & Burton, W. B. 1997, *Atlas of Galactic Neutral Hydrogen* (Cambridge University Press), 243
- Heiles, C., & Troland, T. H. 2003a, *ApJS*, 145, 329
- . 2003b, *ApJ*, 586, 1067
- Heitsch, F., Burkert, A., Hartmann, L. W., Slyz, A. D., & Devriendt, J. E. G. 2005, *ApJ*, 633, L113
- Hennebelle, P., & Audit, E. 2007, *A&A*, 465, 431
- Hennebelle, P., Audit, E., & Miville-Deschênes, M. A. 2007, *A&A*, 465, 445
- HI4PI Collaboration, Ben Bekhti, N., Flöer, L., et al. 2016, *A&A*, 594, A116
- Hill, A. S., Mac Low, M.-M., Gatto, A., & Ibáñez-Mejía, J. C. 2018, *ApJ*, 862, 55
- Kalberla, P. M. W., Burton, W. B., Hartmann, D., et al. 2005, *A&A*, 440, 775
- Kalberla, P. M. W., & Haud, U. 2018, *A&A*, 619, A58
- Kanekar, N., Subrahmanyam, R., Chengalur, J. N., & Safouris, V. 2003, *MNRAS*, 346, L57
- Kim, C.-G., Ostriker, E. C., & Kim, W.-T. 2013, *ApJ*, 776, 1
- . 2014, *ApJ*, 786, 64
- Knapp, G. R., & Verschuur, G. L. 1972, *AJ*, 77, 717
- Koyama, H., & Inutsuka, S.-i. 2002, *ApJ*, 564, L97
- Krumholz, M. R., McKee, C. F., & Tumlinson, J. 2009, *ApJ*, 693, 216
- Kulkarni, S. R., & Heiles, C. 1988, *Neutral hydrogen and the diffuse interstellar medium*, ed. K. I. Kellermann & G. L. Verschuur (Springer-Verlag), 95–153
- Lee, M.-Y., Stanimirović, S., Murray, C. E., Heiles, C., & Miller, J. 2015, *ApJ*, 809, 56
- Lee, M.-Y., Stanimirović, S., Douglas, K. A., et al. 2012, *ApJ*, 748, 75
- Leung, C.-M., & Liszt, H. S. 1976, *ApJ*, 208, 732
- Liszt, H. 2001, *A&A*, 371, 698
- . 2014a, *ApJ*, 783, 17
- . 2014b, *ApJ*, 780, 10
- Liszt, H. S., Braun, R., & Greisen, E. W. 1993, *AJ*, 106, 2349
- Lockman, F. J., & Savage, B. D. 1995, *ApJS*, 97, 1
- McKee, C. F., & Ostriker, J. P. 1977, *ApJ*, 218, 148
- Mebold, U., Winnberg, A., Kalberla, P. M. W., & Goss, W. M. 1982, *A&A*, 115, 223
- Meyer, D. M., Lauroesch, J. T., Heiles, C., Peek, J. E. G., & Engelhorn, K. 2006, *ApJ*, 650, L67
- Meyer, D. M., Lauroesch, J. T., Peek, J. E. G., & Heiles, C. 2012, *ApJ*, 752, 119
- Murray, C. E., Peek, J. E. G., Lee, M.-Y., & Stanimirović, S. 2018a, *ApJ*, 862, 131
- Murray, C. E., Stanimirović, S., Goss, W. M., et al. 2018b, *ApJS*, 238, 14
- Murray, C. E., Stanimirović, S., Kim, C.-G., et al. 2017, *ApJ*, 837, 55
- Murray, C. E., Lindner, R. R., Stanimirović, S., et al. 2014, *ApJ*, 781, L41
- Murray, C. E., Stanimirović, S., Goss, W. M., et al. 2015, *ApJ*, 804, 89
- Nguyen, H., Dawson, J. R., Miville-Deschênes, M.-A., et al. 2018, *ApJ*, 862, 49
- Payne, H. E., Terzian, Y., & Salpeter, E. E. 1982, *ApJS*, 48, 199
- Peek, J. E. G., Heiles, C., Douglas, K. A., et al. 2011, *ApJS*, 194, 20
- Peek, J. E. G., Babler, B. L., Zheng, Y., et al. 2018, *ApJS*, 234, 2
- Planck Collaboration, Fermi Collaboration, Ade, P. A. R., et al. 2015, *A&A*, 582, A31
- Radhakrishnan, V., Murray, J. D., Lockhart, P., & Whittle, R. P. J. 1972, *ApJS*, 24, 15
- Reich, P., Testori, J. C., & Reich, W. 2001, *A&A*, 376, 861
- Remy, Q., Grenier, I. A., Marshall, D. J., & Casandjian, J. M. 2017, *A&A*, 601, A78
- Roy, N., Kanekar, N., Braun, R., & Chengalur, J. N. 2013, *MNRAS*, 436, 2352
- Saury, E., Miville-Deschênes, M.-A., Hennebelle, P., Audit, E., & Schmidt, W. 2014, *A&A*, 567, A16
- Shaw, G., Ferland, G. J., & Hubeny, I. 2017, *ApJ*, 843, 149
- Silk, J. 1975, *ApJ*, 198, L77
- Silk, J., & Werner, M. W. 1969, *ApJ*, 158, 185
- Stanimirović, S., & Heiles, C. 2005, *ApJ*, 631, 371
- Stanimirović, S., Heiles, C., & Kanekar, N. 2007, in *Astronomical Society of the Pacific Conference Series*, Vol. 365, SINS - Small Ionized and Neutral Structures in the Diffuse Interstellar Medium, ed. M. Haverkorn & W. M. Goss, 22
- Stanimirović, S., Murray, C. E., Lee, M.-Y., Heiles, C., & Miller, J. 2014, *ApJ*, 793, 132
- Stanimirović, S., Putman, M., Heiles, C., et al. 2006, *ApJ*, 653, 1210
- Wakker, B. P., Lockman, F. J., & Brown, J. M. 2011, *ApJ*, 728, 159
- Wannier, P., Andersson, B.-G., Penprase, B. E., & Federman, S. R. 1999, *ApJ*, 510, 291
- Watson, W. D. 1972, *ApJ*, 176, 103
- Wertheim, G. K., Butler, M. A., West, K. W., & Buchanan, D. N. E. 1974, *Review of Scientific Instruments*, 45, 1369
- Wolfire, M. G., Hollenbach, D., & McKee, C. F. 2010, *ApJ*, 716, 1191
- Wolfire, M. G., Hollenbach, D., McKee, C. F., Tielens, A. G. G. M., & Bakes, E. L. O. 1995, *ApJ*, 443, 152
- Wolfire, M. G., McKee, C. F., Hollenbach, D., & Tielens, A. G. G. M. 2003, *ApJ*, 587, 278
- Wouthuysen, S. A. 1952, *AJ*, 57, 31

TABLE 3
PARAMETERS FOR PSEUDO-VOIGT AND GAUSSIAN FITS
(SEE SECTION 4 FOR DETAILED DESCRIPTIONS)

l/b	pseudo-Voigt										Gaussian									
	T_B (K)	τ (10^{-2})	V_{lsr} ($km s^{-1}$)	ΔV ($km s^{-1}$)	η	T_s (K)	N_{HI} ($10^{20} cm^{-2}$)	F or O	T_B (K)	τ (10^{-2})	V_{lsr} ($km s^{-1}$)	ΔV ($km s^{-1}$)	T_s (K)	N_{HI} ($10^{20} cm^{-2}$)	F or O					
188.07/0.04	24.81	1.84±0.1	-2.29±0.03	1.53±0.06	0.0±0.0	29.49±2.21	1.61±0.16	2	29.13	1.87±0.01	-2.29±0.0	1.5±0.01	34.44±0.74	1.87±0.04	2					
188.07/0.04	37.12	0.68±0.02	0.98±0.32	5.99±0.37	0.0±0.0	79.42±17.9	5.86±1.39	1	37.11	0.63±0.0	1.02±0.04	6.14±0.05	58.0±3.46	4.37±0.26	4					
188.07/0.04	59.76	1.1±0.13	4.42±0.13	1.99±0.28	0.0±0.0	89.58±9.69	3.8±0.8	0	33.89	1.1±0.01	4.47±0.01	2.06±0.02	50.8±2.77	2.23±0.13	3					
188.07/0.04	48.47	1.08±0.11	7.32±0.18	2.75±0.61	0.0±0.0	73.39±7.99	4.23±1.13	3	30.27	0.98±0.02	7.28±0.01	2.44±0.04	48.45±3.4	2.25±0.17	0					
188.07/0.04	16.08	0.55±0.04	10.78±0.43	3.51±1.16	0.0±0.0	38.01±12.07	1.44±0.67	4	34.67	0.56±0.0	10.69±0.05	4.95±0.15	80.86±6.19	4.35±0.36	5					
188.07/0.04	11.44	0.64±0.04	15.61±0.2	3.98±0.36	0.0±0.0	24.2±2.93	1.19±0.19	5	13.23	0.67±0.0	15.88±0.02	3.28±0.02	27.1±2.65	1.16±0.11	1					
188.07/0.04	59.37±2.93	<0.035	-2.86±0.32	9.38±0.49	1.0±0.0	>1410.7	13.25±1.05	0.53±0.13	10.08±0.48	<0.038	1.64±0.2	34.56±0.49	>263.34	6.76±0.33	0.41±0.01					
188.07/0.04	54.14±8.22	<0.05	1.79±0.09	3.66±0.33	0.0±0.0	>1076.34	3.85±0.68	0.53±0.16	110.31±3.23	<0.068	4.14±0.22	14.69±0.26	>1617.88	31.43±1.07	0.3±0.01					
188.07/0.04	-	-	-	-	-	-	-	-	-	-	-	-	-	-	-					
188.07/0.04	39.81±13.95	<0.086	9.57±0.92	7.2±1.85	0.24±0.14	>461.11	6.19±2.72	0.33±0.1	-	-	-	-	-	-	-					
188.07/0.04	85.79±13.53	<0.089	9.88±0.92	15.22±0.52	0.0±0.0	>962.55	25.34±4.09	0.43±0.15	-	-	-	-	-	-	-					
188.07/0.04	-	-	-	-	-	-	-	-	-	-	-	-	-	-	-					
187.41/-11.34	5.79	0.04±0.0	-21.53±0.11	2.61±0.32	0.19±0.27	147.78±17	0.3±0.06	0	35.13±3.66	<0.062	14.68±0.46	11.45±0.39	>569.53	7.8±0.85	0.17±0.01					
187.41/-11.34	2.59	0.02±0.0	-6.21±0.32	4.35±0.77	0.44±0.39	130.6±15.78	0.3±0.01	1	5.58	0.04±0.0	-21.39±0.04	3.42±0.1	142.29±8.02	0.33±0.02	0					
187.41/-11.34	18.86	0.25±0.01	-0.48±0.07	3.19±0.11	0.07±0.17	85.24±2.27	1.37±0.14	3	2.07	0.33±0.0	0.62±0.13	2.5±0.42	207.55±26.95	0.11±0.03	6					
187.41/-11.34	17.21	0.22±0.01	1.6±0.05	2.14±0.13	1.0±0.0	87.16±3.22	1.19±0.11	2	13.65	0.25±0.0	-0.4±0.04	2.96±0.06	61.69±2.19	0.89±0.04	5					
187.41/-11.34	-	-	-	-	-	-	-	-	8.09	0.17±0.01	1.62±0.02	1.8±0.04	51.74±3.71	0.31±0.03	4					
187.41/-11.34	-	-	-	-	-	-	-	-	27.91	0.06±0.0	2.37±0.17	14.09±0.26	479.28±12.24	7.26±0.35	2					
187.41/-11.34	16.49	1.06±0.01	6.43±0.02	2.35±0.03	0.0±0.0	25.23±2.72	1.22±0.13	4	31.18	1.04±0.0	6.43±0.01	2.31±0.01	48.23±1.39	2.25±0.07	3					
187.41/-11.34	9.23	0.43±0.01	9.17±0.06	2.73±0.1	0.15±0.03	26.4±4.44	0.64±0.11	5	18.8	0.4±0.0	9.16±0.02	2.7±0.03	57.03±2.56	1.2±0.06	1					
187.41/-11.34	-	-	-	-	-	-	-	-	2.9±0.12	<0.004	-29.83±1.63	37.84±2.17	>828.55	2.13±0.15	0.51±0.02					
187.41/-11.34	3.71±0.31	<0.012	-18.22±2.47	51.07±2.58	0.0±0.0	>305.44	3.68±0.36	0.47±0.3	7.99±0.45	<0.009	2.16±0.57	29.76±1.03	>884.8	4.61±0.3	0.47±0.02					
187.41/-11.34	29.28±2.42	<0.008	3.21±0.29	16.37±0.2	0.1±0.09	>3507.26	9.76±0.91	0.32±0.25	-	-	-	-	-	-	-					
187.41/-11.34	30.35±2.84	<0.017	7.32±0.11	6.4±0.28	0.35±0.23	>1778.38	4.4±0.62	0.41±0.28	18.5±0.63	<0.01	6.95±0.14	9.68±0.38	>1810.39	3.47±0.18	0.44±0.01					
193.12/8.3	27.1	0.12±0.03	-9.22±0.44	8.78±0.59	0.0±0.0	239.62±2.68	4.99±1.21	4	-	-	-	-	-	-	-					
193.12/8.3	-	-	-	-	-	-	-	-	35.02	0.21±0.0	-8.52±0.02	7.92±0.06	184.86±1.63	5.83±0.09	3					
193.12/8.3	40.84	1.55±0.15	-7.52±0.04	1.85±0.12	0.27±0.18	51.84±0.85	3.27±0.46	1	39.78	1.45±0.01	-7.52±0.0	1.8±0.01	51.97±0.89	2.64±0.02	2					
193.12/8.3	6.33	0.08±0.01	6.4±0.21	4.96±0.5	0.0±0.0	82.34±2.82	0.65±0.09	2	8.01	0.05±0.0	6.34±0.04	5.09±0.1	104.0±2.56	0.85±0.03	3					
193.12/8.3	4.56	0.05±0.01	12.36±0.29	2.58±0.09	0.0±0.0	93.41±5.73	0.25±0.09	3	6.0	0.08±0.0	12.36±0.04	2.55±0.11	123.19±5.39	0.33±0.02	4					
193.12/8.3	2.86	0.04±0.01	17.73±0.37	4.1±1.0	0.0±0.0	73.04±5.34	0.22±0.07	0	3.82	0.04±0.0	4.21±0.2	97.53±4.95	0.3±0.02	0						
193.12/8.3	0.53	0.03±0.01	24.46±0.27	2.89±0.63	0.0±0.0	18.09±5.25	0.03±0.01	5	0.75	0.03±0.0	24.48±0.07	2.89±0.16	25.42±4.96	0.05±0.01	5					
193.12/8.3	0.98±0.05	<0.013	-56.83±0.54	20.92±1.75	1.0±0.0	>73.77	0.59±0.06	1.0±0.0	0.87±0.04	<0.011	-57.32±0.53	25.44±1.42	>78.6	0.43±0.03	1.0±0.0					
193.12/8.3	-	-	-	-	-	-	-	-	21.26±0.11	<0.023	5.89±0.07	31.48±0.11	>910.62	12.98±0.08	0.0±0.0					
193.12/8.3	22.04±0.14	<0.023	6.43±0.07	30.18±0.17	0.04±0.02	>950.77	13.12±0.17	0.26±0.01	1.66	0.02±0.0	-8.92±0.08	2.75±0.18	83.72±12.21	0.08±0.01	0					
166.64/-33.6	1.41	0.02±0.0	-8.99±0.08	4.37±0.21	0.0±0.0	71.38±8.83	0.07±0.01	0	2.65	0.4±0.0	-0.41±0.02	4.28±0.02	89.93±2.31	3.0±0.08	4					
166.64/-33.6	20.27	0.39±0.01	-0.48±0.09	4.19±0.09	0.0±0.0	62.78±7.29	2.01±0.24	4	1.99	0.19±0.0	1.23±0.01	1.64±0.04	48.41±2.54	0.3±0.02	3					
166.64/-33.6	7.9	0.21±0.02	1.22±0.03	1.74±0.13	0.0±0.0	41.69±5.66	0.29±0.05	1	8.21	0.11±0.0	6.85±0.03	4.13±0.06	117.21±18.3	1.0±0.16	2					
166.64/-33.6	5.83	0.09±0.01	6.65±0.22	4.54±0.38	0.0±0.0	67.75±8.25	0.55±0.11	3	12.21	0.03±0.0	7.91±0.04	1.22±0.02	161.12±40.51	0.11±0.03	1					
166.64/-33.6	7.07	0.04±0.01	7.68±0.21	1.84±0.62	0.0±0.0	180.35±54.08	0.27±0.14	2	4.76	0.13±0.0	4.22±0.78	24.9±0.78	>439.01	2.04±0.19	0.47±0.08					
166.64/-33.6	28.87±4.44	<0.009	-1.03±0.15	6.92±0.48	1.0±0.0	>3289.69	5.72±0.97	0.51±0.09	25.56±2.29	<0.01	0.05±0.43	9.08±0.42	>2496.26	4.5±0.45	0.36±0.08					
166.64/-33.6	-	-	-	-	-	-	-	-	-	-	-	-	-	-	-					
166.64/-33.6	15.37±0.96	<0.011	4.42±0.22	12.02±0.28	0.0±0.0	>1459.71	3.58±0.24	0.45±0.08	7.3±2.43	<0.019	8.35±1.74	8.92±1.6	>389.75	1.26±0.48	0.4±0.07					
166.64/-33.6	-	-	-	-	-	-	-	-	3.86	0.18±0.01	-11.94±0.02	1.35±0.04	23.41±1.66	0.11±0.01	0					
201.53/0.51	3.31	0.18±0.02	-11.92±0.05	1.4±0.14	0.02±0.33	20.07±1.5	0.1±0.02	0	63.65	3.51±0.05	4.66±0.01	3.91±0.02	67.67±3.44	18.04±0.96	6					
201.53/0.51	85.13	2.91±0.36	4.63±0.06	4.37±0.2	0.17±0.06	90.03±2.94	24.08±3.36	4	63.65	3.51±0.05	4.66±0.01	3.91±0.02	67.67±3.44	18.04±0.96	6					
201.53/0.51	18.26	0.41±0.02	13.18±1.27	20.48±1.36	0.0±0.0	54.28±11.54	8.9±0.2	2	33.07	0.48±0.0	12.72±0.12	23.0±0.2	86.70±20.23	18.4±4.31	7					
201.53/0.51	26.11	0.38±0.06	20.59±0.18	1.76±0.55	1.0±0.0	92.91±3.85	1.55±0.57	6	17.39	0.25±0.01	20.43±0.03	3.09±0.05	78.6±5.52	0.6±0.05	1					
201.53/0.51	24.11	0.71±0.08	23.37±0.13	2.52±0.3	0.0±0.0	47.42±2.02	1.64±0.28	1	21.36	0.74±0.01	23.39±0.02	3.09±0.07	40.85±3.1	1.82±0.14	5					
201.53/0.51	25.46	0.51±0.03	31.41±0.37	10.77±0.57	0.0±0.0	63.72±2.78	6.83±0.64	5	27.87	0.55±0.01	31.0±0.06	6.55±0.13	65.89±2.04	4.63±0.18	2					
201.53/0.51	20.74	1.94±0.32	33.74±0.05	1.34±0.12	0.0±0.0	24.22±1.0	1.23±0.24	3	21.86	1.91±0.03	33.8±0.01	1.47±0.02	25.66±0.94	1.39±0.06	3					
201.53/0.51	-	-	-	-	-	-	-	-	8.49	0.13±0.0	39.0±0.12	5.35±0.21	69.67±5.03	0.97±0.08	4					
201.53/0.51	-	-	-	-	-	-	-	-	29.4±5.46	<0.104	3.3±0.76	16.44±0.72	>282.22	9.37±1.79	0.5±0.0					
201.53/0.51	59.64±2.73	<0.148	5.69±0.24	14.94±0.31	0.41±0.03	>401.98	20.66±1.06	0.0±0.0	15.36±1.14	<0.052	8.68±0.12	3.41±0.3	>298.1	1.02±0.12	0.5±0.0					
201.53/0.51	63.39±2.08	<0.061	24.84±0.39	20.76±0.32	0.0±0.0	>1038.28	25.52±0.93	0.34±0.01	-	-	-	-	-	-	-					
201.53/0.51	-	-	-	-	-	-	-	-	59.8±3.8	<0.074	25.01±0.74	20.51±0.55	>806.11	23.79±1.64	0.5±0.0					
186.76/-7.11	1.38	0.01±0.0	-23.1±0.2	3.69±0.48	0.0±0.0	138.2±10.03	0.12±0.02	0	0.41	0.01±0.0	-23.04±0.15	3.79±0.36	41.64±11.05	0.04±0.01	0					
186.76/-7.11	29.84	0.5±0.02	1.77±0.02	2.15±0.07	0.19±0.12	75.84±2.89	1.73±0.15	1	11.29	0.48±0.0	1.76±0.0	2.08±0.01	29.62±10.55	0.58±0.21	3					
186.76/-7.11	51.78	0.22±0.01	5.78±0.23	7.95±0.3	0.0±0.0	262.22±10.78	8.73±0.55	2	14.51	0.52±0.0	5.53±0.03	8.37±0.05	73.48±71.36	2.67±2.61	1					
186.76/-7.11	10.65	0.16±0.01	9.62±0.04	1.99±0.11	0.0±0.0	72.04±6.56	0.44±0.05	3	12.8	0.17±0.0	9.59±0.01	1.88±0.03	81.88±8.57	0.49±0.05	2					
186.76/-7.11	28.19±3.17	<0.014	-1.35±0.22	17.78±1.02	1.0±0.0	>1972.23	14.35±1.81	0.42±0.16	13.83±2.99	<0.021	-1.14±1.47	10.49±1.41	>763.65	2.8±0.71	0.4±0.16					
186.76/-7.11	-	-	-	-	-	-	-	-	15.28±0.3	<0.018	0.32±0.09	34.7±0.3	>739.53	10.29±0.22	0.38±0.16					
186.76/-7.11	-	-	-	-	-	-	-	-	25.11±2.7	<0.021	1.69±0.07	4.46±0.4								

TABLE 3 (CONT)

l/b ($^{\circ}$)	pseudo-Voigt										Gaussian									
	T_B (K)	τ (10^{-2})	V_{lsr} ($km s^{-1}$)	ΔV ($km s^{-1}$)	η	T_s (K)	N_{HI} ($10^{20} cm^{-2}$)	F	σ	O	T_B (K)	τ (10^{-2})	V_{lsr} ($km s^{-1}$)	ΔV ($km s^{-1}$)	T_s (K)	N_{HI} ($10^{20} cm^{-2}$)	F	σ	O	
203.75/14.63	5.2	0.06 \pm 0.01	-3.46 \pm 0.28	3.29 \pm 0.67	0.0 \pm 0.0	89.34 \pm 6.49	0.33 \pm 0.09	1	-	-	6.59	-	-2.9 \pm 0.08	4.62 \pm 0.18	85.65 \pm 6.15	0.6 \pm 0.05	1	-	-	
203.75/14.63	-	-	-	-	-	-	-	-	-	-	8.66	0.13 \pm 0.0	0.67 \pm 0.03	2.24 \pm 0.08	71.0 \pm 3.89	0.39 \pm 0.03	2	-	-	
203.75/14.63	9.51	0.15 \pm 0.01	0.66 \pm 0.14	3.01 \pm 0.51	1.0 \pm 0.0	68.3 \pm 3.52	0.87 \pm 0.17	0	-	-	2.88	0.06 \pm 0.0	4.95 \pm 0.25	5.91 \pm 0.41	9.4 \pm 13.8	0.31 \pm 0.09	3	-	-	
203.75/14.63	3.89	-	-	-	-	-	-	-	-	-	2.19	0.23 \pm 0.06	2	-	-	-	-	-	-	
203.75/14.63	10.48 \pm 0.41	0.02 \pm 0.01	6.51 \pm 0.11	2.23 \pm 0.32	0.49 \pm 0.38	34.36 \pm 3.1	0.23 \pm 0.06	2	-	-	-	-	-	-	-	-	-	-	-	
203.75/14.63	-	-	-	-	-	-	-	-	-	-	-	-	-	-	-	-	-	-	-	
203.75/14.63	-	-	-	-	-	-	-	-	-	-	-	-	-	-	-	-	-	-	-	
203.75/14.63	5.56 \pm 0.32	<0.025	6.56 \pm 0.28	30.17 \pm 0.92	0.33 \pm 0.07	>218.61	3.77 \pm 0.27	0.5 \pm 0.3	-	-	12.45 \pm 0.6	<0.035	0.96 \pm 0.29	15.59 \pm 0.48	>353.07	3.77 \pm 0.22	0.0 \pm 0.0	-	-	
203.75/14.63	1.64 \pm 0.43	<0.027	11.36 \pm 0.15	2.23 \pm 0.41	0.06 \pm 0.67	>59.73	0.07 \pm 0.03	1.0 \pm 0.0	-	-	2.51 \pm 0.43	<0.025	6.66 \pm 0.5	41.23 \pm 2.42	>98.6	2.0 \pm 0.37	0.15 \pm 0.05	-	-	
203.75/14.63	9.54	0.12 \pm 0.02	-8.86 \pm 0.13	1.96 \pm 0.25	0.0 \pm 0.0	84.39 \pm 3.84	0.4 \pm 0.09	0	-	-	1.72 \pm 0.27	<0.022	11.68 \pm 0.15	2.23 \pm 0.4	>78.83	0.07 \pm 0.02	0.5 \pm 0.08	-	-	
196.84/-13.74	17.98	1.23 \pm 0.05	4.76 \pm 0.04	2.09 \pm 0.09	0.16 \pm 0.07	25.41 \pm 0.65	1.36 \pm 0.09	1	-	-	10.38	<0.013	17.17 \pm 1.63	13.88 \pm 2.8	>97.26	0.35 \pm 0.11	0.48 \pm 0.08	-	-	
196.84/-13.74	21.0	0.82 \pm 0.41	8.47 \pm 0.08	1.98 \pm 0.39	0.0 \pm 0.0	37.52 \pm 0.8	1.18 \pm 0.64	2	-	-	13.45	0.12 \pm 0.0	-8.85 \pm 0.02	2.05 \pm 0.05	95.77 \pm 3.39	0.46 \pm 0.02	0	-	-	
196.84/-13.74	19.27	-	-	-	-	-	-	-	-	-	19.41	0.23 \pm 0.02	3.5 \pm 0.21	3.13 \pm 0.22	49.43 \pm 3.02	0.68 \pm 0.09	4	-	-	
196.84/-13.74	8.96 \pm 0.13	<0.025	-8.21 \pm 0.23	13.33 \pm 0.54	0.78 \pm 0.06	>364.78	3.17 \pm 0.15	0.5 \pm 0.29	-	-	13.45	1.2 \pm 0.04	4.86 \pm 0.01	1.61 \pm 0.03	27.78 \pm 0.66	1.04 \pm 0.05	3	-	-	
196.84/-13.74	54.18 \pm 0.52	<0.026	6.77 \pm 0.05	9.01 \pm 0.09	0.0 \pm 0.0	>2073.91	9.47 \pm 0.13	0.28 \pm 0.18	-	-	23.35	0.51 \pm 0.02	8.58 \pm 0.01	1.45 \pm 0.04	33.67 \pm 1.13	0.49 \pm 0.03	2	-	-	
196.84/-13.74	16.22 \pm 0.16	<0.038	18.08 \pm 0.14	12.18 \pm 0.24	0.37 \pm 0.03	>428.69	4.51 \pm 0.12	0.5 \pm 0.29	-	-	-	0.73 \pm 0.02	8.89 \pm 0.02	3.48 \pm 0.03	45.07 \pm 1.52	2.23 \pm 0.09	1	-	-	
196.84/-13.74	42.77	-	-	-	-	-	-	-	-	-	-	-	-	-	-	-	-	-	-	
196.84/-13.74	-	-	-	-	-	-	-	-	-	-	-	-	-	-	-	-	-	-	-	
196.84/-13.74	39.49	0.64 \pm 0.07	6.06 \pm 0.14	2.4 \pm 0.42	0.0 \pm 0.0	83.53 \pm 2.42	2.47 \pm 0.51	1	-	-	53.86	0.73 \pm 0.01	4.41 \pm 0.06	4.96 \pm 0.07	103.95 \pm 1.01	7.27 \pm 0.15	8	-	-	
196.84/-13.74	64.56	1.05 \pm 0.09	10.49 \pm 0.13	4.48 \pm 0.43	0.0 \pm 0.0	99.32 \pm 1.13	9.04 \pm 1.17	5	-	-	31.03	0.37 \pm 0.04	6.3 \pm 0.06	1.55 \pm 0.11	100.33 \pm 3.38	1.13 \pm 0.15	5	-	-	
196.84/-13.74	-	-	-	-	-	-	-	-	-	-	52.15	0.63 \pm 0.05	8.68 \pm 0.23	2.58 \pm 0.53	111.57 \pm 1.49	3.52 \pm 0.77	2	-	-	
196.84/-13.74	-	-	-	-	-	-	-	-	-	-	67.86	1.25 \pm 0.15	10.52 \pm 0.05	1.81 \pm 0.11	95.11 \pm 0.97	4.17 \pm 0.58	9	-	-	
196.84/-13.74	-	-	-	-	-	-	-	-	-	-	55.02	0.91 \pm 0.03	12.69 \pm 0.03	1.95 \pm 0.08	92.09 \pm 1.3	3.16 \pm 0.17	9	-	-	
196.84/-13.74	-	-	-	-	-	-	-	-	-	-	20.2	0.39 \pm 0.04	15.5 \pm 0.04	2.96 \pm 0.19	62.55 \pm 2.41	1.39 \pm 0.19	6	-	-	
196.84/-13.74	40.43	0.67 \pm 0.04	18.12 \pm 0.53	12.01 \pm 1.61	0.0 \pm 0.0	82.79 \pm 3.46	12.91 \pm 1.98	6	-	-	46.15	0.6 \pm 0.03	19.24 \pm 0.03	2.77 \pm 0.09	102.28 \pm 1.33	3.29 \pm 0.19	1	-	-	
196.84/-13.74	51.48	0.42 \pm 0.08	19.38 \pm 0.16	2.08 \pm 0.42	0.0 \pm 0.0	150.11 \pm 6.2	2.55 \pm 0.71	2	-	-	30.1	0.48 \pm 0.02	20.59 \pm 0.4	11.45 \pm 0.36	78.95 \pm 2.99	8.38 \pm 0.54	7	-	-	
196.84/-13.74	28.32	0.55 \pm 0.17	26.44 \pm 0.12	1.14 \pm 0.34	0.0 \pm 0.0	66.94 \pm 1.82	0.82 \pm 0.35	3	-	-	37.03	0.78 \pm 0.03	26.48 \pm 0.02	1.37 \pm 0.04	68.37 \pm 1.22	1.41 \pm 0.08	4	-	-	
196.84/-13.74	45.61	1.04 \pm 0.09	27.8 \pm 0.18	3.01 \pm 0.28	0.0 \pm 0.0	70.54 \pm 0.86	4.29 \pm 0.54	4	-	-	44.06	0.95 \pm 0.01	28.06 \pm 0.04	2.56 \pm 0.05	71.85 \pm 0.91	3.37 \pm 0.1	3	-	-	
196.84/-13.74	-	-	-	-	-	-	-	-	-	-	2.28 \pm 0.11	<0.016	-16.55 \pm 1.62	28.68 \pm 2.62	>142.31	1.27 \pm 0.13	0.5 \pm 0.02	-	-	
196.84/-13.74	66.04 \pm 3.08	<0.054	6.4 \pm 0.12	11.37 \pm 0.29	1.0 \pm 0.0	>1233.03	21.5 \pm 1.14	0.39 \pm 0.04	-	-	-	-	-	-	-	-	-	-	-	
196.84/-13.74	-	-	-	-	-	-	-	-	-	-	100.82 \pm 1.88	<0.063	15.38 \pm 0.07	24.85 \pm 0.17	>1594.08	48.6 \pm 0.96	0.0 \pm 0.0	-	-	
196.84/-13.74	-	-	-	-	-	-	-	-	-	-	-	-	-	-	-	-	-	-	-	
196.84/-13.74	26.25	<0.073	18.96 \pm 0.19	21.24 \pm 0.14	0.0 \pm 0.0	>1057.99	31.87 \pm 1.06	0.14 \pm 0.02	-	-	-	-	-	-	-	-	-	-	-	
173.15/-33.29	43.37	1.03 \pm 0.19	3.49 \pm 0.15	1.9 \pm 0.63	0.0 \pm 0.0	67.45 \pm 0.64	2.55 \pm 0.96	3	-	-	30.12	0.54 \pm 0.04	3.17 \pm 0.19	4.36 \pm 0.15	72.18 \pm 4.38	3.32 \pm 0.32	1	-	-	
173.15/-33.29	39.11	1.1 \pm 0.12	5.37 \pm 0.17	1.65 \pm 0.33	0.0 \pm 0.0	58.63 \pm 1.05	2.06 \pm 0.48	1	-	-	17.99	0.88 \pm 0.04	3.48 \pm 0.02	1.47 \pm 0.05	40.87 \pm 2.71	0.68 \pm 0.07	4	-	-	
173.15/-33.29	12.96	0.34 \pm 0.19	8.56 \pm 0.3	1.14 \pm 0.73	0.0 \pm 0.0	44.95 \pm 3.77	0.34 \pm 0.29	4	-	-	23.35	0.93 \pm 0.05	5.36 \pm 0.01	1.68 \pm 0.04	38.57 \pm 3.12	1.17 \pm 0.12	3	-	-	
173.15/-33.29	42.25	2.06 \pm 0.1	9.35 \pm 0.08	4.24 \pm 0.13	0.0 \pm 0.02	48.42 \pm 4.54	8.23 \pm 0.91	2	-	-	33.35	0.35 \pm 0.02	8.57 \pm 0.03	1.27 \pm 0.09	112.92 \pm 2.12	0.98 \pm 0.21	2	-	-	
173.15/-33.29	-	-	-	-	-	-	-	-	-	-	24.15	2.06 \pm 0.02	9.39 \pm 0.02	4.15 \pm 0.02	27.68 \pm 7.82	4.58 \pm 1.3	0	-	-	
173.15/-33.29	-	-	-	-	-	-	-	-	-	-	0.93 \pm 0.13	<0.021	-1.19 \pm 1.12	42.63 \pm 2.9	>43.64	0.77 \pm 0.12	0.5 \pm 0.04	-	-	
173.15/-33.29	25.56 \pm 0.83	<0.04	5.39 \pm 0.08	13.15 \pm 0.2	0.28 \pm 0.02	>637.29	7.38 \pm 0.27	0.28 \pm 0.03	-	-	18.27 \pm 1.84	<0.043	5.47 \pm 0.14	14.87 \pm 0.42	>423.54	5.27 \pm 0.55	0.29 \pm 0.03	-	-	
173.15/-33.29	-	-	-	-	-	-	-	-	-	-	44.53 \pm 4.93	<0.038	7.22 \pm 0.2	8.18 \pm 0.31	>1183.81	7.07 \pm 0.83	0.14 \pm 0.02	-	-	
173.15/-33.29	56.11 \pm 7.01	<0.038	9.28 \pm 0.03	6.28 \pm 0.22	0.0 \pm 0.0	>1472.01	6.83 \pm 0.89	0.28 \pm 0.03	-	-	-	-	-	-	-	-	-	-	-	
173.15/-33.29	-	-	-	-	-	-	-	-	-	-	53.01 \pm 10.41	<0.044	10.06 \pm 0.12	4.52 \pm 0.18	>1202.46	4.65 \pm 0.93	0.55 \pm 0.04	-	-	
173.15/-33.29	24.77	0.61 \pm 0.08	-0.63 \pm 0.06	1.77 \pm 0.18	0.24 \pm 0.56	54.25 \pm 0.94	1.27 \pm 0.37	5	-	-	-	-	-	-	-	-	-	-	-	
173.15/-33.29	76.55	0.8 \pm 0.19	6.66 \pm 1.98	13.01 \pm 1.39	0.0 \pm 0.05	139.01 \pm 2.74	28.24 \pm 7.32	0	-	-	9.8	0.61 \pm 0.01	-0.68 \pm 0.01	2.0 \pm 0.02	21.47 \pm 1.9	0.51 \pm 0.05	1	-	-	
197.15/-0.85	23.36	1.12 \pm 0.29	9.13 \pm 0.19	2.79 \pm 1.04	1.0 \pm 0.0	34.67 \pm 4.22	3.11 \pm 1.46	1	-	-	69.42	1.25 \pm 0.0	8.75 \pm 0.01	13.53 \pm 0.03	97.3 \pm 4.55	31.95 \pm 1.5	0	-	-	
197.15/-0.85	19.07	0.44 \pm 0.25	13.47 \pm 0.33	3.38 \pm 1.26	0.0 \pm 0.0	53.56 \pm 6.32	1.54 \pm 1.06	4	-	-	-	-	-	-	-	-	-	-	-	
197.15/-0.85	39.71	0.86 \pm 0.15	17.61 \pm 0.45	2.28 \pm 0.4	0.0 \pm 0.0	68.84 \pm 3.22	2.62 \pm 0.66	2	-	-	25.19	0.71 \pm 0.01	17.74 \pm 0.01	1.83 \pm 0.02	49.55 \pm 3.63	1.26 \pm 0.1	2	-	-	
197.15/-0.85	31.12	0.57 \pm 0.1	21.0 \pm 0.33	4.72 \pm 1.06	0.0 \pm 0.0	71.63 \pm 3.24														

TABLE 3 (CONT)

l/b ($^{\circ}$)	pseudo-Voigt							Gaussian							
	T_B (K)	τ (10^{-2})	V_{lsr} (kms^{-1})	ΔV (kms^{-1})	η	T_s (K)	N_{HI} ($10^{20}cm^{-2}$)	F or O	T_B (K)	τ (10^{-2})	V_{lsr} (kms^{-1})	ΔV (kms^{-1})	T_s (K)	N_{HI} ($10^{20}cm^{-2}$)	F or O
202.29/11.53	2.94	0.12±0.01	-3.11±0.09	1.82±0.22	0.0±0.0	25.96±2.29	0.11±0.02	1	3.16	0.12±0.0	-3.12±0.02	1.81±0.05	27.96±2.41	0.12±0.01	1
202.29/11.53	2.49	0.04±0.01	0.03±0.68	7.67±1.33	1.0±0.0	63.41±19.62	0.61±0.25	0	4.9	0.04±0.0	-0.28±0.14	8.31±0.24	124.92±7.0	0.89±0.06	0
202.29/11.53	-	-	-	-	-	-	-	-	-	0.52±0.12	-28.29±5.77	28.03±7.93	>33.59	0.28±0.1	0.5±0.29
202.29/11.53	1.13±0.3	<0.015	-18.05±7.71	32.09±10.49	0.92±0.54	>77.18	1.01±0.46	0.5±0.29	-	-	-	-	-	-	-
202.29/11.53	6.39±2.86	<0.028	-3.6±1.21	14.8±2.56	0.0±0.0	>230.9	1.83±0.88	0.5±0.29	-	-	-	-	-	0.39±0.06	0.5±0.29
202.29/11.53	3.59±0.64	<0.024	3.84±0.14	4.28±0.84	1.0±0.0	>147.57	0.44±0.12	0.5±0.29	-	-	-	-	-	0.19±0.02	0.5±0.29
202.29/11.53	-	-	-	-	-	-	-	-	8.31±0.18	<0.031	4.84±0.57	29.31±1.16	>265.54	4.72±0.21	0.5±0.29
202.29/11.53	5.97±0.79	<0.018	9.83±3.42	25.34±5.03	0.0±0.0	>339.71	2.94±0.7	0.5±0.29	-	-	-	-	-	1.16±0.06	1.0±0.0
202.29/11.53	2.95±0.18	<0.015	36.55±0.61	19.29±0.98	0.83±0.13	>201.65	1.54±0.14	1.0±0.0	-	-	-	-	-	1.61±0.01	1.0±0.0
170.59/-36.24	-	-	-	-	-	-	-	-	7.3	0.16±0.01	-0.55±0.31	4.63±0.36	49.36±15.1	0.71±0.23	3
170.59/-36.24	17.43	0.55±0.02	1.01±0.09	2.64±0.15	1.0±0.0	41.2±1.37	1.71±0.13	3	15.62	0.41±0.02	1.03±0.02	1.8±0.06	46.45±1.63	0.67±0.05	1
170.59/-36.24	25.89	0.57±0.09	4.1±0.19	2.32±0.34	0.0±0.0	59.58±1.51	1.53±0.33	1	26.98	0.7±0.01	4.19±0.04	2.96±0.1	53.59±2.79	2.14±0.14	4
170.59/-36.24	42.14	2.08±0.49	7.93±0.09	3.67±0.23	0.0±0.0	48.16±0.88	7.14±1.75	2	56.84	2.15±0.02	7.88±0.02	3.2±0.06	64.33±0.98	8.59±0.23	2
170.59/-36.24	32.82	2.08±0.17	10.85±0.13	1.19±0.49	0.0±0.0	37.51±0.54	1.81±0.76	4	23.02	2.08±0.08	10.81±0.01	1.18±0.04	26.31±1.4	1.25±0.09	5
170.59/-36.24	30.79	1.74±0.11	12.6±0.27	3.95±0.31	0.0±0.0	37.34±2.91	4.99±0.64	0	37.39	1.81±0.02	12.42±0.04	4.16±0.04	44.71±1.53	6.53±0.24	0
170.59/-36.24	-	-	-	-	-	-	-	-	14.19±0.59	<0.047	3.72±0.07	17.99±0.21	>299.59	4.95±0.22	0
170.59/-36.24	24.33±0.62	<0.048	4.39±0.06	14.53±0.14	0.16±0.01	>503.85	7.38±0.21	0.7±0.03	-	-	-	-	-	5.13±1.05	0.1±0.01
170.59/-36.24	-	-	-	-	-	-	-	-	35.72±2.13	<0.041	5.03±0.35	7.4±1.44	>878.28	5.13±1.05	0.1±0.01
170.59/-36.24	110.8±5.7	<0.045	11.13±0.13	3.31±0.24	0.0±0.0	>2465.63	7.1±0.64	0.03±0.02	40.21±1.74	<0.045	11.16±0.07	3.45±0.17	>894.89	2.69±0.18	0.58±0.01
203.42/15.42	3.91	0.05±0.01	1.37±0.22	1.91±0.66	0.21±0.96	80.1±5.33	0.15±0.09	0	2.19	0.05±0.0	1.35±0.05	1.99±0.11	44.93±12.16	0.08±0.02	0
203.42/15.42	-	-	-	-	-	-	-	-	2.96±0.94	<0.027	-5.76±1.29	7.82±1.24	>109.24	0.45±0.16	0.47±0.42
203.42/15.42	-	-	-	-	-	-	-	-	4.39±2.14	<0.027	0.21±0.21	4.33±0.73	>165.63	0.37±0.19	0.48±0.4
203.42/15.42	11.88±0.48	<0.027	1.25±0.05	12.49±0.35	0.73±0.08	>445.99	3.87±0.22	0.5±0.43	-	-	-	-	-	-	-
203.42/15.42	-	-	-	-	-	-	-	-	7.2±1.53	<0.025	3.0±1.33	9.09±1.43	>293.08	1.27±0.34	0.54±0.42
203.42/15.42	-	-	-	-	-	-	-	-	4.54±0.32	<0.027	5.58±0.4	27.47±1.51	>170.13	2.42±0.22	0.55±0.43
203.42/15.42	2.88±0.36	<0.022	8.29±0.97	30.73±0.94	0.0±0.0	>129.81	1.72±0.22	0.5±0.43	0.77±0.36	<0.021	8.43±1.76	54.41±8.92	>36.16	0.81±0.41	0.59±0.39
207.31/1.15	17.35	0.11±0.02	6.81±0.98	10.04±1.83	0.0±0.0	166.53±3.51	3.57±0.9	3	14.54	0.14±0.0	6.66±0.06	7.89±0.14	111.3±18.8	2.35±0.4	0
207.31/1.15	11.77	0.4±0.07	17.32±0.16	2.46±0.44	0.28±0.88	35.7±1.16	0.77±0.34	0	8.68	0.34±0.01	17.27±0.02	2.28±0.05	30.11±1.48	0.45±0.03	5
207.31/1.15	30.91	0.44±0.03	23.26±0.41	7.67±0.93	0.0±0.0	86.84±1.1	5.66±0.8	4	29.71	0.41±0.0	22.97±0.04	9.22±0.1	88.33±1.08	6.52±0.11	1
207.31/1.15	49.47	0.64±0.21	39.35±2.42	9.0±2.59	0.06±0.13	104.65±6.6	12.0±3.5	1	56.59	0.73±0.01	39.64±0.13	8.52±0.15	109.22±15.59	13.25±1.93	3
207.31/1.15	36.58	1.32±0.43	43.09±0.21	4.11±1.04	0.0±0.0	49.92±4.67	5.25±2.23	2	39.32	1.36±0.03	43.35±0.01	3.58±0.06	52.9±3.7	5.01±0.38	4
207.31/1.15	15.83	0.36±0.1	49.09±0.24	2.22±0.7	0.28±0.54	52.35±2.55	0.91±0.44	5	13.21	0.35±0.01	49.1±0.02	2.35±0.05	44.73±2.51	0.72±0.05	2
207.31/1.15	-	-	-	-	-	-	-	-	4.57±0.56	<0.046	0.66±0.43	6.02±0.56	>99.41	0.53±0.08	0.5±0.02
207.31/1.15	-	-	-	-	-	-	-	-	14.33±1.24	<0.114	10.72±0.35	7.12±0.56	>126.01	1.98±0.23	0.53±0.02
207.31/1.15	9.01±0.37	<0.091	11.24±0.14	6.52±0.38	0.0±0.0	>98.73	1.14±0.08	0.5±0.02	-	-	-	-	-	-	-
207.31/1.15	45.45±0.42	<0.08	26.06±0.18	34.97±0.2	0.0±0.0	>564.64	30.84±0.33	0.0±0.0	-	-	-	-	-	-	-
207.31/1.15	-	-	-	-	-	-	-	-	44.89±0.34	<0.087	26.63±0.07	35.24±0.09	>516.61	30.69±0.25	0.01±0.0
207.31/1.15	36.72±2.44	<0.138	42.28±0.35	8.25±0.5	0.15±0.09	>266.18	6.28±0.62	0.13±0.01	-	-	-	-	-	-	-
189.21/-6.93	-	-	-	-	-	-	-	-	25.33±7.58	<0.16	42.94±1.34	9.56±0.92	>158.71	4.7±1.48	0.19±0.01
189.21/-6.93	-	-	-	-	-	-	-	-	7.03	0.14±0.04	-2.34±1.38	4.61±1.85	53.83±7.58	0.67±0.35	0
189.21/-6.93	-	-	-	-	-	-	-	-	13.65	0.27±0.04	2.24±0.49	4.0±2.07	57.69±6.31	1.19±0.66	1
189.21/-6.93	36.43	0.27±0.02	2.93±0.91	9.73±1.16	0.0±0.0	153.94±12.11	7.72±1.31	3	-	-	-	-	-	-	-
189.21/-6.93	13.34	0.37±0.07	6.5±0.15	2.69±0.52	0.0±0.0	43.15±2.62	0.83±0.23	2	13.54	0.53±0.05	6.42±0.27	3.32±0.63	32.92±2.63	1.13±0.26	2
189.21/-6.93	9.66	0.47±0.06	10.52±0.1	1.98±0.29	0.0±0.0	25.77±1.66	0.47±0.1	1	8.64	0.51±0.05	10.5±0.11	2.07±0.34	21.62±2.17	0.44±0.1	3
189.21/-6.93	2.69	0.05±0.03	12.83±0.52	1.36±1.21	0.0±0.0	55.11±8.3	0.08±0.08	0	2.86	0.06±0.03	12.87±0.6	1.64±0.66	49.1±8.29	0.1±0.06	4
189.21/-6.93	1.0	0.02±0.01	23.3±0.8	4.91±2.19	1.0±0.0	50.58±8.03	0.16±0.1	4	1.1	0.02±0.01	23.59±0.96	7.53±2.24	55.51±17.66	0.14±0.08	5
189.21/-6.93	-	-	-	-	-	-	-	-	0.65±0.26	<0.026	-13.85±22.9	50.58±14.93	>24.84	0.63±0.31	1.0±0.0
189.21/-6.93	13.65±1.01	<0.099	-2.97±0.46	14.54±0.51	1.0±0.0	>137.57	5.68±0.47	0.45±0.08	-	-	-	-	-	-	-
189.21/-6.93	-	-	-	-	-	-	-	-	25.08±7.66	<0.067	2.19±1.72	14.58±1.7	>373.71	7.09±2.32	0.54±0.43
189.21/-6.93	-	-	-	-	-	-	-	-	15.82±1.55	<0.074	4.25±0.33	31.54±1.85	>212.64	9.68±1.11	0.46±0.43
189.21/-6.93	14.07±0.44	<0.08	5.87±0.26	29.13±0.33	0.0±0.0	>176.71	7.95±0.27	0.36±0.08	-	-	-	-	-	-	-
189.21/-6.93	-	-	-	-	-	-	-	-	50.61±8.72	<0.046	7.15±0.13	9.66±0.45	>1104.92	9.48±1.69	0.58±0.27
189.21/-6.93	49.22±1.64	<0.06	7.73±0.18	9.51±0.18	0.0±0.0	>818.81	9.08±0.35	0.27±0.05	-	-	-	-	-	-	-

TABLE 3 (CONT)

l/b	pseudo-Voigt										Gaussian									
	T_B (K)	τ (10^{-2})	V_{lsr} ($km s^{-1}$)	ΔV ($km s^{-1}$)	η	T_s (K)	N_{HI} ($10^{20} cm^{-2}$)	F	σ	O	T_B (K)	τ (10^{-2})	V_{lsr} ($km s^{-1}$)	ΔV ($km s^{-1}$)	T_s (K)	N_{HI} ($10^{20} cm^{-2}$)	F	σ	O	
207.31/12.37	5.04	-	-	-	-	128.59±39.6	0.54±0.26	0	-	-	5.05	0.04±0.0	-	5.43±0.45	128.67±5.07	0.55±0.06	1	-	-	
207.31/12.37	11.37	-	-	-	-	100.52±22.82	1.1±0.34	1	-	-	10.6	0.1±0.01	-	4.29±0.81	111.35±2.81	0.95±0.22	0	-	-	
207.31/12.37	-	-	-	-	-	-	-	-	-	-	5.37	0.06±0.02	-	2.6±0.64	92.25±1.74	0.26±0.12	2	-	-	
207.31/12.37	-	-	-	-	-	-	-	-	-	-	0.89	0.04±0.0	-	2.13±0.19	22.75±1.75	0.04±0.01	3	-	-	
207.31/12.37	6.88±1.13	-	-	-	-	>221.52	2.3±0.47	0.99±0.08	-	-	-	-	-	-	-	-	-	-	-	
207.31/12.37	-	-	-	-	-	>138.54	0.34±0.17	0.49±0.06	-	-	4.55±0.12	<0.032	-	10.95±0.28	>142.11	0.97±0.04	0.5±0.17	-	-	
207.31/12.37	4.31±2.05	-	-	-	-	>142.04	2.36±0.93	0.13±0.25	-	-	4.16±0.18	<0.031	-	3.82±0.06	>133.77	0.31±0.01	0.53±0.16	-	-	
207.31/12.37	7.86±1.23	-	-	-	-	-	-	-	-	-	-	-	-	-	-	-	-	-	-	
207.31/12.37	-	-	-	-	-	-	-	-	-	-	4.68±0.05	<0.039	-	8.87±0.43	>119.75	0.81±0.04	0.52±0.17	-	-	
207.31/12.37	-	-	-	-	-	-	-	-	-	-	5.18±0.03	<0.023	-	43.23±0.14	>325.24	4.35±0.03	0.5±0.17	-	-	
207.31/12.37	6.36±0.69	-	-	-	-	>115.84	1.05±0.16	1.0±0.0	-	-	4.55±0.05	<0.045	-	5.38±0.08	>100.44	0.48±0.01	0.49±0.17	-	-	
207.31/12.37	2.6±0.44	-	-	-	-	>121.88	1.4±0.32	0.38±0.44	-	-	-	-	-	-	-	-	-	-	-	
207.31/12.37	0.48±0.07	-	-	-	-	>21.25	0.15±0.03	1.0±0.0	-	-	-	-	-	-	-	-	-	-	-	
207.31/12.37	-	-	-	-	-	-	-	-	-	-	0.36±0.01	<0.024	-	13.81±0.55	>15.22	0.1±0.0	1.0±0.0	-	-	
175.7/-18.36	15.16	-	-	-	-	64.05±5.04	1.23±0.3	3	-	-	6.09	0.24±0.0	-	2.43±0.02	28.52±4.52	0.37±0.06	0	-	-	
175.7/-18.36	35.91	-	-	-	-	56.81±1.37	0.69±0.78	1	-	-	48.73	1.01±0.01	-	5.4±0.05	76.65±1.52	8.1±0.21	2	-	-	
175.7/-18.36	17.85	-	-	-	-	38.64±2.85	0.74±0.27	0	-	-	20.87	0.6±0.02	-	1.61±0.05	46.26±1.44	0.87±0.05	3	-	-	
175.7/-18.36	24.17	-	-	-	-	60.49±1.09	1.25±0.38	2	-	-	17.98	0.48±0.02	-	1.98±0.06	47.16±2.72	0.86±0.06	1	-	-	
175.7/-18.36	3.64±0.08	-	-	-	-	>143.27	2.35±0.09	0.5±0.08	-	-	5.03±0.07	<0.023	-	39.71±0.61	>217.83	3.88±0.08	0.51±0.17	-	-	
175.7/-18.36	26.35±1.48	-	-	-	-	>424.56	6.66±0.43	0.24±0.08	-	-	23.87±1.39	<0.072	-	6.5±0.33	>329.68	3.01±0.23	0.41±0.16	-	-	
175.7/-18.36	-	-	-	-	-	-	-	-	-	-	26.04±1.8	<0.068	-	14.66±0.31	>380.23	7.4±0.54	0.31±0.15	-	-	
175.7/-18.36	52.43±1.65	-	-	-	-	>955.6	9.17±0.36	0.16±0.05	-	-	-	-	-	-	-	-	-	-	-	
175.7/-18.36	-	-	-	-	-	-	-	-	-	-	13.28±1.36	<0.068	-	3.84±0.22	>194.24	0.99±0.12	0.45±0.16	-	-	
203.54/-0.27	2.67	-	-	-	-	39.45±5.57	0.14±0.14	0	-	-	3.17	0.07±0.0	-	46.84±5.47	>18.52	0.16±0.02	0	-	-	
203.54/-0.27	20.42	-	-	-	-	63.22±1.55	0.46±0.38	5	-	-	26.51	0.38±0.0	-	5.66±0.06	83.85±1.77	3.55±0.09	1	-	-	
203.54/-0.27	6.5	-	-	-	-	25.06±116.04	2.47±2.18	3	-	-	17.14	0.3±0.0	-	66.12±21.6	1.87±2.91	1.12±0.37	2	-	-	
203.54/-0.27	39.67	-	-	-	-	64.29±1.38	3.58±1.01	4	-	-	50.0	1.07±0.01	-	3.29±0.04	76.1±1.35	5.18±0.13	3	-	-	
203.54/-0.27	77.81	-	-	-	-	93.98±0.9	19.72±3.72	1	-	-	28.55	1.85±0.01	-	5.43±0.07	33.88±9.64	6.61±1.89	5	-	-	
203.54/-0.27	-	-	-	-	-	-	-	2	-	-	34.94	0.77±0.01	-	2.89±0.07	65.07±6.38	2.8±0.29	7	-	-	
203.54/-0.27	72.06	-	-	-	-	106.96±0.82	15.75±2.46	6	-	-	49.03	3.41±0.06	-	2.03±0.02	50.71±4.78	6.8±0.66	6	-	-	
203.54/-0.27	47.66	-	-	-	-	48.31±2.67	5.18±4.4	6	-	-	18.92	0.66±0.01	-	3.5±0.07	39.15±6.55	1.77±0.3	4	-	-	
203.54/-0.27	3.31	-	-	-	-	31.76±3.39	0.25±0.11	7	-	-	2.63	0.11±0.0	-	4.33±0.11	25.25±6.08	0.24±0.06	8	-	-	
203.54/-0.27	14.1±28.63	-	-	-	-	>102.3	0.95±1.98	0.47±0.02	-	-	9.85±2.57	<0.121	-	3.74±1.09	>81.71	0.71±0.28	0.5±0.02	-	-	
203.54/-0.27	47.12±1.05	-	-	-	-	>327.08	21.69±0.57	0.12±0.01	-	-	-	-	-	-	-	-	-	-	-	
203.54/-0.27	-	-	-	-	-	-	-	-	-	-	47.33±2.0	<0.154	-	24.14±0.39	>307.89	22.17±1.0	0.0±0.0	-	-	
203.54/-0.27	-	-	-	-	-	-	-	-	-	-	106.05±14.1	<0.211	-	5.84±0.13	>502.11	12.02±1.62	0.5±0.0	-	-	
203.54/-0.27	-	-	-	-	-	-	-	-	-	-	41.83±4.79	<0.16	-	7.96±0.61	>262.22	6.46±0.89	1.0±0.0	-	-	
203.54/-0.27	38.94±1.19	-	-	-	-	>301.57	16.98±0.59	0.29±0.01	-	-	-	-	-	-	-	-	-	-	-	
203.54/-0.27	-	-	-	-	-	-	-	-	-	-	35.92±5.02	<0.115	-	21.51±0.85	>312.05	14.99±2.18	0.0±0.0	-	-	
164.76/-10.24	6.66	-	-	-	-	136.46±16.66	1.66±0.67	3	-	-	14.9	0.19±0.0	-	2.85±0.09	86.1±2.55	0.92±0.05	0	-	-	
164.76/-10.24	9.59	-	-	-	-	68.82±7.35	0.38±0.19	2	-	-	7.63	0.12±0.0	-	4.53±0.37	67.45±6.98	0.73±0.1	1	-	-	
164.76/-10.24	-	-	-	-	-	-	-	-	-	-	21.64	0.86±0.01	-	3.72±0.05	37.51±1.55	2.33±0.1	2	-	-	
164.76/-10.24	32.3	-	-	-	-	53.01±0.52	4.65±0.68	1	-	-	16.93	0.77±0.01	-	3.18±0.03	31.53±4.62	1.43±0.22	3	-	-	
164.76/-10.24	28.11	-	-	-	-	53.75±0.49	2.17±0.19	0	-	-	21.64	0.86±0.01	-	4.06±0.02	37.51±1.55	2.33±0.1	2	-	-	
164.76/-10.24	2.65±0.06	-	-	-	-	>102.06	1.65±0.08	1.0±0.0	-	-	16.93	0.77±0.01	-	3.18±0.03	31.53±4.62	1.43±0.22	3	-	-	
164.76/-10.24	4.52±0.15	-	-	-	-	>108.74	2.62±0.27	0.5±0.08	-	-	-	-	-	-	-	-	-	-	-	
164.76/-10.24	-	-	-	-	-	-	-	-	-	-	6.92±0.19	<0.065	-	37.8±0.7	>106.04	5.07±0.17	0.47±0.4	-	-	
164.76/-10.24	16.7±0.67	-	-	-	-	>151.21	3.01±0.27	0.5±0.08	-	-	11.97±0.33	<0.112	-	11.46±0.36	>107.21	2.66±0.11	0.48±0.41	-	-	
164.76/-10.24	38.42±0.48	-	-	-	-	>546.16	8.56±0.13	0.24±0.05	-	-	33.37±1.38	<0.069	-	9.93±0.44	>181.13	6.43±0.39	0.39±0.36	-	-	
164.76/-10.24	-	-	-	-	-	-	-	-	-	-	8.43±2.58	<0.06	-	5.1±0.44	>139.57	0.83±0.27	0.47±0.4	-	-	
206.09/13.67	4.77	-	-	-	-	81.87±8.96	0.39±0.25	0.5±0.42	-	-	3.31	0.05±0.0	-	67.81±4.1	-	0.26±0.03	0	-	-	
206.09/13.67	5.33±1.28	-	-	-	-	>148.94	2.03±0.52	-	-	-	-	-	-	-	-	-	-	-	-	
206.09/13.67	-	-	-	-	-	-	-	-	-	-	7.96±0.32	<0.032	-	2.11±0.32	16.52±0.66	>248.99	2.55±0.15	0.5±0.42	-	
206.09/13.67	5.91±1.68	-	-	-	-	>158.25	1.56±0.66	0.5±0.42	-	-	2.19±0.31	<0.035	-	48.79±4.32	>63.4	2.08±0.35	0.5±0.42	-	-	
206.09/13.67	-	-	-	-	-	-	-	-	-	-	4.75±0.26	<0.032	-	15.36±0.87	>150.15	1.41±0.11	0.5±0.42	-	-	
206.09/13.67	0.86±0.07	-	-	-	-	>45.65	0.51±0.08	1.0±0.0	-	-	-	-	-	-	-	-	-	-	-	
206.09/13.67	-	-	-	-	-	-	-	-	-	-	0.3±0.13	<0.015								

TABLE 3 (CONT)

l/b	pseudo-Voigt						Gaussian						F or O	
	T_B (K)	τ (10^{-2})	V_{lsr} ($km s^{-1}$)	ΔV ($km s^{-1}$)	η	T_s (K)	N_{HI} ($10^{20} cm^{-2}$)	T_B (K)	τ (10^{-2})	V_{lsr} ($km s^{-1}$)	ΔV ($km s^{-1}$)	T_s (K)		N_{HI} ($10^{20} cm^{-2}$)
171.98/-35.48	13.89	0.23±0.03	-3.5±0.53	4.32±0.9	0.0±0.0	67.58±2.24	1.29±0.33	7.75	0.26±0.01	-3.51±0.11	4.76±0.17	33.85±2.56	0.82±0.07	5
171.98/-35.48	16.26	0.56±0.06	1.44±0.28	3.93±0.91	0.64±0.34	37.92±3.92	2.1±0.63	14.69	0.56±0.01	1.73±0.04	4.36±0.18	34.26±2.37	1.64±0.13	1
171.98/-35.48	-	-	-	-	-	-	-	15.42	0.33±0.03	4.91±0.08	1.75±0.19	54.86±3.61	0.61±0.09	2
171.98/-35.48	6.9	0.3±0.12	6.69±0.2	1.06±0.51	0.0±0.0	26.61±2.14	0.16±0.1	18.32	0.61±0.12	6.56±0.04	1.44±0.14	40.11±1.23	0.68±0.15	3
171.98/-35.48	14.43	0.65±0.07	7.57±0.34	5.88±1.18	0.0±0.0	30.19±3.95	2.22±0.58	4	-	-	-	-	-	3
171.98/-35.48	-	-	-	-	-	-	-	30.67	0.61±0.04	8.11±0.15	2.91±0.46	67.17±1.45	2.31±0.41	4
171.98/-35.48	-	-	-	-	-	-	-	24.18	0.33±0.03	11.21±0.21	3.46±0.23	86.01±1.57	1.93±0.2	0
171.98/-35.48	7.65	0.15±0.1	11.97±0.36	2.23±1.04	0.08±0.69	54.89±3.85	0.38±0.32	-	-	-	-	-	-	0
171.98/-35.48	-	-	-	-	-	-	-	1.26±0.08	<0.025	-15.71±0.26	7.58±0.66	>50.31	0.19±0.02	1.0±0.0
171.98/-35.48	38.58±2.06	<0.1	-0.03±0.12	4.82±0.1	1.0±0.0	>385.88	5.32±0.31	-	-	-	-	-	-	-
171.98/-35.48	-	-	-	-	-	-	-	62.59±1.64	<0.074	4.49±0.05	13.27±0.08	>851.41	16.11±0.43	0.0±0.0
171.98/-35.48	81.76±3.18	<0.081	7.45±0.04	8.7±0.12	0.09±0.01	>1014.14	14.39±0.6	-	-	-	-	-	-	-
203.64/13.91	6.57	0.1±0.03	-2.36±0.89	5.2±1.75	0.28±0.55	69.03±19.65	0.79±0.44	0	-	-	-	-	-	-
203.64/13.91	-	-	-	-	-	-	-	21.59	0.15±0.0	0.11±0.08	9.4±0.16	154.98±5.59	4.18±0.19	1
203.64/13.91	16.06	0.22±0.04	2.06±0.35	3.47±0.7	1.0±0.0	81.34±3.82	1.8±0.49	6.78	0.13±0.01	2.03±0.03	1.51±0.09	55.6±2.67	0.21±0.02	0
203.64/13.91	-	-	-	-	-	-	-	4.05±0.31	<0.037	-6.37±1.0	15.09±1.14	>109.46	1.18±0.13	0.3±0.3
203.64/13.91	10.59±2.34	<0.062	-2.1±0.26	9.75±0.76	0.49±0.23	>170.95	2.48±0.62	-	-	-	-	-	-	-
203.64/13.91	6.25±1.02	<0.077	-0.63±0.16	3.39±0.88	1.0±0.0	>80.91	0.61±0.19	-	-	-	-	-	-	-
203.64/13.91	3.13±0.55	<0.061	8.71±2.05	30.82±2.08	0.0±0.0	>51.66	1.87±0.35	-	-	-	-	-	-	-
203.64/13.91	1.58±0.43	<0.03	14.82±1.04	21.07±3.73	1.0±0.0	>53.27	0.95±0.31	4.75±0.06	<0.033	14.67±0.32	21.99±0.54	>144.56	2.03±0.06	0.3±0.3
176.27/-28.26	19.0	0.13±0.03	-0.59±0.25	3.57±0.54	0.0±0.0	155.87±2.31	1.45±0.35	2.85	0.14±0.0	-0.55±0.03	3.77±0.07	21.81±0.20	0.22±0.62	0
176.27/-28.26	36.67	0.72±0.16	6.68±0.12	1.39±0.26	0.0±0.0	71.45±0.64	1.38±0.4	31.48	1.05±0.02	6.82±0.02	1.68±0.03	48.42±0.74	1.65±0.05	2
176.27/-28.26	69.19	1.45±0.09	8.75±0.14	3.61±0.21	0.09±0.05	90.39±0.32	9.59±0.84	48.65	1.16±0.03	8.99±0.02	2.31±0.05	70.86±0.5	3.68±0.12	3
176.27/-28.26	-	-	-	-	-	-	-	33.91	0.4±0.02	9.3±0.05	4.97±0.09	102.85±1.65	3.96±0.27	1
176.27/-28.26	2.24±0.05	<0.022	-21.57±0.23	19.9±0.69	0.55±0.13	>100.76	1.09±0.07	-	-	-	-	-	-	-
176.27/-28.26	-	-	-	-	-	-	-	2.13±0.04	<0.023	-20.73±0.26	22.15±0.67	>91.5	0.91±0.03	0.1±0.1
176.27/-28.26	-	-	-	-	-	-	-	16.73±8.62	<0.087	-0.87±0.18	4.13±0.19	>192.41	1.34±0.69	0.3±0.17
176.27/-28.26	34.52±0.17	<0.043	4.78±0.03	13.03±0.05	0.01±0.01	>806.55	8.76±0.07	34.03±0.22	<0.043	4.82±0.05	12.7±0.06	>795.04	8.38±0.07	0.6±0.06
190.16/3.91	0.85	0.03±0.01	-72.64±0.77	5.24±1.67	0.0±0.0	28.76±6.38	0.1±0.05	0.57	0.03±0.0	-72.66±0.21	5.29±0.09	19.12±1.22	0.06±0.01	0
190.16/3.91	17.98	0.3±0.03	-8.63±0.39	5.22±0.89	0.0±0.0	69.36±5.44	2.09±0.45	12.66	0.3±0.0	-8.68±0.04	5.19±0.09	48.85±2.14	1.46±0.07	1
190.16/3.91	77.53	1.79±0.14	-1.16±0.14	4.83±0.4	0.0±0.0	93.07±0.4	15.65±1.8	50.93	1.8±0.01	-1.15±0.01	4.86±0.04	61.02±0.16	10.32±0.12	2
190.16/3.91	56.2	0.99±0.09	3.93±0.16	2.67±0.4	0.0±0.0	89.43±1.11	4.61±0.81	31.24	0.91±0.01	3.81±0.02	2.37±0.04	52.28±0.13	2.19±0.05	3
190.16/3.91	56.82	1.16±0.09	9.16±0.14	4.2±0.35	0.0±0.0	82.77±7.03	7.81±1.13	34.79	0.7±0.02	8.9±0.03	6.04±0.1	69.11±0.41	5.67±0.16	4
190.16/3.91	-	-	-	-	-	-	-	22.49	0.73±0.02	9.24±0.02	1.86±0.05	43.41±0.46	1.14±0.05	5
190.16/3.91	5.0	0.19±0.05	20.37±0.33	3.05±0.69	0.0±0.0	28.9±7.87	0.33±0.15	4.69	0.2±0.0	20.29±0.03	2.92±0.06	25.9±0.41	0.29±0.01	6
190.16/3.91	2.08±0.17	<0.043	-73.69±0.23	17.65±1.49	0.75±0.16	>48.61	0.96±0.13	-	-	-	-	-	-	-
190.16/3.91	-	-	-	-	-	-	-	1.78±0.03	<0.035	-72.76±0.04	13.5±0.16	>51.3	0.47±0.01	0.1±0.3
190.16/3.91	13.63±1.96	<0.116	-6.23±0.19	4.65±0.68	0.46±0.37	>117.55	1.5±0.38	12.5±0.27	<0.114	-5.74±0.08	6.29±0.19	>109.96	1.53±0.06	0.4±0.26
190.16/3.91	88.35±1.87	<0.151	6.55±0.14	22.57±0.16	0.13±0.01	>585.63	41.1±0.93	81.19±0.12	<0.15	6.44±0.0	23.81±0.01	>542.88	37.51±0.06	0.3±0.26
190.16/3.91	-	-	-	-	-	-	-	13.64±0.16	<0.132	7.84±0.02	3.97±0.02	>103.04	1.05±0.01	0.6±0.29
190.16/3.91	35.76±7.11	<0.136	8.42±0.15	3.91±0.2	0.29±0.24	>262.0	3.09±0.7	-	-	-	-	-	-	-
190.16/3.91	-	-	-	-	-	-	-	10.22±0.06	<0.135	18.14±0.01	5.65±0.03	>75.56	1.12±0.01	0.6±0.29
190.16/3.91	10.97±1.02	<0.134	18.82±0.22	5.25±0.31	0.0±0.0	>81.93	1.12±0.12	-	-	-	-	-	-	-
205.41/-4.43	53.13	0.65±0.05	5.81±0.21	5.5±0.41	0.0±0.0	111.16±1.3	7.75±0.84	51.67	0.66±0.0	5.82±0.02	5.5±0.04	106.94±1.36	7.48±0.12	0
205.41/-4.43	30.69	0.74±0.09	12.27±0.16	3.43±0.34	0.0±0.0	58.7±1.16	2.88±0.45	36.12	0.72±0.01	12.3±0.01	3.5±0.03	70.37±1.19	3.46±0.07	1
205.41/-4.43	9.15	0.19±0.05	22.58±0.29	2.49±1.12	0.94±0.93	52.87±3.18	0.71±0.43	6.8	0.16±0.0	22.42±0.03	2.25±0.08	46.02±2.72	0.32±0.02	5
205.41/-4.43	25.06	0.31±0.07	32.43±0.34	4.25±1.16	1.0±0.0	94.02±2.88	3.59±1.24	10.43	0.26±0.01	32.48±0.02	1.85±0.05	45.54±8.31	0.42±0.08	4
205.41/-4.43	-	-	-	-	-	-	-	25.44	0.15±0.0	34.79±0.12	18.4±0.26	182.61±2.01	9.56±0.22	2
205.41/-4.43	10.94	0.15±0.02	41.61±0.57	8.06±1.29	0.0±0.0	78.56±6.38	1.86±0.43	4	-	-	-	-	-	-
205.41/-4.43	-	-	-	-	-	-	-	9.07	0.15±0.0	42.11±0.03	2.31±0.09	65.09±2.69	0.44±0.03	3
205.41/-4.43	-	-	-	-	-	-	-	55.31±0.65	<0.1	8.91±0.04	10.35±0.06	>552.23	11.11±0.15	0.49±0.08
205.41/-4.43	66.54±0.57	<0.114	9.7±0.05	11.98±0.07	0.5±0.01	>585.02	19.13±0.22	18.58±0.26	<0.099	23.69±0.08	40.99±0.18	>186.82	14.77±0.22	0.43±0.08
205.41/-4.43	25.97±1.84	<0.17	29.79±0.49	15.38±0.53	0.0±0.0	>152.57	7.75±0.61	-	-	-	-	-	-	-
205.41/-4.43	-	-	-	-	-	-	-	18.22±1.78	<0.177	32.03±0.07	3.59±0.19	>102.7	1.27±0.14	0.43±0.08
205.41/-4.43	12.78±1.65	<0.086	43.56±1.4	18.04±1.13	0.0±0.0	>147.85	4.47±0.64	-	-	-	-	-	-	-

Warm and cool HI gas in the Carinus and Gemina regions

TABLE 3 (CONT)

l/b	pseudo-Voigt										Gaussian									
	T_B ($^{\circ}$)	$(T - T_c)$ (10^{-2})	V_{lsr} (km s^{-1})	ΔV (km s^{-1})	η	T_s (K)	NH (10^{20} cm^{-2})	F	σ	O	T_B (K)	T_c (10^{-2})	V_{lsr} (km s^{-1})	ΔV (km s^{-1})	T_s (K)	NH (10^{20} cm^{-2})	F	σ	O	
199.52/6.04	8.29	0.25 \pm 0.08	0.24 \pm 0.10	2.35 \pm 0.73	0.63 \pm 0.51	37.48 \pm 2.73	0.56 \pm 0.27	0	-	-	6.41	0.25 \pm 0.0	0.45 \pm 0.02	2.59 \pm 0.05	28.99 \pm 2.17	0.36 \pm 0.03	0	-	-	
199.52/6.04	15.73	0.38 \pm 0.05	8.29 \pm 0.39	3.07 \pm 0.66	0.70 \pm 0.0	49.77 \pm 2.59	1.12 \pm 0.29	1	-	-	23.44	0.38 \pm 0.01	8.43 \pm 0.07	3.59 \pm 0.11	74.13 \pm 1.12	1.93 \pm 0.08	1	-	-	
199.52/6.04	17.67	0.53 \pm 0.06	11.31 \pm 0.25	2.57 \pm 0.44	0.06 \pm 0.27	42.96 \pm 1.55	1.16 \pm 0.28	2	-	-	21.16	0.53 \pm 0.01	11.42 \pm 0.04	2.49 \pm 0.06	53.78 \pm 1.1	1.33 \pm 0.05	2	-	-	
199.52/6.04	9.72	0.32 \pm 0.13	32.32 \pm 0.23	0.12 \pm 0.46	1.0 \pm 0.0	25.1 \pm 2.29	0.76 \pm 0.27	3	-	-	15.27	0.61 \pm 0.01	32.54 \pm 0.01	1.86 \pm 0.02	33.43 \pm 1.63	0.73 \pm 0.04	3	-	-	
199.52/6.04	-	<0.033	-56.64 \pm 0.84	36.24 \pm 3.59	1.0 \pm 0.0	>26.53	0.91 \pm 0.1	1.0 \pm 0.0	-	-	-	-	-	-	-	-	-	-	-	
199.52/6.04	-	<0.038	-19.87 \pm 0.46	9.97 \pm 1.39	0.8 \pm 0.4	>32.53	0.33 \pm 0.07	1.0 \pm 0.0	-	-	0.8 \pm 0.04	<0.028	-53.26 \pm 0.96	28.12 \pm 2.33	>28.29	0.43 \pm 0.04	1.0 \pm 0.0	-	-	
199.52/6.04	-	-	-	-	-	-	-	-	-	-	-	-	-	-	-	-	-	-	-	
199.52/6.04	-	<0.067	-7.82 \pm 0.07	6.22 \pm 0.27	0.83 \pm 0.2	>99.95	1.13 \pm 0.1	0.2 \pm 0.29	-	-	3.57 \pm 0.37	<0.035	-10.09 \pm 2.83	28.33 \pm 3.64	>64.8	1.96 \pm 0.32	0.5 \pm 0.29	-	-	
199.52/6.04	-	<0.09	8.13 \pm 0.16	12.94 \pm 0.57	1.0 \pm 0.0	>276.45	9.22 \pm 0.55	0.19 \pm 0.17	-	-	5.44 \pm 0.23	<0.067	-7.92 \pm 0.08	5.25 \pm 0.24	>80.94	0.55 \pm 0.03	1.0 \pm 0.0	-	-	
199.52/6.04	-	<0.084	-	-	-	-	-	-	-	-	-	-	-	-	-	-	-	-	-	
199.52/6.04	19.27 \pm 0.69	-	18.78 \pm 0.07	8.22 \pm 0.36	0.83 \pm 0.2	>228.76	4.28 \pm 0.38	0.37 \pm 0.27	-	-	21.13 \pm 0.81	<0.086	8.73 \pm 0.32	16.91 \pm 0.74	>246.39	6.93 \pm 0.42	0.0 \pm 0.0	-	-	
199.52/6.04	-	-	-	-	-	-	-	-	-	-	15.39 \pm 1.01	<0.084	18.84 \pm 0.1	7.06 \pm 0.3	2.11 \pm 0.17	0.49 \pm 0.29	0.25 \pm 0.18	-	-	
199.09/2.17	49.35	1.28 \pm 0.54	0.2 \pm 0.21	1.19 \pm 0.47	0.0 \pm 0.0	68.36 \pm 1.22	2.03 \pm 1.17	3	-	-	62.23	1.35 \pm 0.03	0.2 \pm 0.01	1.14 \pm 0.02	84.01 \pm 7.95	2.51 \pm 0.25	5	-	-	
199.09/2.17	18.27	0.53 \pm 0.25	1.92 \pm 0.44	0.05 \pm 0.08	0.63 \pm 0.45	43.78 \pm 3.4	2.03 \pm 1.17	3	-	-	13.76	0.54 \pm 0.01	2.04 \pm 0.27	1.87 \pm 0.27	32.97 \pm 15.08	4.79 \pm 2.61	2	-	-	
199.09/2.17	14.42	0.66 \pm 0.3	2.84 \pm 0.58	2.33 \pm 1.42	0.0 \pm 0.0	91.94 \pm 1.14	2.71 \pm 2.2	2	-	-	67.38	0.67 \pm 0.02	0.57 \pm 0.02	1.38 \pm 0.04	4.39 \pm 0.69	4.47 \pm 0.21	1	-	-	
199.09/2.17	60.33	1.24 \pm 0.87	0.66 \pm 0.41	0.0 \pm 0.0	0.0 \pm 0.0	13.83 \pm 4.32	3.38 \pm 3.42	6	-	-	103.5	0.65 \pm 0.02	5.47 \pm 0.04	1.92 \pm 0.09	1.43 \pm 42.16.26	3.42 \pm 0.45	3	-	-	
199.09/2.17	80.57	1.63 \pm 0.98	0.23 \pm 0.3	0.0 \pm 0.0	0.0 \pm 0.0	133.96 \pm 2.39	3.91 \pm 2.94	4	-	-	68.53	0.89 \pm 0.02	0.82 \pm 0.02	1.52 \pm 0.04	1.78 \pm 28.7.95	4.67 \pm 0.28	0	-	-	
199.09/2.17	74.44	1.30 \pm 0.26	13.53 \pm 0.96	7.19 \pm 1.4	0.0 \pm 0.0	102.33 \pm 2.1	18.59 \pm 5.18	1	-	-	78.41	1.29 \pm 0.02	13.46 \pm 0.07	7.41 \pm 0.09	108.19 \pm 1.8	20.08 \pm 0.49	6	-	-	
199.09/2.17	81.01	2.65 \pm 1.8	16.13 \pm 0.25	1.72 \pm 0.55	0.0 \pm 0.0	87.17 \pm 0.88	7.7 \pm 5.8	5	-	-	47.56	2.78 \pm 0.09	16.11 \pm 0.07	1.7 \pm 0.03	50.71 \pm 3.52	4.65 \pm 0.36	4	-	-	
199.09/2.17	-	-	-	-	-	-	-	-	-	-	17.61 \pm 3.33	<0.094	-2.1 \pm 0.29	5.29 \pm 0.61	>188.29	1.81 \pm 0.4	0.68 \pm 0.01	-	-	
199.09/2.17	-	-	-	-	-	-	-	-	-	-	7.12 \pm 0.61	<0.123	3.49 \pm 0.27	39.14 \pm 0.93	>57.97	5.4 \pm 0.48	0.53 \pm 0.01	-	-	
199.09/2.17	-	-	-	-	-	-	-	-	-	-	56.73 \pm 7.79	<0.185	5.08 \pm 0.35	3.74 \pm 1.08	>323.16	4.33 \pm 1.37	0.3 \pm 0.01	-	-	
199.09/2.17	174.49 \pm 3.1	<0.199	7.77 \pm 0.04	18.14 \pm 0.05	0.12 \pm 0.0	>875.25	64.83 \pm 1.17	0.0 \pm 0.0	-	-	133.94 \pm 5.25	<0.221	8.26 \pm 0.22	18.53 \pm 0.19	>605.62	48.13 \pm 1.95	0.28 \pm 0.01	-	-	
199.09/2.17	-	-	-	-	-	-	-	-	-	-	52.48 \pm 3.91	<0.209	10.42 \pm 0.22	3.81 \pm 0.41	>251.49	3.88 \pm 0.51	0.21 \pm 0.01	-	-	
199.09/2.17	50.84 \pm 3.84	<0.143	11.58 \pm 0.16	3.74 \pm 0.35	0.0 \pm 0.0	>356.27	3.69 \pm 0.45	0.0 \pm 0.0	-	-	11.1	0.28 \pm 0.01	-0.48 \pm 0.01	1.74 \pm 0.04	45.47 \pm 2.68	0.43 \pm 0.03	0	-	-	
177.3/-22.24	13.85	0.44 \pm 0.09	-0.39 \pm 0.25	2.3 \pm 0.47	0.34 \pm 0.28	42.01 \pm 2.11	0.88 \pm 0.78	2	-	-	-	-	-	-	-	0.15 \pm 0.53	3	-	-	
177.3/-22.24	27.45	0.76 \pm 0.05	4.0 \pm 0.21	4.81 \pm 0.89	0.0 \pm 0.0	51.56 \pm 4.09	3.67 \pm 0.79	0	-	-	-	-	-	-	-	1.91 \pm 0.14	2	-	-	
177.3/-22.24	-	-	-	-	-	-	-	-	-	-	-	-	-	-	-	5.23 \pm 0.33	4	-	-	
177.3/-22.24	-	-	-	-	-	-	-	-	-	-	-	-	-	-	-	4.72 \pm 0.52	4	-	-	
177.3/-22.24	34.57	3.4 \pm 0.31	9.56 \pm 0.09	3.43 \pm 0.17	0.04 \pm 0.02	35.76 \pm 1.21	8.27 \pm 0.91	1	-	-	42.15	1.13 \pm 0.11	10.47 \pm 0.16	3.45 \pm 0.15	66.27 \pm 2.33	4.62 \pm 0.88	1	-	-	
177.3/-22.24	-	-	-	-	-	-	-	-	-	-	3.05 \pm 0.21	<0.093	-22.94 \pm 0.13	5.17 \pm 0.29	>32.67	0.31 \pm 0.03	1.0 \pm 0.0	-	-	
177.3/-22.24	3.33 \pm 0.15	<0.093	-22.83 \pm 0.16	9.91 \pm 0.56	1.0 \pm 0.0	>35.66	0.95 \pm 0.07	1.0 \pm 0.0	-	-	2.1 \pm 0.09	<0.03	-8.57 \pm 0.64	47.69 \pm 1.07	>70.76	1.94 \pm 0.1	0.51 \pm 0.04	-	-	
177.3/-22.24	-	<0.109	-1.47 \pm 0.75	13.98 \pm 1.22	1.0 \pm 0.0	>45.82	2.0 \pm 0.29	0.5 \pm 0.18	-	-	-	-	-	-	-	0.44 \pm 0.14	0	-	-	
177.3/-22.24	-	-	-	-	-	-	-	-	-	-	6.76 \pm 1.73	<0.086	4.17 \pm 0.15	3.38 \pm 0.67	>78.34	0.61 \pm 0.03	0.61 \pm 0.03	-	-	
177.3/-22.24	51.41 \pm 2.48	<0.071	5.34 \pm 0.22	8.07 \pm 0.38	0.0 \pm 0.0	>726.96	8.05 \pm 0.54	0.44 \pm 0.1	-	-	8.44 \pm 1.07	<0.09	15.87 \pm 0.72	15.87 \pm 0.72	>93.34	2.6 \pm 0.35	0.36 \pm 0.03	-	-	
177.3/-22.24	20.37 \pm 0.98	<0.065	12.06 \pm 0.06	3.5 \pm 0.14	0.96 \pm 0.07	>311.64	2.02 \pm 0.13	0.7 \pm 0.15	-	-	23.59 \pm 2.95	<0.07	9.52 \pm 0.23	5.97 \pm 0.42	>336.31	2.73 \pm 0.39	0.27 \pm 0.04	-	-	
177.3/-22.24	8.06	0.18 \pm 0.02	-18.29 \pm 0.46	9.64 \pm 1.02	0.08 \pm 0.2	48.91 \pm 3.55	1.74 \pm 0.35	0	-	-	-	-	-	-	-	-	-	-	-	
206.72/8.44	5.44	0.07 \pm 0.01	5.22 \pm 0.71	11.8 \pm 1.59	0.0 \pm 0.0	80.46 \pm 32.83	1.3 \pm 0.59	1	-	-	8.98	0.22 \pm 0.0	-17.08 \pm 0.03	8.2 \pm 0.07	45.46 \pm 4.29	1.56 \pm 0.15	-	-	-	
206.72/8.44	1.85	0.05 \pm 0.01	39.86 \pm 0.53	5.56 \pm 1.21	0.0 \pm 0.0	37.99 \pm 8.62	0.19 \pm 0.07	2	-	-	13.88	0.07 \pm 0.0	5.09 \pm 0.11	12.16 \pm 0.25	205.28 \pm 9.07	3.4 \pm 0.49	1	-	-	
206.72/8.44	-	-	-	-	-	-	-	-	-	-	2.24	0.05 \pm 0.0	39.84 \pm 0.1	5.64 \pm 0.26	46.0 \pm 4.52	0.23 \pm 0.35	0.2	-	-	
206.72/8.44	3.13 \pm 0.54	<0.127	-16.08 \pm 0.31	4.14 \pm 0.74	0.0 \pm 0.0	>24.74	0.25 \pm 0.06	0.44 \pm 0.42	-	-	3.7 \pm 0.89	<0.107	-16.85 \pm 2.05	18.92 \pm 1.68	>34.54	1.36 \pm 0.35	0.5 \pm 0.41	-	-	
206.72/8.44	-	-	-	-	-	-	-	-	-	-	6.23 \pm 3.41	<0.038	-5.26 \pm 1.88	8.03 \pm 2.89	>162.18	0.97 \pm 0.64	1.0 \pm 0.0	-	-	
206.72/8.44	3.06 \pm 1.31	<0.058	-0.09 \pm 34.87	32.16 \pm 16.07	0.0 \pm 0.0	>52.42	1.91 \pm 1.26	0.46 \pm 0.39	-	-	-	-	-	-	-	-	-	-	-	
206.72/8.44	20.46 \pm 4.82	<0.077	1.09 \pm 0.24	10.87 \pm 0.97	0.71 \pm 0.14	>266.77	5.76 \pm 1.48	0.0 \pm 0.0	-	-	14.54 \pm 3.78	<0.072	0.76 \pm 0.73	7.63 \pm 0.92	>201.28	2.15 \pm 0.62	0.5 \pm 0.41	-	-	
206.72/8.44	3.36 \pm 1.82	<0.041	13.88 \pm 1.71	11.96 \pm 5.05	0.0 \pm 0.0	>81.94	0.78 \pm 0.53	1.0 \pm 0.0	-	-	-	-	-	-	-	-	-	-	-	
206.72/8.44	5.05 \pm 2.03	<0.033	33.78 \pm 10.02	34.87 \pm 6.65	0.0 \pm 0.0	>151.57	3.42 \pm 1.52	0.33 \pm 0.35	-	-	7.12 \pm 0.51	<0.041	15.39 \pm 0.61	15.2 \pm 1.97	>174.23	2.1 \pm 0.31	1.0 \pm 0.0	-	-	
206.72/8.44	-	-	-	-	-	-	-	-	-	-	-	-	-	-	-	-	-	-	-	
206.72/8.44	3.33 \pm 1.42	<0.041	37.78 \pm 1.06	13.04 \pm 3.2	0.33 \pm 0.37	>81.13	0.97 \pm 0.5	0.48 \pm 0.43	-	-	7.94 \pm 0.44	<0.035	33.76 \pm 0.62	20.27 \pm 1.98	>229.48	3.12 \pm 0.35	0.5 \pm 0.41			

TABLE 3 (CONT.)

l/b ($^{\circ}$)	pseudo-Voigt					Gaussian					F or O	NHI (10^{20} cm^{-2})	T _s (K)	F or O
	T _B (K)	τ (10^{-2})	V _{lsr} (km s^{-1})	ΔV (km s^{-1})	η	T _B (K)	τ (10^{-2})	V _{lsr} (km s^{-1})	ΔV (km s^{-1})					
209.24/-4.64	-	-	8.89±0.23	6.92±0.43	0.0±0.0	-	65.45	0.98±0.01	7.45±0.04	5.09±0.06	104.78±1.42	10.16±0.2	1	
209.24/-4.64	44.35	1.13±0.12	10.81±0.18	1.25±0.42	0.0±0.0	-	75.94	2.32±0.04	10.78±0.01	1.86±0.03	84.22±0.77	7.06±0.18	4	
209.24/-4.64	72.72	2.21±1.56	-	-	0.0±0.0	-	20.04	0.32±0.01	14.01±0.04	3.17±0.09	73.17±6.19	1.43±0.13	0	
209.24/-4.64	-	-	-	-	-	-	26.89	1.15±0.01	22.58±0.01	3.46±0.02	39.35±2.63	3.03±0.21	3	
209.24/-4.64	27.06	1.22±0.16	22.6±0.11	3.16±0.32	0.32±0.15	-	38.4±2.02	0.33±0.03	50.93±7.74	0.33±0.29	110.96±3.15	1.02±0.05	5	
209.24/-4.64	8.81	0.19±0.11	37.69±0.46	1.71±1.16	0.0±0.0	-	23.68	0.24±0.01	37.77±0.03	1.93±0.07	81.27±2.18	0.79±0.04	2	
209.24/-4.64	13.48	0.33±0.1	40.16±0.3	1.71±0.83	1.0±0.0	-	22.84	0.33±0.01	40.18±0.02	1.53±0.04	-	-	-	
209.24/-4.64	159.0±10.63	<0.206	8.69±0.05	8.31±0.17	0.44±0.01	-	-	-	-	-	-	-	-	
209.24/-4.64	37.48±1.26	<0.15	20.29±0.14	7.8±0.24	0.26±0.22	-	83.56±2.08	<0.175	9.28±0.1	10.95±0.14	>477.29	17.75±0.5	0.28±0.03	
209.24/-4.64	-	-	-	-	-	-	-	-	-	-	-	-	-	
209.24/-4.64	-	-	-	-	-	-	43.59±2.07	<0.167	21.41±0.11	5.85±0.17	>260.55	4.94±0.27	0.22±0.03	
209.24/-4.64	-	-	-	-	-	-	17.11±0.55	<0.095	25.67±0.2	46.12±0.37	>179.88	15.31±0.51	0.39±0.04	
209.24/-4.64	23.14±1.34	<0.129	38.62±0.14	6.53±0.28	0.0±0.0	-	-	-	-	-	-	-	-	
209.24/-4.64	28.43±1.06	<0.155	39.79±0.54	28.19±0.79	0.0±0.0	-	35.66±0.43	<0.089	43.16±0.09	18.34±0.18	>398.6	12.69±0.2	0.49±0.04	
209.24/-4.64	16.63±1.08	<0.121	46.71±0.27	10.62±0.58	0.0±0.0	-	-	-	-	-	-	-	-	
209.24/-4.64	3.91	0.16±0.06	-14.09±0.5	3.04±1.26	0.22±1.33	-	4.94	0.22±0.01	-13.76±0.09	4.26±0.17	25.01±6.7	0.45±0.12	-	
174.77/-5.97	21.63	0.49±0.12	-8.46±0.37	4.14±1.37	1.0±0.0	-	31.5	0.44±0.03	-8.73±0.04	3.15±0.14	59.46±4.56	1.59±0.19	-	
174.77/-5.97	-	-	-	-	-	-	24.17	0.2±0.05	-2.9±2.33	8.54±1.49	190.33±77.74	6.34±1.53	-	
174.77/-5.97	18.93	0.54±0.05	1.32±0.36	6.52±0.86	0.0±0.0	-	-	-	-	-	-	-	-	
174.77/-5.97	-	-	-	-	-	-	28.98	0.49±0.16	1.97±0.19	5.32±0.6	74.82±2.98	3.74±1.34	-	
174.77/-5.97	28.02	0.58±0.1	5.84±0.11	1.57±0.32	0.0±0.0	-	23.66	0.6±0.02	5.85±0.02	1.65±0.05	52.44±2.45	1.01±0.06	-	
174.77/-5.97	1.45±0.34	<0.089	-28.16±0.42	4.33±1.24	0.0±0.0	-	-	-	-	-	-	-	-	
174.77/-5.97	1.64±0.79	<0.091	-20.0±0.51	4.38±1.63	0.17±1.97	-	-	-	-	-	-	-	-	
174.77/-5.97	16.69±0.88	<0.121	-13.61±0.21	36.43±0.54	0.0±0.0	-	18.3±0.26	<0.117	-14.11±0.29	34.79±0.34	>155.88	12.35±0.21	0.19±0.03	
174.77/-5.97	-	-	-	-	-	-	-	-	-	-	-	-	-	
174.77/-5.97	28.31±1.77	<0.132	-9.58±0.17	7.93±0.36	0.0±0.0	-	27.07±2.64	<0.137	-10.45±0.18	7.24±0.19	>197.73	3.8±0.38	0.33±0.04	
174.77/-5.97	59.81±1.74	<0.158	0.91±0.08	11.2±0.2	0.0±0.0	-	-	-	-	-	-	-	-	
174.77/-5.97	-	-	-	-	-	-	-	-	-	-	-	-	-	
174.77/-5.97	-	-	-	-	-	-	20.6±13.3	<0.13	2.51±3.69	13.31±2.33	>158.51	5.32±3.56	0.51±0.04	
203.85/5.82	21.05	0.38±0.05	6.36±0.2	3.33±0.67	0.68±0.36	-	16.58±4.09	<0.124	5.57±0.17	4.28±0.47	>133.38	1.38±0.37	0.43±0.04	
203.85/5.82	3.35	0.14±0.03	36.11±0.2	2.63±0.44	0.0±0.0	-	15.53	0.29±0.0	6.56±0.03	4.38±0.06	61.7±18.71	1.52±0.46	-	
203.85/5.82	2.47±0.17	<0.046	-8.54±0.12	3.67±0.47	1.0±0.0	-	2.99	0.14±0.0	36.13±0.04	2.55±0.09	22.88±2.13	0.16±0.02	-	
203.85/5.82	-	-	-	-	-	-	2.04±0.17	<0.047	-8.75±0.12	3.5±0.35	>43.87	0.14±0.02	-	
203.85/5.82	13.96±6.4	<0.119	7.88±0.36	3.98±1.53	0.79±0.63	-	3.35±0.98	<0.045	2.35±2.39	18.83±3.84	>74.07	1.22±0.43	0.20±0.0	
203.85/5.82	-	-	-	-	-	-	-	-	-	-	-	-	-	
203.85/5.82	13.96±6.4	<0.119	7.88±0.36	3.98±1.53	0.79±0.63	-	15.67±2.41	<0.131	9.14±0.61	5.87±0.77	>119.61	1.79±0.36	0.44±0.41	
203.85/5.82	-	-	-	-	-	-	-	-	-	-	-	-	-	
203.85/5.82	9.52±5.29	<0.204	10.44±1.72	4.17±1.53	0.0±0.0	-	-	-	-	-	-	-	-	
203.85/5.82	13.12±0.52	<0.218	10.58±0.41	32.71±0.75	0.06±0.05	-	12.95±1.04	<0.05	16.65±0.31	40.93±0.53	>256.62	10.28±0.84	0.55±0.41	
203.85/5.82	-	-	-	-	-	-	10.92±0.61	<0.082	25.18±0.13	8.71±0.34	>133.99	1.85±0.13	1.0±0.0	
203.85/5.82	12.29±0.46	<0.082	25.12±0.12	9.14±0.33	0.0±0.0	-	8.88±0.36	<0.062	36.73±0.19	12.57±0.38	>143.59	2.17±0.11	0.55±0.41	
203.85/5.82	13.17±0.27	<0.056	36.46±0.19	15.03±0.33	0.43±0.04	-	-	-	-	-	-	-	-	
172.23/-25.66	5.92	0.11±0.35	-0.92±1.11	2.28±2.17	0.0±0.0	-	20.97	0.36±0.0	0.8±0.06	4.18±0.1	69.36±9.8	2.01±0.29	-	
172.23/-25.66	-	-	-	-	-	-	-	-	-	-	-	-	-	
172.23/-25.66	18.33	0.38±0.09	1.36±1.48	3.8±2.67	0.0±0.0	-	2.39	0.11±0.06	5.3±1.35	3.16±1.79	22.99±46.32	0.16±0.35	0.55±0.31	
172.23/-25.66	-	-	-	-	-	-	14.61	0.27±0.14	6.75±0.05	1.88±0.29	61.76±3.68	0.62±0.34	1	
172.23/-25.66	11.25	0.39±0.05	6.54±0.19	2.63±0.58	0.21±1.09	-	16.27	0.31±0.01	9.93±0.05	2.9±0.08	61.04±7.86	1.07±0.14	0.0±0.0	
172.23/-25.66	11.57	0.33±0.06	10.02±0.17	2.33±0.48	0.57±0.44	-	0.66±0.04	<0.027	-40.32±2.18	32.02±3.94	>24.48	0.41±0.06	1.0±0.0	
172.23/-25.66	-	-	-	-	-	-	-	-	-	-	-	-	-	
172.23/-25.66	0.67±0.04	<0.019	-38.84±2.33	35.81±4.8	0.08±0.47	-	-	-	-	-	-	-	-	
172.23/-25.66	3.38±0.35	<0.071	-0.55±1.18	28.06±1.61	0.0±0.0	-	3.6±0.49	<0.069	-0.27±0.97	30.68±1.75	>52.23	2.14±0.31	0.55±0.31	
172.23/-25.66	12.03±4.11	<0.089	3.58±0.12	3.53±0.9	1.0±0.0	-	23.5±4.62	<0.078	3.76±0.82	5.8±0.9	>300.58	2.64±0.66	0.0±0.0	
172.23/-25.66	24.32±4.35	<0.072	5.34±0.09	11.92±0.51	0.08±0.08	-	16.02±3.06	<0.073	5.18±0.16	13.51±0.94	>219.19	4.2±0.85	0.0±0.0	
172.23/-25.66	11.71±2.03	<0.054	10.49±0.18	3.79±0.3	0.0±0.0	-	11.96±2.9	<0.059	10.9±0.46	4.93±0.35	>203.64	1.14±0.29	0.49±0.29	
206.48/5.48	2.94	0.09±0.03	-2.79±0.4	2.77±0.83	0.0±0.0	-	2.57	0.08±0.0	-2.74±0.08	3.09±0.18	33.38±3.1	0.17±0.02	0	
206.48/5.48	20.93	0.59±0.07	7.33±0.11	2.32±0.31	0.25±0.26	-	22.01	0.56±0.01	7.32±0.01	2.52±0.03	51.32±0.83	1.4±0.03	1	
206.48/5.48	2.06	0.08±0.04	41.4±0.46	1.86±1.03	0.0±0.0	-	2.11	0.08±0.01	41.38±0.07	1.94±0.15	27.38±5.03	0.08±0.02	0.49±0.43	
206.48/5.48	15.4±0.86	<0.117	5.35±0.1	11.01±0.38	0.39±0.15	-	13.22±0.25	<0.129	5.2±0.08	10.03±0.23	>102.11	2.58±0.08	0.17±0.25	
206.48/5.48	13.28±0.82	<0.057	19.07±0.6	39.13±0.61	0.09±0.04	-	16.17±0.17	<0.057	19.0±0.07	39.88±0.27	>282.11	12.51±0.16	0.17±0.25	
206.48/5.48	6.43±0.74	<0.113	22.54±0.21	6.31±0.91	1.0±0.0	-	4.41±0.29	<0.125	22.46±0.15	4.28±0.35	>35.27	0.37±0.04	1.0±0.0	
206.48/5.48	10.26±1.07	<0.077	29.5±0.09	6.33±0.43	0.13±0.41	-	10.03±0.32	<0.077	29.4±0.09	6.57±0.27	>130.4	1.28±0.07	1.0±0.0	
206.48/5.48	11.94±0.5	<0.075	39.38±0.37	15.11±0.6	0.0±0.0	-	10.81±0.21	<0.088	39.71±0.19	14.21±0.45	>122.58	2.98±0.11	0.17±0.25	

TABLE 3 (CONT)

l/b	pseudo-Voigt										Gaussian									
	T_B (K)	τ (10^{-2})	V_{var}^{-1} (km s^{-1})	ΔV (km s^{-1})	η	T_s (K)	N_{HI} (10^{20} cm^{-2})	$F^{\text{or } O}$	T_B (K)	τ (10^{-2})	V_{var}^{-1} (km s^{-1})	ΔV (km s^{-1})	T_s (K)	N_{HI} (10^{20} cm^{-2})	$F^{\text{or } O}$					
172.08/2.44	54.15	1.66±0.22	-17.96±0.38	3.56±0.49	0.0±0.0	66.86±0.75	7.67±1.47	1	47.21	1.67±0.02	-17.93±0.03	3.58±0.04	58.16±2.27	6.74±0.28	5					
172.08/2.44	54.06	1.33±0.86	-15.23±0.66	1.64±1.31	0.0±0.0	73.5±1.62	3.12±3.32	0	44.01	1.36±0.04	-15.18±0.03	1.65±0.07	59.21±5.31	2.63±0.27	0					
172.08/2.44	88.32	5.98±7.62	-12.35±0.39	2.37±1.44	0.0±0.0	88.5±4.9	24.33±34.37	2	56.47	6.79±0.42	-12.39±0.02	2.16±0.07	59.54±5.63	16.97±2.0	4					
172.08/2.44	30.27	0.68±0.19	-8.78±1.06	3.09±4.11	0.0±0.0	61.36±5.39	2.49±3.39	3	17.96	0.69±0.01	-9.02±0.08	3.97±0.42	36.03±7.33	1.93±0.45	3					
172.08/2.44	55.95	1.26±0.2	-4.84±0.58	0.0±0.0	0.0±0.0	78.1±1.19	6.9±2.11	4	28.99	1.23±0.02	-4.79±0.05	3.52±0.07	40.97±2.1	3.4±0.22	1					
172.08/2.44	38.7	0.29±0.04	2.88±0.6	6.41±2.02	0.0±0.0	153.72±5.45	5.61±1.92	6	42.39	0.29±0.0	3.03±0.06	6.67±0.2	168.4±6.64	6.33±0.32	2					
172.08/2.44	12.81	0.62±0.11	7.47±0.16	2.2±0.43	0.0±0.0	27.73±2.12	0.73±0.2	5	14.22	0.61±0.01	7.51±0.01	2.13±0.04	31.15±1.7	0.79±0.05	6					
172.08/2.44	-	-	-	-	-	-	-	-	54.46±12.39	<0.217	-16.46±0.89	9.26±0.63	>250.91	9.78±2.32	0.23±0.01					
172.08/2.44	-	-	-	-	-	-	-	-	8.79±0.28	<0.261	-12.24±0.24	44.56±0.62	>33.7	7.6±0.26	0.38±0.01					
172.08/2.44	148.22±5.14	<0.256	-10.6±0.06	13.28±0.19	0.4±0.01	>579.98	46.4±1.72	0.0±0.0	-	-	-	-	-	-	-					
172.08/2.44	-	<0.151	7.8±0.24	8.14±0.28	0.0±0.0	>104.48	2.49±0.14	0.4±0.01	99.17±5.55	<0.231	-8.28±0.43	11.17±0.53	>428.55	21.49±1.58	0.36±0.01					
172.08/2.44	172.08/2.44	-	-	-	0.0±0.0	-	-	-	15.66±0.93	<0.151	7.98±0.33	7.99±0.38	>103.48	2.43±0.18	0.23±0.01					
190.74/2.94	39.12	0.85±0.07	-5.12±0.18	5.5±0.47	0.39±0.13	68.33±4.12	7.38±1.06	1	52.66	0.83±0.0	-5.2±0.01	5.77±0.03	93.37±1.47	8.66±0.18	0					
190.74/2.94	42.13	0.85±0.07	6.11±0.21	8.03±0.61	0.0±0.0	73.57±2.16	9.73±1.09	2	73.17	0.86±0.0	6.04±0.01	8.28±0.04	126.85±1.32	17.42±0.22	1					
190.74/2.94	6.62	0.12±0.03	15.66±0.65	4.21±1.43	0.0±0.0	58.5±3.93	0.57±0.24	0	2.97	0.12±0.0	15.78±0.05	4.17±0.12	26.26±7.16	0.27±0.07	2					
190.74/2.94	2.53	0.1±0.04	28.33±0.37	2.57±0.74	0.0±0.0	26.57±3.45	0.13±0.07	3	2.93	0.1±0.0	28.39±0.04	2.7±0.1	30.74±5.66	0.13±0.02	3					
190.74/2.94	2.9±0.11	<0.043	-63.76±0.11	8.02±0.43	0.83±0.13	>67.62	0.63±0.05	1.0±0.0	2.55±0.08	<0.035	-63.59±0.11	8.97±0.28	>71.8	0.43±0.02	1.0±0.0					
190.74/2.94	4.1±0.32	<0.084	-14.75±0.14	5.04±0.37	0.0±0.0	>48.89	0.4±0.04	0.5±0.17	-	-	-	-	-	-	-					
190.74/2.94	21.57±3.04	<0.117	-4.24±0.24	7.43±0.59	0.0±0.0	>184.65	3.11±0.5	0.03±0.05	3.9±0.28	<0.069	-13.78±0.18	5.76±0.49	>56.35	0.44±0.05	0.5±0.17					
190.74/2.94	-	-	-	-	-	-	-	-	16.73±0.82	<0.115	-1.57±0.15	5.37±0.32	>145.98	1.74±0.13	0.53±0.16					
190.74/2.94	-	-	-	-	-	-	-	-	34.75±1.36	<0.118	7.86±0.11	28.74±0.23	>205.26	19.38±0.77	0.2±0.1					
190.74/2.94	58.81±0.96	<0.101	8.45±0.2	23.2±0.2	0.14±0.01	>583.4	28.28±0.53	0.52±0.16	-	-	-	-	-	-	-					
190.74/2.94	-	-	-	-	-	-	-	-	21.53±0.92	<0.095	14.51±0.14	10.13±0.42	>226.79	4.23±0.25	0.38±0.15					
179.87/-2.83	29.87	0.99±0.12	-15.39±0.09	1.83±0.19	0.0±0.0	47.53±0.68	1.68±0.27	0	13.75	1.01±0.01	-15.4±0.01	1.86±0.02	21.63±1.04	0.79±0.04	1					
179.87/-2.83	76.94	0.38±0.03	-9.35±0.84	11.78±1.25	0.0±0.0	243.38±1.69	20.88±2.8	3	58.89	0.4±0.0	-9.72±0.05	10.2±0.11	178.6±5.55	14.04±0.48	0					
179.87/-2.83	31.0	0.29±0.35	1.39±0.15	4.83±0.33	0.0±0.0	9.16±1.33	9.16±1.33	1	24.97	2.66±0.02	1.36±0.01	5.09±0.03	26.55±1.52	7.06±0.14	2					
179.87/-2.83	20.75	0.39±0.04	7.69±0.27	3.16±0.55	0.0±0.0	64.24±2.23	1.55±0.32	2	10.34	0.38±0.01	7.74±0.03	3.14±0.06	32.7±5.85	0.76±0.14	3					
179.87/-2.83	11.49±0.15	<0.053	-22.7±0.08	9.62±0.18	1.0±0.0	>216.7	3.16±0.07	0.47±0.09	-	<0.058	-21.21±0.14	9.52±0.32	>170.0	1.83±0.09	0.47±0.29					
179.87/-2.83	-	-	-	-	-	-	-	-	9.9±0.36	<0.155	-8.54±0.31	39.62±1.05	>45.62	5.42±0.53	0.31±0.26					
179.87/-2.83	53.02±1.12	<0.212	-2.2±0.1	6.52±0.3	1.0±0.0	>250.0	9.9±0.5	0.28±0.07	76.18±1.91	<0.123	0.48±0.27	16.24±0.4	>618.38	23.99±0.84	0.33±0.16					
179.87/-2.83	59.74±0.96	<0.088	6.15±0.12	10.39±0.16	0.19±0.02	>680.56	13.11±0.31	0.23±0.05	-	-	-	-	-	-	-					
179.87/-2.83	12.42	0.33±0.04	-10.86±0.44	6.86±1.27	0.54±0.26	44.18±17.19	2.43±1.12	0	28.58±2.57	<0.08	7.85±0.09	4.99±0.25	>369.78	2.86±0.29	0.23±0.24					
193.99/5.1	-	-	-	-	-	-	-	-	24.74	0.33±0.0	-10.86±0.03	7.43±0.07	88.03±2.71	4.15±0.14	0					
193.99/5.1	10.44	0.2±0.06	11.54±0.25	2.16±0.73	0.0±0.0	57.61±55.36	0.48±0.5	1	5.05	0.18±0.0	5.0±0.04	2.88±0.09	30.68±6.47	0.31±0.07	2					
193.99/5.1	20.6	0.19±0.04	12.2±0.79	13.24±2.34	0.0±0.0	119.02±95.52	5.72±17.24	2	31.64	0.27±0.0	12.6±0.05	8.94±0.13	133.71±45.17	6.36±2.16	1					
193.99/5.1	13.65	0.33±0.09	23.63±0.31	2.45±0.74	0.0±0.0	48.58±6.37	0.77±0.33	4	14.08	0.35±0.01	23.56±0.02	2.65±0.05	47.88±3.85	0.86±0.07	3					
193.99/5.1	7.01	0.18±0.1	27.75±0.66	2.5±1.45	0.0±0.0	42.53±7.49	0.37±0.31	3	7.42	0.17±0.0	27.88±0.04	2.88±0.09	47.49±7.74	0.46±0.08	4					
193.99/5.1	14.11±4.9	<0.13	-12.03±0.38	7.94±0.72	1.0±0.0	>108.22	3.21±1.15	0.46±0.08	-	-	-	-	-	-	-					
193.99/5.1	38.63±3.46	<0.382	-4.74±0.12	6.92±0.51	0.22±0.22	>101.16	5.79±0.85	0.52±0.08	5.49±1.25	<0.119	-9.59±3.62	25.13±3.03	>46.02	2.68±0.69	0.52±0.29					
193.99/5.1	193.99/5.1	-	-	-	-	-	-	-	34.5±2.77	<0.389	-4.48±1.24	6.03±0.26	>88.58	4.04±0.37	0.59±0.23					
193.99/5.1	32.25±40.76	<0.123	6.99±6.15	13.34±5.61	0.0±0.0	>261.69	8.33±11.12	0.7±0.08	34.71±3.08	<0.129	6.11±1.31	12.71±3.03	>268.05	8.56±2.17	0.27±0.18					
193.99/5.1	30.83±19.62	<0.11	18.31±0.7	7.76±1.7	0.0±0.0	>280.43	4.64±3.12	0.56±0.08	-	-	-	-	-	-	-					
193.99/5.1	32.68±6.46	<0.17	24.76±1.15	9.07±1.24	0.0±0.0	>192.61	5.75±1.18	0.18±0.05	16.38±9.27	<0.114	18.21±0.33	5.2±0.99	>143.75	1.65±0.99	0.43±0.3					
193.99/5.1	3.97±0.4	<0.043	35.11±1.29	14.79±1.41	0.0±0.0	>91.94	1.14±0.16	0.54±0.09	41.96±4.16	<0.2	23.18±0.95	10.6±1.17	>209.35	8.63±1.28	0.26±0.18					
193.99/5.1	-	-	-	-	-	-	-	-	-	-	-	-	-	-	-					
176.36/-24.24	17.54	0.44±0.04	3.91±0.38	7.4±0.6	0.06±0.11	49.27±33.91	3.23±2.26	2	12.0	<0.038	33.88±1.16	13.99±1.29	>97.99	1.01±0.14	0.49±0.28					
176.36/-24.24	26.44	0.7±0.31	1.99±0.52	0.37±0.59	0.0±0.0	52.53±3.71	1.66±0.96	0	23.49	0.45±0.0	4.18±0.03	7.96±0.07	33.12±10.45	2.31±0.73	2					
176.36/-24.24	25.98	0.87±0.12	11.23±0.45	3.36±0.59	0.0±0.0	44.72±6.14	2.53±0.66	1	28.0	0.68±0.03	9.11±0.02	1.93±0.05	47.62±3.4	1.2±0.08	1					
176.36/-24.24	0.74±0.11	<0.026	-22.71±4.64	53.17±5.95	0.0±0.0	>28.02	0.76±0.14	0.85±0.13	29.0	0.88±0.01	11.3±0.04	3.33±0.05	49.55±4.39	2.83±0.26	0					
176.36/-24.24	5.83±0.6	<0.031	-5.66±0.43	13.17±0.93	1.0±0.0	>186.69	2.2±0.28	0.43±0.2	1.74±0.08	<0.037	-8.59±0.68	58.31±1.74	>47.47	1.97±0.11	0.51±0.18					
176.36/-24.24	18.95±4.74	<0.062	0.33±0.08	3.63±0.47	1.0±0.0	>305.81	1.97±0.55	0.35±0.15	23.44±3.7	<0.069	0.73±0.17	3.3±0.22	>338.07	1.5±0.26	0.16±0.11					
176.36/-24.24	-	-	-	-	-	-	-	-	10.7±0.34	<0.084	2.35±0.13	20.43±0.35	>127.71	4.24±0.15	0.6±0.15					
176.36/-24.24	60.79±16.4	<0.072	4.47±0.11	5.06±0.26	0.0±0.0	>846.01	5.97±1.64	0.0±0.0	60.27±5.13	<0.07	4.35±0.08	4.33±0.32	>861.08	5.06±0.57	0.0±0.0					
176.36/-24.24	86.85±7.9	<0.078	10.13±0.19	4.63±0.26	0.32±0.03	>1117.35	8.98±0.96	0.0±0.0	64.87±5.62	<0.076	9.72±0.23	5.22±0.29	>853.93	6.56±0.67	0.0±0.0					

3

Dust – gas relations and OH abundance

Cosmic dust is ubiquitous and strongly correlated with the multiple gas phases of the ISM. The extinction and emission of dust grains have been recognized as effective proxies for the total hydrogen column density (N_{H}), regardless whether the gas is in the form of H_2 or HI (Jenkins & Savage, 1974, Bohlin et al., 1978, Diplas & Savage, 1994, Rachford et al., 2009, Planck Collaboration et al., 2014a). In particular, comparing dust extinction and emission with the amounts of gas derived from the traditional spectral emission line tracers of HI and CO have revealed an extra gas component, which is often referred to as “dark gas”.

Overall linear relationships between dust and gas with constant scaling factors have often been used to convert dust quantities (intensity, extinction, optical depth) to total gas column densities (Bohlin et al., 1978, Jones et al., 2013, Liszt, 2014a, Fukui et al., 2015, Lenz et al., 2017). However, the actual dust/gas mass ratios have been observed to vary significantly from cloud to cloud (Boulanger & Perault, 1988, Heiles et al., 1988, Planck Collaboration et al., 2011a). In addition, variations in the dust-gas conversion factors have been observed in numerous recent studies (Rachford et al., 2002, Vuong et al., 2003, Planck Collaboration et al., 2014a, 2015, Okamoto

et al., 2017, Remy et al., 2017, 2018). All these variations may come from several sources such as changes in the properties of dust grains, different metallicities in different environments, and changes in gas-to-dust mass ratio (e.g. Watson et al., 2011, Planck Collaboration et al., 2014a, Roman-Duval et al., 2014, Hasenberger et al., 2016).

In this Chapter, I used various data sets of gas and dust (opacity-corrected HI column densities from the Arecibo Millennium Survey and 21-SPONGE, newly published Millennium Survey OH data, follow-up CO emission observations, thermal dust emission data from the *Planck* satellite (Planck Collaboration et al., 2014a), new dust reddening maps from Pan-STARRS 1 and 2MASS (Green et al., 2018) to address the questions of which dust quantity traces more significantly the total gas column density, and whether the increase observed in Planck Collaboration et al. 2014a of dust opacity ($\sigma_{353} = \tau_{353}/N_{\text{H}}$) can be explained by dust evolution from diffuse to dense gas regimes, or by the presence of dark gas. In addition, well-constrained gas column densities in the low-to-intermediate column density range $(1\text{--}30) \times 10^{20} \text{ cm}^{-2}$ allow me to evaluate the scaling relations between dust and gas in this regime, then combine with HI and OH data to derive H_2 column densities and the OH abundance ratio $X_{\text{OH}} = N_{\text{OH}}/N_{\text{H}_2}$.

This Chapter presents an article published in July 2018 in *The Astrophysical Journal*. I was the first author in this work: I carried out all data reduction and analysis, largely determined the scientific directions of the paper, led the discussion, and carried out the writing. The co-authors provided comments, gave feedback on the quality of the analysis, and polished the English.



Dust–Gas Scaling Relations and OH Abundance in the Galactic ISM

Hiep Nguyen^{1,2}, J. R. Dawson^{1,2}, M.-A. Miville-Deschênes^{3,4}, Ningyu Tang⁵, Di Li^{5,6}, Carl Heiles⁷, Claire E. Murray⁸, Snežana Stanimirović⁹, Steven J. Gibson¹⁰, N. M. McClure-Griffiths¹¹, Thomas Troland¹², L. Bronfman¹³, and R. Finger¹⁴

¹ Department of Physics and Astronomy and MQ Research Centre in Astronomy, Astrophysics and Astrophotonics, Macquarie University, NSW 2109, Australia
van-hiep.nguyen@hdr.mq.edu.au

² Australia Telescope National Facility, CSIRO Astronomy and Space Science, P.O. Box 76, Epping, NSW 1710, Australia

³ Institut d’Astrophysique Spatiale, CNRS, Univ. Paris-Sud, Université Paris-Saclay, Bât. 121, F-91405, Orsay Cedex, France

⁴ Laboratoire AIM, Paris-Saclay, CEA/IRFU/DAp—CNRS—Université Paris Diderot, F-91191, Gif-sur-Yvette Cedex, France

⁵ CAS Key Laboratory of FAST, NAOC, Chinese Academy of Sciences, People’s Republic of China

⁶ University of Chinese Academy of Sciences, Beijing 100049, People’s Republic of China

⁷ Department of Astronomy, University of California, Berkeley, 601 Campbell Hall 3411, Berkeley, CA 94720-3411, USA

⁸ Space Telescope Science Institute, 3700 San Martin Drive, Baltimore, MD 21218, USA

⁹ Department of Astronomy, University of Wisconsin-Madison, 475 North Charter Street, Madison, WI 53706, USA

¹⁰ Department of Physics and Astronomy, Western Kentucky University, Bowling Green, KY 42101, USA

¹¹ Research School of Astronomy and Astrophysics, Australian National University, Canberra, ACT 2611, Australia

¹² Department of Physics and Astronomy, University of Kentucky, Lexington, Kentucky 40506, USA

¹³ Departamento de Astronomía, Universidad de Chile, Casilla 36, Santiago de Chile, Chile

¹⁴ Astronomy Department, Universidad de Chile, Camino El Observatorio 1515, 1058 Santiago, Chile

Received 2018 February 19; revised 2018 May 21; accepted 2018 May 24; published 2018 July 20

Abstract

Observations of interstellar dust are often used as a proxy for total gas column density N_{H} . By comparing *Planck* thermal dust data (Release 1.2) and new dust reddening maps from Pan-STARRS 1 and 2MASS, with accurate (opacity-corrected) H I column densities and newly published OH data from the Arecibo Millennium survey and 21-SPONGE, we confirm linear correlations between dust optical depth τ_{353} , reddening $E(B - V)$, and the total proton column density N_{H} in the range $(1\text{--}30) \times 10^{20} \text{ cm}^{-2}$, along sightlines with no molecular gas detections in emission. We derive an $N_{\text{H}}/E(B - V)$ ratio of $(9.4 \pm 1.6) \times 10^{21} \text{ cm}^{-2} \text{ mag}^{-1}$ for purely atomic sightlines at $|b| > 5^\circ$, which is 60% higher than the canonical value of Bohlin et al. We report a $\sim 40\%$ increase in opacity $\sigma_{353} = \tau_{353}/N_{\text{H}}$, when moving from the low column density ($N_{\text{H}} < 5 \times 10^{20} \text{ cm}^{-2}$) to the moderate column density ($N_{\text{H}} > 5 \times 10^{20} \text{ cm}^{-2}$) regime, and suggest that this rise is due to the evolution of dust grains in the atomic interstellar medium. Failure to account for H I opacity can cause an additional apparent rise in σ_{353} of the order of a further $\sim 20\%$. We estimate molecular hydrogen column densities N_{H_2} from our derived linear relations, and hence derive the OH/ H_2 abundance ratio of $X_{\text{OH}} \sim 1 \times 10^{-7}$ for all molecular sightlines. Our results show no evidence of systematic trends in OH abundance with N_{H_2} in the range $N_{\text{H}_2} \sim (0.1\text{--}10) \times 10^{21} \text{ cm}^{-2}$. This suggests that OH may be used as a reliable proxy for H_2 in this range, which includes sightlines with both CO-dark and CO-bright gas.

Key words: dust, extinction – ISM: clouds – ISM: molecules

1. Introduction

Observations of neutral hydrogen in the interstellar medium (ISM) have historically been dominated by two radio spectral lines: the 21 cm line of atomic hydrogen (H I) and the microwave emission from carbon monoxide (CO), particularly the CO($J = 1\text{--}0$) line. The former provides direct measurements of the warm neutral medium (WNM), and the cold neutral medium (CNM), which is the precursor to molecular clouds. The latter is widely used as a proxy for molecular hydrogen (H_2), often via the use of an empirical “X-factor,” (e.g., Bolatto et al. 2013). The processes by which CNM and molecular clouds form from warm atomic gas sows the seeds of structure into clouds, laying the foundations for star formation. Being able to observationally track the ISM through this transition is of key importance.

However, there is strong evidence for gas not seen in either H I or CO. This undetected material is often called “dark gas,” following Grenier et al. (2005). These authors found an excess of diffuse gamma-ray emission from the Local ISM, with respect to the expected flux due to cosmic-ray interactions with the gas mass estimated from H I and CO. Similar conclusions have been reached using many different tracers, including

γ -rays (e.g., Abdo et al. 2010; Ackermann et al. 2012, 2011), infrared emission from dust (e.g., Blitz et al. 1990; Reach et al. 1994; Douglas & Taylor 2007; Planck Collaboration et al. 2011, 2014a), dust extinction (e.g., Paradis et al. 2012; Lee et al. 2015), C II emission (Pineda et al. 2013; Langer et al. 2014; Tang et al. 2016), and OH 18 cm emission and absorption (e.g., Wannier et al. 1993; Liszt & Lucas 1996; Barriault et al. 2010; Allen et al. 2012, 2015; Engelke & Allen 2018).

While a minority of studies have suggested that cold, optically thick H I could account for almost all the missing gas mass (Fukui et al. 2015), CO-dark H_2 is generally expected to be a major constituent, particularly in the envelopes of molecular clouds (e.g., Lee et al. 2015). In diffuse molecular regions, H_2 is effectively self-shielded, but CO is typically photodissociated (Tielens & Hollenbach 1985a, 1985b; van Dishoeck & Black 1988; Wolfire et al. 2010; Glover & Mac Low 2011; Lee et al. 2015; Glover & Smith 2016), meaning that CO lines are a poor tracer of H_2 in such environments. Indeed *Herschel* observations of C II suggest that between 20%–75% of the H_2 in the Galactic plane may be CO-dark (Pineda et al. 2013).

For the atomic medium, the mass of warm HI can be computed directly from measured line intensities under the optically thin assumption. However, cold HI with spin temperature $T_s \lesssim 100$ K suffers from significant optical depth effects, leading to an underestimation of the total column density. This difficulty is generally addressed by combining HI absorption and emission profiles observed toward (and immediately adjacent to) bright, compact continuum background sources. Such studies find that the optically thin assumption underestimates the true HI column by no more than a few tens of percent along most Milky Way sightlines (e.g., Dickey et al. 1983, 2000, 2003; Heiles & Troland 2003a, 2003b; Liszt 2014a; Lee et al. 2015); though, the fraction missed in some localized regions may be much higher (Bihr et al. 2015).

Since dust and gas are generally well mixed, absorption due to dust grains has been widely used as a proxy for total gas column density. Early work (e.g., Savage & Jenkins 1972; Bohlin et al. 1978) observed Ly α and H₂ absorption in stellar spectra to calibrate the relationship between total hydrogen column density N_H , and the color excess $E(B - V)$. Similar work was carried out by comparing X-ray absorption with optical extinction, A_V (Reina & Tarengi 1973, Gorenstein 1975). Bohlin et al.’s value of $N_H/E(B - V) = 5.8 \times 10^{21} \text{ cm}^{-2} \text{ mag}^{-1}$ has become a widely accepted standard.

Dust emission is also a powerful tool and requires no background source population. The dust emission spectrum in the bulk of the ISM peaks in the FIR-to-millimeter range, and arises mostly from large grains in thermal equilibrium with the ambient local radiation field (Draine 2003, Draine & Li 2007). It has long been recognized that FIR dust emission could potentially be a better tracer of N_H than HI and CO (de Vries et al. 1987, Heiles et al. 1988, Blitz et al. 1990; Reach et al. 1994). An excess of dust intensity and/or optical depth above a linear correlation with N_H (as measured by HI and CO) is typically found in the range $A_V = 0.3\text{--}2.7$ mag (Planck Collaboration et al. 2011, 2014a, 2014b; Martin et al. 2012), consistent with the range where CO-dark H₂ can exist. Alternative explanations cannot be definitively ruled out, however. These include (1) the evolution of dust grains across the gas phases, (2) underestimation of the total gas column due to significant cold HI opacity, and (3) insufficient sensitivity for CO detection. It has also been impossible to rule out remaining systematic effects in the *Planck* data or bias in the estimate of τ_{353} introduced by the choice of the modified blackbody model.

In this study, we examine the correlations between accurately derived HI column densities and dust-based proxies for N_H . We make use of opacity-corrected HI column densities derived from two surveys: the Arecibo Millennium Survey (MS, Heiles & Troland 2003b, hereafter HT03), and 21-SPONGE (Murray et al. 2015), both of which used on-/off-source measurements toward extragalactic radio continuum sources to derive accurate physical properties for the atomic ISM. We also make use of archival OH data from the Millennium Survey, recently published for the first time in a companion paper, Li et al. (2018). OH is an effective tracer of diffuse molecular regions (Wannier et al. 1993; Liszt & Lucas 1996; Barriault et al. 2010; Allen et al. 2012, 2015; Xu et al. 2016; Li et al. 2018), and has recently been surveyed at

high sensitivity in parts of the Galactic plane (Dawson et al. 2014; Bihr et al. 2015). There exists both theoretical and observational evidence for the close coexistence of interstellar OH and H₂. Observationally, they appear to reside in the same environments, as evidenced by tight relations between their column densities (Weselak & Krelowski 2014). Theoretically, the synthesis of OH is driven by the ions O⁺ and H₃⁺ but requires H₂ as the precursor; once H₂ becomes available, OH can be formed efficiently through the charge-exchange chemical reactions initiated by cosmic-ray ionization (van Dishoeck & Black 1986). Here we combine HI, OH, and dust data sets to obtain new measurements of the abundance ratio, $X_{OH} = N_{OH}/N_{H_2}$ —a key quantity for the interpretation of OH data sets.

The structure of this article is as follows. In Section 2, the observations, the data processing techniques, and corrections on HI are briefly summarized. In Section 3, the results from OH observations are discussed. Section 4 discusses the relationship between τ_{353} , $E(B - V)$ and N_H in the atomic ISM. We finally estimate the OH/H₂ abundance ratio in Section 5 before concluding in Section 6.

2. Data Sets

In this study, we use the all-sky optical depth (τ_{353}) map of the dust model data measured by *Planck*/IRAS (Planck Collaboration et al. 2014a—hereafter PLC2014a), the reddening $E(B - V)$ all-sky map from Green et al. (2018), HI data from both the 21-SPONGE Survey (Murray et al. 2015) and the Millennium Survey (Heiles & Troland 2003a, HT03), OH data from the Millennium Survey (Li et al. 2018), and CO data from the Delingha 14 m Telescope, the Caltech Submillimeter Observatory (CSO), and the IRAM 30 m telescope (Li et al. 2018).

2.1. HI and OH

HI data from the Millennium Arecibo 21 cm Absorption-Line Survey (hereafter MS) was taken toward 79 strong radio sources (typically $S \gtrsim 2$ Jy) using the Arecibo L-wide receiver. The two main lines of ground state OH at 1665.402 and 1667.359 MHz were observed simultaneously toward 72 positions, and OH absorption was detected along 19 of these sightlines (see also Li et al. 2018). The observations are described in detail by HT03. Briefly, their so-called Z16 observation pattern consists of one on-source absorption spectrum toward the background radio source and 16 off-source emission spectra with the innermost positions at 1.0 HPBW and the outermost positions at $\sqrt{2}$ HPBW from the central source. The off-source “expected” emission spectrum, the emission profile we would observe in the absence of the continuum source, is then estimated by modeling the 17-point measurements. In this work, we use the published values of HT03 for the total HI column density, N_{HI} (scaled as described below), and use the off-source (expected) MS emission profiles to compute the HI column density under the optically thin assumption, N_{HI}^* , where required. We compute OH column densities ourselves, as described in Section 3. All OH emission and absorption spectra are scaled to a main-beam temperature scale using a beam efficiency of $\eta_b = 0.5$ (Heiles et al. 2001),

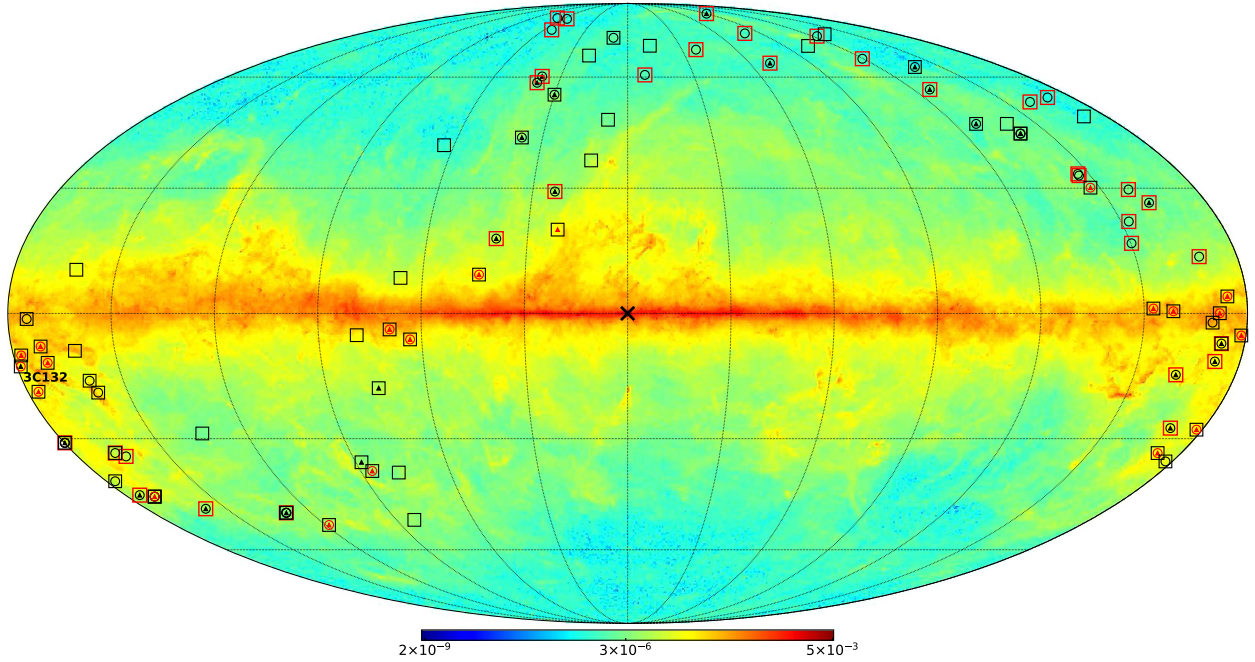


Figure 1. Locations of all 93 sightlines considered in this study, overlaid on the map of dust optical depth τ_{353} . Squares show H I absorption detections (93/93); red circles show OH absorption detections (19/72); black circles show nondetections (51/72); red triangles show CO detections (19/44); and black triangles show nondetections (25/44). For purely atomic sightlines (those with no molecular detection at the threshold discussed in Section 4), the squares are colored red. Note that the absence of a symbol indicates that the sightline was not observed in that particular tracer. The labeled sightline toward 3C132 (far left) shows the single position detected in H I and OH but not detected in CO emissions. The “X” marker labels the center of the Milky Way. Note that the symbols for a small number of sightlines entirely overlap due to their proximity on the sky.

appropriate if the OH is not extended compared to the Arecibo beam size of $3'$.

In order to increase the source sample, we also use H I data from the Very Large Array (VLA) 21-SPONGE Survey, which observed 30 continuum sources, including 16 in common with the Millennium Survey sample (Murray et al. 2015). 21-SPONGE used on-source absorption data from the VLA, combining them with off-source emission profiles observed with Arecibo. Murray et al. (2015) report an excellent agreement between the optical depths measured by the two surveys, demonstrating that the single dish Arecibo absorption profiles are not significantly contaminated with resolved 21 cm emission. Note that in this work we have used an updated scaling of the 21-SPONGE emission profiles, which applies a beam efficiency factor of 0.94 to the Arecibo spectra. The total number of unique sightlines presented in this work is therefore 93. The locations of all observed sources in Galactic coordinates are presented in Figure 1. Where sources were observed in both the MS and 21-SPONGE, we use the MS data.

2.1.1. H I Intensity Scale Corrections

We check our $N_{\text{H I}}^*$ against the Leiden–Argentine–Bonn survey (LAB, Hartmann & Burton 1997; Kalberla et al. 2005) and the HI4PI survey (HI4PI Collaboration et al. 2016). Both are widely regarded as a gold standard in the absolute calibration of Galactic H I. We find that the optically thin column densities derived from 21-SPONGE are consistent with LAB and HI4PI. However, the MS values are systematically lower than both LAB and HI4PI by a factor of ~ 1.14 . A possible explanation for this difference lies in the fact that (in

contrast to 21-SPONGE) the MS did not apply a main-beam efficiency.

To bring the MS data set in-line with LAB, HI4PI, and 21-SPONGE, one might assume that both the on-source and off-source spectra must be rescaled, and the opacity-corrected column densities recomputed according to the method of HT03 (or equivalent). However, $N_{\text{H I}}$ may in fact be obtained from the tabulated values of HT03, with no need to perform a full reanalysis of the data. For warm components, the tabulated values of $N_{\text{H I}}$ are simply scaled by 1.14—appropriate since these were originally computed directly from the integrated off-source (expected) profiles under the optically thin assumption. For cold components, we recall that the radiative transfer equations for the on-source and off-source (expected) spectra in the MS data set are given by:

$$T_{\text{B}}^{\text{ON}}(\nu) = (T_{\text{bg}} + T_{\text{c}})e^{-\tau_{\nu}} + T_{\text{s}}(1 - e^{-\tau_{\nu}}) + T_{\text{rx}} \quad (1)$$

$$T_{\text{B}}^{\text{OFF}}(\nu) = T_{\text{bg}}e^{-\tau_{\nu}} + T_{\text{s}}(1 - e^{-\tau_{\nu}}) + T_{\text{rx}}, \quad (2)$$

where $T_{\text{B}}^{\text{OFF}}(\nu)$ and $T_{\text{B}}^{\text{ON}}(\nu)$ are the main-beam temperatures of the off-source spectrum and on-source spectrum, respectively. T_{s} is the spin temperature, τ_{ν} is the optical depth, T_{rx} is the receiver temperature (~ 25 K), and T_{c} is the main-beam temperature of the continuum source, obtained from the line-free portions of the on-source spectrum. T_{bg} is the continuum background brightness temperature including the 2.7 K isotropic radiation from CMB and the Galactic synchrotron background at the source position. Equations (1) and (2) may be solved for τ_{ν} and T_{s} :

$$e^{-\tau_{\nu}} = \frac{T_{\text{B}}^{\text{ON}}(\nu) - T_{\text{B}}^{\text{OFF}}(\nu)}{T_{\text{c}}}, \quad (3)$$

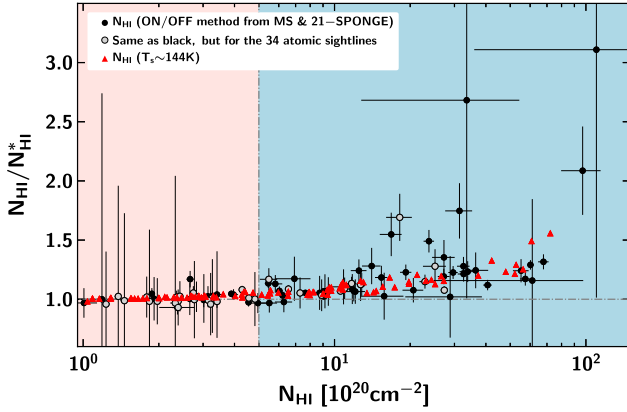


Figure 2. Ratio $f = N_{\text{HI}}/N_{\text{HI}}^*$ as a function of opacity-corrected N_{HI} along 93 sightlines from the MS and 21-SPONGE surveys. Circles show accurate N_{HI} obtained via on- and off-source observations (HT03; scaled as described in the text), with the 34 atomic sightlines (selection criteria described in Section 4) filled gray and all other points filled black. Red triangles show N_{HI} obtained from N_{HI}^* assuming a single isothermal component of $T_s \sim 144$ K. The vertical dashed line is plotted at $N_{\text{HI}} = 5 \times 10^{20} \text{ cm}^{-2}$; the horizontal dashed line marks where $N_{\text{HI}} = N_{\text{HI}}^*$.

$$T_s = \frac{T_{\text{B}}^{\text{OFF}}(\nu) - T_{\text{bg}}e^{-\tau_\nu} - T_{\text{rx}}}{1 - e^{-\tau_\nu}}. \quad (4)$$

From Equation (3), it is clear that optical depth is unchanged by any rescaling, which will affect both the numerator and denominator of the expression identically. Only T_s must be recomputed. This is done on a component-by-component basis from the tabulated Gaussian fit parameters for peak optical depth, τ_0 , peak brightness temperature (scaled by 1.14), and the linewidth $\Delta\nu$. The corrected N_{HI} is obtained from

$$\frac{N_{\text{HI}}}{[10^{18} \text{ cm}^{-2}]} = 1.94 \cdot \tau_0 \cdot \frac{T_s}{[\text{K}]} \cdot \frac{\Delta\nu}{[\text{km s}^{-1}]}, \quad (5)$$

where the factor 1.94 includes the usual constant 1.8224 and the 1.065 arising from the integration over the Gaussian line profile.

2.1.2. N_{HI} versus N_{HI}^*

We show in Figure 2 the correlation between N_{HI} and N_{HI}^* toward all 93 positions. While optically thin H I column density is comparable with the true column density in diffuse/low-density regions with $N_{\text{HI}} \lesssim 5 \times 10^{20} \text{ cm}^{-2}$, opacity effects start to become apparent above $\sim 5 \times 10^{20} \text{ cm}^{-2}$.

If a linear fit is performed to the data, the ratio $f = N_{\text{HI}}/N_{\text{HI}}^*$ may be described as a function of $\log(N_{\text{HI}}^*/10^{20})$ with a slope of (0.19 ± 0.02) and an intercept of (0.89 ± 0.02) (see also Lee et al. 2015). Alternatively, a simple isothermal correction to the optically thin N_{HI}^* data with $T_s \sim 144$ K also yields a good agreement with our data points, as illustrated in Figure 2 (see also Liszt 2014b). This approach also better fits the low N_{HI} plateau, $N_{\text{HI}} < 5 \times 10^{20} \text{ cm}^{-2}$, below which $N_{\text{HI}}^* \approx N_{\text{HI}}$. While a single component with a constant spin temperature is a poor physical description of interstellar H I, it can provide a reasonable (if crude) correction for opacity.

2.2. CO

As described in Li et al. (2018), a CO follow-up survey was conducted toward 44 of the sightlines considered in this work.

The $J = 1-0$ transitions of ^{12}CO , ^{13}CO , and C^{18}O were observed with the Delingha 13.7 m telescope in China. $^{12}\text{CO}(J = 2-1)$ data for 45 sources and $J = 3-2$ data for 8 sources with strong ^{12}CO emission were taken with the 10.4 m CSO on Maunakea, with further supplementary data obtained by the IRAM 30 m telescope. In this work, we use CO data solely to identify and exclude from some parts of the analysis positions with detected CO-bright molecular gas—comprising 19 of the 44 observed positions. These positions are identified in Figure 1.

2.3. Dust

To trace the total gas column density N_{H} , we use publicly available all-sky maps of the 353 GHz dust optical depth (τ_{353}) from the *Planck* satellite. The τ_{353} map was obtained by a modified blackbody (MBB) fit to the first 15 months of 353, 545, and 857 GHz data, together with *IRAS* 100 micron data (for details, see PLC2014a). The angular resolution of this data set is 5 arcmin. In this work, we use the R1.20 data release in Healpix¹⁵ format (Górski et al. 2005). For dust reddening, we employ the newly released all-sky 3D dust map of Green et al. (2018) at an angular resolution of $3'4''$ – $13'7''$, which was derived from 2MASS and the latest Pan-STARRS 1 data photometry. In contrast to emission-based dust maps that depend on the modeling of the temperature, optical depth, and the shape of the emission spectrum, in maps based on stellar photometry reddening values are more directly measured and not contaminated from zodiacal light or large-scale structure. Here we convert the Green et al. (2018) *Bayestar17* dust map to $E(B - V)$ by applying a scaling factor of 0.884, as described in the documentation accompanying the data release.¹⁶

3. OH Data Analysis

The Millennium Survey OH data consists of on-source and off-source “expected” spectra for each of the OH lines. In our companion paper (Li et al. 2018), we use the method of HT03 to derive OH optical depths, excitation temperatures and column densities. Namely, we obtain solutions for the excitation temperature, T_{ex} , and τ via Gaussian fitting (to both the on-source and off-source spectra) that explicitly includes the appropriate treatment of the radiative transfer. In the present work, we use a simpler channel-by-channel method for the derivation of T_{ex} .

The radiative transfer equations for the on-source and off-source (expected) spectra are identical to those for H I, given above in Equations (1) and (2). All terms and their meanings are identical, with the exception that the spin temperature, T_s is replaced by T_{ex} . T_{bg} is the continuum background brightness temperature including the 2.7 K isotropic radiation from CMB and the Galactic synchrotron background at the source position. For consistency with HT03 and Li et al. (2018), we estimate the synchrotron contribution at 1665.402 and 1667.359 MHz from the 408 MHz continuum map of Haslam et al. (1982), by adopting a temperature spectral index of 2.8, such that

$$T_{\text{bg}} = 2.7 + T_{\text{bg},408}(\nu_{\text{OH}}/408)^{-2.8}, \quad (6)$$

resulting in typical values of around 3.5 K. The background continuum contribution from Galactic H II regions may be

¹⁵ <http://healpix.sourceforge.net>

¹⁶ <http://argonaut.skymaps.info/usage>

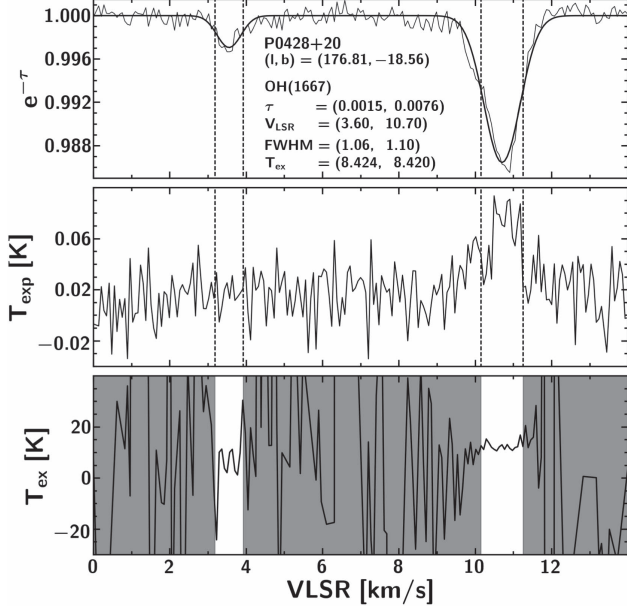


Figure 3. Example of OH 1667 MHz $e^{-\tau}$ (top), expected T_B^{OFF} (middle), and T_{ex} (bottom) spectra for the source P0428+20. The FWHM of the Gaussian fits to the absorption profile are used to define the range over which T_{ex} is computed for each component, shown as white regions in the bottom panel.

safely ignored, since the continuum sources we observed are either at high Galactic latitudes or Galactic anti-center longitudes. Thus, in line-free portions of the off-source spectra:

$$T_B^{\text{OFF}}(\nu) = T_{\text{bg}} + T_{\text{rx}}. \quad (7)$$

In the absence of information about the true gas distribution, we assume that OH clouds cover fully both the continuum source and the main beam of the telescope. We may therefore solve Equations (1) and (2) to derive T_{ex} and τ_{ν} for each of the OH lines, as shown in Equations (3) and (4) for the case of H I.

We fit each OH opacity spectrum (cf. Equation (3)) with a set of Gaussian profiles to obtain the peak optical depth ($\tau_{0,n}$), central velocity ($v_{0,n}$), and FWHM (Δv_n) of each component, n . Equation (4) is then used to calculate excitation temperature spectra. Examples of $e^{-\tau}$, T_B^{OFF} , and T_{ex} spectra are shown in Figure 3, together with their associated Gaussian fits. It can be seen that the T_{ex} spectra are approximately flat within the FWHM of each Gaussian component. We therefore compute an excitation temperature for each component from the mean T_{ex} in the range $v_{0,n} \pm \Delta v/2$.

Figure 4 compares the τ_0 and T_{ex} values obtained from our method with those of Li et al. (2018), demonstrating that the two methods generally return consistent results. Minor differences arise only for the most complex sightlines through the Galactic plane (G197.0+1.1, T0629+10), where the spectra are not simple to analyze; however, even these points are mostly consistent to within the errors.

We compute total OH column densities, N_{OH} , independently from both the 1667 and 1665 MHz lines via:

$$\frac{N_{\text{OH},1667}}{[10^{14} \text{ cm}^{-2}]} = 2.39 \cdot \tau_{1667} \cdot \frac{T_{\text{ex},1667}}{[\text{K}]} \cdot \frac{\Delta v_{1667}}{[\text{km s}^{-2}]}, \quad (8)$$

$$\frac{N_{\text{OH},1665}}{[10^{14} \text{ cm}^{-2}]} = 4.30 \cdot \tau_{1665} \cdot \frac{T_{\text{ex},1665}}{[\text{K}]} \cdot \frac{\Delta v_{1665}}{[\text{km s}^{-2}]}, \quad (9)$$

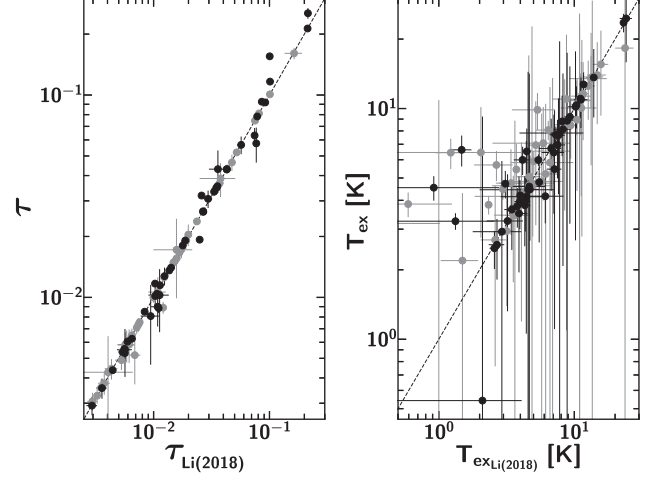


Figure 4. Comparison between derived values of the peak optical depth τ (left panel), and T_{ex} (right panel) for both OH main lines, 1667 MHz (black) and 1665 MHz (gray), as obtained from our companion paper by Li et al. (2018) and the present work. The dashed lines mark where the two values are equal.

where the constants include Einstein A -coefficients of $A_{1667} = 7.778 \times 10^{-11} \text{ s}^{-1}$ and $A_{1665} = 7.177 \times 10^{-11} \text{ s}^{-1}$ for the OH main lines (Destombes et al. 1977). All values of τ_0 , T_{ex} , and N_{OH} are tabulated in Table 1.

4. Dust-based Proxies for Total Neutral Gas Column Density

In this section, we will investigate the correlations between dust properties and the total gas column density N_{H} . Specifically, we consider dust optical depth at 353 GHz, τ_{353} , and reddening, $E(B - V)$, with data sets sourced as described in Section 2.3. When these quantities are used as proxies for N_{H} , a single linear relationship between the measured quantity and N_{H} is typically assumed. In this work, our H I data set provides accurate (opacity-corrected) atomic column densities, while complementary OH and CO data allow us to identify and exclude sightlines with molecular gas (dark or not). We are therefore able to measure τ_{353}/N_{H} and $E(B - V)/N_{\text{H}}$ along a sample of purely atomic sightlines for which N_{H} is very well constrained.

In the following, we consider 34/93 sightlines to be “purely atomic.” These are defined as either (a) sightlines where CO and OH were observed and not detected in emission (16/93), or (b) sightlines where CO was not observed but OH was observed but not detected (18/93 sightlines). In both cases, we require that OH be undetected in the 1667 MHz line to a detection limit of $N_{\text{OH}} < 1 \times 10^{13} \text{ cm}^{-2}$ (see Li et al. 2018), which excludes some positions with weaker continuum background sources. We may confidently assume that these sightlines contain very little or no H_2 and note that all but one of them lie outside the Galactic plane ($|b| > 10^\circ$). Figure 5 shows maps of the immediate vicinity of these sightlines in τ_{353} and $E(B - V)$. Identical maps for the 19 sightlines with OH detections (see also Section 5), are shown in Figure 6.

In all of the following subsections, N_{H} is taken to be equal to $N_{\text{H},1}$, the opacity-corrected H I column density, as derived along sightlines with no molecular gas detected in emission.

Table 1
Parameters for OH Main Lines

Source (Name)	l/b ($^{\circ}$)	OH(1665)					OH(1667)				
		τ	V_{lsr} (km s^{-1})	ΔV (km s^{-1})	T_{ex} (K)	$N(\text{OH})$ (10^{14} cm^{-2})	τ	V_{lsr} (km s^{-1})	ΔV (km s^{-1})	T_{ex} (K)	$N(\text{OH})$ (10^{14} cm^{-2})
3C105	187.6/−33.6	0.0156 ± 0.0003	8.14 ± 0.01	0.95 ± 0.03	4.65 ± 1.86	0.29 ± 0.12	0.0265 ± 0.0004	8.17 ± 0.01	0.94 ± 0.02	3.95 ± 0.95	0.23 ± 0.06
3C105	187.6/−33.6	0.0062 ± 0.0003	10.22 ± 0.02	0.93 ± 0.06	8.5 ± 4.89	0.21 ± 0.12	0.0104 ± 0.0004	10.25 ± 0.02	0.96 ± 0.04	7.66 ± 3.41	0.18 ± 0.08
3C109	181.8/−27.8	0.0023 ± 0.0003	9.15 ± 0.11	1.03 ± 0.26	18.28 ± 27.06	0.18 ± 0.27	0.0036 ± 0.0004	9.24 ± 0.05	0.75 ± 0.12	24.58 ± 8.7	0.16 ± 0.06
3C109	181.8/−27.8	0.0036 ± 0.0003	10.45 ± 0.07	0.98 ± 0.15	13.97 ± 5.41	0.21 ± 0.09	0.0053 ± 0.0004	10.55 ± 0.04	1.02 ± 0.1	13.63 ± 4.48	0.18 ± 0.06
3C123	170.6/−11.7	0.0191 ± 0.0007	3.65 ± 0.06	1.19 ± 0.11	10.92 ± 3.26	1.05 ± 0.33	0.0348 ± 0.0009	3.71 ± 0.04	1.22 ± 0.07	10.92 ± 2.69	1.1 ± 0.28
3C123	170.6/−11.7	0.0431 ± 0.0023	4.43 ± 0.01	0.53 ± 0.03	8.06 ± 0.78	0.78 ± 0.09	0.0919 ± 0.0029	4.46 ± 0.0	0.53 ± 0.01	7.7 ± 0.65	0.89 ± 0.08
3C123	170.6/−11.7	0.0337 ± 0.0008	5.37 ± 0.01	0.91 ± 0.03	11.59 ± 4.3	1.53 ± 0.57	0.0784 ± 0.0009	5.47 ± 0.01	0.92 ± 0.01	8.79 ± 2.57	1.5 ± 0.44
3C131	171.4/−7.8	0.0065 ± 0.0005	4.55 ± 0.02	0.56 ± 0.05	12.52 ± 3.59	0.19 ± 0.06	0.0117 ± 0.0004	4.64 ± 0.01	0.78 ± 0.04	6.96 ± 1.98	0.15 ± 0.04
3C131	171.4/−7.8	0.0073 ± 0.0006	6.81 ± 0.06	2.91 ± 0.23	8.94 ± 4.54	0.82 ± 0.42	0.0089 ± 0.0005	5.84 ± 0.03	0.67 ± 0.08	11.04 ± 2.07	0.16 ± 0.04
3C131	171.4/−7.8	0.0166 ± 0.0007	6.59 ± 0.01	0.42 ± 0.02	5.69 ± 0.85	0.17 ± 0.03	0.0319 ± 0.0007	6.55 ± 0.01	0.45 ± 0.02	5.99 ± 0.84	0.2 ± 0.03
3C131	171.4/−7.8	0.0521 ± 0.0007	7.23 ± 0.0	0.55 ± 0.01	5.91 ± 0.64	0.72 ± 0.08	0.0927 ± 0.0005	7.22 ± 0.0	0.65 ± 0.01	5.98 ± 0.34	0.85 ± 0.05
3C132	178.9/−12.5	0.0033 ± 0.0003	7.82 ± 0.04	0.9 ± 0.1	15.55 ± 6.23	0.19 ± 0.08	0.0056 ± 0.0003	7.79 ± 0.02	0.79 ± 0.06	23.56 ± 2.17	0.25 ± 0.03
3C133	177.7/−9.9	0.1008 ± 0.001	7.66 ± 0.0	0.53 ± 0.0	4.47 ± 0.44	1.01 ± 0.1	0.2132 ± 0.0014	7.68 ± 0.0	0.52 ± 0.0	3.25 ± 0.27	0.85 ± 0.07
3C133	177.7/−9.9	0.0149 ± 0.001	7.94 ± 0.02	1.22 ± 0.04	7.08 ± 3.08	0.55 ± 0.24	0.0333 ± 0.0013	7.96 ± 0.01	1.23 ± 0.02	4.17 ± 0.99	0.4 ± 0.1
3C154	185.6/4.0	0.0266 ± 0.0006	−2.32 ± 0.02	0.74 ± 0.03	2.69 ± 1.93	0.23 ± 0.16	0.0429 ± 0.0006	−2.34 ± 0.01	0.71 ± 0.02	2.57 ± 0.75	0.19 ± 0.05
3C154	185.6/4.0	0.01 ± 0.0006	−1.39 ± 0.04	0.83 ± 0.09	5.2 ± 5.28	0.18 ± 0.19	0.0181 ± 0.0005	−1.34 ± 0.02	0.94 ± 0.05	4.46 ± 1.79	0.18 ± 0.07
3C154	185.6/4.0	0.0038 ± 0.0005	2.23 ± 0.07	1.14 ± 0.17	5.83 ± 6.56	0.11 ± 0.12	0.0054 ± 0.0004	2.19 ± 0.05	1.57 ± 0.13	0.54 ± 8.69	0.01 ± 0.17
3C167	207.3/1.2	0.0106 ± 0.0019	18.46 ± 0.12	1.49 ± 0.35	4.75 ± 17.95	0.32 ± 1.22	0.009 ± 0.0018	17.77 ± 0.15	1.76 ± 0.49	4.59 ± 9.57	0.17 ± 0.36
3C18	118.6/−52.7	0.0031 ± 0.0003	−8.52 ± 0.11	2.64 ± 0.27	10.92 ± 14.88	0.38 ± 0.52	0.006 ± 0.0003	−8.34 ± 0.05	2.61 ± 0.14	9.2 ± 6.04	0.34 ± 0.23
3C18	118.6/−52.7	0.0056 ± 0.0004	−7.82 ± 0.02	0.67 ± 0.07	6.45 ± 3.7	0.1 ± 0.06	0.0079 ± 0.0004	−7.85 ± 0.01	0.6 ± 0.04	4.83 ± 1.6	0.05 ± 0.02
3C207	213.0/30.1	0.015 ± 0.0002	4.55 ± 0.01	0.76 ± 0.01	2.94 ± 1.55	0.14 ± 0.08	0.0266 ± 0.0002	4.55 ± 0.0	0.77 ± 0.01	2.48 ± 0.46	0.12 ± 0.02
3C409	63.4/−6.1	0.0058 ± 0.0011	14.59 ± 0.27	1.68 ± 0.35	11.31 ± 8.53	0.47 ± 0.38	0.0055 ± 0.0015	14.68 ± 0.33	1.52 ± 0.4	7.83 ± 11.73	0.16 ± 0.24
3C409	63.4/−6.1	0.0204 ± 0.0025	15.4 ± 0.01	0.89 ± 0.05	3.18 ± 2.31	0.25 ± 0.18	0.0275 ± 0.0032	15.42 ± 0.01	0.86 ± 0.04	0.62 ± 1.0	0.03 ± 0.06
3C410	69.2/−3.8	0.0044 ± 0.0006	6.32 ± 0.04	1.89 ± 0.15	13.41 ± 11.22	0.47 ± 0.4	0.0079 ± 0.0005	6.38 ± 0.02	2.32 ± 0.09	6.4 ± 5.25	0.28 ± 0.23
3C410	69.2/−3.8	0.0089 ± 0.0006	6.21 ± 0.01	0.65 ± 0.04	8.46 ± 2.4	0.21 ± 0.06	0.0193 ± 0.0005	6.26 ± 0.01	0.81 ± 0.02	3.81 ± 1.28	0.14 ± 0.05
3C410	69.2/−3.8	0.0044 ± 0.0003	10.7 ± 0.03	0.71 ± 0.07	10.06 ± 5.89	0.13 ± 0.08	0.0085 ± 0.0002	10.71 ± 0.02	0.81 ± 0.04	4.15 ± 3.09	0.07 ± 0.05
3C410	69.2/−3.8	0.0054 ± 0.0002	11.67 ± 0.03	0.84 ± 0.07	4.83 ± 4.66	0.09 ± 0.09	0.0115 ± 0.0002	11.68 ± 0.02	0.82 ± 0.03	2.93 ± 3.0	0.07 ± 0.07
3C454.3	86.1/−38.2	0.0023 ± 0.0001	−9.67 ± 0.03	1.6 ± 0.09	4.63 ± 12.36	0.07 ± 0.19	0.0044 ± 0.0001	−9.54 ± 0.01	1.25 ± 0.04	8.13 ± 6.06	0.1 ± 0.08
3C75	170.3/−44.9	0.0071 ± 0.0005	−10.36 ± 0.04	1.3 ± 0.12	3.45 ± 5.41	0.14 ± 0.21	0.014 ± 0.0008	−10.36 ± 0.03	1.22 ± 0.09	3.51 ± 1.56	0.14 ± 0.06
4C13.67	43.5/9.2	0.0464 ± 0.0043	4.85 ± 0.05	1.1 ± 0.12	10.43 ± 2.77	2.28 ± 0.69	0.0567 ± 0.0057	4.89 ± 0.05	1.12 ± 0.14	10.34 ± 2.13	1.55 ± 0.5
4C22.12	188.1/0.0	0.0058 ± 0.001	−2.84 ± 0.07	0.79 ± 0.19	6.54 ± 7.03	0.13 ± 0.14	0.0102 ± 0.0011	−2.73 ± 0.04	0.78 ± 0.12	6.72 ± 2.32	0.13 ± 0.04
4C22.12	188.1/0.0	0.0172 ± 0.0012	−1.78 ± 0.02	0.56 ± 0.05	5.07 ± 2.12	0.21 ± 0.09	0.0354 ± 0.0013	−1.78 ± 0.01	0.54 ± 0.03	3.78 ± 0.74	0.17 ± 0.03
G196.6+0.2	196.6/0.2	0.0044 ± 0.0005	3.26 ± 0.11	1.94 ± 0.27	10.82 ± 12.22	0.4 ± 0.46	0.0062 ± 0.0005	3.4 ± 0.09	2.38 ± 0.22	8.85 ± 8.6	0.31 ± 0.3
G197.0+1.1	197.0/1.1	0.0126 ± 0.0005	4.83 ± 0.04	1.88 ± 0.09	6.94 ± 3.82	0.7 ± 0.39	0.0191 ± 0.001	4.73 ± 0.04	1.65 ± 0.1	4.8 ± 2.17	0.36 ± 0.16
G197.0+1.1	197.0/1.1	0.0059 ± 0.0009	7.46 ± 0.05	0.65 ± 0.11	0.31 ± 10.58	0.0 ± 0.17	0.0078 ± 0.0015	7.34 ± 0.06	0.65 ± 0.14	1.61 ± 5.87	0.02 ± 0.07
G197.0+1.1	197.0/1.1	0.0049 ± 0.0005	17.01 ± 0.12	2.47 ± 0.28	10.99 ± 9.9	0.57 ± 0.52	0.0081 ± 0.0034	16.26 ± 0.17	0.91 ± 0.3	6.45 ± 2.95	0.11 ± 0.08
G197.0+1.1	197.0/1.1	0.0052 ± 0.0015	17.59 ± 0.03	0.25 ± 0.08	9.87 ± 1.81	0.05 ± 0.03	0.0127 ± 0.0013	17.38 ± 0.2	1.46 ± 0.35	5.46 ± 4.35	0.24 ± 0.2
G197.0+1.1	197.0/1.1	0.0237 ± 0.001	32.01 ± 0.01	0.57 ± 0.03	4.75 ± 1.92	0.27 ± 0.11	0.043 ± 0.0017	32.01 ± 0.01	0.54 ± 0.02	3.96 ± 1.04	0.22 ± 0.06
P0428+20	176.8/−18.6	0.0014 ± 0.0002	3.6 ± 0.08	1.01 ± 0.19	13.48 ± 7.8	0.08 ± 0.05	0.0029 ± 0.0003	3.54 ± 0.03	0.69 ± 0.08	4.45 ± 9.98	0.02 ± 0.05
P0428+20	176.8/−18.6	0.0075 ± 0.0002	10.7 ± 0.02	1.09 ± 0.04	13.49 ± 3.45	0.47 ± 0.12	0.0136 ± 0.0002	10.7 ± 0.01	1.1 ± 0.02	12.72 ± 1.62	0.45 ± 0.06
T0526+24	181.4/−5.2	0.0172 ± 0.0073	7.55 ± 0.29	1.9 ± 1.13	13.7 ± 15.65	1.91 ± 2.59	0.043 ± 0.0102	7.56 ± 0.14	2.43 ± 0.75	10.19 ± 7.5	2.52 ± 2.1
T0629+10	201.5/0.5	0.0043 ± 0.0022	0.16 ± 0.0	0.65 ± 0.4	4.16 ± 2.97	0.05 ± 0.05	0.0103 ± 0.0035	0.35 ± 0.0	1.18 ± 0.41	3.25 ± 1.93	0.09 ± 0.07
T0629+10	201.5/0.5	0.0387 ± 0.0074	3.14 ± 0.13	1.1 ± 0.0	3.85 ± 0.47	0.7 ± 0.16	0.0577 ± 0.0113	3.07 ± 0.14	1.1 ± 0.0	4.54 ± 0.55	0.68 ± 0.16
T0629+10	201.5/0.5	0.0169 ± 0.0015	1.46 ± 0.07	1.39 ± 0.26	2.19 ± 2.11	0.22 ± 0.22	0.0281 ± 0.0029	1.51 ± 0.08	1.23 ± 0.25	2.9 ± 0.91	0.24 ± 0.09

Table 1
(Continued)

Source (Name)	l/b ($^{\circ}$)	OH(1665)					OH(1667)				
		τ	V_{lsr} (km s^{-1})	ΔV (km s^{-1})	T_{ex} (K)	$N(\text{OH})$ (10^{14} cm^{-2})	τ	V_{lsr} (km s^{-1})	ΔV (km s^{-1})	T_{ex} (K)	$N(\text{OH})$ (10^{14} cm^{-2})
T0629+10	201.5/0.5	0.1607 ± 0.0104	3.6 ± 0.01	0.61 ± 0.02	3.83 ± 0.35	1.59 ± 0.19	0.2536 ± 0.0154	3.6 ± 0.01	0.65 ± 0.03	4.72 ± 0.64	1.84 ± 0.29
T0629+10	201.5/0.5	0.0811 ± 0.002	4.62 ± 0.01	0.76 ± 0.03	6.43 ± 0.97	1.68 ± 0.27	0.1553 ± 0.0037	4.61 ± 0.01	0.67 ± 0.03	6.62 ± 1.01	1.63 ± 0.26
T0629+10	201.5/0.5	0.0747 ± 0.0018	6.09 ± 0.02	1.06 ± 0.05	5.44 ± 1.58	1.84 ± 0.54	0.1165 ± 0.003	6.06 ± 0.02	1.17 ± 0.07	6.52 ± 1.67	2.1 ± 0.55
T0629+10	201.5/0.5	0.0367 ± 0.0031	7.0 ± 0.02	0.49 ± 0.06	4.36 ± 0.68	0.33 ± 0.07	0.0631 ± 0.0056	7.0 ± 0.02	0.5 ± 0.06	4.2 ± 0.3	0.31 ± 0.05
T0629+10	201.5/0.5	0.0174 ± 0.0018	7.9 ± 0.05	0.83 ± 0.13	3.44 ± 1.67	0.21 ± 0.11	0.0307 ± 0.003	7.91 ± 0.05	0.82 ± 0.13	3.65 ± 1.21	0.22 ± 0.08

Table 2
34 Atomic Sightlines

Sources (Name)	l/b ($^\circ$)	N_{HI} (10^{20} cm^{-2})	N_{HI}^* (10^{20} cm^{-2})	$\sigma_{\tau}(\text{OH}_{1667})$ (10^{-4})	$N_{\text{H}_2}(\text{upper limit})^a$ (10^{20} cm^{-2})	τ_{353} (10^{-6})	$E(B - V)$ (10^{-2} mag)
3C33	129.4/−49.3	3.25 ± 0.0	3.2 ± 0.1	12.14	0.6	2.16 ± 0.07	3.54 ± 0.42
3C142.1	197.6/−14.5	25.11 ± 2.6	19.6 ± 0.8	10.55	0.52	21.53 ± 0.72	21.71 ± 0.81
3C138	187.4/−11.3	22.9 ± 1.1	19.9 ± 0.3	5.02	0.25	21.63 ± 0.81	17.47 ± 0.59
3C79	164.1/−34.5	10.86 ± 1.2	9.8 ± 0.8	37.03	1.84	9.23 ± 0.37	12.67 ± 0.78
3C78	174.9/−44.5	11.69 ± 0.5	10.3 ± 0.2	13.25	0.66	12.45 ± 0.63	14.64 ± 1.07
3C310	38.5/60.2	4.29 ± 0.1	4.0 ± 0.1	16.19	0.8	3.48 ± 0.15	2.75 ± 0.53
3C315	39.4/58.3	5.48 ± 0.4	4.7 ± 0.0	12.96	0.64	3.98 ± 0.09	5.63 ± 0.26
3C234	200.2/52.7	1.84 ± 0.0	1.9 ± 1.1	12.66	0.63	0.78 ± 0.03	1.64 ± 0.56
3C236	190.1/54.0	1.38 ± 0.0	1.3 ± 1.2	10.72	0.53	0.7 ± 0.03	2.04 ± 0.49
3C64	157.8/−48.2	7.29 ± 0.2	6.9 ± 0.8	33.12	1.65	6.55 ± 0.35	9.01 ± 0.36
P0531+19	186.8/−7.1	27.33 ± 0.7	25.4 ± 0.3	6.37	0.32	20.75 ± 0.62	20.54 ± 1.3
P0820+22	201.4/29.7	4.82 ± 0.2	4.8 ± 1.1	7.09	0.35	3.73 ± 0.11	2.56 ± 0.4
3C192	197.9/26.4	4.56 ± 0.1	4.5 ± 0.1	20.66	1.03	3.38 ± 0.08	4.05 ± 0.53
3C98	179.8/−31.0	12.7 ± 0.5	11.3 ± 1.3	12.26	0.61	13.72 ± 0.41	17.73 ± 1.02
3C273	289.9/64.4	2.35 ± 0.0	2.3 ± 0.1	21.0	1.04	1.3 ± 0.09	1.98 ± 0.41
DW0742+10	209.8/16.6	2.77 ± 0.0	2.8 ± 0.9	8.01	0.4	1.6 ± 0.03	1.99 ± 0.25
3C172.0	191.2/13.4	8.89 ± 0.2	8.6 ± 1.1	13.02	0.65	5.66 ± 0.08	4.7 ± 0.52
3C293	54.6/76.1	1.46 ± 0.1	1.5 ± 1.1	6.24	0.31	1.31 ± 0.09	2.83 ± 0.75
3C120	190.4/−27.4	18.17 ± 2.1	10.7 ± 0.1	28.29	1.41	29.26 ± 1.08	22.74 ± 1.03
CTA21	166.6/−33.6	10.97 ± 0.4	10.0 ± 0.8	27.35	1.36	10.39 ± 0.44	13.3 ± 0.96
P1117+14	240.4/65.8	1.79 ± 0.0	1.8 ± 0.3	15.0	0.75	1.5 ± 0.04	2.73 ± 0.54
3C264.0	237.0/73.6	1.97 ± 0.0	2.0 ± 0.4	6.29	0.31	1.64 ± 0.08	2.88 ± 0.34
3C208.1	213.6/33.6	3.15 ± 0.1	3.2 ± 0.2	18.67	0.93	3.12 ± 0.04	2.93 ± 0.43
3C208.0	213.7/33.2	3.41 ± 0.1	3.5 ± 0.2	19.69	0.98	3.38 ± 0.07	4.37 ± 0.47
4C32.44	67.2/81.0	1.23 ± 0.0	1.3 ± 0.6	9.88	0.49	0.81 ± 0.02	1.94 ± 0.29
3C272.1	280.6/74.7	2.82 ± 0.0	2.8 ± 0.3	10.24	0.51	1.73 ± 0.28	2.43 ± 0.31
4C07.32	322.2/68.8	2.43 ± 0.0	2.4 ± 0.3	30.7	1.53	2.32 ± 0.06	4.3 ± 0.41
3C245	233.1/56.3	2.39 ± 0.0	2.4 ± 0.2	11.36	0.56	2.22 ± 0.06	2.71 ± 0.36
3C348	23.0/29.2	6.56 ± 0.2	6.0 ± 0.1	16.51	0.82	5.7 ± 0.15	9.8 ± 0.33
3C286	56.5/80.7	2.33 ± 0.1	2.4 ± 2.7	7.13	0.35	0.81 ± 0.05	2.75 ± 0.74
4C13.65	39.3/17.7	10.56 ± 0.2	9.9 ± 0.1	20.01	0.99	11.8 ± 0.39	15.63 ± 0.6
3C190.0	207.6/21.8	3.21 ± 0.0	3.4 ± 0.9	17.57	0.87	2.41 ± 0.03	1.96 ± 0.42
3C274.1	269.9/83.2	2.74 ± 0.0	2.6 ± 0.1	13.13	0.65	2.34 ± 0.02	2.64 ± 0.42
3C298	352.2/60.7	2.39 ± 0.4	2.6 ± 0.1	10.69	0.53	1.3 ± 0.07	1.97 ± 0.39

Note.

^a Estimated from OH(1667) 3σ detection limits using $T_{\text{ex}} = 3.5 \text{ K}$, $\text{FWHM} = 1 \text{ km s}^{-1}$ and $N_{\text{OH}}/N_{\text{H}_2} = 10^{-7}$ (see Section 5).

4.1. N_{H} from Dust Optical Depth τ_{353}

We adopt the all-sky map of dust optical depth τ_{353} computed by [PLC2014a](#). This was derived from an MBB empirical fit to *IRAS* and *Planck* maps at 3000, 857, 545, and 353 GHz, described by the expression:

$$I_\nu = \tau_{353} B_\nu(T_{\text{dust}}) \left(\frac{\nu}{353} \right)^{\beta_{\text{dust}}}. \quad (10)$$

Here, τ_{353} , dust temperature, T_{dust} , and spectral index, β_{dust} , are the three free parameters, and $B_\nu(T_{\text{dust}})$ is the *Planck* function for dust at temperature T_{dust} which is, in this model, considered to be uniform along each sightline (see [PLC2014a](#) for more details). The relation between dust optical depth and total gas column density can then be written as:

$$\tau_{353} = \frac{I_{353}}{B_{353}(T_{\text{dust}})} = \kappa_{353} r \mu m_{\text{H}} N_{\text{H}} = \sigma_{353} N_{\text{H}}, \quad (11)$$

where σ_{353} is the dust opacity, κ_{353} is the dust emissivity cross-section per unit mass ($\text{cm}^2 \text{ g}^{-1}$), r is the dust-to-gas mass ratio,

μ is the mean molecular weight, and m_{H} is the mass of a hydrogen atom.

Figure 7 shows the correlation between N_{H} and τ_{353} . A tight linear trend can be seen with a Pearson coefficient of 0.95. The value of σ_{353} from the orthogonal distance regression (Boggs & Rogers 1990) linear fit is $(7.9 \pm 0.6) \times 10^{-27} \text{ cm}^2 \text{ H}^{-1}$ (the intercept is set to 0), where the quoted uncertainties are the 95% confidence limits estimated from pair bootstrap resampling. This is consistent to within the uncertainties with that obtained by [PLC2014a](#) based on all-sky HI data from LAB, $(6.6 \pm 1.7) \times 10^{-27} \text{ cm}^2 \text{ H}^{-1}$. Note that here we have quoted the [PLC2014a](#) measurement made toward low N_{HI} positions, because the lack of any HI opacity correction in that work makes this value the most reliable. However, our fit is consistent with all of the σ_{353} values presented in that work (which was based on the *Planck* R1.20 data release), to within the quoted uncertainties.

Small systematic deviations from the linear fit, evident at the high and low column density ends of the plot, are discussed further in Section 4.3.

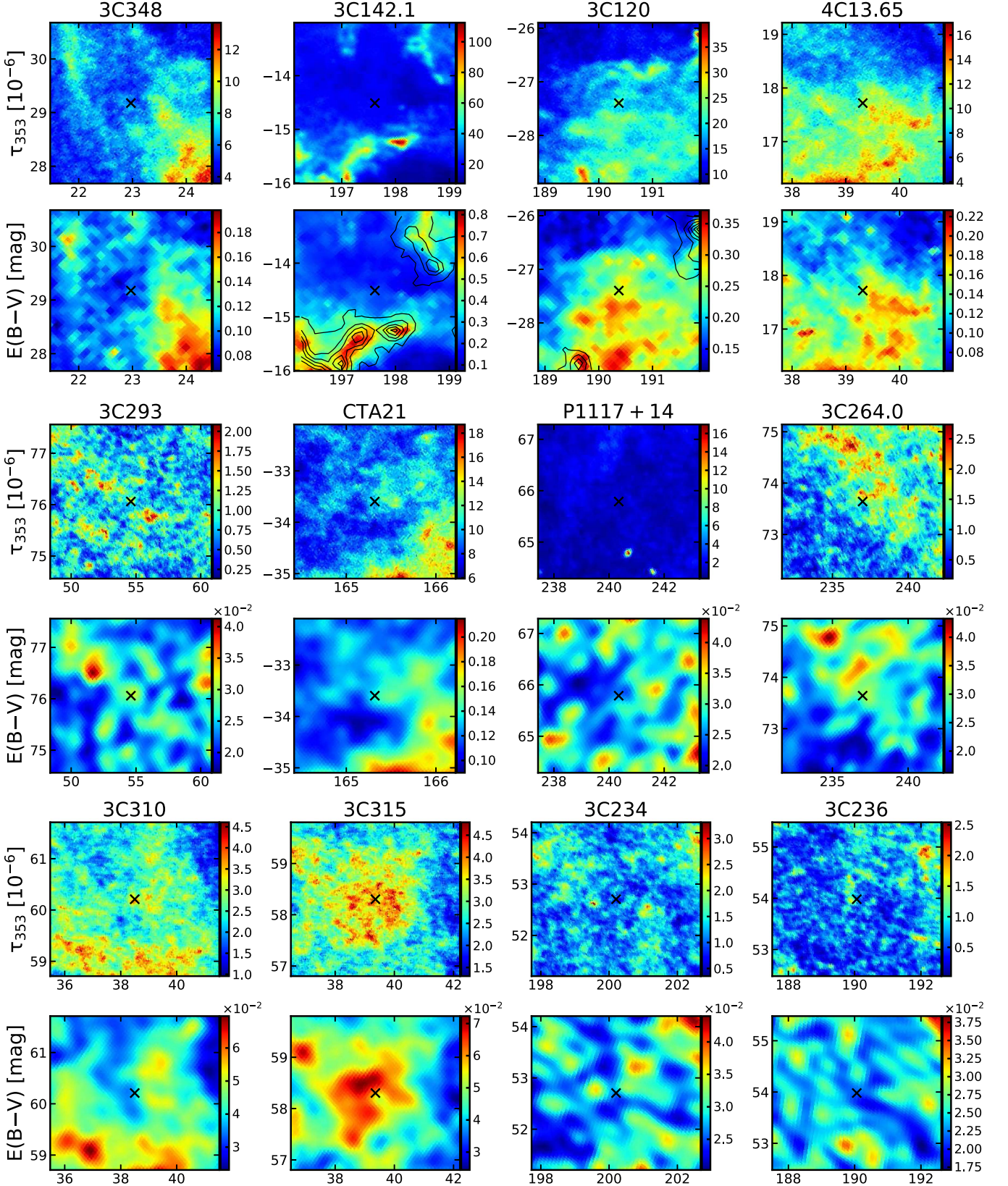


Figure 5. Maps of the immediate vicinity of the 34 “purely atomic” sightlines toward background radio sources. Dust maps ($3^\circ \times 3^\circ$ in Galactic coordinates) are adopted from Planck Collaboration et al. (2014a; τ_{353} , Nside = 2048) and Green et al. (2018; $E(B - V)$, Nside = 1024). The “X” markers show the locations of the radio sources. The contours represent the integrated intensity $W_{\text{CO}(1-0)}$ from the all-sky extension to the maps of Dame et al. (2001; T. Dame 2018, private communication). The base level is at 0.25 K km s^{-1} , the typical sensitivity of the CfA CO survey, and the other contour levels are evenly spaced from the base to the maximum in each map area.

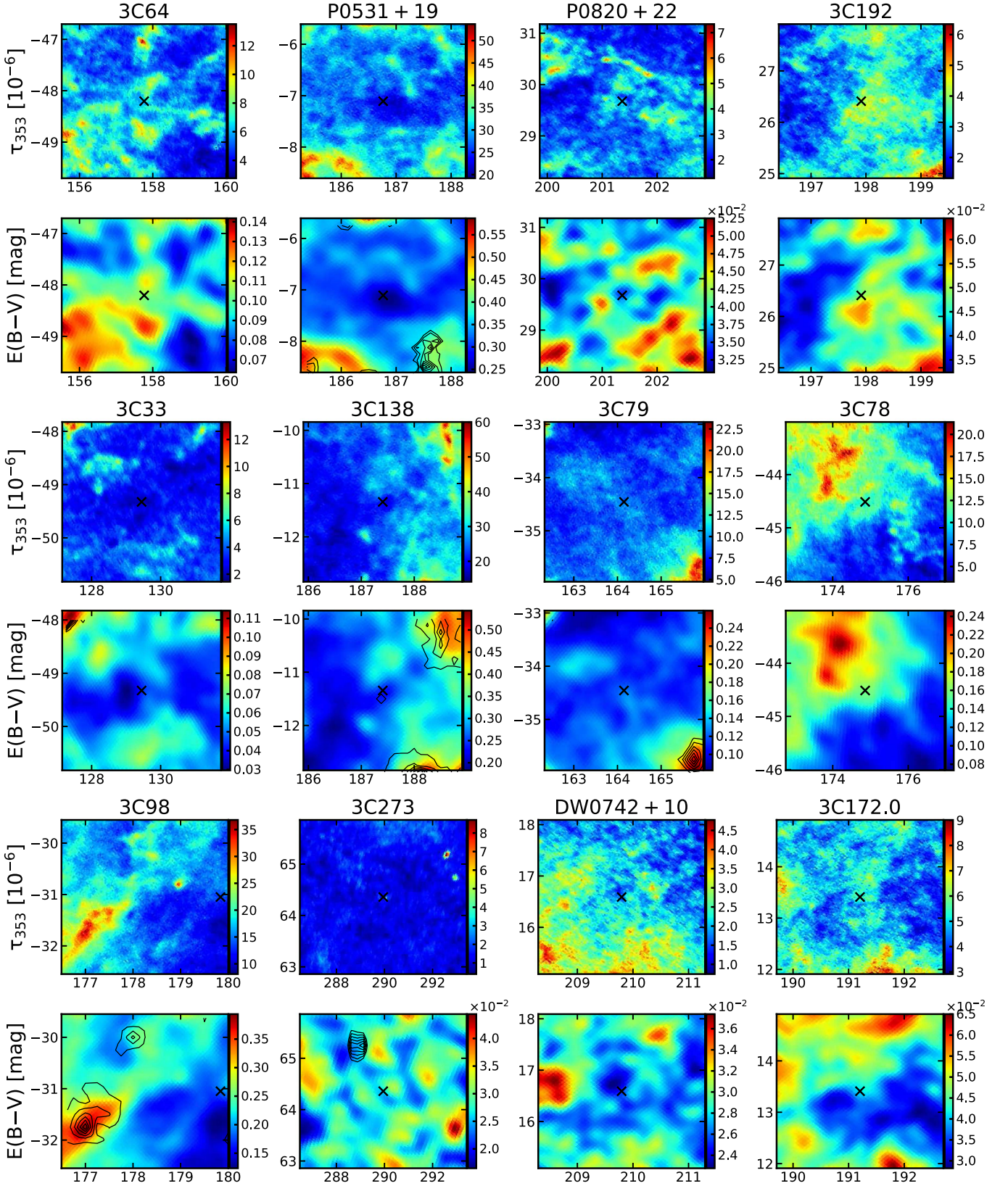


Figure 5. (Continued.)

In order to examine the possible contribution of molecular gas to N_H along the 34 atomic sightlines, we estimate upper limits on N_{H_2} from the 3σ OH detection limits using an

abundance ratio of $X_{OH} = 10^{-7}$ (see Section 5). These values are tabulated in Table 2, and the resulting upper limits on N_H are shown as gray triangles in Figure 7. As

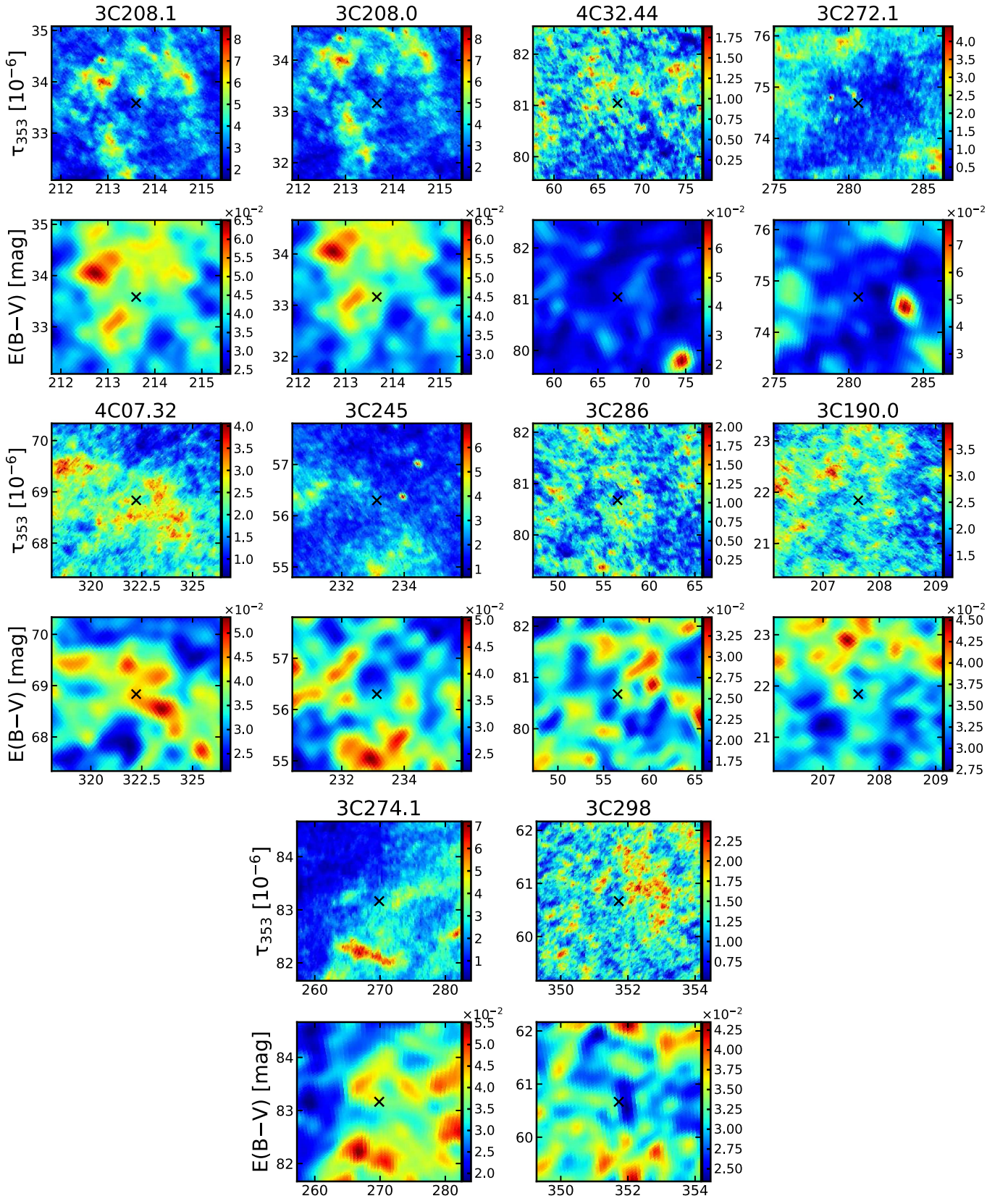


Figure 5. (Continued.)

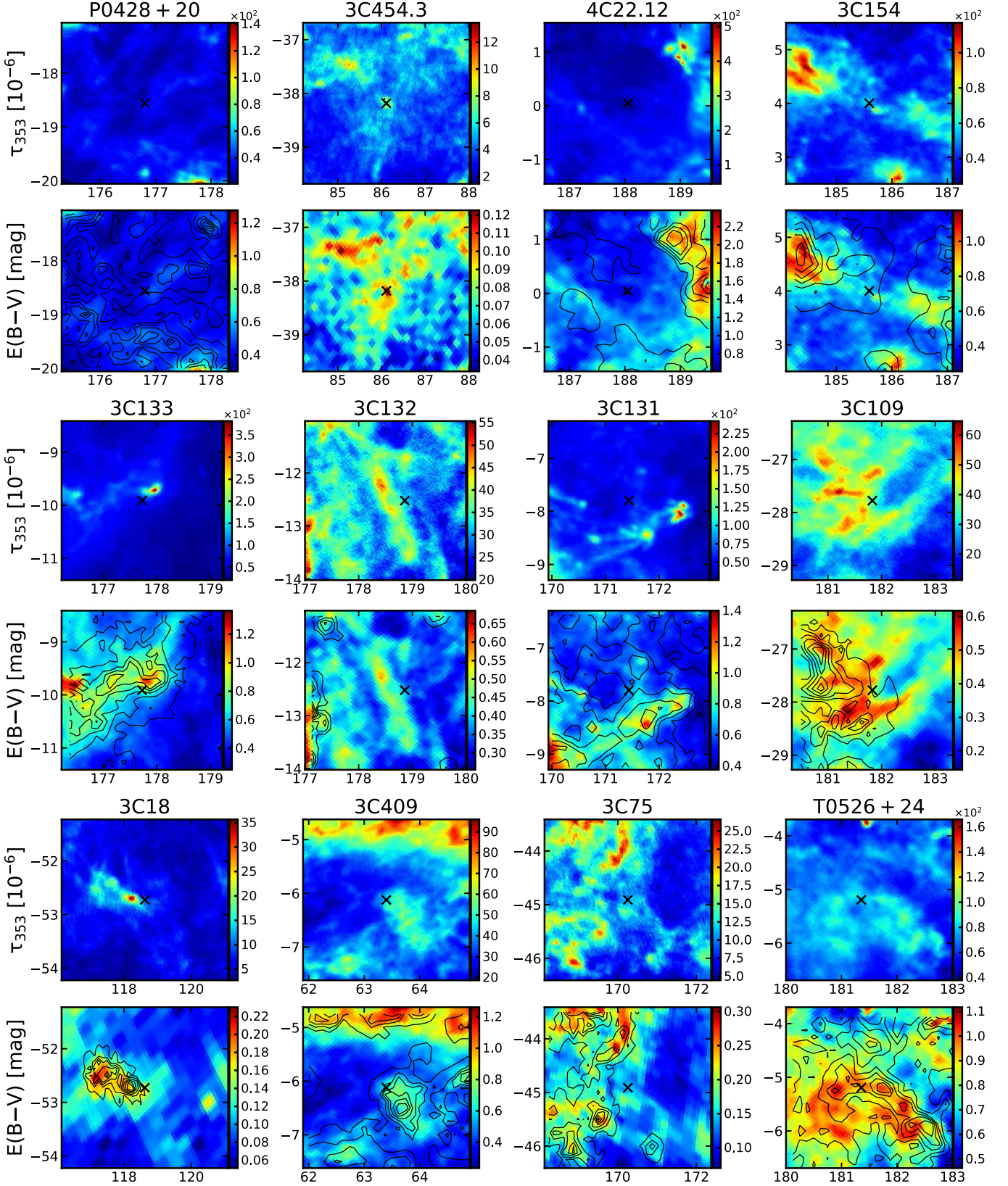


Figure 6. Maps of the immediate vicinity of the 19 OH-detected sightlines toward background radio sources. Dust maps ($3^\circ \times 3^\circ$ in Galactic coordinates) are adopted from Planck Collaboration et al. (2014a; τ_{353} , $N_{\text{side}} = 2048$) and Green et al. (2018; $E(B - V)$, $N_{\text{side}} = 1024$). The “X” markers show the locations of the radio sources. The contours represent the integrated intensity $W_{\text{CO}(1-0)}$ from the all-sky extension to the maps of Dame et al. (2001; T. Dame 2018, private communication). The base level is at 0.25 K km s^{-1} , the typical sensitivity of the CfA CO survey, and the other contour levels are evenly spaced from the base to the maximum in each map area.

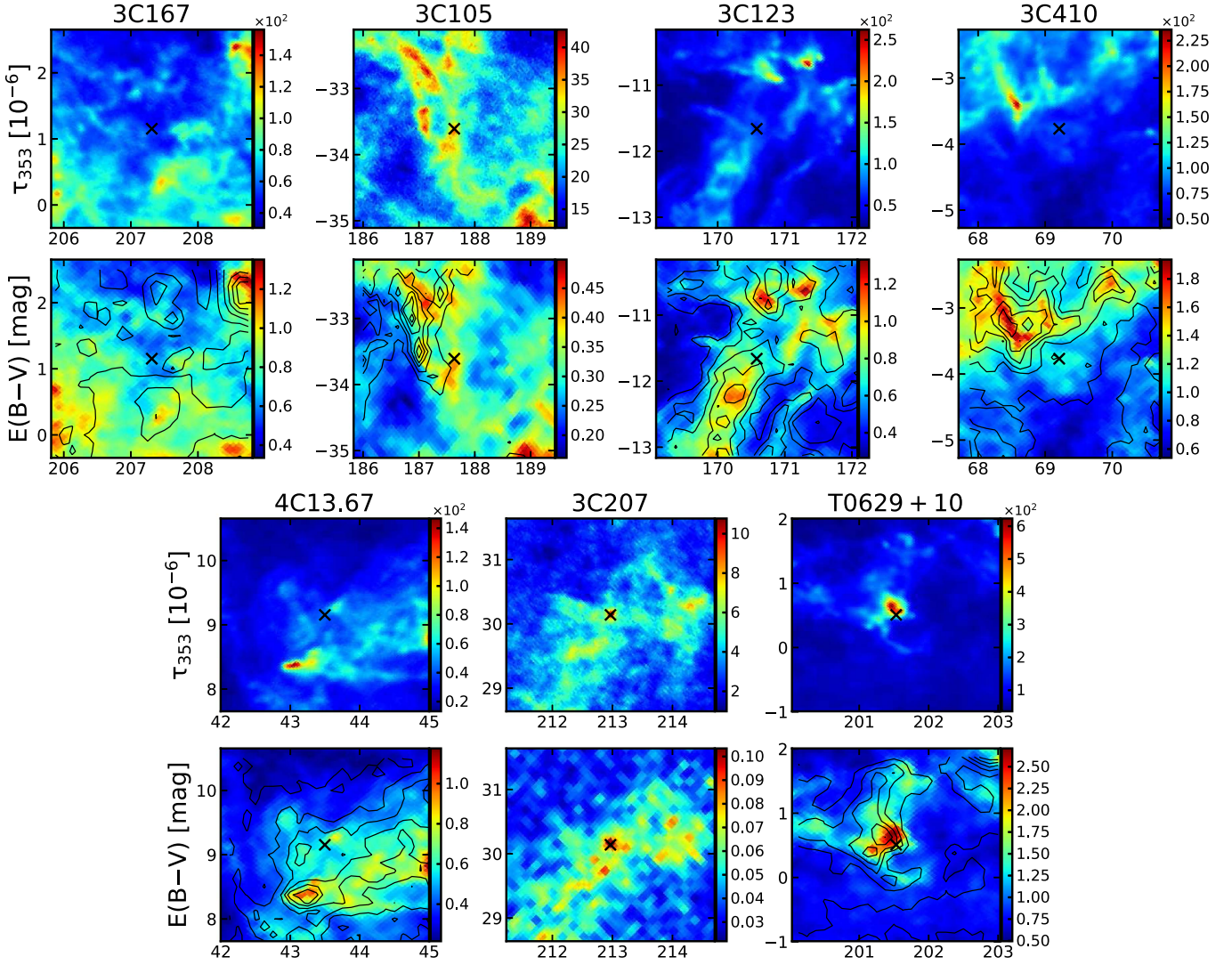


Figure 6. (Continued.)

expected, the σ_{353} obtained from the fit to these upper limits is lower, at $(6.4 \pm 0.3) \times 10^{-27} \text{ cm}^2 \text{ H}^{-1}$. However, while some molecular gas may indeed be present at low levels, these limits should be considered as extreme upper bounds on the true molecular column density. This is particularly true for the most diffuse sightlines with the lowest column density ($N_{\text{H I}} < 5 \times 10^{20} \text{ cm}^{-2}$), where the observational upper limits may appear to raise N_{H} by up to $\sim 50\%$. Molecules are not expected to be well-shielded at such low columns (and indeed even CNM is largely absent along these sightlines in our data). Even for higher column density data points, it can be readily seen from Figures 5 that all sightlines considered in this analysis lie well away from even the faintest outskirts of CO-bright molecular gas complexes. We also note that the deviations from the linear fit that will be discussed in more detail below could not be removed by any selective addition of molecular gas at levels up to these limits.

We next compare our results with the dust opacity σ_{353} derived by Fukui et al. (2015) (plotted on Figure 7 as a dashed line). These authors derived a smaller value than in

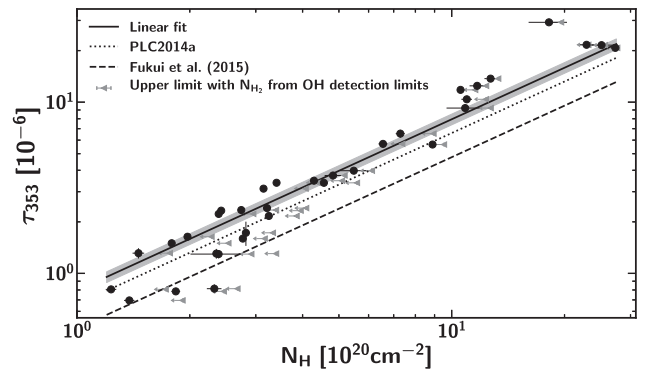


Figure 7. τ_{353} vs. N_{H} along the 34 purely atomic sightlines described in the text. Gray triangles indicate the upper limits for N_{H} along these 34 atomic sightlines with N_{H_2} estimated from the 3σ OH detection limits using an abundance ratio $N_{\text{OH}}/N_{\text{H}_2} = 10^{-7}$. The thick solid line shows the linear fit to the data in this work, the dotted line shows the conversion factor derived by PLC2014a, and the dashed line shows the conversion factor derived by Fukui et al. (2015). (Note that all these works use the same τ_{353} map). τ_{353} error bars are from the uncertainty map of PLC2014a; the shaded region represents the 95% confidence intervals for the linear fit, estimated from pair bootstrap resampling.

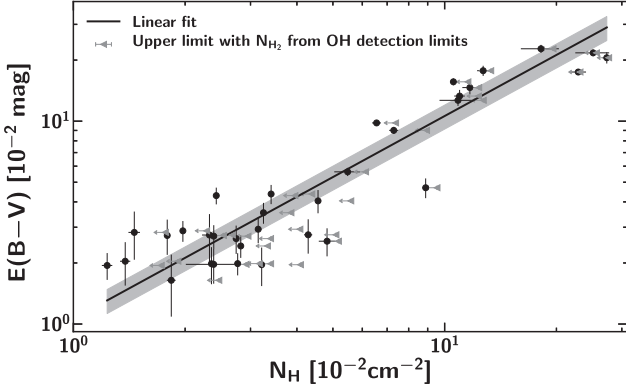


Figure 8. Correlation between N_H and dust reddening $E(B - V)$ from Green et al. (2018) along 34 atomic sightlines. Gray triangles indicate the upper limits for N_H along these 34 atomic sightlines, with N_{H_2} estimated from the 3σ OH detection limits using an abundance ratio $N_{OH}/N_{H_2} = 10^{-7}$. The errorbar on $E(B - V)$ along each sightline is the standard deviation of the 20 Markov Chain realizations of $E(B - V)$ at infinite distance; the shaded region represents the 95% confidence intervals for the linear fit, estimated from pair bootstrap resampling.

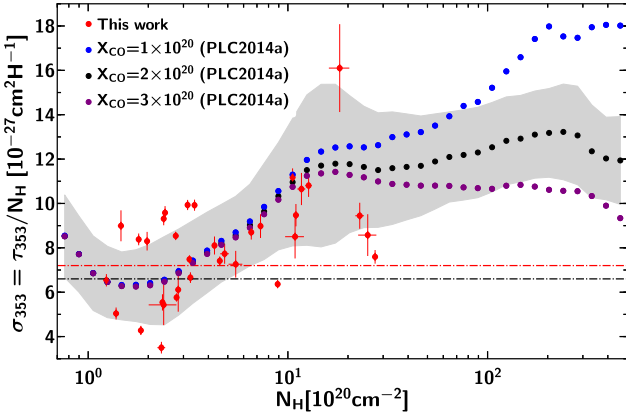


Figure 9. Dust opacity σ_{353} vs. total column density N_H along the 34 purely atomic sightlines presented in this work (red points), overlaid on σ_{353} derived for the whole sky at $30'$ resolution from PLC2014a. Here, blue points assume an $X_{CO} = 1.0 \times 10^{20}$, black assume $X_{CO} = 2.0 \times 10^{20}$, and violet assume $X_{CO} = 3.0 \times 10^{20}$. The gray envelope is the standard deviation of these all-sky measurements for $X_{CO} = 2.0 \times 10^{20}$. The red and black dashed lines show, respectively, the constant σ_{353} derived from the linear fit in Section 4.1 and that obtained from PLC2014a for the low column density regime.

the present work (by a factor of ~ 1.5), by restricting their fit to only the warmest dust temperatures, under the assumption that these most reliably select for genuinely optically thin HI. They then applied this factor to the *Planck* τ_{353} map (excluding $|b| < 15^\circ$ and CO-bright sightlines) to estimate N_{H_1} , assuming that the contribution from CO-dark H_2 was negligible. This resulted in N_{H_1} values ~ 2 – 2.5 times higher than under the optically thin assumption, and motivated their hypothesis that significantly more optically thick HI exists than is usually assumed. However, we find that while the σ_{353} of Fukui et al. (2015) may be a good fit to some sightlines in the very low N_{H_1} regime ($\lesssim 3 \times 10^{20} \text{ cm}^{-2}$), it overestimates N_{H_1} at larger column densities by $\sim 50\%$. Indeed, as will be discussed below, σ_{353} is not expected to remain constant as dust evolves. This (combined with some

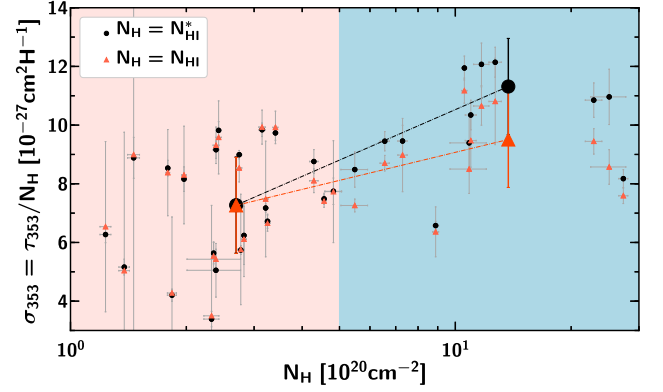


Figure 10. Dust opacity σ_{353} vs. total column density N_H along the 34 purely atomic sightlines presented in this work using true N_{H_1} (red) and $N_{H_1}^*$ (black) as the total gas column density N_H . The large data points are the average values for the low-density ($N_H < 5 \times 10^{20} \text{ cm}^{-2}$) and high-density ($N_H > 5 \times 10^{20} \text{ cm}^{-2}$) regions (error bars on these points are the standard error of the mean). Note that two data points, one black ($\sigma_{353} = 27.2 \times 10^{-27} \text{ cm}^2 \text{ H}^{-1}$) and one red ($\sigma_{353} = 16.1 \times 10^{-27} \text{ cm}^2 \text{ H}^{-1}$), at $N_H = 18.2 \times 10^{20} \text{ cm}^{-2}$ are not shown, but are included in the averages.

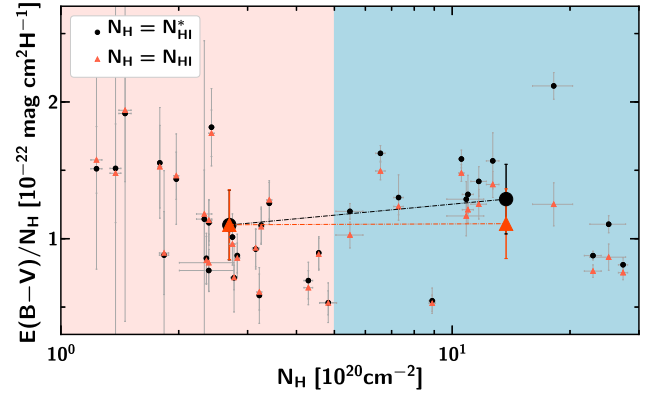


Figure 11. Ratio $E(B - V)/N_H$ as a function of N_H along the 34 purely atomic sightlines presented in this work, using true N_{H_1} (red) and $N_{H_1}^*$ (black) as the total gas column density N_H . The large data points are the average values for the low-density ($N_H < 5 \times 10^{20} \text{ cm}^{-2}$) and high-density ($N_H > 5 \times 10^{20} \text{ cm}^{-2}$) regions (error bars for these points are the standard error on the mean).

contribution from CO-dark H_2) may reconcile the apparent discrepancy between their findings and absorption/emission-based measurements of the opacity-corrected HI column.

4.2. N_H from Dust Reddening $E(B - V)$

Reddening caused by the absorption and scattering of light by dust grains is defined as:

$$E(B - V) = \frac{A_V}{R_V} = 1.086 \frac{\kappa_V}{R_V} r \mu m_H N_H, \quad (12)$$

where A_V is the dust extinction, R_V is an empirical coefficient correlated with the average grain size, and all other symbols are defined as before. In the Milky Way, R_V is typically assumed to be 3.1 (Schultz & Wiemer 1975), but it may vary between 2.5 and 6.0 along different sightlines (Goodman et al. 1995; Draine 2003).

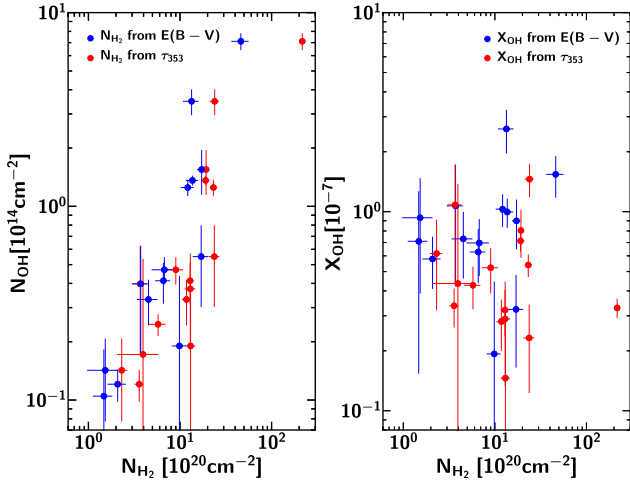


Figure 12. Left: N_{OH} as a function of N_{H_2} obtained from the two N_{H} proxies, $E(B - V)$ (blue) and τ_{353} (red). Right: X_{OH} derived from the two proxies as a function of N_{H_2} .

The ratio $\langle N_{\text{H}}/E(B - V) \rangle = 5.8 \times 10^{21} \text{ cm}^{-2} \text{ mag}^{-1}$ (Bohlin et al. 1978) is a widely accepted standard, used in many fields of astrophysics to connect reddening measurements to gas column density. This value was derived from Ly α and H $_2$ line absorption measurements toward 100 stars (see also Savage et al. 1977), and has been replicated over the years via similar methodology (e.g., Shull & van Steenberg 1985; Diplaz & Savage 1994; Rachford et al. 2009). However, a number of recent works using HI 21 cm data have found significantly higher values (PLC2014a; Liszt 2014a; Lenz et al. 2017).

Here we use the all-sky map of $E(B - V)$ from Green et al. (2018) to estimate the ratio $N_{\text{H}}/E(B - V)$ for our sample of purely atomic sightlines, at $|b| > 5^\circ$. The results are shown in Figure 8. It can be seen that $E(B - V)$ and N_{H} are strongly linearly correlated, with a Pearson coefficient of 0.93. The ratio obtained from the linear fit is $N_{\text{H}}/E(B - V) = (9.4 \pm 1.6) \times 10^{21} \text{ cm}^{-2} \text{ mag}^{-1}$ (the intercept is also set to be 0), where the quoted uncertainties are the 95% confidence limits estimated from pair bootstrap resampling. This value is a factor of 1.6 higher than that in Bohlin et al. (1978).

The value obtained here is consistent with the estimate of Lenz et al. (2017): $N_{\text{H}}/E(B - V) = 8.8 \times 10^{21} \text{ cm}^{-2} \text{ mag}^{-1}$ (no uncertainty is given in that work). These authors compared optically thin HI column density from HI4PI (Collaboration et al. 2016) with various estimates of $E(B - V)$ from Schlegel et al. (1998), Peek & Graves (2010), Schlafly et al. (2014), PLC2014a, and Meisner & Finkbeiner (2015). We note that the estimate of Lenz et al. (2017) is only valid for $N_{\text{H}} < 4 \times 10^{20} \text{ cm}^{-2}$, where it seems safe to assume that the 21 cm emission is optically thin. Our value is also close to that of Liszt (2014a), who find $N_{\text{H}_1}/E(B - V) = 8.3 \times 10^{21} \text{ cm}^{-2} \text{ mag}^{-1}$ (also given without uncertainty) for $|b| \geq 20^\circ$ and $0.015 \lesssim E(B - V) \lesssim 0.075$, by comparing HI data from LAB and $E(B - V)$ from Schlegel et al. (1998). The methodology used by these two studies differs in a number of details. For instance, Liszt (2014a) did not apply a gain correction to the Schlegel et al. (1998) map (whereas Lenz et al. 2017 scaled it down by 12%), and did not smooth it to the LAB angular resolution ($30'$). However, Liszt (2014a) did apply an empirical correction factor to account for HI opacity (albeit one whose effects on high-latitude sightlines was small). These

details may account for the difference between the values obtained by these two otherwise similar studies.

We also note that, like the present work, these studies did not take into account the potential contribution of dust associated with the diffuse warm ionized gas (WIM). This would tend to produce a flattening of the $E(B - V)$ versus N_{H_1} relation at low N_{H_1} and therefore increase the value of $N_{\text{H}_1}/E(B - V)$ artificially. Because we are able to accurately probe a large column density range (up to $3 \times 10^{21} \text{ cm}^{-2}$), we would naively expect our estimate of $N_{\text{H}}/E(B - V)$ to be less affected by WIM bias than either Liszt (2014a) or Lenz et al. (2017; which would tend to have a greater effect on lower column data points). While more work is needed to quantify the contribution of the WIM on dust emission/absorption measurements at low $E(B - V)$, we consider it unlikely to account for the difference between our work and historically lower measurements of the $N_{\text{H}}/E(B - V)$ ratio.

Despite minor differences between these three studies, it is clear that they point to a $N_{\text{H}_1}/E(B - V)$ value of $(\sim 8\text{--}9) \times 10^{21} \text{ cm}^{-2} \text{ mag}^{-1}$. This is 40%–60% higher than the traditional value of Bohlin et al. (1978), which has been used by most models of interstellar dust as a reference point to set the dust-to-gas ratio (e.g., Draine & Fraisse 2009; Jones et al. 2013). We note that if N_{H} is replaced with upper limits (as discussed in Section 4.1), $N_{\text{H}}/E(B - V)$ climbs yet higher, leaving this key conclusion unaffected.

4.3. Disentangling the Effects of Grain Evolution and Dark Gas on σ_{353}

A number of studies have used the correlation between τ_{353} and N_{H} , particularly with regards to the search for dark gas (e.g., Planck Collaboration et al. 2011; Fukui et al. 2014, 2015; Reach et al. 2015). It is clear that τ_{353} and N_{H} are in general linearly correlated only if σ_{353} is a constant. However, it is recognized that σ_{353} is sensitive to grain evolution, and significant variations in the ratio N_{H}/τ_{353} have been observed, particularly when transitioning to the high-density, molecular regime (e.g., Planck Collaboration et al. 2014a, 2015; Okamoto et al. 2017; Remy et al. 2017). The origin of observed variations in σ_{353} may relate to a change in dust properties via κ_{353} , and/or a variation in the dust-to-gas ratio r , but may also include a contribution due to the presence of dark gas, if this is unaccounted for in the estimated N_{H} .

PLC2014a presented the variation in σ_{353} with N_{H} at $30'$ resolution over the entire sky. In that work, N_{H} was derived from $(N_{\text{H}_1}^* + X_{\text{CO}} W_{\text{CO}})$, thus dark gas (both optically thick HI and CO-dark H $_2$) was unaccounted for. We reproduce their data in Figure 9. It can be seen that σ_{353} is roughly flat and at a minimum in a narrow, low column density range $N_{\text{H}} = (1\text{--}3) \times 10^{20} \text{ cm}^{-2}$, then increases linearly until $N_{\text{H}} = 15 \times 10^{20} \text{ cm}^{-2}$, by which point it is almost a factor of 2 higher. It then remains approximately constant for the canonical value of $X_{\text{CO}} = 2.0 \times 10^{20} \text{ cm}^{-2} \text{ K}^{-1} \text{ km}^{-1} \text{ s}$. A key issue for dark gas studies is disentangling how much of the initial rise in σ_{353} is due to changing grain properties and how much is due to the contribution of unseen material, whether it be opaque HI or diffuse H $_2$. (Note also the upturn in σ_{353} seen at the lowest N_{H} , which may be due to the presence of unaccounted-for protons in the warm ionized medium.)

The column density range probed by our purely atomic sightlines, $N_{\text{H}} = (1 \sim 30) \times 10^{20} \text{ cm}^{-2}$ well samples the range where σ_{353} undergoes its first linear increase. Dark gas is also

fully accounted for in our data, since H I is opacity-corrected, and no molecular gas is detected in emission along these sightlines. To quantify the effect of ignoring H I opacity on σ_{353} , we compare σ_{353} deduced from the true, opacity-corrected $N_{\text{H I}}$ with that deduced under the optically thin assumption. The results are shown in Figure 10. In low column density regions ($N_{\text{H}} < 5 \times 10^{20} \text{ cm}^{-2}$), each σ_{353} pair from $N_{\text{H I}}$ and $N_{\text{H I}}^*$ are comparable. However, at higher column densities ($N_{\text{H}} > 5 \times 10^{20} \text{ cm}^{-2}$) σ_{353} from true $N_{\text{H I}}$ is systematically lower than that measured from $N_{\text{H I}}^*$. On average, σ_{353} obtained from optically thin H I column density increases by ~ 1.6 when going from low to high column density regions; whereas σ_{353} from true $N_{\text{H I}}$ increases by ~ 1.4 . This suggests that if H I opacity is not explicitly corrected for, it can account for around one-third (1/3) of the increase of σ_{353} observed during the transition from diffuse to dense atomic regimes. The remaining of two-thirds (2/3) must arise due to changes in dust properties.

From Equation (11), we see that σ_{353} is a function of the dust-to-gas mass ratio, r , and the dust emissivity cross-section, κ_{353} , which depends on the composition and structure of dust grains. Given the uncertainties on the efficiency of the physical processes involved in the evolution of interstellar dust grains, it is difficult at this point to conclude if the variations of σ_{353} observed here are due to an increase of the dust mass (i.e., r) or to a change in the dust emission properties (i.e., κ_{353}). Using the dust model of Jones et al. (2013), Ysard et al. (2015) suggest that most of the variations in the dust emission observed by *Planck* in the diffuse ISM could be explained by relatively small variations in the dust properties. That interpretation would favor a scenario in which the increase of σ_{353} from diffuse to denser gas is caused by the growth of thin mantles via the accretion of atoms and molecules from the gas phase. Even though this process would increase the mass of grains (and therefore increase r), the change of the structure of the grain surface would lead to a larger increase in κ_{353} . Alternatively, it is possible that this systematic variation of τ_{353}/N_{H} could be due to residual large-scale systematic effects in the *Planck* data, or to the fact that the modified blackbody model introduces a bias in the estimate of τ_{353} . Neither of these explanations can be ruled out.

Figure 9 shows σ_{353} as a function of N_{H} superimposed on the results from PLC2014a. It can be seen that we observe a similar rise in σ_{353} in the column density range $(\sim 5\text{--}30) \times 10^{20} \text{ cm}^{-2}$, but less extreme. In particular, most of our data points in the higher column density range ($N_{\text{H}} > 5 \times 10^{20} \text{ cm}^{-2}$) are found below the PLC2014a trend, which is derived from the mean values of σ_{353} over the whole sky in N_{H} bins. This is true even if we use $N_{\text{H I}}^*$ rather than $N_{\text{H I}}$ to derive σ_{353} , indicating that optically thick H I alone cannot shift our data points high enough for a perfect match. This is consistent with the fact that we are examining purely atomic sightlines, and likely happens because we are sampling comparatively low number densities ($n_{\text{H}} \lesssim 10\text{--}100 \text{ cm}^{-3}$; a mixture of WNM and CNM), whereas the sample in PLC2014a includes molecular gas in the N_{H} bins, presumably with a higher κ_{353} . However, in diffuse regions with $N_{\text{H}} < 5 \times 10^{20} \text{ cm}^{-2}$, the mean value of σ_{353} from our sample is comparable with that from PLC2014a.

4.4. $E(B - V)$ as the More Reliable Proxy for N_{H} ?

We have seen that along 34 atomic sightlines $E(B - V)$ shows a tight linear correlation with N_{H} in the column density range $N_{\text{H}} = (1 \sim 30) \times 10^{20} \text{ cm}^{-2}$. τ_{353} also shows a good linear relation with N_{H} but with systematic deviations as described above.

Figure 11 replicates Figure 10 but for $E(B - V)$ rather than τ_{353} . Although the sample used here is small, these figures demonstrate clearly that the ratio $E(B - V)/N_{\text{H}}$ is more stable than τ_{353}/N_{H} over the range of column densities and sightlines covered by our analysis. In fact, with N_{H} corrected for optical depth effects, our data are compatible with a constant value for $E(B - V)/N_{\text{H}}$, up to $N_{\text{H}} = 30 \times 10^{20} \text{ cm}^{-2}$. On the other hand, we have observed an increase of τ_{353}/N_{H} with N_{H} , which we suggest may be due to an increase of the dust emissivity (an increase of r and/or κ_{353} without significantly affecting the dust absorption cross-section). While we are unfortunately unable to follow how these relations evolve at higher A_V and in molecular gas, our results nevertheless suggest that the $E(B - V)$ maps of Green et al. (2018) are a more reliable proxy for N_{H} than the current release of *Planck* τ_{353} in low-to-moderate column density regimes.

5. OH Abundance Ratio X_{OH}

The rotational lines of CO are widely used to probe the physical properties of H_2 clouds, but in diffuse molecular regimes where CO is not detectable in emission other species and transitions must be considered as alternative tracers of H_2 . Among these, the ground-state main lines of OH are a promising dark gas tracer; they are readily detectable in translucent/diffuse molecular clouds (e.g., Magnani & Siskind 1990; Barriault et al. 2010), and since OH is considered to be a precursor molecule necessary for the formation of CO in diffuse regions (Black & Dalgarno 1977; Barriault et al. 2010), it is expected to be abundant in low-CO density/abundance regimes.

The utility of OH as a tracer of CO-dark H_2 depends on our ability to constrain the OH/ H_2 abundance ratio, $X_{\text{OH}} = N_{\text{OH}}/N_{\text{H}_2}$. From an observational perspective, this requires good estimates of both the OH and H_2 column densities, the latter of which often cannot be observed directly. Many efforts (both modeling and observational) have been devoted to deriving X_{OH} in different environmental conditions, which we summarize below:

1. Astrochemical models by Black & Dalgarno (1977) found $X_{\text{OH}} \sim 10^{-7}$ for the case of ζ Ophiuchi cloud.
2. Nineteen comprehensive models of diffuse interstellar clouds with n_{H} from 250 to 1000 cm^{-3} , T_{K} from 20 to 100 K and A_V from 0.62 to 2.12 mag (van Dishoeck & Black 1986) found OH/ H_2 abundances from 1.6×10^{-8} to 2.9×10^{-7} .
3. The OH abundance with respect to H_2 from chemical models of diffuse clouds was found to vary from 7.8×10^{-9} to 8.3×10^{-8} with $A_V = (0.1\text{--}1)$ mag, $T_{\text{K}} = (50\text{--}100)$ K and $n = (50\text{--}1000) \text{ cm}^{-3}$ (Viala 1986).
4. Six model calculations (that differ in depletion factors of heavy elements and cosmic-ray ionization rate) by Nercissian et al. (1988) toward molecular gas in front of the star HD 29647 in Taurus found OH/ H_2 ratios between 5.3×10^{-8} and 2.5×10^{-6} .

5. From OH observations toward high-latitude clouds using the 43 m NRAO telescope, Magnani et al. (1988) derived X_{OH} values between 4.8×10^{-7} to 4×10^{-6} in the range of $A_V = (0.4\text{--}1.1)$ mag, assuming that $N_{\text{H}_2} = 9.4 \times 10^{20} A_V$. However, we note that the excitation temperatures of the OH main lines were assumed to be equal, $T_{\text{ex},1665} = T_{\text{ex},1667}$, likely resulting in overestimation of N_{OH} (see Crutcher 1979; Dawson et al. 2014).
6. Andersson & Wannier (1993) obtained an OH abundance of $\sim 10^{-7}$ from models of halos around dark molecular clouds.
7. Combining N_{OH} data from Roueff (1996) and Felenbok & Roueff (1996) with measurements of N_{H_2} from Savage et al. (1977, using UV absorption), Rachford et al. (2002, using UV absorption) and Joseph et al. (1986, using CO emission), Liszt & Lucas (2002) find $X_{\text{OH}} = (1.0 \pm 0.2) \times 10^{-7}$ toward diffuse clouds.
8. Weselak et al. (2010) derived OH abundances of $(1.05 \pm 0.24) \times 10^{-7}$ from absorption-line observations of five translucent sightlines, with molecular hydrogen column densities N_{H_2} measured through UV absorption by (Rachford et al. 2002, 2009).
9. Xu et al. (2016) report that X_{OH} decreases from 8×10^{-7} to 1×10^{-7} across a boundary region of the Taurus molecular cloud, over the range $A_V = 0.4\text{--}2.7$ mag. N_{H_2} was obtained from an integration of A_V -based estimates of the H_2 volume density (assuming $N_{\text{H}_2} = 9.4 \times 10^{20} A_V$).
10. Recently, Rugel et al. (2018) report a median $X_{\text{OH}} \sim 1.3 \times 10^{-7}$ from THOR Survey observations of OH absorption in the first Milky Way quadrant, with N_{H_2} estimated from $^{13}\text{CO}(1-0)$.

Overall, while model calculations tend to produce some variation in the OH abundance ratio over different parts of parameter space (8×10^{-9} – 4×10^{-6}), observationally determined measurements of X_{OH} cluster fairly tightly around 10^{-7} , with some suggestion that this may decrease for denser sightlines.

In this paper, we determine our own OH abundances, using the MS data set to provide N_{OH} and N_{H_1} ; then employing τ_{353} and $E(B - V)$ (along with our own conversion factors) to compute molecular hydrogen column densities as $N_{\text{H}_2} = \frac{1}{2}(N_{\text{H}} - N_{\text{H}_1})$. We note that since this dust-based estimate of N_{H_2} cannot be decomposed in velocity space, the OH abundances are determined in an integrated fashion for each sightline, and not on a component-by-component basis. While CO was detected along all but one sightline, it was not detected toward all velocity components, meaning that our abundances are generally computed for a mixture of CO-dark and CO-bright H_2 (for further details, see Li et al. 2018).

The OH column densities derived in Section 3 are derived from direct measurements of T_{ex} and τ . This means that they should be accurate compared to methods that rely on assumptions about these variables (see, e.g., Crutcher 1979; Dawson et al. 2014). In computing N_{H} , we assume that the linear correlations (deduced from τ_{353} , $E(B - V)$ and N_{H_1} toward 34 atomic sightlines) still hold in molecular regions. In this manner, estimates of the OH/ H_2 abundance ratio can be obtained within a range of visual extinction $A_V = (0.25\text{--}4.8)$ mag. We note that, of our 19 OH-bright sightlines, 5 produce N_{H_2} that is either negative or consistent with zero to within the measurement uncertainties; these are excluded from the analysis.

Figure 12 shows N_{OH} and X_{OH} as functions of N_{H_2} . We find that N_{OH} increases approximately linearly with N_{H_2} , and the OH/ H_2 abundance ratio is approximately consistent for the two methods, with no evidence of and systematic trends with increasing column density. Differences arise due to the overestimation of N_{H} derived from τ_{353} along dense sightlines compared to N_{H} from $E(B - V)$. As discussed in Section 4, σ_{353} varies by up to a factor of 2 in the range of $N_{\text{H}} = (1 \sim 30) \times 10^{20} \text{ cm}^{-2}$, whereas the ratio $\langle N_{\text{H}}/E(B - V) \rangle$ is quite constant. The mean and standard deviation of the X_{OH} distribution deduced from $E(B - V)$ is $(0.9 \pm 0.6) \times 10^{-7}$, which is close to the canonical value of $\sim 1 \times 10^{-7}$, and double the X_{OH} from τ_{353} , $(0.5 \pm 0.3) \times 10^{-7}$. We regard the higher value as more reliable.

6. Conclusions

We have combined accurate, opacity-corrected HI column densities from the Arecibo Millennium Survey and 21-SPONGE with thermal dust data from the *Planck* satellite and the new $E(B - V)$ maps of Green et al. (2018). We have also made use of newly published Millennium Survey OH data and information on CO detections from Li et al. (2018). In combination, these data sets allow us to select reliable subsamples of purely atomic (or partially molecular) sightlines, and hence assess the impact of HI opacity on the scaling relations commonly used to convert dust data to total proton column density N_{H} . They also allow us to make new measurements of the OH/ H_2 abundance ratio, which is essential in interpreting the next generation of OH data sets. Our key conclusions are as follows:





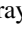
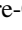

1. HI opacity effects become important above $N_{\text{H}_1} > 5 \times 10^{20} \text{ cm}^{-2}$; below this value the optically thin assumption may usually be considered reliable.
2. Along purely atomic sightlines with $N_{\text{H}} = N_{\text{H}_1} = (1\text{--}30) \times 10^{20} \text{ cm}^{-2}$, the dust opacity, $\sigma_{353} = \tau_{353}/N_{\text{H}}$, is $\sim 40\%$ higher for moderate-to-high column densities than low (defined as above and below $N_{\text{H}} = 5 \times 10^{20} \text{ cm}^{-2}$). We have argued that this rise is likely due to the evolution of dust grains in the atomic ISM, although large-scale systematics in the *Planck* data cannot be definitively ruled out. Failure to account for HI opacity can cause an additional apparent rise of the order of $\sim 20\%$.
3. For purely atomic sightlines, we measure a $N_{\text{H}}/E(B - V)$ ratio of $(9.4 \pm 1.6) \times 10^{21} \text{ cm}^{-2} \text{ mag}^{-1}$. This is consistent with Lenz et al. (2017) and Liszt (2014a), but 60% higher than the canonical value from Bohlin et al. (1978).
4. Our results suggest that N_{H} derived from the $E(B - V)$ map of Green et al. (2018) is more reliable than that obtained from the τ_{353} map of PLC2014a in low-to-moderate column density regimes.
5. We measure the OH/ H_2 abundance ratio, X_{OH} , along a sample of 16 molecular sightlines. We find $X_{\text{OH}} \sim 1 \times 10^{-7}$, with no evidence of a systematic trend with column density. Since our sightlines include both CO-dark and CO-bright molecular gas components, this suggests that OH may be used as a reliable proxy for H_2 over a broad range of molecular regimes.

J.R.D. is the recipient of an Australian Research Council (ARC) DECRA Fellowship (project number DE170101086). D.L. thanks the supports from the National Key R&D Program

of China (2017YFA0402600) and the CAS International Partnership Program (No.114A11KYSB20160008). N.M.-G. acknowledges the support of the ARC through Future Fellowship FT150100024. L.B. acknowledges the support from CONICYT grant PFB06. We are indebted to Professor Mark Wardle for providing us with valuable advice and support. We gratefully acknowledge discussions with Dr. Cormac Purcell and Anita Petzler. Finally, we thank the anonymous referee for comments and criticisms that allowed us to improve the paper.

This research has made use of the NASA/IPAC Infrared Science Archive, which is operated by the Jet Propulsion Laboratory, California Institute of Technology, under contract with the National Aeronautics and Space Administration.

ORCID iDs

Hiep Nguyen  <https://orcid.org/0000-0002-2712-4156>
 J. R. Dawson  <https://orcid.org/0000-0003-0235-3347>
 Ningyu Tang  <https://orcid.org/0000-0002-2169-0472>
 Di Li  <https://orcid.org/0000-0003-3010-7661>
 Claire E. Murray  <https://orcid.org/0000-0002-7743-8129>
 N. M. McClure-Griffiths  <https://orcid.org/0000-0003-2730-957X>
 L. Bronfman  <https://orcid.org/0000-0002-9574-8454>

References

- Abdo, A. A., Ackermann, M., Ajello, M., et al. 2010, *ApJ*, **710**, 133
 Ackermann, M., Ajello, M., Allafort, A., et al. 2012, *ApJ*, **755**, 22
 Ackermann, M., Ajello, M., Baldini, L., et al. 2011, *ApJ*, **726**, 81
 Allen, R. J., Hogg, D. E., & Engelke, P. D. 2015, *AJ*, **149**, 123
 Allen, R. J., Ivetto Rodríguez, M., Black, J. H., & Booth, R. S. 2012, *AJ*, **143**, 97
 Andersson, B.-G., & Wannier, P. G. 1993, *ApJ*, **402**, 585
 Barriault, L., Joncas, G., Lockman, F. J., & Martin, P. G. 2010, *MNRAS*, **407**, 2645
 Bähr, S., Beuther, H., Ott, J., et al. 2015, *A&A*, **580**, A112
 Black, J. H., & Dalgarno, A. 1977, *ApJS*, **34**, 405
 Blitz, L., Bazell, D., & Desert, F. X. 1990, *ApJL*, **352**, L13
 Boggs, P. T., & Rogers, J. E. 1990, *Contemporary Mathematics*, **112**, 186
 Bohlin, R. C., Savage, B. D., & Drake, J. F. 1978, *ApJ*, **224**, 132
 Bolatto, A. D., Wolfire, M., & Leroy, A. K. 2013, *ARA&A*, **51**, 207
 Crutcher, R. M. 1979, *ApJ*, **234**, 881
 Dame, T. M., Hartmann, D., & Thaddeus, P. 2001, *ApJ*, **547**, 792
 Dawson, J. R., Walsh, A. J., Jones, P. A., et al. 2014, *MNRAS*, **439**, 1596
 de Vries, H. W., Heithausen, A., & Thaddeus, P. 1987, *ApJ*, **319**, 723
 Destombes, J. L., Marliere, C., Baudry, A., & Brillet, J. 1977, *A&A*, **60**, 55
 Dickey, J. M., Kulkarni, S. R., van Gorkom, J. H., & Heiles, C. E. 1983, *ApJS*, **53**, 591
 Dickey, J. M., McClure-Griffiths, N. M., Gaensler, B. M., & Green, A. J. 2003, *ApJ*, **585**, 801
 Dickey, J. M., Mebold, U., Stanimirovic, S., & Staveley-Smith, L. 2000, *ApJ*, **536**, 756
 Diplas, A., & Savage, B. D. 1994, *ApJ*, **427**, 274
 Douglas, K. A., & Taylor, A. R. 2007, *ApJ*, **659**, 426
 Draine, B. T. 2003, *ARA&A*, **41**, 241
 Draine, B. T., & Fraisse, A. A. 2009, *ApJ*, **696**, 1
 Draine, B. T., & Li, A. 2007, *ApJ*, **657**, 810
 Engelke, P. D., & Allen, R. J. 2018, *ApJ*, **858**, 57
 Felenbok, P., & Roueff, E. 1996, *ApJL*, **465**, L57
 Fukui, Y., Okamoto, R., Kaji, R., et al. 2014, *ApJ*, **796**, 59
 Fukui, Y., Torii, K., Onishi, T., et al. 2015, *ApJ*, **798**, 6
 Glover, S. C. O., & Mac Low, M.-M. 2011, *MNRAS*, **412**, 337
 Glover, S. C. O., & Smith, R. J. 2016, *MNRAS*, **462**, 3011
 Goodman, A. A., Jones, T. J., Lada, E. A., & Myers, P. C. 1995, *ApJ*, **448**, 748
 Gorenstein, P. 1975, *ApJ*, **198**, 95
 Górski, K. M., Hivon, E., Banday, A. J., et al. 2005, *ApJ*, **622**, 759
 Green, G. M., Schlafly, E. F., Finkbeiner, D., et al. 2018, *MNRAS*, **478**, 651
 Grenier, I. A., Casandjian, J.-M., & Terrier, R. 2005, *Sci*, **307**, 1292
 Hartmann, D., & Burton, W. B. 1997, *Atlas of Galactic Neutral Hydrogen* (Cambridge: Cambridge Univ. Press)
 Haslam, C. G. T., Salter, C. J., Stoffel, H., & Wilson, W. E. 1982, *A&AS*, **47**, 1
 Heiles, C., Perillat, P., Nolan, M., et al. 2001, *PASP*, **113**, 1247
 Heiles, C., Reach, W. T., & Koo, B.-C. 1988, *ApJ*, **332**, 313
 Heiles, C., & Troland, T. H. 2003a, *ApJS*, **145**, 329
 Heiles, C., & Troland, T. H. 2003b, *ApJ*, **586**, 1067
 HI4PI Collaboration, Ben Bekhti, N., Flöer, L., et al. 2016, *A&A*, **594**, A116
 Jones, A. P., Fanciullo, L., Köhler, M., et al. 2013, *A&A*, **558**, A62
 Joseph, C. L., Snow, T. P., Jr., Seab, C. G., & Crutcher, R. M. 1986, *ApJ*, **309**, 771
 Kalberla, P. M. W., Burton, W. B., Hartmann, D., et al. 2005, *A&A*, **440**, 775
 Langer, W. D., Velusamy, T., Pineda, J. L., Willacy, K., & Goldsmith, P. F. 2014, *A&A*, **561**, A122
 Lee, M.-Y., Stanimirović, S., Murray, C. E., Heiles, C., & Miller, J. 2015, *ApJ*, **809**, 56
 Lenz, D., Hensley, B. S., & Doré, O. 2017, *ApJ*, **846**, 38
 Li, D., Tang, N., Nguyen, H., et al. 2018, *ApJS*, **235**, 1
 Liszt, H. 2014a, *ApJ*, **783**, 17
 Liszt, H. 2014b, *ApJ*, **780**, 10
 Liszt, H., & Lucas, R. 1996, *A&A*, **314**, 917
 Liszt, H., & Lucas, R. 2002, *A&A*, **391**, 693
 Magnani, L., Blitz, L., & Wouterloot, J. G. A. 1988, *ApJ*, **326**, 909
 Magnani, L., & Siskind, L. 1990, *ApJ*, **359**, 355
 Martin, P. G., Roy, A., Bontemps, S., et al. 2012, *ApJ*, **751**, 28
 Meisner, A. M., & Finkbeiner, D. P. 2015, *ApJ*, **798**, 88
 Murray, C. E., Stanimirović, S., Goss, W. M., et al. 2015, *ApJ*, **804**, 89
 Nercessian, E., Benayoun, J. J., & Viala, Y. P. 1988, *A&A*, **195**, 245
 Okamoto, R., Yamamoto, H., Tachihara, K., et al. 2017, *ApJ*, **838**, 132
 Paradis, D., Dobashi, K., Shimoikura, T., et al. 2012, *A&A*, **543**, A103
 Peek, J. E. G., & Graves, G. J. 2010, *ApJ*, **719**, 415
 Pineda, J. L., Langer, W. D., Velusamy, T., & Goldsmith, P. F. 2013, *A&A*, **554**, A103
 Planck Collaboration, Abergel, A., Ade, P. A. R., et al. 2014a, *A&A*, **571**, A11
 Planck Collaboration, Abergel, A., Ade, P. A. R., et al. 2014b, *A&A*, **566**, A55
 Planck Collaboration, Ade, P. A. R., Aghanim, N., et al. 2011, *A&A*, **536**, A19
 Planck Collaboration, Fermi Collaboration, Ade, P. A. R., et al. 2015, *A&A*, **582**, A31
 Rachford, B. L., Snow, T. P., Destree, J. D., et al. 2009, *ApJS*, **180**, 125
 Rachford, B. L., Snow, T. P., Tumlinson, J., et al. 2002, *ApJ*, **577**, 221
 Reach, W. T., Heiles, C., & Bernard, J.-P. 2015, *ApJ*, **811**, 118
 Reach, W. T., Koo, B.-C., & Heiles, C. 1994, *ApJ*, **429**, 672
 Reina, C., & Tarengi, M. 1973, *A&A*, **26**, 257
 Remy, Q., Grenier, I. A., Marshall, D. J., & Casandjian, J. M. 2017, *A&A*, **601**, A78
 Roueff, E. 1996, *MNRAS*, **279**, L37
 Rugel, M. R., Beuther, H., Bähr, S., et al. 2018, *A&A*, in press (arXiv:1803.04794)
 Savage, B. D., Bohlin, R. C., Drake, J. F., & Budich, W. 1977, *ApJ*, **216**, 291
 Savage, B. D., & Jenkins, E. B. 1972, *ApJ*, **172**, 491
 Schlafly, E. F., Green, G., Finkbeiner, D. P., et al. 2014, *ApJ*, **786**, 29
 Schlegel, D. J., Finkbeiner, D. P., & Davis, M. 1998, *ApJ*, **500**, 525
 Schultz, G. V., & Wiemer, W. 1975, *A&A*, **43**, 133
 Shull, J. M., & van Steenberg, M. E. 1985, *ApJ*, **294**, 599
 Tang, N., Li, D., Heiles, C., et al. 2016, *A&A*, **593**, A42
 Tielens, A. G. G. M., & Hollenbach, D. 1985a, *ApJ*, **291**, 747
 Tielens, A. G. G. M., & Hollenbach, D. 1985b, *ApJ*, **291**, 722
 van Dishoeck, E. F., & Black, J. H. 1986, *ApJS*, **62**, 109
 van Dishoeck, E. F., & Black, J. H. 1988, *ApJ*, **334**, 771
 Viala, Y. P. 1986, *A&AS*, **64**, 391
 Wannier, P. G., Andersson, B.-G., Federman, S. R., et al. 1993, *ApJ*, **407**, 163
 Weselak, T., Galazutdinov, G. A., Beletsky, Y., & Krelowski, J. 2010, *MNRAS*, **402**, 1991
 Weselak, T., & Krelowski, J. 2014, arXiv:1410.3026
 Wolfire, M. G., Hollenbach, D., & McKee, C. F. 2010, *ApJ*, **716**, 1191
 Xu, D., Li, D., Yue, N., & Goldsmith, P. F. 2016, *ApJ*, **819**, 22
 Ysard, N., Köhler, M., Jones, A., et al. 2015, *A&A*, **577**, A110

4

OH as a reliable tracer of “CO-dark” gas

Stars are formed in molecular clouds composed predominantly of H_2 . It would be ideal if we could probe the physical and chemical properties of these clouds, and track the star formation process, directly from H_2 observations. Unfortunately the molecule is not directly detectable in the typical cold environments of molecular clouds, at temperatures of 10–40 K. Instead, line emission from CO, the second abundant molecule in the ISM, has traditionally been used as the most common tracer of H_2 . However, recent observational and theoretical studies have shown that a significant fraction of the molecular hydrogen gas is unseen by CO (e.g. Grenier et al., 2005, Langer et al., 2010, Planck Collaboration et al., 2011a, Pineda et al., 2013, Smith et al., 2014, Tang et al., 2016). This implies a need for alternative tracers of the molecular ISM, among which the OH molecule, with a low critical density of $\sim 10 \text{ cm}^{-3}$, appears to be a promising candidate. The possibility of OH as a reliable tracer of “CO-dark” molecular gas is the main topic of this Chapter.

In this work, we used emission-absorption measurements of HI and OH from the Arecibo Millennium Survey (Heiles & Troland, 2003a) and a follow-up CO survey along 44 lines of sight to address the question on whether the 18 cm ground-state OH lines can trace molecular gas

effectively, and whether there exist any correlations between OH, CO and H_I in the local ISM. We also quantify the “CO-dark” molecular gas, and carry out a detailed analysis on the OH excitation to investigate whether or not the two OH main lines at 1665 and 1667 GHz generally share a common excitation temperature.

The following presents an article published in March 2018 in The Astrophysical Journal Supplement Series. I contributed to this paper as a co-author. I carried out all the analysis of the OH data (Sections 2.1, 3, and 4.1), which forms the core part of this study. However, I did not contribute significantly to the CO analysis and the discussion on quantifying dark molecular gas.



Where is OH and Does It Trace the Dark Molecular Gas (DMG)?

Di Li^{1,2,3} , Ningyu Tang¹ , Hiep Nguyen^{4,5} , J. R. Dawson^{4,5} , Carl Heiles⁶ , Duo Xu^{1,3,7} , Zhichen Pan¹ , Paul F. Goldsmith⁸ , Steven J. Gibson⁹ , Claire E. Murray^{10,11} , Tim Robishaw¹² , N. M. McClure-Griffiths¹³ , John Dickey¹⁴ , Jorge Pineda⁸ , Snežana Stanimirović¹⁰ , L. Bronfman¹⁵ , and Thomas Troland¹⁶
The PRIMO Collaboration¹⁷

¹ National Astronomical Observatories, CAS, Beijing 100012, People's Republic of China; dili@nao.cas.cn, nytang@nao.cas.cn

² Key Laboratory of Radio Astronomy, Nanjing, Chinese Academy of Science, People's Republic of China

³ University of Chinese Academy of Sciences, Beijing 100049, People's Republic of China

⁴ Department of Physics and Astronomy and MQ Research Centre in Astronomy, Astrophysics and Astrophotonics, Macquarie University, NSW 2109, Australia

⁵ Australia Telescope National Facility, CSIRO Astronomy and Space Science, P.O. Box 76, Epping, NSW 1710, Australia

⁶ Department of Astronomy, University of California, Berkeley, 601 Campbell Hall 3411, Berkeley, CA 94720-3411, USA

⁷ Department of Astronomy, The University of Texas at Austin, Austin, TX 78712, USA

⁸ Jet Propulsion Laboratory, California Institute of Technology, 4800 Oak Grove Drive, Pasadena, CA 91109, USA

⁹ Western Kentucky University, Dept. of Physics and Astronomy, 1906 College Heights Boulevard, Bowling Green, KY 42101, USA

¹⁰ University of Wisconsin, Department of Astronomy, 475 N Charter Street, Madison, WI 53706, USA

¹¹ Space Telescope Science Institute, 3700 San Martin Drive, Baltimore, MD 21218, USA

¹² Dominion Radio Astrophysical Observatory, National Research Council, P.O. Box 248, Penticton, BC, V2A 6J9, Canada

¹³ Research School for Astronomy & Astrophysics, Australian National University, Canberra, ACT 2611, Australia

¹⁴ University of Tasmania, School of Maths and Physics, Hobart, TAS 7001, Australia

¹⁵ Departamento de Astronomía, Universidad de Chile, Casilla 36, Santiago de Chile, Chile

¹⁶ Department of Physics and Astronomy, University of Kentucky, Lexington, Kentucky 40506, USA

Received 2017 November 3; revised 2018 January 8; accepted 2018 January 10; published 2018 February 16

Abstract

Hydroxyl (OH) is expected to be abundant in diffuse interstellar molecular gas because it forms along with H₂ under similar conditions and forms within a similar extinction range. We have analyzed absorption measurements of OH at 1665 MHz and 1667 MHz toward 44 extragalactic continuum sources, together with the $J = 1-0$ transitions of ¹²CO, ¹³CO, and C¹⁸O, and the $J = 2-1$ transition of ¹²CO. The excitation temperatures of OH were found to follow a modified lognormal distribution $f(T_{\text{ex}}) \propto \frac{1}{\sqrt{2\pi}\sigma} \exp\left[-\frac{[\ln(T_{\text{ex}}) - \ln(3.4 \text{ K})]^2}{2\sigma^2}\right]$, the peak of which is close to the temperature of the Galactic emission background (CMB+synchrotron). In fact, 90% of the OH has excitation temperatures within 2 K of the Galactic background at the same location, providing a plausible explanation for the apparent difficulty of mapping this abundant molecule in emission. The opacities of OH were found to be small and to peak around 0.01. For gas at intermediate extinctions ($A_V \sim 0.05-2$ mag), the detection rate of OH with a detection limit $N(\text{OH}) \simeq 10^{12} \text{ cm}^{-2}$ is approximately independent of A_V . We conclude that OH is abundant in the diffuse molecular gas and OH absorption is a good tracer of “dark molecular gas (DMG).” The measured fraction of DMG depends on the assumed detection threshold of the CO data set. The next generation of highly sensitive low-frequency radio telescopes, such as FAST and SKA, will make feasible the systematic inventory of diffuse molecular gas through decomposing, in velocity, the molecular (e.g., OH and CH) absorption profiles toward background continuum sources with numbers exceeding what is currently available by orders of magnitude.

Key words: evolution – ISM: clouds – ISM: molecules

Supporting material: figure set

1. Introduction

The two relatively denser phases of the interstellar medium (ISM) are the atomic cold neutral medium (CNM) traced by the H I λ 21 cm hyperfine structure line and the “standard” molecular (H₂) clouds, usually traced by CO. CO has historically been the most important tracer of molecular hydrogen, which remains largely invisible due to its lack of emission at temperatures in the molecular ISM. Empirically, CO intensities have been used as an indicator of the total molecular mass in the Milky Way and external galaxies through the so-called “X-factor,” with numerous caveats, not least of which is the large opacities of CO transitions. Gases in these two phases dominate the masses of star-forming clouds

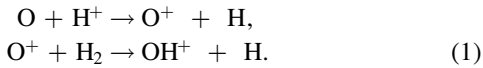
on a galactic scale. The measured ISM gas mass from H I and CO is thus the foundation of many key quantities for understanding galaxy evolution and star formation, such as the star formation efficiency.

A growing body of evidence, however, indicates the existence of gas traced by neither H I nor CO. Comparative studies (e.g., de Vries et al. 1987) of Infrared Astronomy Satellite (IRAS) dust images and gas maps in H I and CO revealed an apparent “excess” of dust emission. The Planck Collaboration et al. (2011) clearly showed excess dust opacity in the intermediate extinction range $A_V \sim 0.05-2$ mag, roughly corresponding to the self-shielding thresholds of H₂ and ¹³CO, respectively. The missing gas, or rather, the undetected gas component, is widely referred to as dark gas, popularized as a common term by Grenier et al. (2005). These

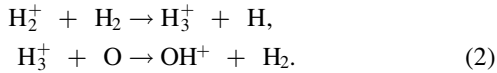
¹⁷ Pacific Rim Interstellar Matter Observers; <http://ism.bao.ac.cn/primo>.

authors found more diffuse gamma-ray emission observed by the Energetic Gamma Ray Experiment Telescope (EGRET) than can be explained by cosmic ray interactions with the observed H-nuclei. Observations of the THz fine structure C^+ line also helped reveal the dark gas, from which the C^+ line strength is stronger than can be produced by only H I gas (Langer et al. 2010; Pineda et al. 2013; Langer et al. 2014). A minority within the ISM community has argued that dark gas can be explained by underestimated H I opacities (Fukui et al. 2015), which is in contrast with some other recent works (Stanimirović et al. 2014; Lee et al. 2015). We focus here on the dark molecular gas (DMG), more specifically CO-dark molecular gas.

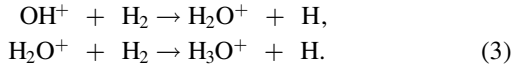
ISM chemistry and PDR models predict the existence of H_2 in regions where CO is not detectable (Wolfire et al. 2010). CO can be have low abundance due to photodissociation in unshielded regions and/or can be heavily subthermal due to low collisional excitation rates in the diffuse gas. OH, or hydroxyl, was the first interstellar molecule detected at radio wavelengths (Weinreb et al. 1963). It can form efficiently through relatively rapid routes, including charge-exchange reactions initiated by cosmic ray ionization once H_2 becomes available (van Dishoeck & Black 1988). Starting from H^+ ,



Also starting from H_2^+ ,

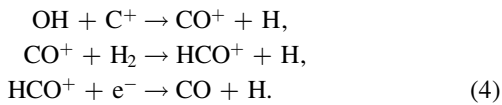


OH^+ then reacts with H_2 to form H_2O^+ , which continues onto H_3O^+ ,



H_2O^+ and H_3O^+ recombine with electrons to form OH.

OH can join the carbon reaction chain through reaction with C^+ and eventually produce CO,



Widespread and abundant OH, along with HCO^+ and C^+ , is thus expected in diffuse and intermediate extinction regions.

OH has been widely detected throughout the Galactic plane (e.g., Caswell & Haynes 1975; Turner 1979; Boyce & Cohen 1994; Dawson et al. 2014; Bihr et al. 2015), in local molecular clouds (e.g., Sancisi et al. 1974; Wouterloot & Habing 1985; Harju et al. 2000), and in high-latitude translucent and cirrus clouds (e.g., Grossmann et al. 1990; Barriault et al. 2010; Cotten et al. 2012). Crucially, a small number of studies have confirmed OH extending outside CO-bright regions (Wannier et al. 1993; Liszt & Lucas 1996; Allen et al. 2012, 2015), and/or associated with narrow H I absorption features (Dickey et al. 1981; Liszt & Lucas 1996; Li & Goldsmith 2003), confirming its viability as a dark gas tracer. OH and HCO^+ have been shown to be tightly correlated in absorption measurements against extragalactic continuum sources (Liszt & Lucas 1996; Lucas & Liszt 1996).

Because OH in emission is typically very weak, large-scale OH maps remain rare, particularly for diffuse molecular gas, which should presumably be dominated by DMG. Detectability often hinges on the presence of a bright continuum background against which the OH lines can be seen in absorption: either the bright diffuse emission of the inner Galactic plane (e.g., Dawson et al. 2014) or bright, compact extragalactic/Galactic sources (e.g., Goss 1968; Nguyen-Q-Rieu et al. 1976; Crutcher 1977, 1979; Dickey et al. 1981; Colgan et al. 1989; Liszt & Lucas 1996). This latter approach has the additional advantage that on-source and off-source comparisons can be made directly to derive optical depths and excitation temperatures. This is the approach we take in this work.

Heiles & Troland (2003a, 2003b) published the Millennium Survey of 21 cm line absorption toward 79 continuum sources. The ON-OFF technique and Gaussian decomposition analysis allowed them to provide direct measurements of the excitation temperature and column density of H I components. Given that the Millennium sources are generally out of the Plane, the absorption components are biased toward local gas. The large gain of Arecibo and the substantial integration time spent on each source made the Millennium Survey one of the most sensitive surveys of the diffuse ISM. Among the most significant findings is the fact that a substantial fraction of the CNM lies below the canonical 100 K temperature predicted by phased ISM models (Field et al. 1969; McKee & Ostriker 1977) for maintaining pressure balance. The existence of cold gas in significant quantities points to the necessity of utilizing absorption measurements for a comprehensive census of ISM, taking into account the general Galactic radiation field.

The L-wide receiver at Arecibo allows for simultaneous observation of H I and OH. This was carried out by the Millennium Survey, but the OH data have remained unpublished until now. To analyze these OH absorption measurements in the context of DMG, we conducted 3 mm and 1 mm CO observations toward the Millennium sources and performed a combined analysis of their excitation and abundances.

This paper is organized as follows. In Section 2, we describe the observations of H I, OH, and CO. In Section 3, we analyze the OH line excitations and other properties. In Section 4, we explore the relation between these three spectral tracers. Discussions and conclusions are presented in Sections 5 and 6, respectively.

2. Observations

2.1. H I and OH

During the Millennium Survey, the Λ -doubling transitions of ground-state OH at 1665.402 and 1667.359 MHz were obtained simultaneously with H I using the Arecibo L-wide receiver towards 72 of the 79 survey positions. These sources typically had a flux density $S_{1.4 \text{ GHz}} \gtrsim 2 \text{ Jy}$, and thus produced antenna temperatures in excess of about 20 K at Arecibo. The observations followed the strategy described by Heiles (2001) and Heiles & Troland (2003a, 2003b)—the so-called Z17 method for obtaining and analyzing absorption spectra toward continuum sources. In this method, half of the integration time was spent on-source, with the remaining time divided evenly among 16 OFF positions. The OFF spectra were then used to reconstruct the “expected” background gas spectrum, which would have been seen were there no continuum source present. The bandwidth of the OH observations was 0.78 MHz, with a

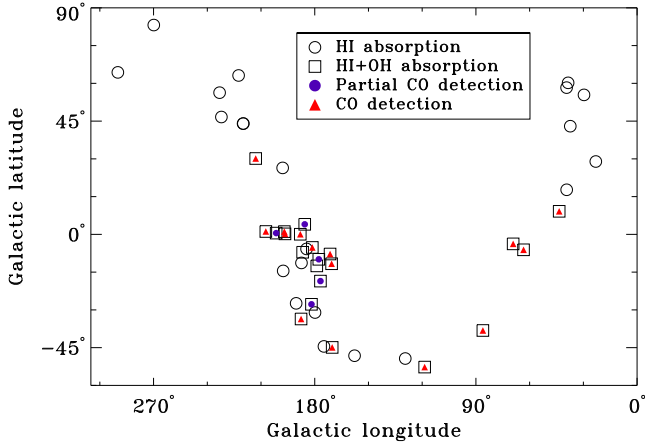


Figure 1. Locations of background continuum sources in Galactic coordinates. This plot shows only the 44 sources towards which H I OH and CO were observed. The open circles represent sources with detected H I absorption only. The squares represent sources with detected H I and OH absorption. The red triangles represent sources with CO detections, in which every detected OH component is also seen in CO. The blue dots represent sources with CO detections, in which some OH components do not have corresponding CO detections. We call these sources “partial CO detections.”

channel width of 381 KHz, corresponding to a velocity resolution of 0.068 km s^{-1} . An rms of 28 mK (T_A) per channel was achieved with 2 hr of total integration time. Twenty-one sightlines exhibited OH absorption.

2.2. CO

We conducted a follow-up CO survey of 44 of the Millennium sightlines for which OH data were taken. Figure 1 shows the distribution of all observed sources in Galactic coordinates.

The $J = 1-0$ transitions of CO, ^{13}CO , and C^{18}O were observed with the Purple Mountain Observatory Delingha (PMODLH) 13.7 m telescope of the Chinese Academy of Sciences. All numbers reported in this section are in units of T_{mb} , since the Delingha system automatically corrected for the main-beam antenna efficiency. The three transitions were observed simultaneously with the 3 mm SIS receiver in 2013 March, 2013 May, 2014 May, and 2016 May. The FFTS wide-band spectral backend has a bandwidth of 1 GHz at a frequency resolution of 61.0 kHz, which corresponds to 0.159 km s^{-1} at 115.0 GHz and 0.166 km s^{-1} at 110.0 GHz. Position-switching mode was used with reference positions selected from the IRAS Sky Survey Atlas.¹⁸ The system temperature varied from 210 K to 350 K for CO, and 140 K to 225 K for the ^{13}CO and C^{18}O observations. The resulting rms is $\sim 60 \text{ mK}$ for a 0.159 km s^{-1} channel for ^{12}CO and $\sim 30 \text{ mK}$ for a 0.166 km s^{-1} channel for ^{13}CO and C^{18}O , respectively.

The $^{12}\text{CO}(J = 2-1)$ data were taken with the Caltech Submillimeter Observatory (CSO) 10.4 m on Maunakea in 2013 July, October, and December. The system temperature varied from 230 to 300 K for $^{12}\text{CO}(J = 2-1)$, resulting in an rms of $\sim 35 \text{ mK}$ at a velocity resolution of 0.16 km s^{-1} .

To achieve consistent sensitivity among sightlines, $^{12}\text{CO}(J = 2-1)$ spectra toward 3 sources were also obtained with the IRAM 30 m telescope in frequency-switching mode on 2016 May 22 and 23. The integration times of these

observation were between 30 and 90 minutes, resulting in an rms of less than 20 mK at a velocity resolution of 0.25 km s^{-1} .

The astronomical software package Gildas/CLASS¹⁹ was used for data reduction, including baseline removal and Gaussian fitting.

3. OH Properties

3.1. Radiative Transfer and Gaussian Analysis

The equations of radiative transfer for ON/OFF source measurements may be written as

$$T_A^{\text{ON}}(\nu)/\eta_b = (T_{\text{ex}} - T_{\text{bg}} - T_c)(1 - e^{-\tau_\nu}) \quad (\text{K}), \quad (5)$$

$$T_A^{\text{OFF}}(\nu)/\eta_b = (T_{\text{ex}} - T_{\text{bg}})(1 - e^{-\tau_\nu}) \quad (\text{K}), \quad (6)$$

where we assumed a main-beam efficiency $\eta_b = 0.5$ according to Heiles et al. (2001) in all subsequent calculations. T_{ex} and τ_ν are the excitation temperature and optical depth of the cold cloud, respectively. $T_A^{\text{ON}}(\nu)$ and $T_A^{\text{OFF}}(\nu)$ are antenna temperatures toward and offset from the continuum source, respectively. Here, T_c is the compact continuum source brightness temperature, and T_{bg} is the background brightness temperature, consisting of the 2.7 K isotropic CMB and the Galactic synchrotron background at the source position. We adopted the same treatment of the background continuum (Heiles & Troland 2003a)

$$T_{\text{bg}} = 2.7 + T_{\text{bg}408}(\nu_{\text{OH}}/408 \text{ MHz})^{-2.8}, \quad (7)$$

where $T_{\text{bg}408}$ comes from Haslam et al. (1982). The background continuum contribution from Galactic H II regions can be safely ignored, since our sources are either at high Galactic latitudes or Galactic Anti-Center longitudes. Typical T_{bg} values are thus found to be around 3.3 K.

We decomposed the OH spectra into Gaussian components to evaluate the physical properties of OH clouds along the line of sight. Following the methodology of Heiles & Troland (2003a), we assumed a two-phase medium, in which cold gas components are seen in both absorption and emission (i.e., in both the opacity and brightness temperature profiles), while warm gas appears only in emission, i.e., only in brightness temperature (see Heiles & Troland (2003a) for further details). While this technique is generally applicable for both H I and OH, we have only detected OH in absorption in this work. “Warm” OH components in emission have been observed by Liszt & Lucas (1996), although only by the NRAO 43 m and not with the VLA or Nancay in their study. This is consistent with our results in that there is no OH warm enough ($> \text{a few hundred K}$) in our Arecibo beam to be seen in emission, nor do we expect it from astrochemistry considerations.

In brief, the expected profile $T_{\text{exp}}(\nu)$ consists of both emission and absorption components:

$$T_{\text{exp}}(\nu) = T_{\text{B,cold}}(\nu) + T_{\text{B,warm}}(\nu), \quad (8)$$

where $T_{\text{B,cold}}(\nu)$ is the brightness temperature of the cold gas and $T_{\text{B,warm}}(\nu)$ is the brightness temperature of the warm gas. Both components contribute to the emission profile.

The opacity spectrum is obtained by combining the on- and off-source spectra (Equations (5) and (6)), and contains only

¹⁸ <http://irsa.ipac.caltech.edu/data/ISSA/>

¹⁹ <http://www.iram.fr/IRAMFR/GILDAS/>

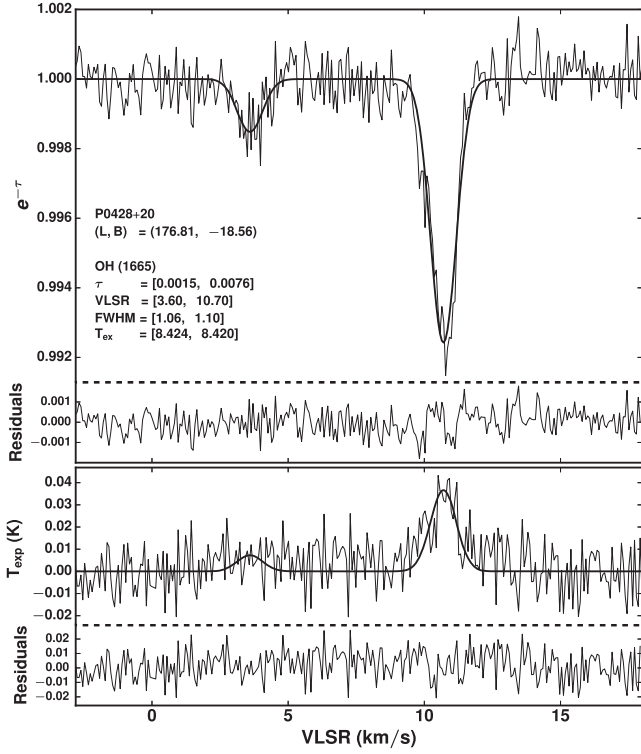


Figure 2. Illustration of derived parameters from the fits to the absorption (upper panel) and expected emission (lower panel) profiles for the source P0428+20. The thin solid lines show the data; the thick solid lines are the fits. The solid lines below the dashed lines present the residuals for absorption and fitted expected emission, respectively.

cold gas seen in absorption. First, we fit the observed opacity spectrum $e^{-\tau(v)}$ with a set of N Gaussian components.

Next, we fit the expected emission profile, T_{exp} , which is assumed to also consist of the N cold components seen in the absorption spectrum, plus any warm components seen only in emission. We further assume that each component is independent and isothermal with an excitation temperature $T_{\text{ex},n}$:

$$\tau(v) = \sum_{n=0}^{N-1} \tau_{0,n} e^{-[(v-v_{0,n})/\delta v_n]^2}. \quad (9)$$

Here, $\tau_{0,n}$, $v_{0,n}$, and δv_n are respectively the peak optical depth, central V_{LSR} , and $1/e$ -width of component n . All the values of $\tau_{0,n}$, $v_{0,n}$, and δv_n were then obtained through least-squares fitting. The contribution of the cold components is given by

$$T_{\text{B,cold}}(v) = \sum_{n=0}^{N-1} T_{\text{ex},n} (1 - e^{-\tau_n(v)}) e^{-\sum_{m=0}^{n-1} \tau_m(v)}, \quad (10)$$

where subscript m describes the M absorbing clouds lying in front of the n th cloud. When $n = 0$, the summation over m takes no effect, as there is no foreground cloud.

We obtained the values of excitation temperature $T_{\text{ex},n}$ from this fit. As in Heiles & Troland (2003a), we experimented with all possible orders along the line of sight and retained the one that yields the smallest residuals.

In total, we detected 48 OH components toward 21 sightlines. Example spectra and fits are shown in Figures 2 and 3.

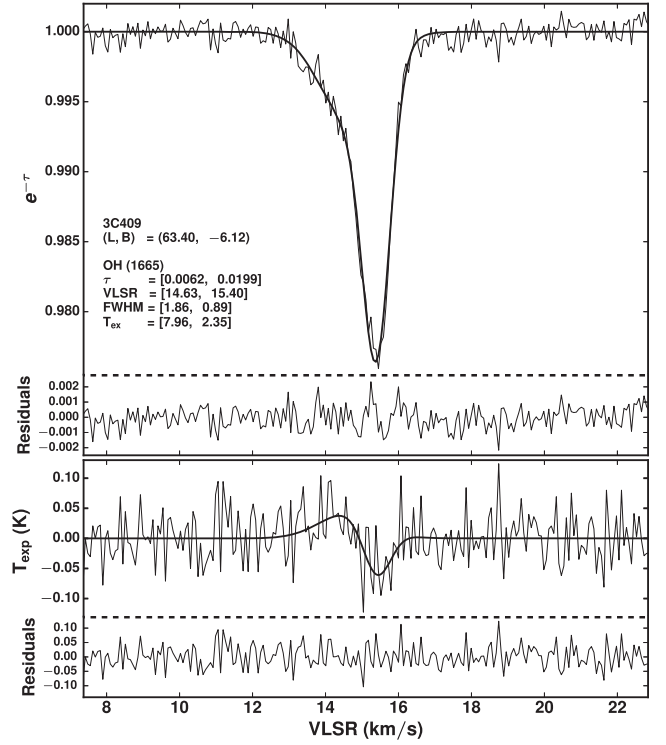


Figure 3. Data for the source 3C409. See Figure 2 for a complete description.

3.2. OH Excitation and Optical Depth

Our fitting scheme provides measurements of the excitation conditions and optical depths of the OH gas.

Figure 4 shows a histogram of optical depths in the two OH main lines, with the 1665 line scaled by a factor of 9/5 (see below). The measured optical depth of both lines peaks at very low values of ~ 0.01 , with a longer tail extending as high as 0.21 in the 1667 line. As can be seen in Table 2, the uncertainties on these values are generally very small. The OH gas probed by absorption is thus quite optically thin.

As seen in Figure 5, OH excitation temperatures in the two main lines peak at ~ 3 –4 K and are similar for the two lines. The majority ($\sim 90\%$) of the components show T_{ex} values within 2 K of the diffuse continuum background temperature, T_{bg} , consistent with measurements from past work (e.g., Nguyen-Q-Rieu et al. 1976; Crutcher 1979; Dickey et al. 1981). The probability density distribution (PDF) of the OH excitation temperature can be fitted by a modified normalized lognormal function,²⁰

$$f(T_{\text{ex}}) \propto \frac{1}{\sqrt{2\pi}\sigma} \exp\left[-\frac{[\ln(T_{\text{ex}}) - \ln(T_{\text{ex}}^0)]^2}{2\sigma^2}\right]. \quad (11)$$

The fit parameters are sensitive to the binning and statistical weighting of the data and are not unique. We chose one solution that preserves the tail of relatively high T_{ex} . The exact numerical values are less meaningful than the location of the distribution peak and the rough trend of T_{ex} , which are represented in the current fitting. The fit results are shown in Figure 6 and Table 1. The statistical uncertainties are small.

²⁰ Equation (11) differs from the standard lognormal function of x in that it has no variable (x) in the denominator.

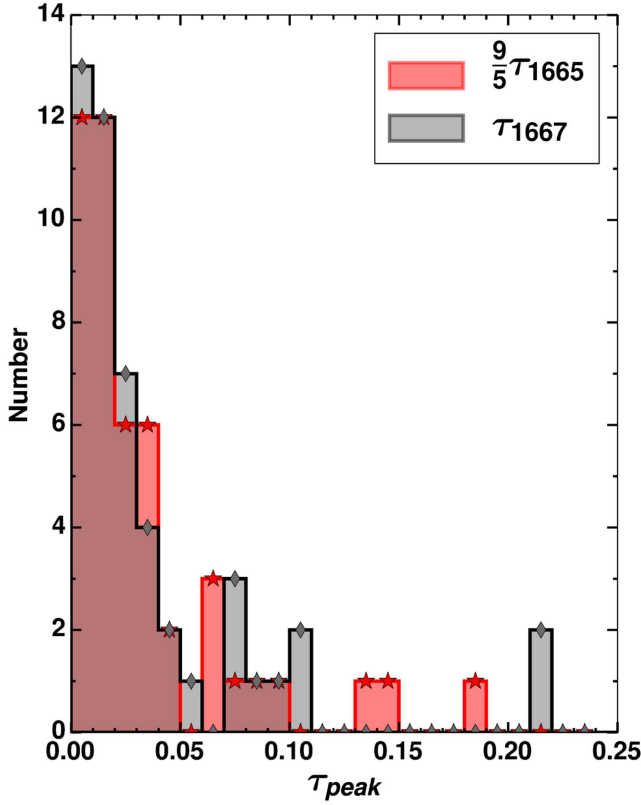


Figure 4. Histogram of peak optical depths of the OH Gaussian components. The black bars show the results for the 1667 MHz line and the red bars show 1.8 times the results for the 1665 MHz line.

Similar numerical values are found in fitting both the 1665 and 1667 transitions. A simple average of the two sets of fit parameters is also presented in Table 1. Given the unbiased nature of absorption-selected sightlines and the fact that almost half of the detected OH components lie at low Galactic latitudes ($|b| < 5^\circ$), such a generic distribution function may be representative of OH excitation conditions in the Galactic ISM. This tentative conclusion will be refined by future observations.

The combined results of T_{ex} and τ reflect the complexities in OH excitation. When the level populations of the OH ground states are in LTE, the excitation temperatures of the 1665 and 1667 MHz lines are equal, and their optical depth ratio ($R_{67/65} = \tau_{1667}/\tau_{1665}$) is 1.8. In general, however, we do not expect OH to be thermally excited. The satellite lines (at 1612 and 1720 MHz) commonly show highly anomalous excitation patterns, with T_{ex} that are strongly subthermal in one line, and either very high or negative (masing) in the other (e.g., Dawson et al. 2014). This may occur due to far-IR or infrared pumping, which can lead to selective overpopulation of either the $F = 1$ or the $F = 2$ level pair (e.g., Guibert et al. 1978). The result is that the main line T_{ex} may be very similar, despite the system as a whole being strongly non-thermally excited.

As shown in Figure 7, most OH components deviate from LTE at more than the formal 1σ uncertainties propagated from the Gaussian fits. The difference between the excitation temperatures, however, mainly falls within 2 K ($|\Delta T_{\text{ex}}| < 2$ K), consistent with values observed in previous absorption measurements toward continuum sources (e.g., Nguyen-Q-Rieu et al. 1976; Crutcher 1977, 1979; Dickey et al. 1981).

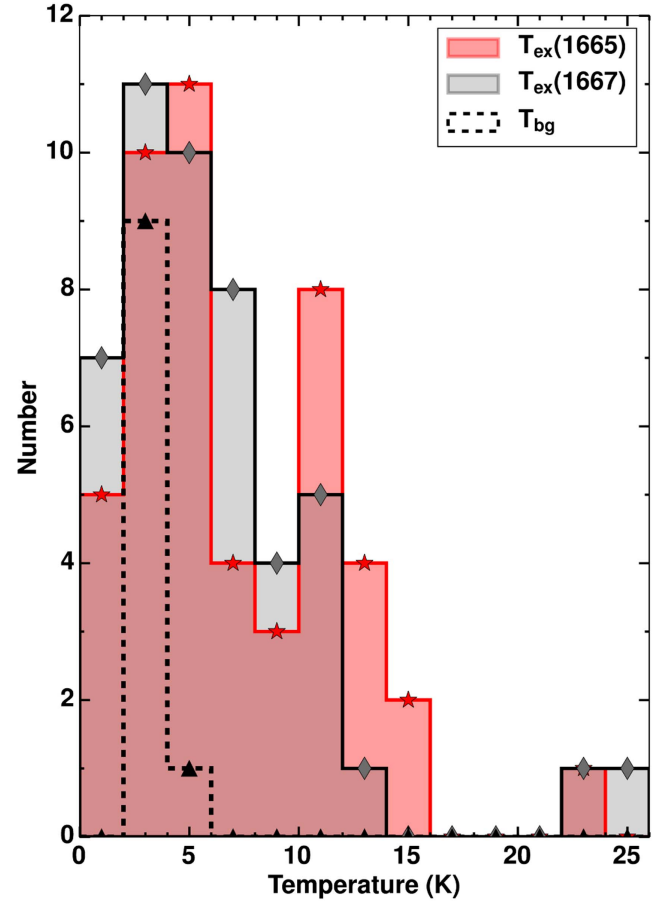


Figure 5. Histograms of excitation temperature, T_{ex} , of the Gaussian components for the two OH main lines, and the background continuum temperature T_{bg} . The number histogram of T_{bg} has been scaled by a factor of 0.5, for ease of visualization.

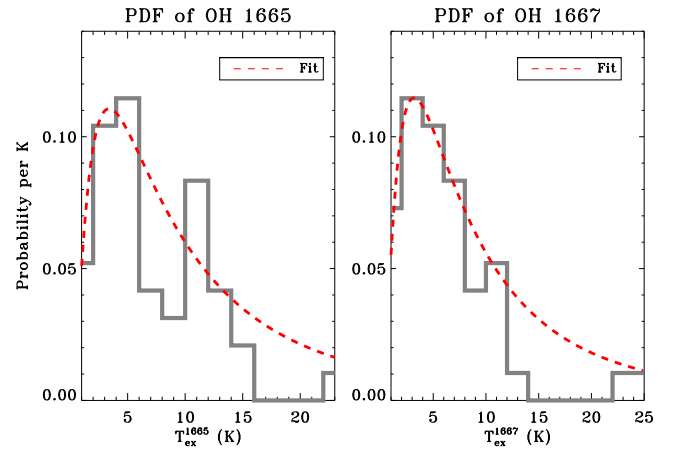


Figure 6. Fitting results of the PDFs of OH excitation temperature for both the 1665 and 1667 lines. Fit parameters are given in Table 1.

3.3. OH Column Density

The column densities of the OH components were computed independently from each line according to

$$N(\text{OH})_{1667} = \frac{8\pi k T_{\text{ex},1667} \nu_{1667}^2}{A_{1667} c^3 h} \frac{16}{5} \int \tau_{1667} dv, \quad (12)$$

Table 1Lognormal Fit Parameters for the OH T_{ex} Distribution, as Shown in Figure 6

Line	Fitted $T_{\text{ex}}^{0\text{a}}$	Fitted σ^{a}
OH 1665	3.4	0.98
OH 1667	3.2	0.96
OH average	3.3	0.97

Note.^a Parameter defined in Equation (11).

$$N(\text{OH})_{1665} = \frac{8\pi k T_{\text{ex},1665} \nu_{1665}^2}{A_{1665} c^3 h} \frac{16}{3} \int \tau_{1665} dv, \quad (13)$$

where $A_{1667} = 7.778 \times 10^{-11} \text{ s}^{-1}$ and $A_{1665} = 7.177 \times 10^{-11} \text{ s}^{-1}$ are the Einstein A-coefficients of the OH main lines (Destombes et al. 1977). The values are tabulated in Table 2 and discussed below.

4. The Relation between H I, CO, and OH

4.1. OH and H I

Regardless of the complexities in the OH excitation, the measured line ratios are generally close to the LTE value of 5/9 with a relatively small scatter. To appropriately utilize both transitions while minimizing the impact of the poorer S/N in the 1665 line, we estimate the total OH column density as $N(\text{OH}) = \frac{5}{14}N(1665) + \frac{9}{14}N(1667)$. The OH column densities obtained with this method are plotted against the H I column density of each Gaussian component in Figure 8 on a component-by-component basis. Since the H I components are always wider than OH lines, the sum of all OH components was used when multiple OH components coincide with one H I component.

For non-detections, an upper limit was estimated based on the 1667 MHz spectrum alone, assuming a single Gaussian optical depth spectrum, with a FWHM of 1.0 km/s and peak τ equal to 3 times the spectral rms. For instance, an rms of 1667 MHz absorption spectrum toward 3C138 is 31 mK in brightness temperature. T_{ex} was assumed to be equal to 3.5 K, the peak of the lognormal function fitted to the T_{ex} distribution in Figure 6. These values are plotted as triangles in Figure 8. Our absorption data set typically has a detection limit around $N(\text{OH}) \simeq 10^{12} \text{ cm}^{-2}$, with a number of higher limits occurring toward weaker continuum background sources.

Many H I components have no detectable OH. Where OH is detected, there is some suggestion of a weak correlation between the OH and H I column densities. For $N(\text{H I})$ between 10^{20} and 10^{21} cm^{-2} most sources are consistent with an $[\text{OH}]/[\text{H I}]$ abundance ratio $\sim 10^{-7}$.

4.2. OH and CO

Both CO and OH are widely used molecular tracers in the ISM. Allen et al. (2012, 2015) performed a pilot OH survey toward the Galactic plane around $l \approx 105^\circ$ and demonstrated the presence of CO-dark molecular gas (DMG): CO emission was absent in more than half of the detected OH spectral features (see also Wannier et al. 1993 and Barriault et al. 2010). Xu & Li (2016) took OH observations across a boundary of the Taurus molecular cloud, revealing that the fraction of DMG decreases from 0.8 in the outer CO poor region to 0.2 in the inner CO abundant region.

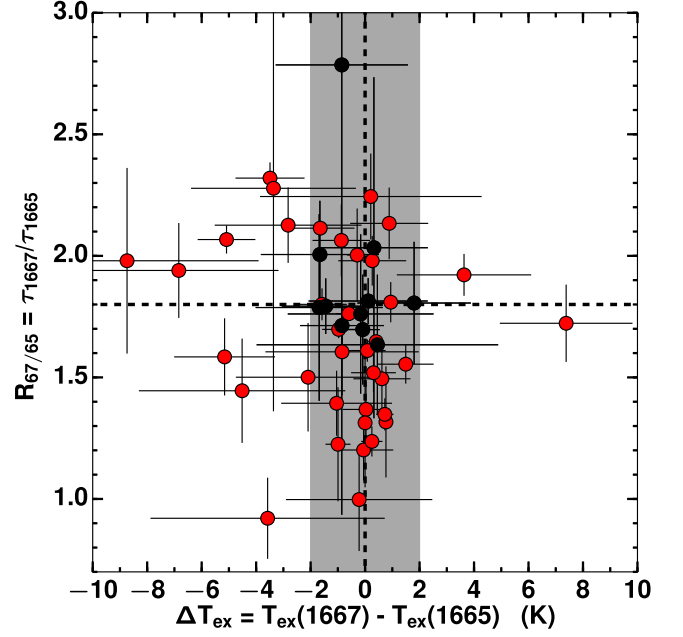


Figure 7. Optical depth ratio ($R_{67/65} = \tau_{1667}/\tau_{1665}$) as a function of excitation temperature difference ($T_{\text{ex}}(1667) - T_{\text{ex}}(1665)$) for the 1667 and 1665 MHz OH lines. The horizontal and vertical dashed lines indicate 1.8 and 0.0, the values for LTE excitation. The error bars indicate the 1σ formal uncertainties propagated through from the Gaussian fits. The black points are those consistent with LTE to within the 1σ errors; the red points are inconsistent. The vertical shaded region represents $|\Delta T_{\text{ex}}| < 2 \text{ K}$.

Our explicit measurements of CO and OH properties allow us to examine the relation between CO and OH again. Nine OH components are identified as DMG clouds and will be discussed in detail in Section 4.3. We focus here on molecular clouds with both OH and CO detections.

CO emission was detected toward 40/49 OH components. CO column density, $N(\text{CO})$, is calculated differently for each of the following three cases:

1. Detection of only $^{12}\text{CO}(J=1-0)$.
2. Detection of both $^{12}\text{CO}(J=1-0)$ and $^{12}\text{CO}(J=2-1)$.
3. Detection of three lines, $^{12}\text{CO}(J=1-0)$, $^{12}\text{CO}(J=2-1)$, and $^{13}\text{CO}(J=1-0)$ simultaneously.

In LTE, the total column density N_{tot} of a two-level transition from upper level u to lower level l is given by

$$N_{\text{tot}} = \frac{8\pi\nu^3}{c^3 A_{ul}} \frac{Q_{\text{rot}}}{g_u} \frac{e^{E_u/kT_{\text{ex}}}}{e^{h\nu/kT_{\text{ex}}} - 1} \int \tau_\nu dv, \quad (14)$$

where A_{ul} is the spontaneous emission coefficient for transitions between levels u and l , g_u is the degeneracy of level u , E_u is the energy of level u , and T_{ex} is the excitation temperature. Q_{rot} is the rotational partition function, given by

$$Q_{\text{rot}} \approx \frac{kT_{\text{ex}}}{hB_0} + \frac{1}{3} + \frac{1}{15} \left(\frac{hB_0}{kT_{\text{ex}}} \right) + \frac{4}{315} \left(\frac{hB_0}{kT_{\text{ex}}} \right)^2 + \frac{1}{315} \left(\frac{hB_0}{kT_{\text{ex}}} \right)^3, \quad (15)$$

which is good to $<1\%$ when $T_{\text{ex}} > 2 \text{ K}$. B_0 is the rotational constant of the molecule.

Table 2
Gaussian Fit Parameters for OH main Lines

Source	l/b	OH(1665)					OH(1667)				
		τ	V_{lsr} (km s ⁻¹)	ΔV (km s ⁻¹)	T_{ex} (K)	$N(\text{OH})$ (10 ¹⁴ cm ⁻²)	τ	V_{lsr} (km s ⁻¹)	ΔV (km s ⁻¹)	T_{ex} (K)	$N(\text{OH})$ (10 ¹⁴ cm ⁻²)
(Name)	($^{\circ}$)										
3C105	187.6/-33.6	0.0158 ± 0.0003	8.14 ± 0.01	0.97 ± 0.02	4.93 ± 0.5	0.32 ± 0.26	0.0268 ± 0.0003	8.17 ± 0.0	0.96 ± 0.01	3.96 ± 0.34	0.24 ± 0.13
3C105	187.6/-33.6	0.0062 ± 0.0003	10.23 ± 0.02	1.03 ± 0.05	8.49 ± 1.26	0.23 ± 0.44	0.0107 ± 0.0003	10.26 ± 0.01	1.03 ± 0.03	7.64 ± 0.88	0.2 ± 0.22
3C109	181.8/-27.8	0.0022 ± 0.0003	9.16 ± 0.1	1.0 ± 0.24	23.68 ± 3.66	0.22 ± 0.73	0.0036 ± 0.0004	9.22 ± 0.07	1.02 ± 0.17	24.13 ± 2.5	0.21 ± 0.36
3C109	181.8/-27.8	0.0035 ± 0.0003	10.44 ± 0.06	0.95 ± 0.15	14.76 ± 2.33	0.21 ± 0.56	0.0057 ± 0.0004	10.58 ± 0.05	1.04 ± 0.11	13.92 ± 1.58	0.19 ± 0.29
3C123	170.6/-11.7	0.0191 ± 0.0008	3.65 ± 0.06	1.19 ± 0.11	11.08 ± 1.79	1.08 ± 1.26	0.0347 ± 0.0012	3.71 ± 0.06	1.22 ± 0.1	11.2 ± 1.26	1.13 ± 0.69
3C123	170.6/-11.7	0.0431 ± 0.0023	4.43 ± 0.01	0.53 ± 0.03	6.42 ± 1.22	0.62 ± 0.57	0.0919 ± 0.004	4.46 ± 0.01	0.53 ± 0.02	7.31 ± 0.75	0.84 ± 0.29
3C123	170.6/-11.7	0.0338 ± 0.0008	5.37 ± 0.01	0.92 ± 0.04	11.62 ± 1.11	1.53 ± 0.8	0.0784 ± 0.0012	5.47 ± 0.01	0.92 ± 0.02	8.13 ± 0.61	1.38 ± 0.37
3C131	171.4/-7.8	0.0065 ± 0.0005	4.55 ± 0.02	0.56 ± 0.06	12.67 ± 1.53	0.2 ± 0.3	0.0103 ± 0.0006	4.56 ± 0.02	0.62 ± 0.05	7.51 ± 1.04	0.11 ± 0.16
3C131	171.4/-7.8	0.0074 ± 0.0006	6.8 ± 0.06	2.97 ± 0.2	10.46 ± 0.86	0.98 ± 0.94	0.0111 ± 0.0005	6.68 ± 0.05	3.32 ± 0.15	11.08 ± 0.59	0.96 ± 0.49
3C131	171.4/-7.8	0.0167 ± 0.0007	6.59 ± 0.01	0.42 ± 0.02	2.66 ± 0.84	0.08 ± 0.19	0.0259 ± 0.0008	6.58 ± 0.01	0.43 ± 0.02	4.15 ± 0.58	0.11 ± 0.1
3C131	171.4/-7.8	0.0521 ± 0.0007	7.23 ± 0.0	0.55 ± 0.01	5.03 ± 0.25	0.62 ± 0.13	0.0858 ± 0.0007	7.23 ± 0.0	0.59 ± 0.01	5.43 ± 0.16	0.65 ± 0.07
3C132	178.9/-12.5	0.0033 ± 0.0002	7.82 ± 0.03	0.89 ± 0.08	15.72 ± 2.08	0.19 ± 0.45	0.0056 ± 0.0003	7.79 ± 0.02	0.81 ± 0.05	23.1 ± 1.27	0.25 ± 0.18
3C133	177.7/-9.9	0.1009 ± 0.001	7.66 ± 0.0	0.53 ± 0.0	2.97 ± 0.22	0.68 ± 0.16	0.2132 ± 0.0016	7.68 ± 0.0	0.52 ± 0.0	1.33 ± 1.24	0.35 ± 0.7
3C133	177.7/-9.9	0.0148 ± 0.001	7.94 ± 0.02	1.23 ± 0.03	5.9 ± 3.41	0.46 ± 2.18	0.0333 ± 0.0015	7.96 ± 0.02	1.23 ± 0.02	6.11 ± 2.22	0.59 ± 1.18
3C154	185.6/4.0	0.0266 ± 0.0006	-2.32 ± 0.01	0.74 ± 0.03	2.61 ± 0.57	0.22 ± 0.3	0.0428 ± 0.0007	-2.34 ± 0.01	0.71 ± 0.02	2.69 ± 0.35	0.19 ± 0.12
3C154	185.6/4.0	0.01 ± 0.0005	-1.39 ± 0.04	0.83 ± 0.09	6.15 ± 1.43	0.22 ± 0.51	0.0179 ± 0.0006	-1.34 ± 0.03	0.91 ± 0.06	4.7 ± 0.74	0.18 ± 0.21
3C154	185.6/4.0	0.0038 ± 0.0004	2.23 ± 0.06	1.12 ± 0.16	6.62 ± 3.22	0.12 ± 0.95	0.0054 ± 0.0005	2.18 ± 0.06	1.33 ± 0.14	2.1 ± 1.99	0.04 ± 0.46
3C167	207.3/1.2	0.0109 ± 0.0019	18.53 ± 0.11	1.27 ± 0.26	4.87 ± 2.23	0.29 ± 1.26	0.0108 ± 0.0013	17.66 ± 0.16	2.71 ± 0.4	4.65 ± 1.49	0.32 ± 1.0
3C18	118.6/-52.7	0.003 ± 0.0003	-8.53 ± 0.11	2.5 ± 0.19	10.93 ± 1.99	0.35 ± 1.16	0.006 ± 0.0003	-8.33 ± 0.05	2.5 ± 0.1	9.27 ± 0.86	0.33 ± 0.39
3C18	118.6/-52.7	0.0056 ± 0.0004	-7.82 ± 0.02	0.68 ± 0.06	2.05 ± 2.03	0.03 ± 0.44	0.0078 ± 0.0005	-7.85 ± 0.01	0.6 ± 0.04	1.0 ± 0.0	0.01 ± 0.0
3C207	213.0/30.1	0.0152 ± 0.0002	4.55 ± 0.01	0.77 ± 0.01	3.17 ± 0.42	0.16 ± 0.17	0.0268 ± 0.0002	4.55 ± 0.0	0.78 ± 0.01	2.57 ± 0.2	0.13 ± 0.06
3C409	63.4/-6.1	0.0062 ± 0.0007	14.63 ± 0.14	1.86 ± 0.15	11.37 ± 1.9	0.55 ± 1.19	0.0057 ± 0.0008	14.7 ± 0.18	1.68 ± 0.18	7.8 ± 3.86	0.18 ± 1.15
3C409	63.4/-6.1	0.0199 ± 0.0012	15.4 ± 0.01	0.89 ± 0.04	0.17 ± 0.86	0.01 ± 0.46	0.0273 ± 0.0016	15.41 ± 0.01	0.86 ± 0.03	0.2 ± 0.0	0.01 ± 0.0
3C410	69.2/-3.8	0.0121 ± 0.0003	6.25 ± 0.01	1.03 ± 0.03	9.4 ± 0.97	0.5 ± 0.47	0.025 ± 0.0004	6.29 ± 0.01	1.19 ± 0.02	4.31 ± 0.43	0.3 ± 0.19
3C410	69.2/-3.8	0.0043 ± 0.0003	10.7 ± 0.04	0.7 ± 0.09	11.26 ± 3.32	0.14 ± 0.65	0.0084 ± 0.0005	10.72 ± 0.04	0.8 ± 0.09	4.42 ± 1.55	0.07 ± 0.27
3C410	69.2/-3.8	0.0053 ± 0.0003	11.67 ± 0.04	0.84 ± 0.09	5.74 ± 2.44	0.11 ± 0.64	0.0114 ± 0.0005	11.68 ± 0.03	0.81 ± 0.07	2.92 ± 1.14	0.06 ± 0.23
3C454.3	86.1/-38.2	0.0023 ± 0.0001	-9.67 ± 0.03	1.63 ± 0.07	4.61 ± 2.14	0.07 ± 0.72	0.0044 ± 0.0001	-9.55 ± 0.02	1.37 ± 0.04	8.25 ± 1.22	0.12 ± 0.26
3C75	170.3/-44.9	0.0072 ± 0.0003	-10.36 ± 0.03	1.32 ± 0.07	3.64 ± 1.09	0.15 ± 0.52	0.0142 ± 0.0003	-10.36 ± 0.02	1.25 ± 0.04	3.91 ± 0.6	0.16 ± 0.21
4C13.67	43.5/9.2	0.0474 ± 0.0037	4.88 ± 0.05	1.3 ± 0.12	10.43 ± 0.9	2.73 ± 1.13	0.057 ± 0.004	4.95 ± 0.05	1.46 ± 0.12	10.37 ± 0.62	2.04 ± 0.56
4C22.12	188.1/0.0	0.0059 ± 0.0009	-2.84 ± 0.06	0.79 ± 0.17	6.91 ± 2.35	0.14 ± 0.61	0.0103 ± 0.001	-2.73 ± 0.04	0.8 ± 0.11	6.75 ± 1.28	0.13 ± 0.25
4C22.12	188.1/0.0	0.0172 ± 0.0011	-1.78 ± 0.02	0.56 ± 0.05	4.67 ± 0.95	0.19 ± 0.3	0.0356 ± 0.0012	-1.78 ± 0.01	0.54 ± 0.02	3.8 ± 0.46	0.17 ± 0.11
GI96.6+0.2	196.6/0.2	0.0043 ± 0.0005	3.22 ± 0.1	1.67 ± 0.25	10.95 ± 2.34	0.34 ± 1.1	0.0065 ± 0.0005	3.43 ± 0.09	2.5 ± 0.24	8.85 ± 1.24	0.34 ± 0.59
GI97.0+1.1	197.0/1.1	0.0124 ± 0.0005	4.83 ± 0.03	1.84 ± 0.09	5.2 ± 0.65	0.5 ± 0.57	0.0188 ± 0.0007	4.72 ± 0.03	1.59 ± 0.07	5.51 ± 0.5	0.39 ± 0.26
GI97.0+1.1	197.0/1.1	0.0057 ± 0.0008	7.46 ± 0.04	0.61 ± 0.1	1.0 ± 0.0	0.01 ± 0.0	0.0075 ± 0.0011	7.34 ± 0.04	0.6 ± 0.1	1.0 ± 0.0	0.01 ± 0.0
GI97.0+1.1	197.0/1.1	0.0053 ± 0.0006	16.41 ± 0.09	1.17 ± 0.22	8.76 ± 1.91	0.23 ± 0.69	0.0094 ± 0.0017	16.34 ± 0.12	0.95 ± 0.19	7.07 ± 1.33	0.15 ± 0.29
GI97.0+1.1	197.0/1.1	0.0069 ± 0.0008	17.65 ± 0.05	0.71 ± 0.12	5.35 ± 1.88	0.11 ± 0.47	0.0124 ± 0.001	17.45 ± 0.12	1.22 ± 0.21	7.15 ± 0.89	0.26 ± 0.29
GI97.0+1.1	197.0/1.1	0.0237 ± 0.0009	32.01 ± 0.01	0.56 ± 0.02	3.41 ± 0.62	0.19 ± 0.23	0.0428 ± 0.0012	32.01 ± 0.01	0.53 ± 0.02	4.35 ± 0.39	0.23 ± 0.1
P0428+20	176.8/-18.6	0.0015 ± 0.0002	3.6 ± 0.08	1.06 ± 0.2	13.3 ± 4.09	0.09 ± 0.71	0.0029 ± 0.0003	3.55 ± 0.04	0.75 ± 0.09	4.56 ± 2.56	0.02 ± 0.25
P0428+20	176.8/-18.6	0.0076 ± 0.0002	10.7 ± 0.02	1.1 ± 0.04	13.29 ± 0.79	0.47 ± 0.32	0.0137 ± 0.0003	10.7 ± 0.01	1.11 ± 0.02	11.71 ± 0.45	0.42 ± 0.14
P0531+19	186.8/-7.1	0.0011 ± 0.00024	1.559 ± 0.087	0.814 ± 0.214	3.49 ± 4.37	0.0133 ± 0.0169	0.00089 ± 0.00024	1.85 ± 0.139	1.053 ± 0.346	4.01 ± 7.1	0.0089 ± 0.0162
T0526+24	181.4/-5.2	0.0158 ± 0.0058	7.58 ± 0.29	1.66 ± 0.74	13.57 ± 2.78	1.51 ± 2.61	0.0359 ± 0.0059	7.49 ± 0.15	1.97 ± 0.39	10.21 ± 1.2	1.7 ± 1.15
T0629+10	201.5/0.5	0.004 ± 0.0026	0.16 ± 0.19	0.64 ± 0.49	4.07 ± 2.23	0.05 ± 0.39	0.0113 ± 0.0023	0.33 ± 0.22	0.97 ± 0.43	3.22 ± 0.96	0.08 ± 0.24
T0629+10	201.5/0.5	0.0378 ± 0.0129	3.13 ± 0.28	0.99 ± 0.43	0.59 ± 0.66	0.09 ± 0.54	0.0769 ± 0.0046	4.17 ± 0.06	3.17 ± 0.22	0.92 ± 1.87	0.53 ± 3.88
T0629+10	201.5/0.5	0.0168 ± 0.0016	1.47 ± 0.11	1.43 ± 0.44	1.49 ± 0.46	0.15 ± 0.37	0.0206 ± 0.0034	1.3 ± 0.1	0.8 ± 0.2	0.5 ± 0.0	0.02 ± 0.01

Table 2
(Continued)

Source (Name)	l/b ($^{\circ}$)	OH(1665)					OH(1667)				
		τ	V_{lsr} (km s^{-1})	ΔV (km s^{-1})	T_{ex} (K)	$N(\text{OH})$ (10^{14} cm^{-2})	τ	V_{lsr} (km s^{-1})	ΔV (km s^{-1})	T_{ex} (K)	$N(\text{OH})$ (10^{14} cm^{-2})
T0629+10	201.5/0.5	0.163 ± 0.0281	3.61 ± 0.02	0.61 ± 0.04	2.33 ± 0.13	0.98 ± 0.22	0.2147 ± 0.0045	3.55 ± 0.0	0.6 ± 0.02	3.1 ± 0.13	0.95 ± 0.09
T0629+10	201.5/0.5	0.0812 ± 0.002	4.62 ± 0.01	0.78 ± 0.03	1.23 ± 0.29	0.33 ± 0.27	0.1004 ± 0.0044	4.64 ± 0.01	0.36 ± 0.02	1.48 ± 0.26	0.13 ± 0.07
T0629+10	201.5/0.5	0.075 ± 0.0018	6.09 ± 0.02	1.05 ± 0.05	3.74 ± 0.2	1.25 ± 0.25	0.1011 ± 0.0043	6.1 ± 0.01	0.64 ± 0.04	4.46 ± 0.25	0.69 ± 0.13
T0629+10	201.5/0.5	0.0371 ± 0.0031	6.99 ± 0.02	0.49 ± 0.06	4.28 ± 0.29	0.33 ± 0.13	0.0744 ± 0.0036	6.93 ± 0.02	0.64 ± 0.05	3.99 ± 0.22	0.45 ± 0.1
T0629+10	201.5/0.5	0.0174 ± 0.0018	7.9 ± 0.05	0.83 ± 0.13	3.54 ± 0.46	0.22 ± 0.22	0.0295 ± 0.0025	7.95 ± 0.03	0.71 ± 0.08	3.46 ± 0.42	0.17 ± 0.12

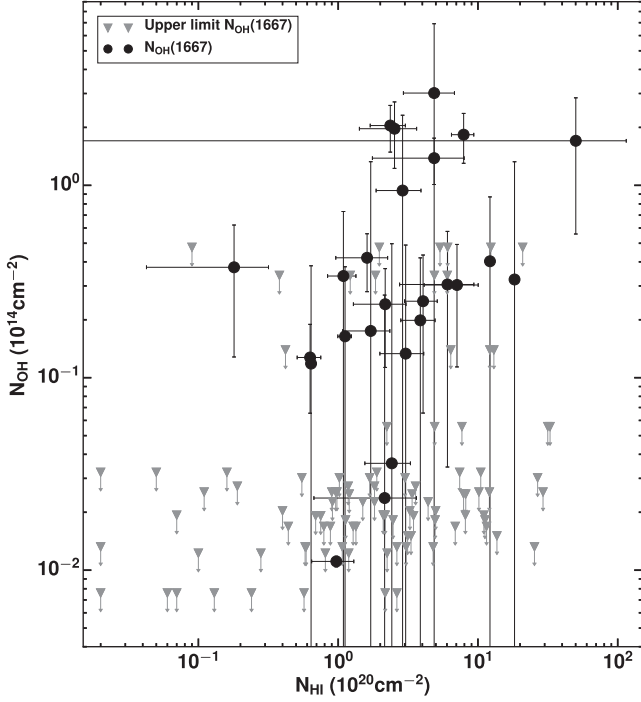


Figure 8. OH column densities derived from the 1667 line, $N(\text{OH})$, vs. H I column densities, $N(\text{H I})$, both on a Gaussian component-by-component basis. The triangles depict approximate upper limits for H I components where OH was not detected (see Section 4.1).

τ_ν is the optical depth of the line, and is related to brightness temperature, T_b , through the radiative transfer equation

$$J(T_b) = f[J(T_{\text{ex}}) - J(T_{\text{bg}})][1 - e^{-\tau_\nu}], \quad (16)$$

where f is the beam filling factor and $J(T) = (h\nu/k)/(e^{h\nu/kT} - 1)$.

When only $^{12}\text{CO}(J=1-0)$ is detected (case 1), we do not adopt the optically thick assumption but adopt the assumption that the excitation temperature of ^{12}CO is 10 K as suggested by Goldsmith et al. (2008) in the Taurus cloud. Optical depth τ_ν can be derived from Equation (16). Then the total column density of ^{12}CO can be derived through the combination of Equations (14) and (15).

For case 2, we adopted the assumption of optically thin $^{12}\text{CO}(J=1-0)$ and $^{12}\text{CO}(J=2-1)$ lines. This is reasonable since there is no $^{13}\text{CO}(J=1-0)$ detection and the corrected antenna temperatures of CO are smaller than 1 K (see, e.g., source 3C105 in Figure 13). The excitation temperature of ^{12}CO , T_{ex} , is then obtained from the following equation

$$\frac{e^{11.06/T_{\text{bg}} - 16.59/T_{\text{ex}}} - e^{-5.53/T_{\text{ex}}}}{e^{5.53/T_{\text{bg}} - 5.53/T_{\text{ex}}} - 1} = \frac{\nu_{21}^3 A_{10} g_1}{2\nu_{10}^3 A_{21} g_2} \times \left[\frac{e^{11.06/T_{\text{bg}}} - 1}{e^{5.53/T_{\text{bg}}} - 1} \right] \frac{\int T_{\text{R}}^{21} dv}{\int T_{\text{R}}^{10} dv}, \quad (17)$$

where $T_{\text{R}} = J(T_b)$. Once T_{ex} in Equation (17) is determined, $N(^{12}\text{CO})$ is derived as done in case 1.

When both $^{12}\text{CO}(J=1-0)$ and $^{13}\text{CO}(J=1-0)$ are detected as in case 3, we assume $\tau_{10}(^{12}\text{CO}) \gg 1$ and derive T_{ex} and

$\tau_{10}(^{13}\text{CO})$ via:

$$T_{\text{ex}} = 5.53 \left\{ \ln \left[1 + \frac{5.532}{T_{\text{R}}(^{12}\text{CO}) + 0.819} \right] \right\}^{-1}. \quad (18)$$

$$\tau_{10}(^{13}\text{CO}) = -\ln \left\{ 1 - \frac{T_{\text{R}}(^{13}\text{CO})}{5.29} [e^{5.29/T_{\text{ex}}} - 1]^{-1} - 0.16 \right\}^{-1}. \quad (19)$$

$N_{\text{tot}}(^{13}\text{CO})$ is then obtained using Equation (15), from which we compute $N_{\text{tot}}(^{12}\text{CO})$ by assuming $[^{12}\text{C}]/[^{13}\text{C}] = 68$ (Milam et al. 2005).

The central velocities of derived OH components are used as initial estimates for CO fitting with the CLASS/GILDAS software. The properties of the fitted CO components are shown in Table 3, and the above calculations of CO excitation temperature and total column density are based on the derived Gaussian fitting results. The coincidence between OH and CO components is judged by central velocity. The velocity difference should be less than 0.5 km s^{-1} . We plot the relation between OH and CO column density in Figure 9. A positive correlation between $\log(N(\text{OH}))$ and $\log(N(\text{CO}))$ is seen. Least-squares fitting yields the relation $\log(N(\text{OH})) = 8.16_{-0.898}^{+0.898} + 0.316_{-0.054}^{+0.054} \log(N(\text{CO}))$. The linear Pearson correlation coefficient is 0.69, indicating a strong correlation. This result is consistent with Allen et al. (2015), where an apparent correlation was found between strong ^{12}CO emission and OH emission.

4.3. CO-dark Molecular Gas

All-sky CFA CO survey data (Dame et al. 2001) have been widely used to investigate the distribution of CO on large scales. Planck Collaboration et al. (2011), for example, analyzed Planck data along with the CFA CO survey to probe the large-scale DMG distribution. In principle, the definition of a DMG cloud depends on the sensitivity of the CO data employed. For example, Donate & Magnani (2017) found that the fraction of CO-dark molecular gas relative to total H_2 decreased from 58% to 30% in the Pegasus-Pisces region when higher sensitivity CO data were taken. In this study, the representative 1σ sensitivity of CFA CO data is about $\sigma_{\text{CFA}} = 0.25 \text{ K per } 0.65 \text{ km s}^{-1}$. Using this as an illustrative detection threshold, we here identify components as “DMG-threshold clouds” in cases where CO emission would be undetected at $3\sigma_{\text{CFA}}$ but is detected at the higher sensitivity of the present work.

We compare the Gaussian components seen in H I absorption, OH absorption, and CO emission. A total of 219 H I and 49 OH absorption components were detected. Most OH components can be associated with an H I component within a velocity offset of 1.0 km s^{-1} , except for three sources with offsets of about 1.5 km s^{-1} . There are four general categories of clouds, three of which are illustrated in Figure 10. Toward 3C192, only H I is present, typical of CNM. Toward 3C133, H I, OH, and several CO and CO isotopologues are all detected, which is representative of “normal” molecular clouds. Toward 3C132, there exists a component with H I and OH absorption, but no CO emission, representing DMG. An example of a DMG-threshold cloud can be found in the spectra of 3C109 (Figure 13), where only weak (0.1 K) CO is detected. In our sample, there are 77.6% CNM, 4.1% DMG, 6.9% DMG-threshold, and 11.4% molecular clouds. In terms of

Table 3
Gaussian Fit Parameters of CO Data

Source (Name)	l/b ($^{\circ}$)	$^{12}\text{CO}(1-0)$			$^{12}\text{CO}(2-1)$			$^{13}\text{CO}(1-0)$			O^b	$N(^{12}\text{CO})$ (10^{17}) cm^{-2}
		T_{peak}^a K	V_{lsr} (km s^{-1})	ΔV (km s^{-1})	T_{peak}^a K	V_{lsr} (km s^{-1})	ΔV (km s^{-1})	T_{peak}^a K	V_{lsr} (km s^{-1})	ΔV (km s^{-1})		
3C105	187.6/−33.6	1.0	8.07 ± 0.03	0.77 ± 0.06	0.3	8.05 ± 0.03	0.45 ± 0.06	0	0.1032 ± 0.0083
3C105	187.6/−33.6	0.9	10.81 ± 0.03	0.68 ± 0.09	0.3	10.20 ± 0.03	0.74 ± 0.08	1	0.0651 ± 0.0082
3C109	181.8/−27.8	0	...
3C109	181.8/−27.8	0.1	10.69 ± 0.15	1.52 ± 0.42	1	0.0206 ± 0.0057
3C123	170.6/−11.7	2.8	3.99 ± 0.00	1.87 ± 0.03	1.4	3.75 ± 0.03	1.71 ± 0.10	0.1	3.87 ± 0.23	1.33 ± 0.38	0	1.7736 ± 0.0312
3C123	170.6/−11.7	3.2	4.18 ± 0.00	0.47 ± 0.01	2.2	4.07 ± 0.01	0.51 ± 0.03	1.1	4.41 ± 0.01	0.48 ± 0.02	1	5.1962 ± 0.1415
3C123	170.6/−11.7	3.2	5.21 ± 0.01	1.62 ± 0.02	1.8	5.14 ± 0.03	1.43 ± 0.07	0.3	5.17 ± 0.06	0.93 ± 0.14	2	3.1336 ± 0.0483
3C131	171.4/−7.8	0.7	4.59 ± 0.16	0.71 ± 0.16	0.4	4.56 ± 0.05	0.84 ± 0.13	0	0.0506 ± 0.0113
3C131	171.4/−7.8	1.8	6.88 ± 0.16	2.07 ± 0.16	0.9	6.92 ± 0.01	1.64 ± 0.10	0.2	6.81 ± 0.05	0.96 ± 0.12	1	3.2982 ± 0.3194
3C131	171.4/−7.8	1.2	6.64 ± 0.16	0.72 ± 0.16	0.8	6.64 ± 0.03	0.67 ± 0.06	2	0.0842 ± 0.0187
3C131	171.4/−7.8	0.7	7.18 ± 0.16	0.48 ± 0.16	0.3	7.10 ± 0.04	0.41 ± 0.01	3	0.0335 ± 0.0112
3C132	178.9/−12.5	0	...
3C133	177.7/−9.9	3.1	7.43 ± 0.00	0.86 ± 0.01	2.0	7.50 ± 0.01	0.81 ± 0.02	0.3	7.36 ± 0.03	0.70 ± 0.06	0	2.0087 ± 0.0248
3C133	177.7/−9.9	1	...
3C154	185.6/4.0	3.7	-2.41 ± 0.01	1.23 ± 0.02	2.1	-2.37 ± 0.35	1.24 ± 0.35	0.9	-2.06 ± 0.01	1.13 ± 0.03	0	8.6360 ± 0.1185
3C154	185.6/4.0	3.0	-1.62 ± 0.01	0.94 ± 0.01	1.5	-1.57 ± 0.35	0.79 ± 0.35	1	0.2972 ± 0.0047
3C154	185.6/4.0	2	...
3C167	207.3/1.2	0.7	17.47 ± 0.31	1.59 ± 0.57	0.3	17.64 ± 0.25	1.62 ± 0.32	0	0.1098 ± 0.0394
3C18	118.6/−52.7	0.5	-8.22 ± 0.06	1.31 ± 0.14	0.1	-8.32 ± 0.14	0.56 ± 0.32	0	0.1078 ± 0.0117
3C18	118.6/−52.7	0.2	-7.10 ± 0.08	0.40 ± 0.15	0.1	-7.74 ± 0.17	0.33 ± 0.30	1	0.0082 ± 0.0030
3C207	213.0/30.1	0.4	4.79 ± 0.02	1.00 ± 0.04	0.2	4.74 ± 0.09	0.80 ± 0.19	0	0.0443 ± 0.0019
3C409	63.4/−6.1	0.2	13.82 ± 0.30	1.25 ± 0.44	0.2	14.44 ± 0.24	2.08 ± 0.23	0	0.0281 ± 0.0099
3C409	63.4/−6.1	1.3	15.20 ± 0.04	1.13 ± 0.08	0.6	15.23 ± 0.01	1.02 ± 0.05	1	0.1479 ± 0.0105
3C410	69.2/−3.8	1.4	5.96 ± 0.01	0.81 ± 0.04	1.1	5.92 ± 0.01	0.52 ± 0.03	0.1	5.74 ± 0.06	0.73 ± 0.26	0	0.7262 ± 0.0545
3C410	69.2/−3.8	0.2	10.97 ± 0.27	0.45 ± 0.64	1	0.0154 ± 0.0219
3C410	69.2/−3.8	0.2	11.54 ± 0.40	0.44 ± 0.50	2	0.0168 ± 0.0192
3C454.3	86.1/−38.2	0.9	-9.41 ± 0.03	0.79 ± 0.07	0.2	-9.62 ± 0.05	1.20 ± 0.14	0	0.0713 ± 0.0063
3C75	170.3/−44.9	1.6	-10.28 ± 0.01	0.90 ± 0.03	1.1	-10.29 ± 0.02	0.62 ± 0.05	0	0.1420 ± 0.0042
4C13.67	43.5/9.2	6.6	4.75 ± 0.01	1.54 ± 0.02	3.5	4.89 ± 0.01	1.65 ± 0.02	1.2	4.91 ± 0.01	0.99 ± 0.03	0	15.6457 ± 0.1521
4C22.12	188.1/0.0	1.6	-2.58 ± 0.16	0.94 ± 0.16	1.0	-2.44 ± 0.01	1.19 ± 0.03	0.2	-2.47 ± 0.12	0.82 ± 0.21	0	1.9370 ± 0.2582
4C22.12	188.1/0.0	1.3	-1.96 ± 0.16	0.67 ± 0.16	1	0.1639 ± 0.0387
G196.6+0.2	196.6/0.2	0.3	3.42 ± 0.14	2.14 ± 0.25	0	0.0575 ± 0.0067
G197.0+1.1	197.0/1.1	2.9	5.07 ± 0.16	1.93 ± 0.16	1.4	4.92 ± 0.03	1.90 ± 0.05	0.2	5.04 ± 0.10	1.39 ± 0.24	0	2.2626 ± 0.1892
G197.0+1.1	197.0/1.1	0.8	7.18 ± 0.16	1.01 ± 0.16	0.6	7.33 ± 0.04	1.20 ± 0.08	1	0.0825 ± 0.0130
G197.0+1.1	197.0/1.1	0.4	16.34 ± 0.16	0.97 ± 0.16	0.0	16.63 ± 0.35	2.60 ± 0.35	2	0.0395 ± 0.0065
G197.0+1.1	197.0/1.1	0.4	17.39 ± 0.16	1.18 ± 0.16	0.1	17.52 ± 0.35	1.86 ± 0.35	3	0.0489 ± 0.0066
G197.0+1.1	197.0/1.1	0.5	32.24 ± 0.05	1.24 ± 0.02	0.3	32.28 ± 0.35	0.76 ± 0.35	4	0.0704 ± 0.0010
P0428+20	176.8/−18.6	0	...
P0428+20	176.8/−18.6	0.9	10.71 ± 0.02	0.89 ± 0.05	0.3	10.59 ± 0.06	0.98 ± 0.14	1	0.0857 ± 0.0049
T0526+24	181.4/−5.2	8.0	6.86 ± 0.00	1.07 ± 0.01	6.3	6.90 ± 0.00	0.89 ± 0.01	0.5	6.95 ± 0.02	0.83 ± 0.04	0	3.3663 ± 0.0226
T0629+10	201.5/0.5	0	...
T0629+10	201.5/0.5	1	...
T0629+10	201.5/0.5	1.2	1.13 ± 0.16	2.20 ± 0.16	0.5	1.30 ± 0.16	2.24 ± 0.16	2	0.2812 ± 0.0203
T0629+10	201.5/0.5	5.5	2.85 ± 0.16	1.25 ± 0.16	5.0	2.74 ± 0.16	1.15 ± 0.16	4.1	3.71 ± 0.17	1.64 ± 0.17	3	59.8330 ± 8.2582

Table 3
(Continued)

Source (Name)	l/b ($^{\circ}$)	$^{12}\text{CO}(1-0)$			$^{12}\text{CO}(2-1)$			$^{13}\text{CO}(1-0)$			O^b	$N(^{12}\text{CO})$ (10^{17}) cm^{-2}
		T_{peak}^a K	V_{lsr} (km s^{-1})	ΔV (km s^{-1})	T_{peak}^a K	V_{lsr} (km s^{-1})	ΔV (km s^{-1})	T_{peak}^a K	V_{lsr} (km s^{-1})	ΔV (km s^{-1})		
T0629+10	201.5/0.5	8.3	4.49 ± 0.16	1.85 ± 0.16	7.4	4.58 ± 0.16	1.63 ± 0.16	2.5	4.99 ± 0.17	1.06 ± 0.17	4	36.1908 ± 3.5195
T0629+10	201.5/0.5	6.6	6.19 ± 0.16	1.40 ± 0.16	6.1	6.36 ± 0.16	1.33 ± 0.16	3.7	6.01 ± 0.17	0.74 ± 0.17	5	51.6879 ± 6.1885
T0629+10	201.5/0.5	1.9	7.16 ± 0.16	1.57 ± 0.16	1.4	7.28 ± 0.16	1.39 ± 0.16	1.2	6.66 ± 0.17	0.75 ± 0.17	6	21.8699 ± 2.4927
T0629+10	201.5/0.5	7	...

Notes.
^a T_{peak} : Peak brightness temperature corrected for main-beam efficiency of the telescope.
^b O : Order of the cold components along the line of sight, beginning with 0; larger numbers mean larger distances along the line of sight.

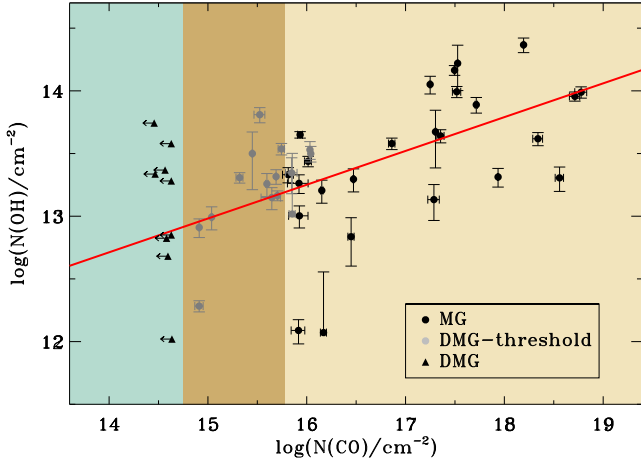


Figure 9. CO column densities, $N(\text{CO})$, vs. OH column densities, $N(\text{OH})$ for three categories of clouds. Molecular clouds (MG) with CO detections are represented with black filled circles in the light yellow region. DMG-threshold clouds are represented by gray filled circles in the dark yellow region. In these clouds, CO emission is detected at the CO sensitivity of this work but would be detected at less than 3σ under a CO sensitivity of $0.25 \text{ K per } 0.65 \text{ km s}^{-1}$, typical of the CFA CO survey (Dame et al. 2001). The black triangles in the blue region represent DMG clouds in which CO emission is not detected at the CO sensitivity of the present work. The red solid line represents the least-squares fit result to the MG and DMG-threshold clouds.

detectability in absorption, the apparent DMG clouds (DMG and DMG-threshold) are similar to molecular clouds with CO emission.

The statistics of hydrogen column density are presented in Figure 11. The hydrogen column density of DMG clouds (DMG and DMG-threshold) falls between $N(\text{H}) \sim 10^{20} \text{ cm}^{-2}$ and $4 \times 10^{21} \text{ cm}^{-2}$, corresponding to a extinction range $A_V \sim 0.05$ to 2 mag. Within this “intermediate” extinction range, the self-shielding of H_2 is complete, while that of CO is not. All $N(\text{H})$ in this work refer to hydrogen column density based on H I absorption and CO emission measurements. Comparison with $N(\text{H}_2)$ based on Planck results will be published in a separate paper (Hiep et al. in prep). The abundance of measured CO is thus expected to be less than the canonical value of 10^{-4} and to vary with extinction. Our detection statistics of OH in DMGs are consistent with a picture in which gas in this intermediate extinction range is still evolving chemically. OH is thus a potentially good tracer of diffuse gas with intermediate extinction, namely between the self-shielding thresholds of H_2 and CO. Such a suggestion has been borne out by detailed studies of individual regions with more complete information. Xu & Li (2016), for example, found much tighter X-factors in both OH and CH than in CO, for gases in the intermediate extinction region of the Taurus molecular cloud.

5. Implications of the Absorption Survey

The expected locations and abundance of OH should make it an excellent tracer of DMG. However, due both to low optical depths and low contrast between the main line excitation temperatures and the Galactic diffuse continuum background, OH is generally difficult to detect in emission. Large-scale mapping of OH therefore requires extremely high sensitivity observations and/or the existence of a bright continuum background against which the lines may be seen in absorption. A handful of studies have accomplished the former over very

limited regions in the Northern Hemisphere local ISM (Barriault et al. 2010; Allen et al. 2012, 2015; Cotten et al. 2012). The SPLASH project (Dawson et al. 2014) has greatly improved on the sensitivities of previous large-scale surveys in the south, to map OH (primarily in absorption) over >150 square degrees of the bright inner Galaxy. However, for outer-Galaxy and off-plane regions, the most practical approach will make use of upcoming radio telescopes to conduct comprehensive absorption surveys, of the kind piloted here.

The Five-hundred-meter Aperture Spherical radio Telescope (FAST) commenced observing in 2016 September. The unprecedented sensitivity of FAST and its early science instruments (Li et al. 2013) should make feasible an H I+OH absorption survey, in the mode of the Millennium Survey, but with 10 times more sources. Figure 12 shows the distribution of potential continuum sources available to FAST. In the coming decades, the SKA1 will provide the survey speed and sensitivity to measure absorption with a source density of between a few to a few tens per square degree (McClure-Griffiths et al. 2015). This makes feasible an all-sky “absorption-image,” mapping out a fine grid of ISM excitation temperature and column density over a very large fraction of the sky. Based on similar excitation and sensitivity considerations, ALMA is a powerful instrument for obtaining systematic and sensitive absorption measurements of millimeter lines in diffuse gas. CO and HCO^+ in diffuse gas, in particular, will be much better constrained in terms of excitation temperature and column densities through ALMA absorption observations than through emission measurements. Combining both radio and millimeter absorption surveys in the coming decade, we will quantify the DMG and provide definitive answers to questions like the global star formation efficiency.

6. Conclusions

Utilizing unpublished OH absorption measurements from the Millennium Survey and our own follow-up CO surveys, we carried out an analysis of the excitation conditions and quantity of OH along 44 sightlines through the Local ISM and Galactic Plane. CO was observed toward these positions. 49 OH components were detected toward 22 of these sightlines. The conclusions are as follows:

1. The excitation temperature of OH peaks around 3.4 K and follows a modified normalized lognormal distribution,

$$f(T_{\text{ex}}) \propto \frac{1}{\sqrt{2\pi}\sigma} \exp\left[-\frac{[\ln(T_{\text{ex}}) - \ln(3.4 \text{ K})]^2}{2\sigma^2}\right].$$

The majority of OH gas in our sample, presumably representative of the Milky Way, thus has an excitation temperature close to the background (CMB plus synchrotron), providing an explanation of why OH has historically been so difficult to detect in emission.

2. The OH main lines are generally not in LTE, with a moderate excitation temperature difference of $|T_{\text{ex}}(1667) - T_{\text{ex}}(1665)| < 2 \text{ K}$.
3. The OH emission is optically thin; the distribution of τ_{1667} peaks at ~ 0.01 , with the highest value in our sample being equal to 0.22.
4. A weak correlation between $N(\text{OH})$ and $N(\text{H I})$ was found. The abundance ratio $[\text{OH}]/[\text{H I}]$ has a median of 10^{-7} .

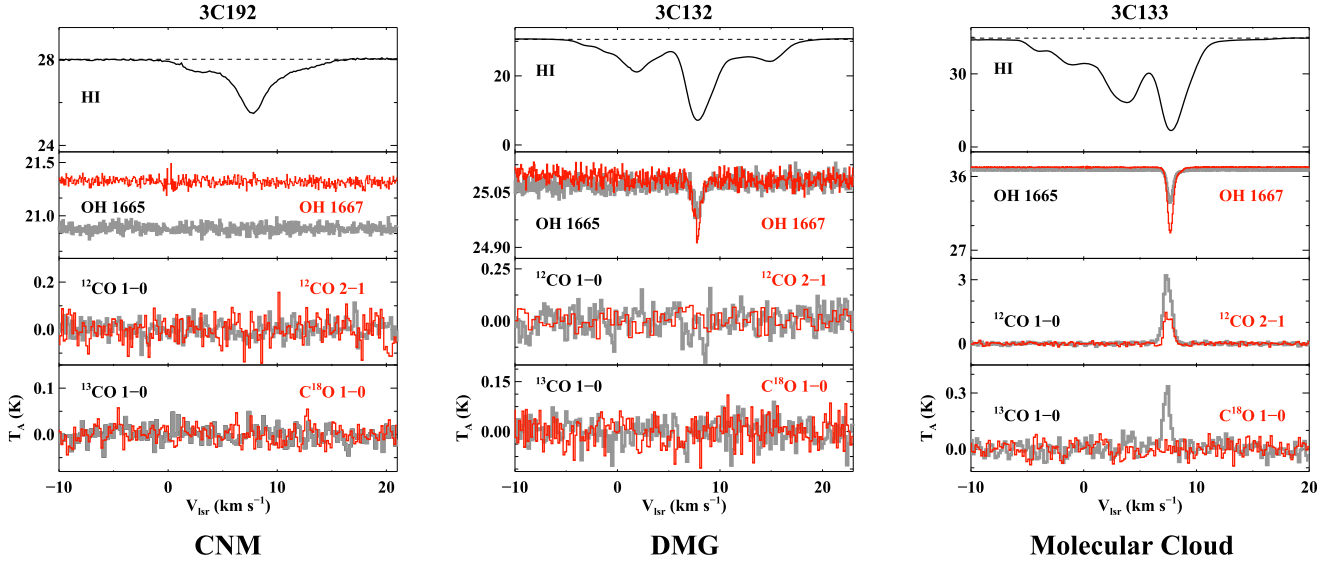


Figure 10. Representative spectra as described in Section 4.3. The 3C192 sightline has only H I seen in absorption. One component of the 3C133 sightline has OH and H I in absorption and CO and its isotopologues in emission. The 3C132 sightline has one gas component with both OH and H I, but no detectable CO transitions.

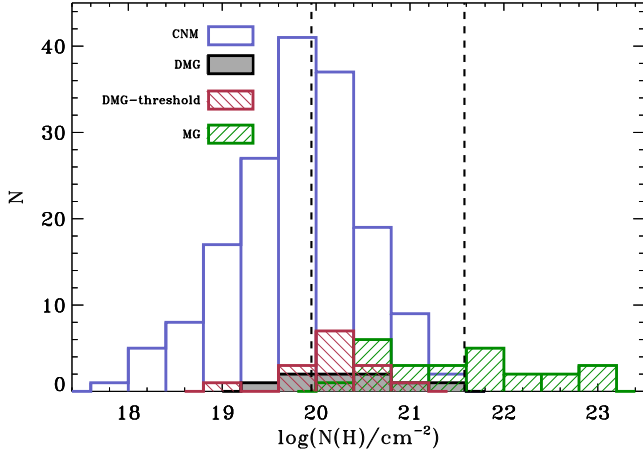


Figure 11. Histogram of hydrogen column density, $N(H)$, for CNM (blue), DMG (filled gray), the DMG-threshold (red), and the molecular cloud (MG, green). $N(H)$ contains contributions from H I for CNM, DMG, and the DMG-threshold cloud. Both H I and H₂ (transforming from CO measurements, $N(H_2) = N(CO)/1 \times 10^{-4}$) are included for the MG cloud. The left and right dashed lines represent $N(H) = 9.4 \times 10^{19} \text{ cm}^{-2}$ (visual extinction $A_V = 0.05 \text{ mag}$) and $3.8 \times 10^{21} \text{ cm}^{-2}$ ($A_V = 2 \text{ mag}$), respectively.

5. $N(OH)$ and $N(CO)$ are linearly correlated when both are detected, which is consistent with previous observations.
6. Whether a cloud is designated as DMG depends on the sensitivity of the CO data. By comparing with the CfA CO survey data of Dame et al. (2001) we find that the fraction of DMG components would increase by a factor of ~ 2.5 compared to our results, had this less sensitive data set been used. To highlight this difference, we designated clouds that would be “CO-dark” in the CfA survey as “DMG-threshold” clouds in this work.
7. About 49% of all detected OH absorption clouds are CO-dark, namely, either DMG or DMG-threshold. The absence of CO emission toward these OH components implies that OH serves as a more effective tracer than

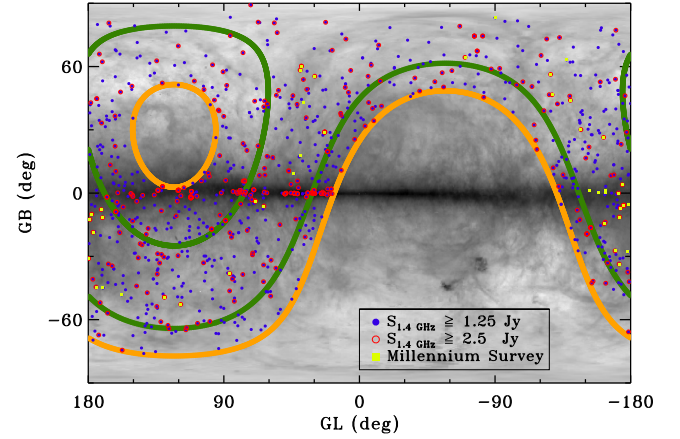


Figure 12. Distribution of continuum point sources within the area of FAST sky coverage (limits shown with orange), which covers a declination range of $-14^\circ 35'$ to $65^\circ 65'$. The red circles represent 372 sources with flux densities greater than 2.5 Jy in the NVSS survey. In initial observation periods, FAST will adopt a drift scan mode. The threshold of 2.5 Jy corresponds to a 3σ detection in OH absorption for gas with an optical depth of 0.01, in a drift scan of 12 s, at a velocity resolution of 0.25 km s^{-1} , with a system temperature of 25 K. The blue filled circles represent 1071 sources with flux densities greater than 1.25 Jy in the NVSS survey. The threshold of 1.25 Jy allows for a 3σ detection for OH having an optical depth of 5.5×10^{-3} in a total observing time of 10 minutes (ON+OFF) in tracking mode. The gray background is the integrated H I intensity map from the LAB H I survey (Hartmann & Burton 1997; Arnal et al. 2000; Bajaja et al. 2005). The limits of the coverage of Arecibo are shown with green solid lines. The positions of the 44 point sources used in this paper are plotted with yellow filled squares.

CO of diffuse molecular gas within $A_V \sim 0.05$ to 2 mag.

8. Given the low opacity and the low excitation temperature of the Galactic OH gas, sensitive absorption surveys made feasible by upcoming large telescopes, such as FAST and SKA, are needed for a comprehensive inventory of Galactic cold gas.

This work is supported by the National Key R&D Program of China 2017YFA0402600 and International

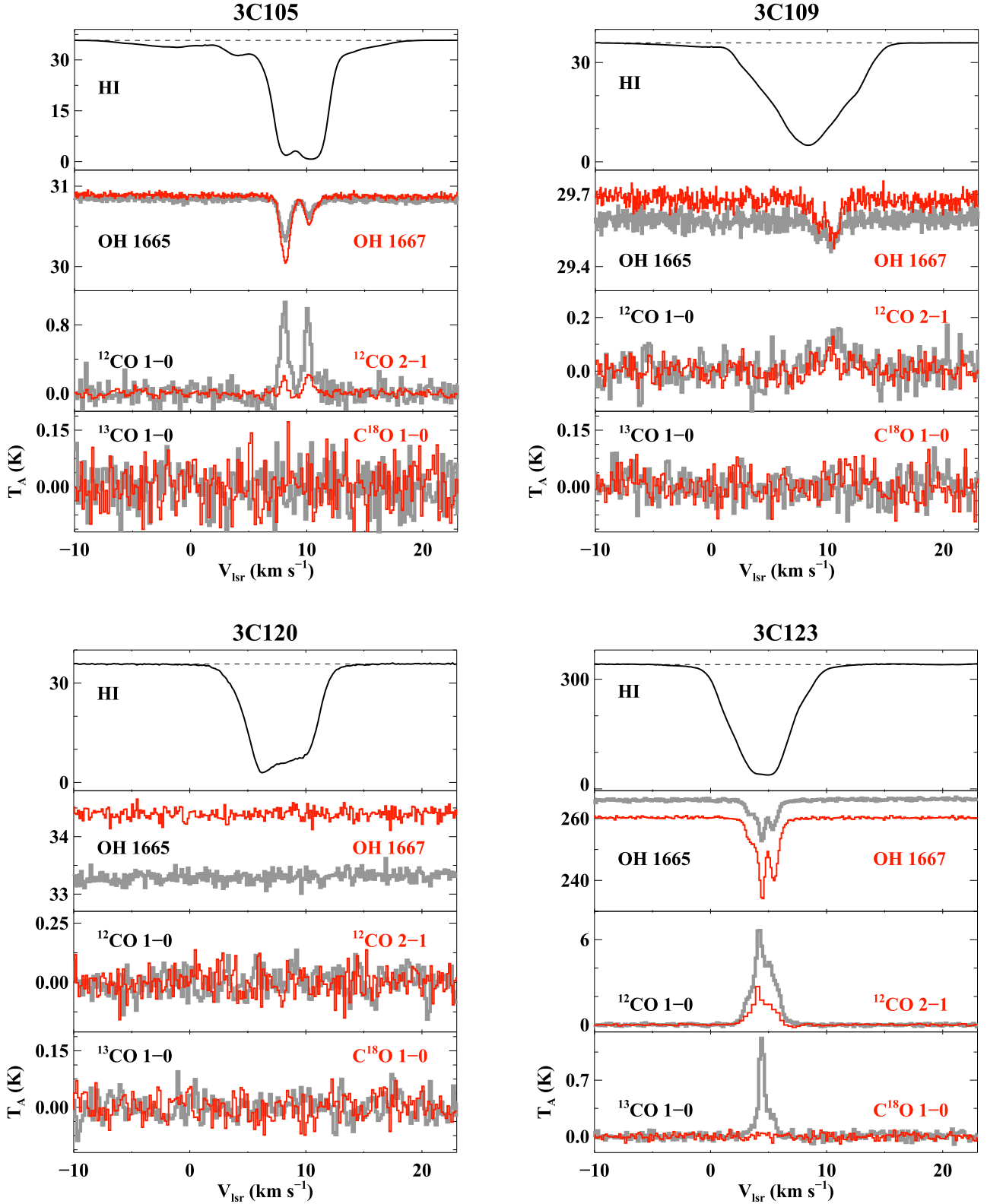











Figure 13. Reference spectra of H I, OH, and CO toward continuum sources. (The complete figure set (11 images) is available.)

Partnership Program of Chinese Academy of Sciences No. 114A11KYSB20160008. D.L. acknowledges support from the “CAS Interdisciplinary Innovation Team” program. J.R.D. is

the recipient of an Australian Research Council DECRA Fellowship (project number DE170101086). This work was carried out in part at the Jet Propulsion Laboratory, which is

operated for NASA by the California Institute of Technology. L.B. acknowledges support from CONICYT Project PFB06. CO data were observed with the Delingha 13.7 m telescope of the Qinghai Station of Purple Mountain Observatory (PMODLH), the Caltech Submillimeter Observatory (CSO), and the IRAM 30 m telescope. The authors appreciate all the staff members of the PMODLH, CSO, and the IRAM 30 m Observatory for their help during the observations. We thank Lei Qian and Lei Zhu for their help in CSO observations.

ORCID iDs

Di Li  <https://orcid.org/0000-0003-3010-7661>
 Ningyu Tang  <https://orcid.org/0000-0002-2169-0472>
 J. R. Dawson  <https://orcid.org/0000-0003-0235-3347>
 Paul F. Goldsmith  <https://orcid.org/0000-0002-6622-8396>
 Steven J. Gibson  <https://orcid.org/0000-0002-1495-760X>
 Claire E. Murray  <https://orcid.org/0000-0002-7743-8129>
 N. M. McClure-Griffiths  <https://orcid.org/0000-0003-2730-957X>
 John Dickey  <https://orcid.org/0000-0002-6300-7459>
 Jorge Pineda  <https://orcid.org/0000-0001-8898-2800>
 L. Bronfman  <https://orcid.org/0000-0002-9574-8454>

References

- Allen, R. J., Hogg, D. E., & Engelke, P. D. 2015, *AJ*, **149**, 123
 Allen, R. J., Ivette Rodríguez, M., Black, J. H., & Booth, R. S. 2012, *AJ*, **143**, 97
 Arnal, E. M., Bajaja, E., Larrarte, J. J., Morras, R., & Pöppel, W. G. L. 2000, *A&AS*, **142**, 35
 Bajaja, E., Arnal, E. M., Larrarte, J. J., et al. 2005, *A&A*, **440**, 767
 Barriault, L., Joncas, G., Lockman, F. J., & Martin, P. G. 2010, *MNRAS*, **407**, 2645
 Bihr, S., Beuther, H., Ott, J., et al. 2015, *A&A*, **580**, A112
 Boyce, P. J., & Cohen, R. J. 1994, *A&AS*, **107**, 563
 Caswell, J. L., & Haynes, R. F. 1975, *MNRAS*, **173**, 649
 Colgan, S. W. J., Salpeter, E. E., & Terzian, Y. 1989, *ApJ*, **336**, 231
 Cotten, D. L., Magnani, L., Wennerstrom, E. A., Douglas, K. A., & Onello, J. S. 2012, *AJ*, **144**, 163
 Crutcher, R. M. 1977, *ApJ*, **216**, 308
 Crutcher, R. M. 1979, *ApJ*, **234**, 881
 Dame, T. M., Hartmann, D., & Thaddeus, P. 2001, *ApJ*, **547**, 792
 Dawson, J. R., Walsh, A. J., Jones, P. A., et al. 2014, *MNRAS*, **439**, 1596
 de Vries, H. W., Heithausen, A., & Thaddeus, P. 1987, *ApJ*, **319**, 723
 Destombes, J. L., Marliere, C., Baudry, A., & Brillet, J. 1977, *A&A*, **60**, 55
 Dickey, J. M., Crovisier, J., & Kazes, I. 1981, *A&A*, **98**, 271
 Donate, E., & Magnani, L. 2017, *MNRAS*, **472**, 3169
 Field, G. B., Goldsmith, D. W., & Habing, H. J. 1969, *ApJL*, **155**, L149
 Fukui, Y., Torii, K., Onishi, T., et al. 2015, *ApJ*, **798**, 6
 Goldsmith, P. F., Heyer, M., Narayanan, G., et al. 2008, *ApJ*, **680**, 428
 Goss, W. M. 1968, *ApJS*, **15**, 131
 Grenier, I. A., Casandjian, J.-M., & Terrier, R. 2005, *Sci*, **307**, 1292
 Grossmann, V., Heithausen, A., Meyerdierts, H., & Mebold, U. 1990, *A&A*, **240**, 400
 Guibert, J., Rieu, N. Q., & Elitzur, M. 1978, *A&A*, **66**, 395
 Harju, J., Winnberg, A., & Wouterloot, J. G. A. 2000, *A&A*, **353**, 1065
 Hartmann, D., & Burton, W. B. 1997, *Atlas of Galactic Neutral Hydrogen* (Cambridge: Cambridge Univ. Press), 243
 Haslam, C. G. T., Salter, C. J., Stoffel, H., & Wilson, W. E. 1982, *A&AS*, **47**, 1
 Heiles, C. 2001, *ApJL*, **551**, L105
 Heiles, C., Perillat, P., Nolan, M., et al. 2001, *PASP*, **113**, 1247
 Heiles, C., & Troland, T. H. 2003a, *ApJ*, **586**, 1067
 Heiles, C., & Troland, T. H. 2003b, *ApJS*, **145**, 329
 Langer, W. D., Velusamy, T., Pineda, J. L., et al. 2010, *A&A*, **521**, L17
 Langer, W. D., Velusamy, T., Pineda, J. L., Willacy, K., & Goldsmith, P. F. 2014, *A&A*, **561**, A122
 Lee, M.-Y., Stanimirović, S., Murray, C. E., Heiles, C., & Miller, J. 2015, *ApJ*, **809**, 56
 Li, D., & Goldsmith, P. F. 2003, *ApJ*, **585**, 823
 Li, D., Nan, R., & Pan, Z. 2013, in *IAU Symp. 291, Neutron Stars and Pulsars: Challenges and Opportunities after 80 Years*, ed. J. van Leeuwen (Cambridge: Cambridge Univ. Press), 325
 Liszt, H., & Lucas, R. 1996, *A&A*, **314**, 917
 Lucas, R., & Liszt, H. 1996, *A&A*, **307**, 237
 McClure-Griffiths, N. M., Stanimirovic, S., Murray, C., et al. 2015, in *Advancing Astrophysics with the Square Kilometre Array (ASKA14)*, The Hydrogen Universe (Trieste: SISSA), 130
 McKee, C. F., & Ostriker, J. P. 1977, *ApJ*, **218**, 148
 Milam, S. N., Savage, C., Brewster, M. A., Ziurys, L. M., & Wyckoff, S. 2005, *ApJ*, **634**, 1126
 Nguyen-Q-Rieu, Winnberg, A., Guibert, J., et al. 1976, *A&A*, **46**, 413
 Pineda, J. L., Goldsmith, P. F., Chapman, N., et al. 2010, *ApJ*, **721**, 686
 Pineda, J. L., Langer, W. D., Velusamy, T., & Goldsmith, P. F. 2013, *A&A*, **554**, A103
 Planck Collaboration, Ade, P. A. R., Aghanim, N., et al. 2011, *A&A*, **536**, A19
 Sancisi, R., Goss, W. M., Anderson, C., Johansson, L. E. B., & Winnberg, A. 1974, *A&A*, **35**, 445
 Stanimirović, S., Murray, C. E., Lee, M.-Y., Heiles, C., & Miller, J. 2014, *ApJ*, **793**, 132
 Turner, B. E. 1979, *A&AS*, **37**, 1
 van Dishoeck, E. F., & Black, J. H. 1988, *ApJ*, **334**, 771
 Wannier, P. G., Andersson, B.-G., Federman, S. R., et al. 1993, *ApJ*, **407**, 163
 Weinreb, S., Barrett, A. H., Meeks, M. L., & Henry, J. C. 1963, *Natur*, **200**, 829
 Wolfire, M. G., Hollenbach, D., & McKee, C. F. 2010, *ApJ*, **716**, 1191
 Wouterloot, J. G. A., & Habing, H. J. 1985, *A&AS*, **60**, 43
 Xu, D., & Li, D. 2016, *ApJ*, **833**, 90

5

Conclusions and future work

5.1 Conclusions

The interstellar medium (ISM) within the Galaxy is a dynamic and multiphase medium – the result of complex interactions between cooling and heating, and dynamic processes which both structure the gas, and keep it from settling in an equilibrium state. The ISM provides raw fuel for stars to form, then serves as a repository into which those stars expel the enriched material produced via nuclear fusion during their lifetimes. The flows of material and energy back and forth between this gas reservoir and stars drives the evolution of galaxies. A comprehensive understanding of how stars form and interact with the ISM is therefore essential, and requires following the transition of hydrogen gas from its warm atomic phase into cold, gravitationally unstable molecular complexes, as well as constraining the relationships between gas and dust at every stage. However, to date, observations have not well constrained the properties (temperature, density and mass fraction) of each gas phase, nor the dust-gas relation in different environments. These parameters determine the formation efficiency of the molecular clouds (MC) where stars are born, and provide important

information for ISM models.

In this thesis, with the use of multi-wavelength datasets observed by ground- and space-based telescopes, I have presented large-scale observational investigations into the multiphase atomic gas in the Galactic ISM, examined several tracers of different neutral gas phases, as well as explored some aspects of the relation between gas and dust in interstellar space. Specifically, I have examined the impact of HI opacity effects in producing an atomic component of the so-called “dark gas”, and contributed to quantifying the amount of CO-dark molecular gas along local ISM sightlines. Here, comparing the emission/absorption of the OH ground-state lines with CO emission measurements allowed us to assess the potential of OH as a effective tracer of the molecular ISM, finding that it is able to trace molecular gas that CO observations typically do not. As well as a detailed consideration of the excitation of OH main lines 1665 and 1667 MHz, I also made new measurements of the OH abundance relative to H_2 – an essential parameter for translating measured column densities into total gas masses. As another highlight of this work, I have disentangled the contribution made by dark gas and the evolution of dust grains to the observed increase of dust opacity (σ_{353}) along atomic sightlines with diffuse-to-intermediate column densities. In a general sense, this study provides new observational constraints on the properties of the atomic ISM, refines our tools for tracing gas in different phases, and offers new information on the environment-dependent relationships between gas and dust.

In Chapter 2, I reported 21 cm emission and absorption measurements from the GNOME (Galactic Neutral Opacity and Molecular Excitation) Survey, which aims to characterise the properties of the atomic hydrogen gas in the proximity of five different molecular clouds (Taurus, California, Rosette, Mon OB1, NGC2264). Following the decomposition and radiative transfer method of Heiles & Troland (2003a), I directly estimated HI optical depths, temperatures and column densities for CNM and WNM Gaussian components. These output parameters are generally in excellent agreement with previous observations of different sky regions that used the same methodology (Heiles & Troland, 2003a, Stanimirović et al., 2014, Lee et al., 2015, Murray et al., 2015), which has some interesting implications.

In particular, the properties of individual CNM components in our survey toward the three characteristic physical regions I identify (diffuse $b > 5^\circ$, in-Plane $|b| < 5^\circ$, and around giant molecular clouds $b < -5^\circ$) are consistent, and also consistent with those of previous observations along all-sky sightlines and in/around the Perseus molecular cloud (Heiles & Troland, 2003b, Stanimirović et al., 2014, Murray et al., 2015). This suggests a universality of cold HI gas properties

through out the Galactic ISM. Conversely, the *fraction* of cold gas around molecular clouds is higher than in diffuse regions, potentially supporting a staged build-up scenario for GMCs: from WNM-rich gas to CNM-rich gas to molecular clouds, with a high fraction of cold gas required for molecules to form. Both of these two points are still suggestions inferred from (a few) observational attempts, therefore more observations (and also theories) are needed before stronger conclusions can be drawn. However, these surveys showed that CNM is ubiquitous and can be formed anywhere in the ISM with a fraction strongly determined by the local conditions of heating, cooling and dynamical processes. This indicates that the evolution of gas in the Galactic ISM and the formation of molecular clouds are more complicated than the classic hierarchical transition of atomic hydrogen from warm gas on the skins of clouds to cool gas in intermediate layers, and cold, dense molecular gas in the central regions. Combining the two points (the universality of CNM properties and the higher CNM fraction around molecular clouds) not only highlights the important role of CNM in the formation of molecular clouds, but also may permit us to discriminate between different models of MC formation.

The temperature of the WNM is not directly estimated in my work due to limited optical depth sensitivity ($\sigma_\tau \sim 5 \times 10^{-3}$ per 1 km s^{-1}), but upper limits on the kinetic temperature can be inferred from WNM line widths. I found that the WNM comprises $\sim 60\%$ of the total atomic gas, and 40% of this lies in the thermally unstable regime ($500\text{--}5000 \text{ K}$), implying the fractions of CNM, unstable neutral medium (UNM) and WNM (by mass) are 40% , 24% and 36% , respectively. This thermally unstable fraction is consistent with the findings of previous emission-absorption studies (Heiles & Troland, 2003b, Roy et al., 2013b, Murray et al., 2015, 2018b), but slightly lower than the $\sim 41\%$ recently estimated from decomposition of all-sky emission spectra from the HI4PI survey (Kalberla & Haud, 2018). Numerical ISM models including thermal and dynamical processes (turbulence, shocks driven by supernova, time-dependent heating), and sometimes magnetic fields, have found a significant fraction of atomic gas ($10\text{--}50\%$) in the thermally unstable range (e.g. Gazol et al., 2001, Audit & Hennebelle, 2005, de Avillez & Breitschwerdt, 2005, Saury et al., 2014). More recent numerical analyses with detailed prescriptions of various heating and cooling mechanisms found that the fraction of UNM is no more than 20% (e.g. Kim et al., 2013, Hill et al., 2018). Our observations have provided additional constraints on the fractions of each atomic ISM phases, which together with the findings from previous surveys could be a useful input parameter for theoretical ISM models.

In this Chapter, I also assessed the impact of opacity effects by comparing the “true” opacity-corrected) HI column density (N_{HI}) inferred from my spectral decompositions, with that obtained from emission spectra under the optically thin assumption (N_{HI}^*). The cold, optically thick HI missing from N_{HI}^* is often classified as a component of dark gas, and is thought to dominate the dark ISM by a minority of authors (e.g. Fukui et al., 2014, 2015). I found that the correction factor $f = N_{\text{HI}}/N_{\text{HI}}^*$ increases (from 1.0–1.7) with increasing total HI column density, over my measured range of $(5\text{--}110) \times 10^{20} \text{ cm}^{-2}$. This result agrees well with the findings of Heiles & Troland (2003b), Dickey et al. (2003), Lee et al. (2015), Bihr et al. (2015) and Murray et al. (2018b), implying that corrections for opacity are more important for high column densities. However, the variation of the correction factor with column density was quite different for each individual region I examined; thus region-dependent approaches are required for HI opacity correction.

Indeed, I examined two methods of opacity correction: A linear fit of the correction factor f with $\log_{10}(N_{\text{HI}}^*)$, and the use of region-dependent uniform spin temperatures. However, separate linear fits do not well describe the variation of correction factor as a function of column density for each subregion; we prefer the uniform spin temperature method. This method with a uniform T_s has also been used by a few studies to correct for the amount of HI gas missed under the optically thin assumption (e.g. Liszt, 2014b, Remy et al., 2017), though without considering regional variations. A key suggestion of my work is that in order to build an accurate map of dark gas, not only is the uniform T_s approach likely preferred for HI opacity correction, but also that it is crucial to take into account regional variations in the best fit T_s . To be specific, with an appropriate spin temperature, the “true” HI column density of a sky region can be estimated from emission data (which can be easily observed along any directions). About half of the all-sky HI map satisfies the optically thin assumption with $N_{\text{HI}} \leq 5 \times 10^{20} \text{ cm}^{-2}$ (HI4PI Collaboration et al., 2016), thus one may need to correct for the opacity effects in the other half – mostly within the Galactic plane region or in/around molecular clouds. But given the fact that the (spin) temperature of HI gas varies from cloud to cloud and region to region, it is important to obtain an empirical representative temperature of the region/cloud in question. One of the most direct methods is to conduct on-/off-source measurements toward radio continuum background sources behind the regions/clouds, then a comparison between “true” N_{HI} from spectral decompositions and optically thin N_{HI}^* will give the expected spin temperature. The number of sightlines in a sample would depend on the size of the regions and the availability of radio continuum sources, but the measurements for absorption and emission are definitely feasible with the use of available large single dish

telescopes and interferometric arrays.

In Chapter 3, I combined several data sets at various wavelengths to investigate the relation between gas and dust in the ISM. I found that in general, dust optical depth τ_{353} and dust reddening $E(B-V)$ linearly correlate with total gas column density N_{H} in the range $(1-30) \times 10^{20} \text{ cm}^{-2}$, along atomic sightlines with no molecular gas detections. However, while a deviation of τ_{353} away from the linear relation is noticed, especially at the low and high ends of N_{H} , the reddening follows gas column density quite well along the linear fit. By comparing the variations of specific reddening $\sigma_V = E(B-V)/N_{\text{H}}$ and dust opacity $\sigma_{353} = \tau_{353}/N_{\text{H}}$ as a function of total N_{H} , I confirmed that the new $E(B-V)$ map (from Green et al. 2018) is the more reliable proxy for total gas column density (at least for the purely atomic sightlines considered) than the τ_{353} map from Planck Collaboration et al. (2014a).

In this analysis of purely atomic sightlines, I measured a $N_{\text{H}}/E(B-V)$ ratio of $(9.4 \pm 1.6) \times 10^{21} \text{ cm}^{-2} \text{ mag}^{-1}$. This agrees well with recent observations by Planck Collaboration et al. (2014a), Liszt (2014a) and (Lenz et al., 2015), despite differences in methodology between these studies. The values of $N_{\text{H}}/E(B-V)$ in these works are in the range $(\sim 8-9) \times 10^{21} \text{ cm}^{-2} \text{ mag}^{-1}$ – about 40–60% higher than the canonical value of Bohlin et al. (1978), which has historically been used as a standard tool for conversion between gas and dust. Here I have not explored the reasons for these differences, however my results do suggest that caution should be exercised when using this widely-accepted conversion factor.

Interestingly, with well-constrained gas column densities along sightlines without molecular detections, I was able to separate the effects of dust grain evolution and dark gas (optically thick HI) from the observed increase of dust opacity $\sigma_{353} = \tau_{353}/N_{\text{H}}$ in the total gas column density range $(1-30) \times 10^{20} \text{ cm}^{-2}$. This increase was previously reported by Planck Collaboration et al. (2014a), and seen also in my work. To be specific, my results suggest that HI opacity can account for around 30% of the increase of dust opacity seen in the transition from diffuse to dense atomic column densities, with changes in grain properties responsible for the remaining of 70%. While I do not explore the underlying mechanisms of this evolution in my work, recent models suggest that in the diffuse ISM such changes could occur via the accretion of ice mantles on the grain surfaces, leading to changes in their structure, composition and emissivity (Ysard et al., 2015, Jones, 2016).

Using a sample of 16 molecular sightlines, I combined my dust-scaling relations, OH column densities, and opacity-corrected N_{HI} to derive the OH/H₂ abundance ratio. The results were scattered around an average value of $X_{\text{OH}} \sim 1 \times 10^{-7}$ for N_{H_2} (when inferred from $E(B-V)$) and X_{OH}

$\sim 0.5 \times 10^{-7}$ (for N_{H_2} estimated from τ_{353}). Theoretical studies have found values of X_{OH} that vary widely, from $\sim 8 \times 10^{-9}$ to $\sim 4 \times 10^{-6}$ (Black & Dalgarno, 1977, Viala, 1986, Andersson & Wannier, 1993), whereas observations measure X_{OH} scattered as much as an order of magnitude around 1×10^{-7} (Magnani et al., 1988, Liszt & Lucas, 2002, Weselak et al., 2010). While some authors have also observed a decreasing trend in X_{OH} with increasing N_{H_2} (Xu et al., 2016, Rugel et al., 2018), the results of current work do not show any obvious systematic trends in X_{OH} with molecular column density. In addition, our 16 sightlines sample both CO-dark and CO-bright molecular gas, and suggest that the OH molecule may be used as a reliable tracer for the molecular ISM the range $N_{\text{H}_2} \sim (1-100) \times 10^{20} \text{ cm}^{-2}$ (for both CO-dark and CO-bright gas). Since $E(B-V)$ may be a better proxy for N_{H} , the abundance ratio X_{OH} of 1×10^{-7} is preferred.

The project in Chapter 4 is a study of OH excitation and the dark molecular gas using emission/absorption measurements, to which I contributed as a co-author. We made use of OH absorption measurements from the Arecibo Millennium Survey (Heiles & Troland, 2003a) and a follow-up CO survey. The OH main line (1665 and 1667 MHz) excitation temperatures peak at ~ 3.4 K, close to the temperature of background continuum (CMB + synchrotron), providing a convincing reason why OH has been difficult to detect in emission. But OH absorption is readily detected. Thus as in the case of HI, future work may rely on emission/absorption measurements at high sensitivity to probe the properties of OH.

In addition, we confirmed that the main lines are optically thin, with optical depths τ_{OH} always below 0.25, and a distribution of τ_{OH} peaking at very low values of ~ 0.01 . In general, these two main lines are not in local thermodynamic equilibrium (LTE), with measured excitation temperature differences of $|T_{\text{ex}}(1667) - T_{\text{ex}}(1665)| < 2\text{K}$, consistent with the findings of Crutcher (1979) and Dawson et al. (2014). Therefore, any assumptions of LTE for OH require extreme care, otherwise the derived OH column densities will deviate greatly from their true values.

About half of all detected OH absorption components did not have corresponding CO emission detections. This implies that the ground-state OH main lines trace molecular gas more effectively than CO emission – the same conclusions that have drawn by previous studies (Allen et al., 2015, Tang et al., 2017). Indeed, the ability of OH to trace H_2 in diffuse molecular regions where CO is photodissociated have been suggested by a number of observational studies (Wouterloot, 1981, Magnani et al., 1988, Andersson & Wannier, 1993, Wannier et al., 1993, Cotten et al., 2012, Li et al., 2015, Rugel et al., 2018, Engelke & Allen, 2018). But improved observational capabilities with high sensitivity have recently allowed it to take up its inherent role of an effective tracer for

the molecular ISM.

In attempting to gain insight into the nature of dark gas and methods for its detection, the projects in this PhD thesis exclusively focused on gas and dust in the ISM of the Milky Way galaxy – where the dark gas is indeed a sub-dominant component, so that correct measurements with better tracers for molecular gas would lead to a change in the mass budget of the ISM gas by tens of percent (e.g. $\sim 30\%$ of the molecular mass of the Galactic ISM as estimated from the Herschel GOT C⁺ surveys - Pineda et al. 2013). This change should not be ignored, however it may be a small effect compared to the amount of dark gas in other galaxies, where this undetected material is potentially a dominant component of the star-forming portion of their ISM. Indeed, evidence for CO-dark molecular gas has been found in other galaxies, from the surveys conducted by Israel (1997), Madden et al. (1997), Requena-Torres et al. (2016) and Fahrion et al. (2017). These observations used either dust emission at FIR wavelengths (Israel, 1997) or the C⁺ 158 μm fine structure line (Madden et al., 1997, Requena-Torres et al., 2016, Fahrion et al., 2017) to unveil the presence of large amounts of CO-dark molecular gas in the low-metallicity environments of the Magellanic irregular galaxies. These studies found that CO-dark gas dominates the molecular gas mass in these systems, with on average a fraction of $\sim 79\%$ of the total H₂ mass not detected by CO emission. Furthermore, this fraction seems to be sensitive to the evolutionary stage of the regions: while the highest CO-dark gas fraction is found in the most evolved star forming regions, it is lower in younger, more metal-rich and compact regions (Fahrion et al., 2017).

5.2 Future work

In the near future, the GNOMES collaboration will continue to perform OH and HI observations towards a large sample of 194 radio continuum sources (Figure 5.1) that can be seen by the Arecibo telescope (we may have more sightlines than displayed here, as some of our projects have been approved). About 120 these continuum sources have been observed by Heiles & Troland (2003a), Stanimirović et al. (2014) and the current work. However, a large number of the sightlines missed the measurements of all four OH ground-state lines. The surveys cover large regions of interest, through different Galactic environments such as diffuse ISM, in and around molecular clouds. This will allow us to further investigate the properties of not only cold and warm atomic HI gas, but also molecular gas over a large sky area. We will be able to derive accurate estimates of column densities and temperatures for both the atomic and molecular gas, and begin to measure

the variations in properties of these phases in the Galactic environment.

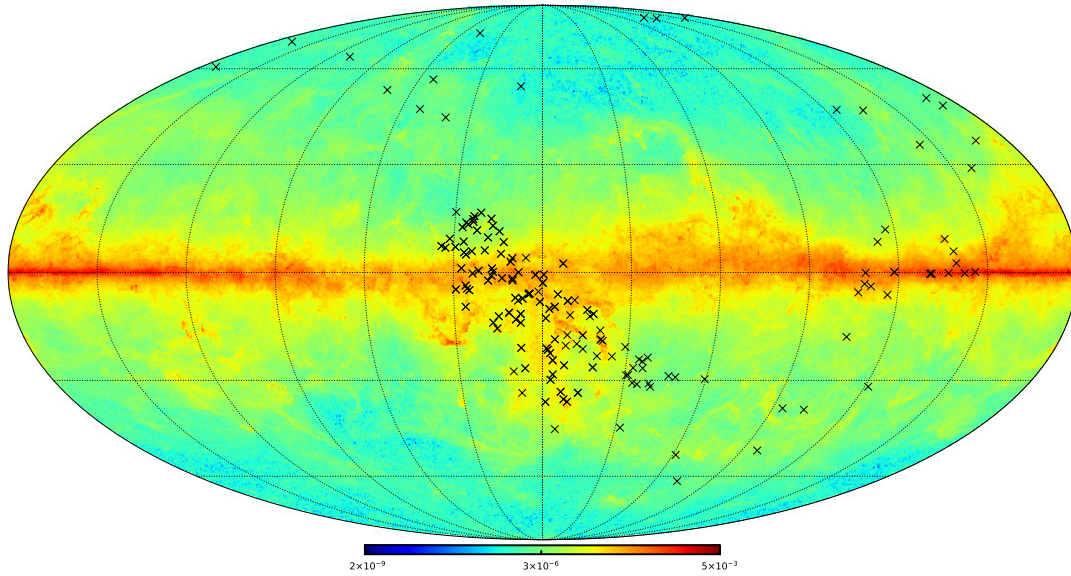


Figure 5.1: Locations of 194 radio continuum sources used in the GNOME survey for emission and absorption measurements of HI and OH, overlaid on the *Planck* map of dust optical depth, τ_{353} (Planck Collaboration et al., 2014a). The Galactic coordinates at center of the figure are ($l = 180^\circ$, $b = 0^\circ$).

Obtaining accurate measurements of the temperature, density and mass fraction of HI in every phase is crucial to understand the transition from warm to cold gas, and also provides important constraints for numerical studies examining the impact of dynamic processes in building ISM structure. However, due to the low optical depth of the WNM, extremely high sensitivity observations are required to detect it in absorption. Fortunately, this can be achieved with interferometric observations. Future work of this kind is needed to further constrain the mass distribution of atomic gas as a function of temperature. Since both emission and absorption spectra are required to directly derive HI physical parameters, the most effective observation strategy is, possibly, to use the interferometric facilities for absorption, and the best available single-dish for complementary emission (e.g. as done in the 21-SPONGE survey by Murray et al. 2015, 2018b).

Moreover, with new releases of dust data from the *Planck* Collaboration and Pan-STARRS 1 and 2MASS (Green et al., 2018), I hope to examine the variations of specific reddening (σ_V) and dust opacity (σ_{353}) in the transition from diffuse to dense regions to further calibrate the dust-gas relation, and assess the performance of dust reddening and dust optical depth as proxies for total gas column density (N_H). This would address outstanding questions on how dust grains evolve

in diffuse regimes dominated by warm atomic gas, and which dust observables trace the total hydrogen gas more effectively. The observations from the GNOMES collaboration will provide great opportunities to obtain accurate HI and OH column densities simultaneously, with OH data giving access to the molecular column density, and HI data also give additional information on optically thin HI column density (N_{HI}^*), as well as the opacity-corrected N_{HI} . As a consequence, well-constrained estimates of total gas column density can be obtained, which I would then combine with dust data to probe how the dust-gas scaling factors (σ_V and σ_{353}) vary with gas column density. The flatness of these relations are the criteria by which to judge the quality of dust observables in tracing the total hydrogen gas. In the same fashion, but with the total gas column density inferred from optically thin HI and available CO emission ($N_{\text{H}} = N_{\text{HI}}^* + X_{\text{CO}}W_{\text{CO}}$), a comparison of the behavior of each scaling factor may reveal the relative contributions of dark gas and changes in grain properties.

I plan to use the findings of Chapter 1, together with the new GNOMES results, and combine these with available CO data, as well as alternative tracers of molecular hydrogen (such as OH) and dust-based estimates of the total proton column density, to construct dark gas maps of the Taurus and Gemini regions. As the first step, this thesis work has established opacity-corrected HI maps (N_{HI}) for these regions, and new GNOMES data with more sightlines through these regions will also help to improve the maps. Then I will derive the total hydrogen column density (N_{H}) from newly-released *Planck* dust opacity data (if applicable) and reddening data (Green et al., 2018) using dust-gas scaling factors. The molecular column density can be estimated either from the difference between N_{H} and N_{HI} , or from OH with our OH abundance ratio X_{OH} . Comparing these N_{H_2} maps with the N_{H_2} inferred from CO data will allow me to quantify the CO-dark gas and its distribution in the two regions. To obtain accurate CO-dark gas maps, I will compute the distances to the gas clouds, and match the gas components along lines of sight.

Finally, the work presented in this thesis should be considered as a little contribution to the big picture of the evolution of the ISM in galaxies. Ultimately, it provides auxiliary observational constraints on physical properties of the atomic and molecular gas, and also on the relationship between gas and dust in interstellar space. In practice, directly measuring the temperature, density and mass fraction of hydrogen gas (especially the warm component) is challenging, as is tracking the flow of gas into star formation. Understanding the evolution of dust grains in different environments in the ISM is connected to these challenges, and has complexities all of its own. The next generation of large radio telescopes (such as FAST and the SKA) will provide high sensitivity and

high resolution observations to address these challenges – at least from the perspective of radio spectral lines. The coming years will be an exciting time for the studies of the Galactic interstellar medium, a time to explore the Universe from home – our Milky Way.

Bibliography

- Abdo, A. A., Ackermann, M., Ajello, M., et al. 2010, *ApJ*, 710, 133
- Ackermann, M., Ajello, M., Baldini, L., et al. 2011, *ApJ*, 726, 81
- Ackermann, M., Ajello, M., Allafort, A., et al. 2012, *ApJ*, 755, 22
- Allen, R. J., Hogg, D. E., & Engelke, P. D. 2015, *AJ*, 149, 123
- Allen, R. J., Ivette Rodríguez, M., Black, J. H., & Booth, R. S. 2012, *AJ*, 143, 97
- Andersson, B.-G., & Wannier, P. G. 1993, *ApJ*, 402, 585
- Arendt, R. G., Odegard, N., Weiland, J. L., et al. 1998, *ApJ*, 508, 74
- Audit, E., & Hennebelle, P. 2005, *A&A*, 433, 1
- . 2010, *A&A*, 511, A76
- Ballesteros-Paredes, J., Hartmann, L., & Vázquez-Semadeni, E. 1999, *ApJ*, 527, 285
- Barlow, M. J., & Silk, J. 1976, *ApJ*, 207, 131
- Barriault, L., Joncas, G., Lockman, F. J., & Martin, P. G. 2010, *MNRAS*, 407, 2645
- Begum, A., Stanimirović, S., Goss, W. M., et al. 2010, *ApJ*, 725, 1779
- Bihr, S., Beuther, H., Ott, J., et al. 2015, *A&A*, 580, A112
- Biswas, S. 2013, *Cosmic Perspectives in Space Physics, Astrophysics and Space Science Library* (Springer Netherlands)
- Black, J. H., & Dalgarno, A. 1977, *ApJS*, 34, 405

- Blitz, L., Bazell, D., & Desert, F. X. 1990, *ApJL*, 352, L13
- Blitz, L., & Rosolowsky, E. 2004, *ApJL*, 612, L29
- Blitz, L., & Thaddeus, P. 1980, *ApJ*, 241, 676
- Bohlin, R. C., Savage, B. D., & Drake, J. F. 1978, *ApJ*, 224, 132
- Bolatto, A. D., Wolfire, M., & Leroy, A. K. 2013, *ARAA*, 51, 207
- Boulanger, F. 1999, in *Astronomical Society of the Pacific Conference Series*, Vol. 168, *New Perspectives on the Interstellar Medium*, ed. A. R. Taylor, T. L. Landecker, & G. Joncas, 173
- Boulanger, F., Abergel, A., Bernard, J.-P., et al. 1996, *A&A*, 312, 256
- Boulanger, F., & Perault, M. 1988, *ApJ*, 330, 964
- Bowey, J. E., & Adamson, A. J. 2001, *MNRAS*, 320, 131
- Bowey, J. E., Adamson, A. J., & Yates, J. A. 2003, *MNRAS*, 340, 1173
- Braun, R., & Walterbos, R. A. M. 1992, *ApJ*, 386, 120
- Byleveld, S. E., Melrose, D. B., & Cram, L. E. 1993, *Proceedings of the Astronomical Society of Australia*, 10, 218
- Cardelli, J. A., Clayton, G. C., & Mathis, J. S. 1989, *ApJ*, 345, 245
- Carilli, C. L., Dwarakanath, K. S., & Goss, W. M. 1998, *ApJL*, 502, L79
- Cazaux, S., & Tielens, A. G. G. M. 2004, *ApJ*, 604, 222
- Cernuschi, F., & Codina, S. 1967, *AJ*, 72, 788
- Chokshi, A., Tielens, A. G. G. M., & Hollenbach, D. 1993, *ApJ*, 407, 806
- Clark, B. G. 1965, *ApJ*, 142, 1398
- Clark, P. C., Glover, S. C. O., Klessen, R. S., & Bonnell, I. A. 2012, *MNRAS*, 424, 2599
- Compiègne, M., Abergel, A., Verstraete, L., & Habart, E. 2008, *A&A*, 491, 797
- Compiègne, M., Verstraete, L., Jones, A., et al. 2011, *A&A*, 525, A103

- Cotten, D. L., Magnani, L., Wennerstrom, E. A., Douglas, K. A., & Onello, J. S. 2012, *AJ*, 144, 163
- Cox, D. P. 1979, *ApJ*, 234, 863
- Crutcher, R. M. 1979, *ApJ*, 234, 881
- Dalgarno, A., Oppenheimer, M., & Berry, R. S. 1973, *ApJL*, 183, L21
- Dame, T. M., Hartmann, D., & Thaddeus, P. 2001, *ApJ*, 547, 792
- Dame, T. M., & Thaddeus, P. 1985, *ApJ*, 297, 751
- Dame, T. M., Ungerechts, H., Cohen, R. S., et al. 1987, *ApJ*, 322, 706
- Dawson, J. R., Walsh, A. J., Jones, P. A., et al. 2014, *MNRAS*, 439, 1596
- de Avillez, M. A. 2000, *MNRAS*, 315, 479
- de Avillez, M. A., & Breitschwerdt, D. 2005, *A&A*, 436, 585
- de Avillez, M. A., & Mac Low, M.-M. 2001, *ApJL*, 551, L57
- de Jong, T. 1972, *A&A*, 20, 263
- Deguchi, S., & Watson, W. D. 1985, *ApJ*, 290, 578
- Desert, F. X., Bazell, D., & Boulanger, F. 1988, *ApJ*, 334, 815
- Desert, F.-X., Boulanger, F., & Puget, J. L. 1990, *A&A*, 237, 215
- Destombes, J. L., Marliere, C., Baudry, A., & Brillet, J. 1977, *A&A*, 60, 55
- deVries, H. W., Heithausen, A., & Thaddeus, P. 1987, *ApJ*, 319, 723
- Dickey, J. M., Crovisier, J., & Kazes, I. 1981, *A&A*, 98, 271
- Dickey, J. M., Kulkarni, S. R., van Gorkom, J. H., & Heiles, C. E. 1983, *ApJS*, 53, 591
- Dickey, J. M., & Lockman, F. J. 1990, *ARAA*, 28, 215
- Dickey, J. M., McClure-Griffiths, N. M., Gaensler, B. M., & Green, A. J. 2003, *ApJ*, 585, 801
- Dickey, J. M., Mebold, U., Stanimirovic, S., & Staveley-Smith, L. 2000, *ApJ*, 536, 756

- Dickey, J. M., Salpeter, E. E., & Terzian, Y. 1977, *ApJL*, 211, L77
- . 1978, *ApJS*, 36, 77
- Dickey, J. M., Strasser, S., Gaensler, B. M., et al. 2009, *ApJ*, 693, 1250
- Diplas, A., & Savage, B. D. 1994, *ApJS*, 93, 211
- Dobbs, C. L., Burkert, A., & Pringle, J. E. 2011, *MNRAS*, 417, 1318
- Dobbs, C. L., Glover, S. C. O., Clark, P. C., & Klessen, R. S. 2008, *MNRAS*, 389, 1097
- Douglas, K. A., & Taylor, A. R. 2007, *ApJ*, 659, 426
- Draine, B. T. 1978, *ApJS*, 36, 595
- Draine, B. T. 1990, in *Astronomical Society of the Pacific Conference Series*, Vol. 12, *The Evolution of the Interstellar Medium*, ed. L. Blitz, 193–205
- . 2003, *ARAA*, 41, 241
- Draine, B. T. 2009, in *Astronomical Society of the Pacific Conference Series*, Vol. 414, *Cosmic Dust - Near and Far*, ed. T. Henning, E. Grün, & J. Steinacker, 453
- . 2011, *Physics of the Interstellar and Intergalactic Medium* (Princeton University Press)
- Draine, B. T., & Fraise, A. A. 2009, *ApJ*, 696, 1
- Draine, B. T., & Lee, H. M. 1984, *ApJ*, 285, 89
- Draine, B. T., & Li, A. 2007, *ApJ*, 657, 810
- Draine, B. T., & Salpeter, E. E. 1979, *ApJ*, 231, 77
- Dwarakanath, K. S., Carilli, C. L., & Goss, W. M. 2002, *ApJ*, 567, 940
- Dwek, E., & Scalo, J. M. 1980, *ApJ*, 239, 193
- Dwek, E., Arendt, R. G., Fixsen, D. J., et al. 1997, *ApJ*, 475, 565
- Efremov, Y. N. 1995, *AJ*, 110, 2757
- Elmegreen, B. G., & Elmegreen, D. M. 1983, *MNRAS*, 203, 31

- Engargiola, G., Plambeck, R. L., Rosolowsky, E., & Blitz, L. 2003, *ApJS*, 149, 343
- Engelke, P. D., & Allen, R. J. 2018, ArXiv e-prints, arXiv:1803.09819
- Ewen, H. I., & Purcell, E. M. 1951, *Nature*, 168, 356
- Fahrion, K., Cormier, D., Bigiel, F., et al. 2017, *A&A*, 599, A9
- Field, G. B. 1965, *ApJ*, 142, 531
- . 1974, *ApJ*, 187, 453
- Field, G. B., Goldsmith, D. W., & Habing, H. J. 1969, *ApJL*, 155, L149
- Field, G. B., Somerville, W. B., & Dressler, K. 1966, *ARAA*, 4, 207
- Fitzpatrick, E. L. 1999, *PASP*, 111, 63
- Flagey, N., Boulanger, F., Verstraete, L., et al. 2006, *A&A*, 453, 969
- Foster, J. B., Mandel, K. S., Pineda, J. E., et al. 2013, *MNRAS*, 428, 1606
- Fukui, Y., Torii, K., Onishi, T., et al. 2015, *ApJ*, 798, 6
- Fukui, Y., Okamoto, R., Kaji, R., et al. 2014, *ApJ*, 796, 59
- Galametz, M., Kennicutt, R. C., Albrecht, M., et al. 2012, *MNRAS*, 425, 763
- Gazol, A., Vázquez-Semadeni, E., Sánchez-Salcedo, F. J., & Scalo, J. 2001, *ApJL*, 557, L121
- Gazol-Patiño, A., & Passot, T. 1999, *ApJ*, 518, 748
- Giard, M., Lamarre, J. M., Pajot, F., & Serra, G. 1994, *A&A*, 286, 203
- Gibson, S. J. 2002, in *Astronomical Society of the Pacific Conference Series*, Vol. 276, *Seeing Through the Dust: The Detection of HI and the Exploration of the ISM in Galaxies*, ed. A. R. Taylor, T. L. Landecker, & A. G. Willis, 235
- Gibson, S. J. 2010, in *Astronomical Society of the Pacific Conference Series*, Vol. 438, *The Dynamic Interstellar Medium: A Celebration of the Canadian Galactic Plane Survey*, ed. R. Kothes, T. L. Landecker, & A. G. Willis, 111
- Gillmon, K., Shull, J. M., Tumlinson, J., & Danforth, C. 2006, *ApJ*, 636, 891

- Glover, S. C. O. 2003, *ApJ*, 584, 331
- Glover, S. C. O., & Mac Low, M.-M. 2007, *ApJ*, 659, 1317
- . 2011, *MNRAS*, 412, 337
- Glover, S. C. O., & Smith, R. J. 2016, *MNRAS*, 462, 3011
- Goldreich, P., & Lynden-Bell, D. 1965, *MNRAS*, 130, 97
- Goldsmith, P. F., Bergin, E. A., & Lis, D. C. 1997, *ApJ*, 491, 615
- Goldsmith, P. F., Heyer, M., Narayanan, G., et al. 2008, *ApJ*, 680, 428
- Gorenstein, P. 1975, *ApJ*, 198, 95
- Gould, R. J., & Salpeter, E. E. 1963, *ApJ*, 138, 393
- Green, G. M., Schlafly, E. F., Finkbeiner, D., et al. 2018, *ArXiv e-prints*, arXiv:1801.03555
- Greisen, E. W. 1973, *ApJ*, 184, 363
- Grenier, I. A., Casandjian, J.-M., & Terrier, R. 2005, *Science*, 307, 1292
- Güver, T., & Özel, F. 2009, *MNRAS*, 400, 2050
- Hagen, J. P., Lilley, A. E., & McClain, E. F. 1955, *ApJ*, 122, 361
- Hartmann, L., Ballesteros-Paredes, J., & Bergin, E. A. 2001, *ApJ*, 562, 852
- Hasenberger, B., Forbrich, J., Alves, J., et al. 2016, *A&A*, 593, A7
- Hausman, M. A. 1981, *ApJ*, 245, 72
- . 1982, *ApJ*, 261, 532
- Heiles, C., Reach, W. T., & Koo, B.-C. 1988, *ApJ*, 332, 313
- Heiles, C., & Troland, T. H. 2003a, *ApJS*, 145, 329
- . 2003b, *ApJ*, 586, 1067
- Heitsch, F., & Hartmann, L. 2008, *ApJ*, 689, 290

- Hennnebelle, P., Banerjee, R., Vázquez-Semadeni, E., Klessen, R. S., & Audit, E. 2008, *A&A*, 486, L43
- Herbst, E., & Klemperer, W. 1973, *ApJ*, 185, 505
- Herzberg, G. 1955, in *Liege International Astrophysical Colloquia*, Vol. 6, *Liege International Astrophysical Colloquia*, 291–331
- Heyer, M., & Dame, T. M. 2015, *ARAA*, 53, 583
- HI4PI Collaboration, Ben Bekhti, N., Flöer, L., et al. 2016, *A&A*, 594, A116
- Hildebrand, R. H. 1983, *QJRAS*, 24, 267
- Hill, A. S., Mac Low, M.-M., Gatto, A., & Ibáñez-Mejía, J. C. 2018, *ApJ*, 862, 55
- Hirashita, H. 2000, *PASJ*, 52, 585
- . 2012, *MNRAS*, 422, 1263
- Hollenbach, D., & McKee, C. F. 1979, *ApJS*, 41, 555
- Hollenbach, D., & Salpeter, E. E. 1971, *ApJ*, 163, 155
- Hopkins, P. F., Quataert, E., & Murray, N. 2011, *MNRAS*, 417, 950
- Huntress, Jr., W. T. 1977, *ApJS*, 33, 495
- Inoue, A. K. 2003, *PASJ*, 55, 901
- Inoue, T., & Inutsuka, S.-i. 2009, *ApJ*, 704, 161
- Israel, F. P. 1997, *A&A*, 328, 471
- Jenkins, E. 1989, in *IAU Symposium*, Vol. 135, *Interstellar Dust*, ed. L. J. Allamandola & A. G. G. M. Tielens, 23
- Jenkins, E. B., & Savage, B. D. 1974, *ApJ*, 187, 243
- Jenkins, E. B., & Tripp, T. M. 2011, *ApJ*, 734, 65
- Jones, A. P. 2004, in *Astronomical Society of the Pacific Conference Series*, Vol. 309, *Astrophysics of Dust*, ed. A. N. Witt, G. C. Clayton, & B. T. Draine, 347

- Jones, A. P. 2016, *Royal Society Open Science*, 3, 160224
- Jones, A. P., Fanciullo, L., Köhler, M., et al. 2013, *A&A*, 558, A62
- Jones, A. P., Köhler, M., Ysard, N., Bocchio, M., & Verstraete, L. 2017, *A&A*, 602, A46
- Jones, A. P., & Nuth, J. A. 2011, *A&A*, 530, A44
- Jones, A. P., Tielens, A. G. G. M., & Hollenbach, D. J. 1996, *ApJ*, 469, 740
- Jones, A. P., Tielens, A. G. G. M., Hollenbach, D. J., & McKee, C. F. 1994, *ApJ*, 433, 797
- Kalberla, P. M. W., Burton, W. B., Hartmann, D., et al. 2005, *A&A*, 440, 775
- Kalberla, P. M. W., & Haud, U. 2018, *A&A*, 619, A58
- Kanekar, N., Braun, R., & Roy, N. 2011, *ApJL*, 737, L33
- Kanekar, N., Subrahmanyan, R., Chengalur, J. N., & Safouris, V. 2003, *MNRAS*, 346, L57
- Kim, C.-G., Kim, W.-T., & Ostriker, E. C. 2011, *ApJ*, 743, 25
- Kim, C.-G., Ostriker, E. C., & Kim, W.-T. 2013, *ApJ*, 776, 1
- . 2014, *ApJ*, 786, 64
- Kim, W.-T., & Ostriker, E. C. 2001, *ApJ*, 559, 70
- . 2006, *ApJ*, 646, 213
- . 2007, *ApJ*, 660, 1232
- Kim, W.-T., Ostriker, E. C., & Stone, J. M. 2002, *ApJ*, 581, 1080
- Köhler, M., Stepnik, B., Jones, A. P., et al. 2012, *A&A*, 548, A61
- Köhler, M., Ysard, N., & Jones, A. P. 2015, *A&A*, 579, A15
- Koyama, H., & Inutsuka, S.-I. 2000, *ApJ*, 532, 980
- Kozasa, T., Nozawa, T., Tominaga, N., et al. 2009, in *Astronomical Society of the Pacific Conference Series*, Vol. 414, *Cosmic Dust - Near and Far*, ed. T. Henning, E. Grün, & J. Steinacker, 43

- Krumholz, M. R., McKee, C. F., & Tumlinson, J. 2008, *ApJ*, 689, 865
- . 2009, *ApJ*, 693, 216
- Krčo, M., & Goldsmith, P. F. 2010, *ApJ*, 724, 1402
- Kulkarni, S. R., & Heiles, C. 1988, *Neutral hydrogen and the diffuse interstellar medium* (Springer-Verlag), 95–153
- Kwan, J. 1979, *ApJ*, 229, 567
- Kwan, J., & Valdes, F. 1983, *ApJ*, 271, 604
- Lada, C. J. 1976, *ApJS*, 32, 603
- Lada, C. J., Lada, E. A., Clemens, D. P., & Bally, J. 1994, *ApJ*, 429, 694
- Langer, W. D., Velusamy, T., Pineda, J. L., et al. 2010, *A&A*, 521, L17
- Langer, W. D., Velusamy, T., Pineda, J. L., Willacy, K., & Goldsmith, P. F. 2014, *A&A*, 561, A122
- Larson, R. B. 1981, *MNRAS*, 194, 809
- Lee, M.-Y., Stanimirović, S., Murray, C. E., Heiles, C., & Miller, J. 2015, *ApJ*, 809, 56
- Lee, M.-Y., Stanimirović, S., Douglas, K. A., et al. 2012, *ApJ*, 748, 75
- Leitch-Devlin, M. A., & Williams, D. A. 1984, *MNRAS*, 210, 577
- Lenz, D., Hensley, B. S., & Doré, O. 2017, *ApJ*, 846, 38
- Lenz, D., Kerp, J., Flöer, L., et al. 2015, *A&A*, 573, A83
- Lepp, S., & Dalgarno, A. 1988, *ApJ*, 335, 769
- Li, D., & Goldsmith, P. F. 2003, *ApJ*, 585, 823
- Li, D., Xu, D., Heiles, C., Pan, Z., & Tang, N. 2015, *Publication of Korean Astronomical Society*, 30, 75
- Li, D., Tang, N., Nguyen, H., et al. 2018, *ApJS*, 235, 1
- Li, Y., Mac Low, M.-M., & Klessen, R. S. 2005, *ApJ*, 626, 823

- Liszt, H. 2001, *A&A*, 371, 698
- . 2014a, *ApJ*, 783, 17
- . 2014b, *ApJ*, 780, 10
- Liszt, H., & Lucas, R. 1996, *A&A*, 314, 917
- . 2002, *A&A*, 391, 693
- Mac Low, M.-M., Balsara, D. S., Kim, J., & de Avillez, M. A. 2005, *ApJ*, 626, 864
- Mac Low, M.-M., & Glover, S. C. O. 2012, *ApJ*, 746, 135
- Machida, M., Matsumoto, R., Nozawak, S., et al. 2009, *PASJ*, 61, 411
- Madden, S. C., Poglitsch, A., Geis, N., Stacey, G. J., & Townes, C. H. 1997, *ApJ*, 483, 200
- Magnani, L., Blitz, L., & Wouterloot, J. G. A. 1988, *ApJ*, 326, 909
- Magnani, L., & Onello, J. S. 1995, *ApJ*, 443, 169
- Magnani, L., & Siskind, L. 1990, *ApJ*, 359, 355
- Mathis, J. S., Rumpl, W., & Nordsieck, K. H. 1977, *ApJ*, 217, 425
- McCray, R. 1993, *ARAA*, 31, 175
- McCray, R., & Kafatos, M. 1987, *ApJ*, 317, 190
- McCrea, W. H., & McNally, D. 1960, *MNRAS*, 121, 238
- McKee, C. 1989, in *IAU Symposium, Vol. 135, Interstellar Dust*, ed. L. J. Allamandola & A. G. G. M. Tielens, 431
- McKee, C. F., & Ostriker, J. P. 1977, *ApJ*, 218, 148
- Mebold, U., Düsterberg, C., Dickey, J. M., Staveley-Smith, L., & Kalberla, P. 1997, *ApJL*, 490, L65
- Mebold, U., Winnberg, A., Kalberla, P. M. W., & Goss, W. M. 1982, *A&A*, 115, 223
- Meyerdierks, H., & Heithausen, A. 1996, *A&A*, 313, 929

- Miville-Deschênes, M.-A., Boulanger, F., Reach, W. T., & Noriega-Crespo, A. 2005, *ApJL*, 631, L57
- Mouschovias, T. C. 1974, *ApJ*, 192, 37
- Mouschovias, T. C., Kunz, M. W., & Christie, D. A. 2009, *MNRAS*, 397, 14
- Muller, C. A., & Oort, J. H. 1951, *Nature*, 168, 357
- Murray, C. E., Peek, J. E. G., Lee, M.-Y., & Stanimirović, S. 2018a, *ApJ*, 862, 131
- Murray, C. E., Stanimirović, S., Goss, W. M., et al. 2018b, *ApJS*, 238, 14
- . 2015, *ApJ*, 804, 89
- Nercessian, E., Benayoun, J. J., & Viala, Y. P. 1988, *A&A*, 195, 245
- Nguyen, H., Dawson, J. R., Miville-Deschênes, M.-A., et al. 2018, *ApJ*, 862, 49
- Ntormousi, E., Burkert, A., Fierlinger, K., & Heitsch, F. 2011, *ApJ*, 731, 13
- Okamoto, R., Yamamoto, H., Tachihara, K., et al. 2017, *ApJ*, 838, 132
- Oppenheimer, M., & Dalgarno, A. 1974, *ApJ*, 192, 29
- Ormel, C. W., Min, M., Tielens, A. G. G. M., Dominik, C., & Paszun, D. 2011, *A&A*, 532, A43
- Ossenkopf, V. 1993, *A&A*, 280, 617
- Ossenkopf, V., & Henning, T. 1994, *A&A*, 291, 943
- Ostriker, E. C., McKee, C. F., & Leroy, A. K. 2010, *ApJ*, 721, 975
- Paradis, D., Dobashi, K., Shimoikura, T., et al. 2012, *A&A*, 543, A103
- Parker, E. N. 1966, *ApJ*, 145, 811
- Payne, H. E., Dickey, J. M., Salpeter, E. E., & Terzian, Y. 1978, *ApJL*, 221, L95
- Peek, J. E. G., Heiles, C., Douglas, K. A., et al. 2011, *ApJS*, 194, 20
- Peek, J. E. G., Babler, B. L., Zheng, Y., et al. 2018, *ApJS*, 234, 2
- Pillitteri, I., Wolk, S. J., Megeath, S. T., et al. 2013, *ApJ*, 768, 99

- Pineda, J. L., Langer, W. D., Velusamy, T., & Goldsmith, P. F. 2013, *A&A*, 554, A103
- Planck Collaboration, Ade, P. A. R., Aghanim, N., et al. 2011a, *A&A*, 536, A19
- Planck Collaboration, Abergel, A., Ade, P. A. R., et al. 2011b, *A&A*, 536, A21
- . 2014a, *A&A*, 571, A11
- . 2014b, *A&A*, 566, A55
- . 2014c, *A&A*, 566, A55
- . 2014d, *A&A*, 566, A55
- Planck Collaboration, Fermi Collaboration, Ade, P. A. R., et al. 2015, *A&A*, 582, A31
- Pringle, J. E., Allen, R. J., & Lubow, S. H. 2001, *MNRAS*, 327, 663
- Rachford, B. L., Snow, T. P., Tumlinson, J., et al. 2002, *ApJ*, 577, 221
- Rachford, B. L., Snow, T. P., Destree, J. D., et al. 2009, *ApJS*, 180, 125
- Reach, W. T., Koo, B.-C., & Heiles, C. 1994, *ApJ*, 429, 672
- Remy, Q., Grenier, I. A., Marshall, D. J., & Casandjian, J. M. 2017, *A&A*, 601, A78
- . 2018, *A&A*, 616, A71
- Requena-Torres, M. A., Israel, F. P., Okada, Y., et al. 2016, *A&A*, 589, A28
- Robinson, B. J., & McGee, R. X. 1967, *ARAA*, 5, 183
- Rogers, A. E. E., & Barrett, A. H. 1967, in *IAU Symposium, Vol. 31, Radio Astronomy and the Galactic System*, ed. H. van Woerden, 77
- Roman-Duval, J., Israel, F. P., Bolatto, A., et al. 2010, *A&A*, 518, L74
- Roman-Duval, J., Gordon, K. D., Meixner, M., et al. 2014, *ApJ*, 797, 86
- Roy, N., Kanekar, N., Braun, R., & Chengalur, J. N. 2013a, *MNRAS*, 436, 2352
- Roy, N., Kanekar, N., & Chengalur, J. N. 2013b, *MNRAS*, 436, 2366
- Rugel, M. R., Beuther, H., Bihr, S., et al. 2018, *ArXiv e-prints*, arXiv:1803.04794

- Sanders, D. B., Solomon, P. M., & Scoville, N. Z. 1984, *ApJ*, 276, 182
- Saul, D. R., Peek, J. E. G., & Putman, M. E. 2014, *MNRAS*, 441, 2266
- Saury, E., Miville-Deschênes, M.-A., Hennebelle, P., Audit, E., & Schmidt, W. 2014, *A&A*, 567, A16
- Savage, B. D., Bohlin, R. C., Drake, J. F., & Budich, W. 1977, *ApJ*, 216, 291
- Savage, B. D., & Jenkins, E. B. 1972, *ApJ*, 172, 491
- Savage, B. D., & Mathis, J. S. 1979, *ARAA*, 17, 73
- Schlaflly, E. F., Meisner, A. M., Stutz, A. M., et al. 2016, *ApJ*, 821, 78
- Schlegel, D. J., Padmanabhan, N., Finkbeiner, D. P., et al. 2003, in *Bulletin of the American Astronomical Society*, Vol. 36, American Astronomical Society Meeting Abstracts, 589
- Scoville, N. Z., & Hersh, K. 1979, *ApJ*, 229, 578
- Scoville, N. Z., & Solomon, P. M. 1975, *ApJL*, 199, L105
- Silk, J. 1975, *ApJL*, 198, L77
- Silk, J., & Werner, M. W. 1969, *ApJ*, 158, 185
- Singh, P. D., & de Almeida, A. A. 1980, *A&A*, 84, 177
- Smith, R. J., Glover, S. C. O., Clark, P. C., Klessen, R. S., & Springel, V. 2014, *MNRAS*, 441, 1628
- Snow, T. P., & McCall, B. J. 2006, *ARAA*, 44, 367
- Speck, A. K., Barlow, M. J., Sylvester, R. J., & Hofmeister, A. M. 2000, *A&AS*, 146, 437
- Spitzer, Jr., L., & Jenkins, E. B. 1975, *ARAA*, 13, 133
- Stanimirović, S., Murray, C. E., Lee, M.-Y., Heiles, C., & Miller, J. 2014, *ApJ*, 793, 132
- Stecher, T. P., & Williams, D. A. 1967, *ApJL*, 149, L29
- Stepnik, B., Abergel, A., Bernard, J.-P., et al. 2003, *A&A*, 398, 551
- Strasser, S. T., Dickey, J. M., Taylor, A. R., et al. 2007, *AJ*, 134, 2252

- Tachihara, K., Fukui, Y., Hayakawa, T., & Inoue, T. 2018, arXiv e-prints, arXiv:1811.02224
- Tang, N., Li, D., Heiles, C., et al. 2016, *A&A*, 593, A42
- . 2017, *ApJ*, 839, 8
- Tielens, A. G. G. M. 2005, *The Physics and Chemistry of the Interstellar Medium* (Cambridge University Press)
- Tielens, A. G. G. M., & Hollenbach, D. 1985a, *ApJ*, 291, 747
- . 1985b, *ApJ*, 291, 722
- Tielens, A. G. G. M., McKee, C. F., Seab, C. G., & Hollenbach, D. J. 1994, *ApJ*, 431, 321
- Tomisaka, K. 1984, *PASJ*, 36, 457
- Valdivia, V., Hennebelle, P., Gérin, M., & Lesaffre, P. 2016, *A&A*, 587, A76
- Valiante, R., Schneider, R., Bianchi, S., & Andersen, A. C. 2009, *MNRAS*, 397, 1661
- Van Cleve, J. E., Hayward, T. L., Miles, J. W., et al. 1994, *APSS*, 212, 231
- van Dishoeck, E. F. 1990, in *Astronomical Society of the Pacific Conference Series*, Vol. 12, *The Evolution of the Interstellar Medium*, ed. L. Blitz, 207–228
- van Dishoeck, E. F., & Black, J. H. 1986, *ApJS*, 62, 109
- . 1988, *ApJ*, 334, 771
- Vázquez-Semadeni, E., Ryu, D., Passot, T., González, R. F., & Gazol, A. 2006, *ApJ*, 643, 245
- Viala, Y. P. 1986, *A&AS*, 64, 391
- Vuong, M. H., Montmerle, T., Grosso, N., et al. 2003, *A&A*, 408, 581
- Wada, K., Baba, J., & Saitoh, T. R. 2011, *ApJ*, 735, 1
- Wannier, P. G., Andersson, B.-G., Federman, S. R., et al. 1993, *ApJ*, 407, 163
- Watson, D., French, J., Christensen, L., et al. 2011, *ApJ*, 741, 58
- Watson, W. D. 1973, *ApJL*, 183, L17

—. 1974, *ApJ*, 188, 35

Wegner, W. 1993, *ACTAA*, 43, 209

Weingartner, J. C., & Draine, B. T. 1999, *ApJ*, 517, 292

Welty, D. E., & Fowler, J. R. 1992, *ApJ*, 393, 193

Weselak, T., Galazutdinov, G. A., Beletsky, Y., & Krełowski, J. 2010, *MNRAS*, 402, 1991

Wolfire, M. G., Hollenbach, D., & McKee, C. F. 2010, *ApJ*, 716, 1191

Wolfire, M. G., Hollenbach, D., McKee, C. F., Tielens, A. G. G. M., & Bakes, E. L. O. 1995, *ApJ*, 443, 152

Wolfire, M. G., McKee, C. F., Hollenbach, D., & Tielens, A. G. G. M. 2003, *ApJ*, 587, 278

Woodward, P. R. 1976, *ApJ*, 207, 484

Wouterloot, J. G. A. 1981, PhD thesis, Ph. D. thesis, University of Leiden (1981)

Xu, D., Li, D., Yue, N., & Goldsmith, P. F. 2016, *ApJ*, 819, 22

Ysard, N., Köhler, M., Jones, A., et al. 2015, *A&A*, 577, A110

Ysard, N., Abergel, A., Ristorcelli, I., et al. 2013, *A&A*, 559, A133

Zuo, P., Li, D., Peek, J. E. G., et al. 2018, *ApJ*, 867, 13